Wireless Communications and Mobile Computing

Smart Antennas and Intelligent Sensors Based Systems: Enabling Technologies and Applications 2022

Lead Guest Editor: Fawad Zaman
Guest Editors: Hing Cheung So, Daehan Kwak, Farman Ullah, and Sungchang Lee

Smart Antennas and Intelligent Sensors Based Systems: Enabling Technologies and Applications 2022

Wireless Communications and Mobile Computing

Smart Antennas and Intelligent Sensors Based Systems: Enabling Technologies and Applications 2022

Lead Guest Editor: Fawad Zaman
Guest Editors: Hing Cheung So, Daehan Kwak, Farman Ullah, and Sungchang Lee

Contents

Hindawi
Wireless Communications and Mobile Computing
Volume 2022, Article ID 4319779, 15 pages
https://doi.org/10.1155/2022/4319779

Research Article

A Novel Design and Study of a Self-Complimentary Miniaturized Millimeter Wave Antenna for Body-Centric Networks

Turki M. Alanazi,[1] **Mohammad Monirujjaman Khan**,[2] **H. M. Arifur Rahman**,[2] **and Md Nakib Alam Shovon**[2]

[1]*Department of Electrical Engineering, College of Engineering, Jouf University, Sakaka, Saudi Arabia*
[2]*Department of Electrical and Computer Engineering, North South University, Bashundhara, Dhaka 1229, Bangladesh*

Correspondence should be addressed to Mohammad Monirujjaman Khan; monirkhan.qmul@gmail.com

Received 15 February 2022; Accepted 13 August 2022; Published 2 September 2022

Academic Editor: Farman Ullah

A new self-complimentary compact antenna operating at 60 GHz within the millimeter wave frequency range has been presented in this paper. The design is intended for the wireless body-centric network (WBCN). The proposed compact design has a dimension of $4.5 \times 6.03 \times 1.59\,mm^3$. The antenna was designed with multiple geometrical structures held upon a narrow feed line with a rectangular slot and parasitic elements to increase bandwidth. Free space simulations of the antenna produced optimistic results in terms of gain, radiation efficiency, and bandwidth; a maximum gain of 6.7 dB was achieved with an efficiency of 84.5%. Parametric studies were carried out to better understand its nature by modifying the key design aspects and comparing the outcomes. A 3D human torso phantom was virtually created with natural human body properties, and the on-body performance of the design was tested by placing the antenna in its near field. With some slight deviation from their peak performance, on-body simulations displayed better results in most of the cases. The antenna was positioned five different gaps from the torso for future investigations. The result of the distance-based study was amazingly good as the antenna performance was consistent throughout all distances. 10.77 GHz of bandwidth is found for the closest distance to the human torso, while the on-body radiation efficiency is also outstanding; the minimum radiation efficiency recorded is 73.78 when the antenna is just a couple of millimeters away. Overall, the comparison shows that the antenna worked best when it was placed only 2 mm apart from the body. Investigation indicates the antenna is a promising candidate for BCN applications because of its wider bandwidth and better on-body efficiency.

1. Introduction

For many good reasons, millimeter wave antennas grab numerous researchers' attention worldwide while looking for a suitable antenna for BCN or wireless body area networks (WBAN). Millimeter wave (mmWave) microstrip patch antennas have smaller physical dimensions; fit well in small electric devices and equipment; are lightweight, less power-consuming, and less complicated in structure, [1–3]; and are mostly suitable for short-ranged high speed and larger amounts of data transmission [4, 5]. Such properties make mmWave antennas potential candidates for body-centric networks. The mmWave frequency range extends from 30 GHz to 300 GHz, with wavelengths ranging from 10 mm to 1 mm [6–8]. Within this wide frequency range, several frequency bands are free for public use, which has made them more popular among others. Such a popular frequency is 60 GHz within the V-band spectrum, which was assigned as unlicensed by the FCC [9, 10]. But, there are certain challenges while using this frequency for communication, which is the high attenuation for atmospheric absorption. This limits its usage for long-distance communications [6, 10, 11]. However, for body-centric network applications, especially for advanced future healthcare facilities, 60 GHz can be implemented.

However, one big question mark still remains after the creation of a new millimeter wave antenna: will this antenna perform the same while it is in the near-field of a human

body? This becomes the more challenging part of designing a suitable antenna for WBAN or BCN. The performance of the antenna is influenced by the human body's capacitive nature, especially when the antenna is in its near-field. This effect can be noticed in almost all the antenna parameters, such as gain, efficiency, return loss, or bandwidth [12–14]. Sometimes, a perfectly tuned antenna behaves so bizarrely in the near-field of an organic body that it becomes ineligible to operate for human body near-field applications. The good news is that, in most circumstances, a few millimeters can prevent adverse effects on the human body.

Wireless communications find the human body to be an unwelcoming and frequently hostile environment. Human-to-human and human-to-self networking using wearable and embedded wireless sensors is referred to as body-centric wireless communications. WBAN, wireless sensor networks (WSNs), and wireless personal area networks (WPANs) are all included in this topic (WPANs). Advanced healthcare applications, smart home appliances, entertainment, security and identification systems, even in space exploration and military applications, all benefit from body-centric wireless communications [15]. Especially, in wearable computers, a field that focuses on high amounts of computer resources embedded with sensors and interfacing devices, connecting wears requires performing real-time and fast data transfer in the gigabytes per second range. These tasks could be simplified by implementing wireless body area networking (WBAN) with high-speed, contactless wireless data exchange.

In low-frequency operations, electromagnetic waves have greater penetration depth on human bodies [16–18]. But, for millimeter waves, the penetration depth is very low. The popular 60 GHz frequency of V-band has only a 0.5 millimeters of penetration depth on human body which cannot pass through the skin layer of the human body on most of the cases. But, it does not mean only half of a millimeter of the external part of the human body will affect an antenna's performance. Besides, the presence of the human body in close proximity to an antenna works as a catalyst and deviates the antenna's natural performance.

One of the most common fields of BCN or WBAN is the healthcare department, where a patient's vital physical signs are collected with wearable nodes with included antennas. These nodes, placed on different parts of the human body, keep them connected with each other and the master nodes connected with external data servers and online clouds. So, antennas in these systems must withstand their operability while in the near field of a human body. Other short-ranged communication may include connection between multiple devices within the indoor environments of hospital wards.

Few antennas for body-centric networks operating at frequencies lower than mmWave [19–25], i.e., ultra wideband, demonstrated promising results, but had larger physical dimensions. Among the recent research made on millimeter wave designs, few of them performed notably well. Chahat et al. presented and analyzed two printed antenna designs with the RT Duroid 5880 substrate with different techniques [26]; one of them is a linearly polarized antenna, and the other is a linearly polarized aperture coupled patch antenna. The antennas are made with a square-shaped substrate with a 10 mm × 10 mm dimension. Both the designs were tested on an artificially made torso phantom and performed well in terms of gain, efficiency, and SAR analysis.

A disc-shaped wearable antenna for body area networks was presented by Puskely et al. [27] and achieved a gain of 5.2 dB with at least 25% efficiency when positioned close to the human body. An antenna with a 14 mm × 10.5 mm physical size was presented by Wu et al., claimed to be more suitable for body-centric networks with higher gain [19] and a maximum of 63% on-body efficiency. A textile-mounted PIFA antenna was presented by Vilas S. Ubale and Lamba, which was innovative and comfortable for BAN applications and had an operating frequency of 2.45 GHz [28]. Jiang et al. proposed a circularly polarized flexible design for wireless body area network (WBAN) which they claimed to be highly efficient with a maximum efficiency of 79% and 5.2 dB of gain [29]. Brizzi et al. presented two antennas with electromagnetic band gaps with two different structures: cylindrical structures and woodpile planar designs for body area networks operating at 60 GHz frequency [30]. The antennas showed directivity of 7.55 dBi and 6.72 dBi, respectively. According to the authors, the first antenna is better suited for on-body applications. Alibakhshikenari et al. have presented several millimeter wave antenna and array designs [2, 31–36] with unique design methods and techniques. In one research authors proposed a beam scanning leaky wave antenna (LWA) which operates on 55 GHz to 65 GHz. The antenna was designed by the authors using metamaterials and a composite right/left handed transmission line (CRLH-TL).

Except for those mentioned above, a little other research on millimeter wave body area network antennas like [6, 37–39] also produced promising results. This paper proposes a millimeter wave patch antenna design intended for the body-centric network (BCN). Antenna design, free space simulation, parametric study, on-body simulation, distance-based study, and conclusion are the other aspects of the work. The work is divided into seven pieces altogether. The first section discusses on millimeter wave, BCN, and BAN with a few related recent works. The antenna construction is presented and explained in Section 2. Sections 3 and 4 present, respectively, the results of the parametric investigation and the free space simulation. On-body simulation results are evaluated at a distance in Sections 5 and 6. The simulations are used to establish a conclusion in the last portion.

2. Antenna Design

The popular electromagnetic element design and simulation program computer simulation technology (CST) Microwave Studio Suite, which runs on Microsoft Windows, was used to build and simulate the proposed antenna. The antenna is made with a self-complementary design. The radiator patch of the antenna consists of two "U"-shaped bricks placed face-to-face with a chain-like arrangement within a square slot inside a circle. This shape on the top of the antenna has been chosen due to the impedance matching and wider impedance bandwidth of the antenna. There is a slot on

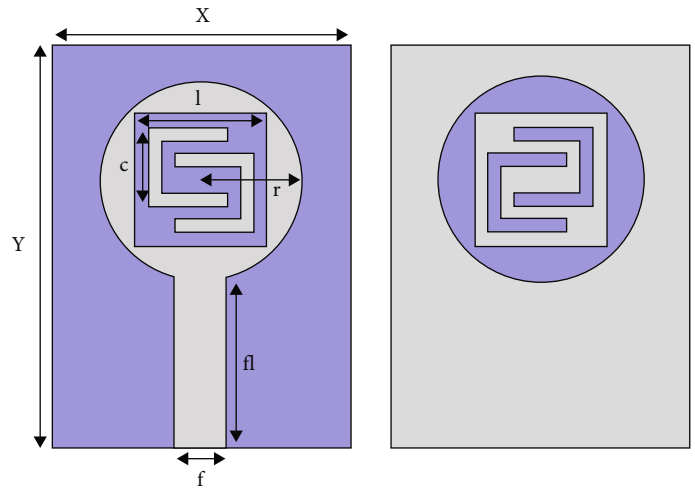

Figure 1: Antenna dimensions.

the ground plane of the antenna, and this was done to obtain the impedance matching and wider bandwidth. Having a ground plane on the backside of the antenna will provide a shield between the antenna and the human body, which will have less effect on the antenna parameters from the human lossy body tissues.

The antenna with the substrate is 9.42 mm long and 4 mm wide. The electrical size of the antenna over the length and width of the substrate of the antenna is 0.53λ and 1.25λ, respectively. The circular patch of the radiator has a radius of 1.5 mm. The square slot has a side length of 4.5 mm on each side. The U bricks have a width of 0.28 mm. The main circular shape is connected to the waveguide port with a feed line. The length of the feed line is 2.57 mm, which is denoted as "fl" in Figure 1, and the width of the feed is $f = 0.8$ mm. The impedance matching of the antenna can be varied by changing the width of the feedline of the antenna. The frequency shifting is possible by changing the size of the circular shape of the radiating element of the proposed antenna.

Table 1 shows the dimensions of the different parts of the antenna, where "x" and "y" are the length and width of the antenna, respectively. Values for the other parameters of Figure 1 can also be found in the table.

Similarly, in Table 2, the thickness of the different layers of the antenna, their materials, and their corresponding permittivity are shown. The material used for the ground and the patch radiator is PEC (perfect electric conductor). Both the layers have a similar thickness of 0.035 mm. The antenna substrate is made of Rogers RT6002 with a dielectric constant of 2.94. Rogers RT6002 has an excellent dimensional stability, and, due to its low-loss property, it is suitable for getting resonant point at higher frequency ranges. Because of this, RT6002 was selected as the substrate material [40–42]. 1.52 mm thick is the substrate layer. Since the ground and the radiator patches are made of perfect electric conductors, their relative permittivity could not be defined.

Figure 2 depicts views of the antenna taken from various angles. Figures 2(a) and 2(b) show the antenna as seen from the front and back, respectively. The antenna's right view and left view are shown in Figures 2(c) and 2(d), respectively. Figures 2(e) and 2(f) depict the antenna from the front and back in three dimensions, with the various layers denoted.

Table 1: Dimensions of the antenna.

S. no.	Parameter	Value (mm)
1	x	4.50
2	y	6.03
3	l	2.00
4	c	1.20
5	r	1.50
6	f	0.80
7	fl	2.57

Table 2: Materials for antenna.

Parameter	Thickness (mm)	Material	Epsilon
Ground	0.035	PEC	—
Substrate	1.52	Rogers RT6002 (loss free)	2.94
Patch radiator	0.035	PEC	—

3. Free Space Simulations

A waveguide fed port was used to excite the antenna for simulations. The port is attached to the bottom surface of the antenna structure, touching the feedline of the radiator and the substrate. The dimension of the port is 3.84×2.305 mm^2. Before starting simulation, open space boundary has been selected with $\lambda/4$ mm of added space from the structure on each surface. For far field simulation, 10 mm of space was accounted for on each surface.

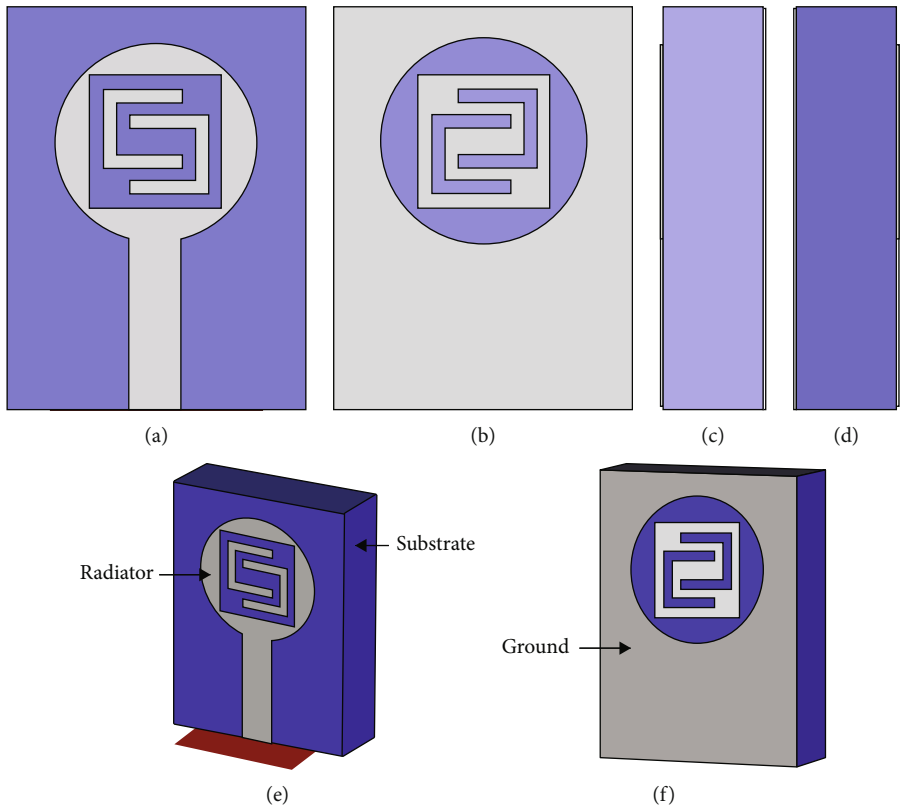

Figure 2: Antenna design: (a) frontage view, (b) rear view, (c) right view, (d) left view, (e) perspective frontage view, and (f) perspective rear view.

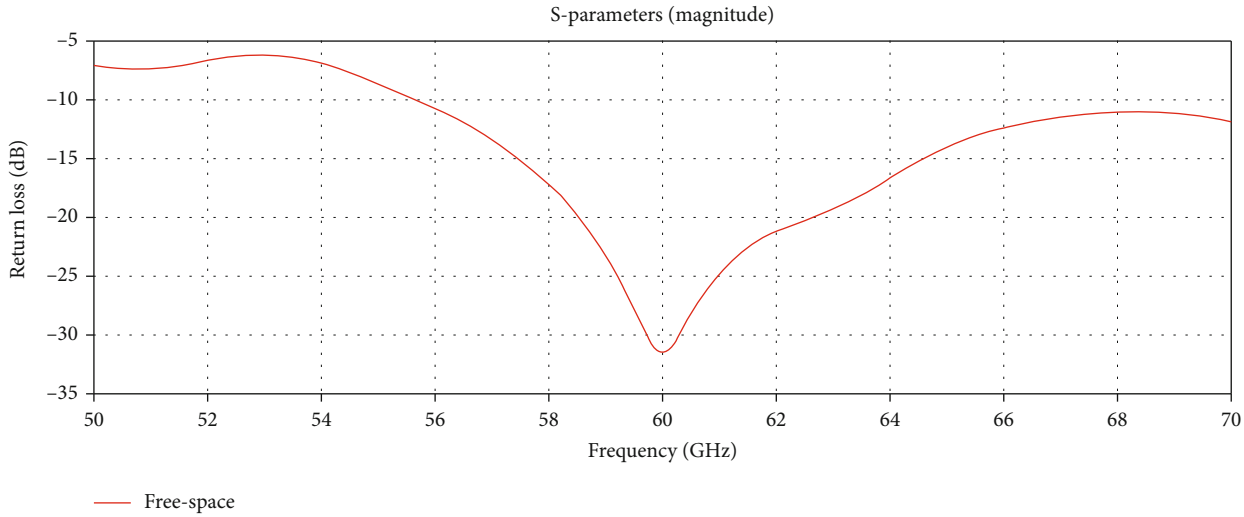

Figure 3: Return loss for free-space.

3.1. Return Loss. Within the frequency range of 50 GHz to 70 GHz, the antenna was modelled in free space. The frequency response is provided below. Figure 3 displays the antenna's return loss performance across the simulated frequency range. At 60 GHz, the resonance can be observed. The antenna becomes operational with less than -10 dB return loss from 57.5 GHz and remains under -10 dB line up to the upper simulated frequency limit. The return loss was found to be -31.45 dB at 60 GHz.

3.2. 3D Radiation Patterns. Figure 4 shows the 3D radiation pattern of the antenna with the transparent pattern and visible antenna structure on the left image and without the structure on the right. The antenna shows maximum gain along the direction of the Y axis with a value of 6.71 dB.

3.3. 2D Radiation Patterns. Two-dimensional radiation patterns on the XY plane and the YZ plane, correspondingly, are shown in Figures 5(a) and 5(b) at 60 GHz. The principal

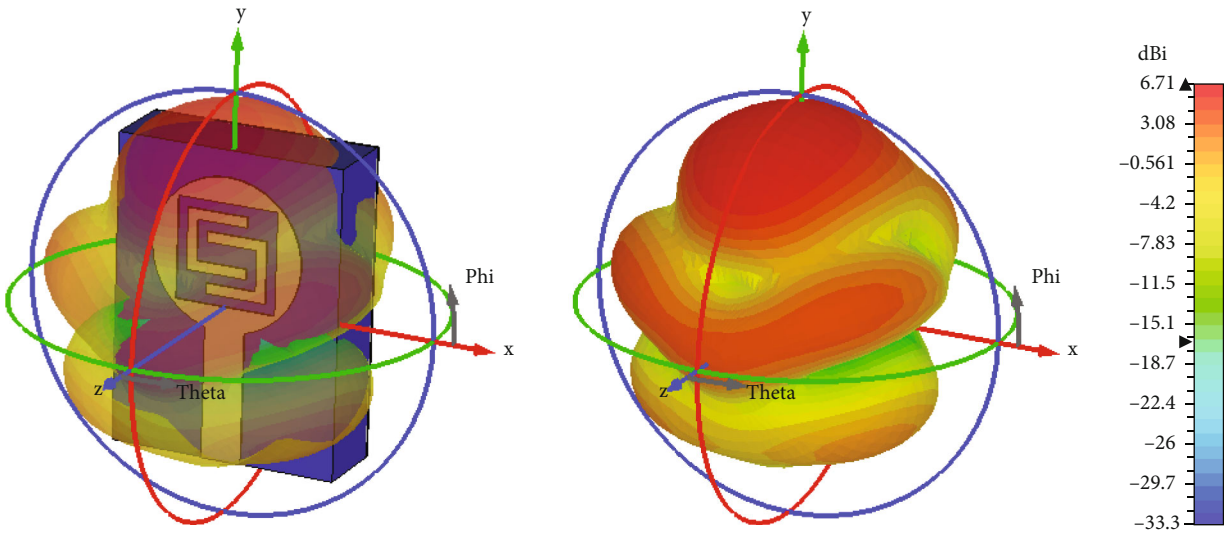

Figure 4: 60 GHz free space 3D radiation pattern.

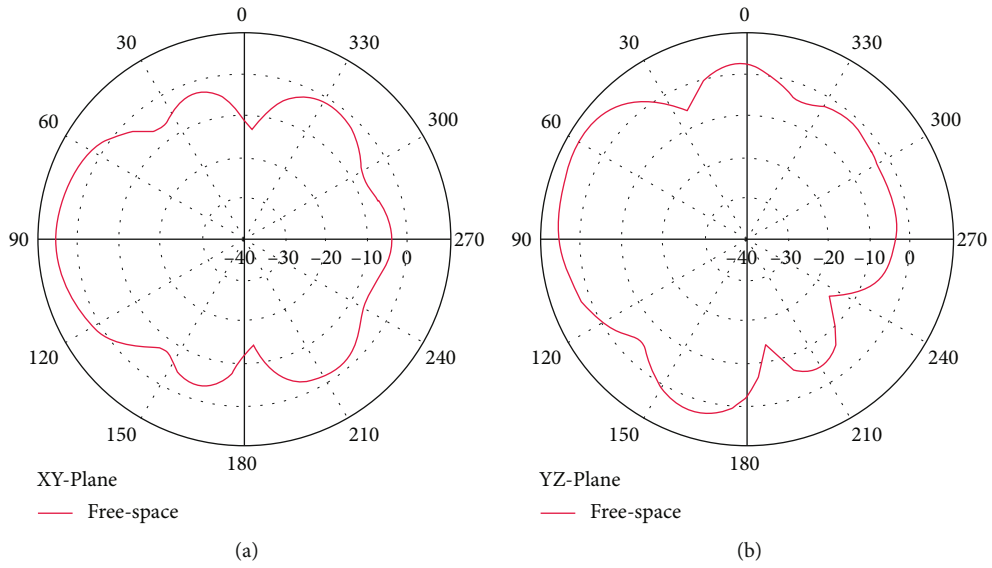

Figure 5: The XY plane and the YZ plane in free space: a 2D radiation pattern for 60 GHz.

lobe orientation of the antenna's radiation pattern in the XY plane is 90 degrees. In the YZ plane pattern, the major lobe orientation is about 60 degrees.

3.4. Analysis of the Surface Current. When the antenna is engaged at a 60 GHz frequency using "port 1," Figure 6 shows the surface current distribution. In the area between the ground plane and the radiator patch, the peak density was 148 amps per meter. At the resonant frequency, Quasi TEM mode propagation was detected at the waveguide excitation.

3.5. VSWR. The antenna's voltage standing wave ratio (VSWR) is shown in Figure 7. At the resonant frequency, the VSWR value is less than 1.1, which is very near to the optimum value.

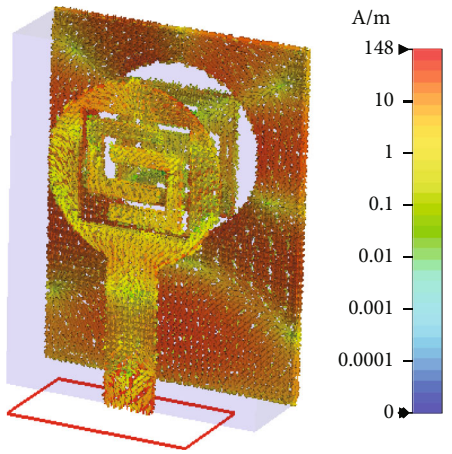

Figure 6: For 60 GHz, the available surface current.

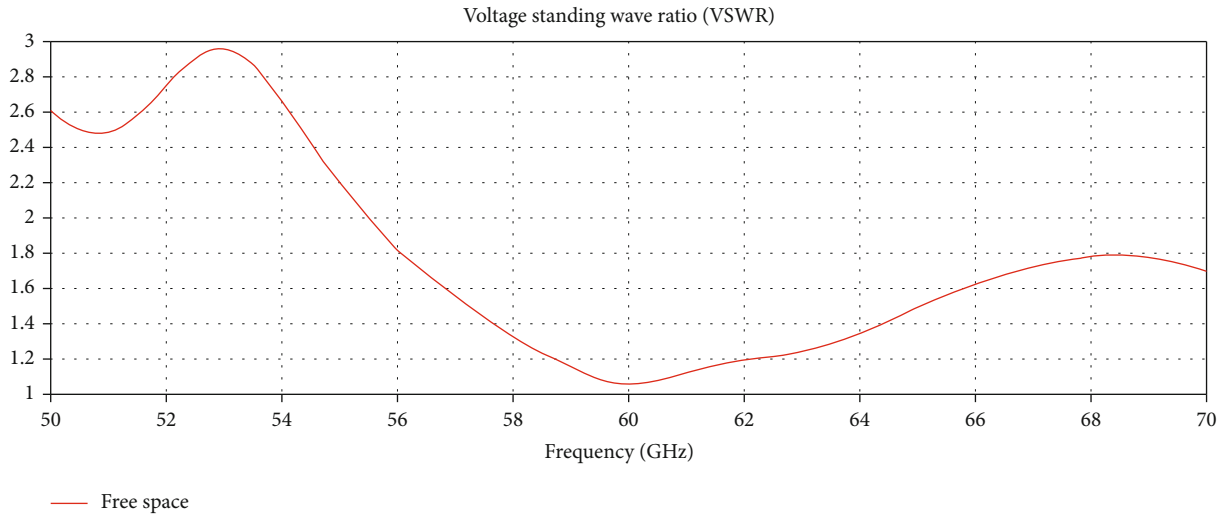

Figure 7: VSWR for free space 60 GHz.

3.6. Efficiency vs. Frequency. Figure 8 shows how the radiation efficiency changes with respect to frequency. Although higher efficiencies can be noticed in other frequencies around 60 GHz, yet it shows more than 84 percent of efficiency in our desired frequency.

3.7. Gain vs. Frequency. Figure 9 presents the maximum gain vs. frequency curve. The gain has gradually increased from 52.5 GHz to 57 GHz but has slightly decreased around 61 GHz before reaching its maximum. Although slightly higher gains can be seen in other frequencies, it still produces 6.7 dBi of gain at our selected frequency of 60 GHz.

4. Parametric Study

The parametric research was conducted after the free space simulations with the previously mentioned dimensions in order to understand the nature of the design and how it affects the output results. The measurements were changed, the simulation was run again, and the results were compared to the base results. The parametric study was done based on the changes in their corresponding return loss response curves. To achieve this, the antenna dimension was altered by varying the antenna substrate's width, which also altered the antenna's overall size.

In Figure 10, return losses are plotted for changing the width of the substrate by first decreasing and then increasing by 0.5 mm. When the substrate's length was reduced to 4 mm, the resonance frequency was slightly displaced to the right, and the green curve shows the antenna's return loss at that point. Similarly, increasing it to 5 mm (blue curve) tilts it to the right. In both cases, return loss values increased more than the original curve found for the original design. When the design is reverted back to the original design, the length of the substrate is varied in a similar manner. The length of the substrate "y" is first decreased to 6 mm and then increased to 6.05 mm.

In the above, Figure 11 presents the return loss responses when the antenna substrate length is changed. The green curve represents the return loss when the length is reduced by 0.03 mm. In this case, the return loss curve is slightly right-shifted with respect to the resonant point. The RL value at 60 GHz remains almost identical to the original design's plot. When the length is increased by 0.02 mm (blue curve), the resonant point is slightly left-shifted. The RL value is also reduced for this scenario.

The antenna's feed width, "fw," is changed after the preceding alteration is made in order to see how it affects the return loss curve. The original feed width was 0.8 mm wide. It was first reduced to 0.6 and the simulation result was plotted. The green line in the above figure (Figure 12) represents the return loss curve for the reduced feed width design, which degrades the RL value and shifts the curve to the right. Then, the feed width is made wider and kept at 1 mm. The blue curve in the figure shows the return loss for this scenario, where the resonant point is slightly left-shifted. The RL value at the selected frequency is somewhat similar to the original design.

A few other tests on the antenna were performed to justify its basic design, such as when the "U"-shaped parasitic elements were not present or when there was no slot at all on the radiator patch. This test also includes the justification of the ground plane's role. The following table presents the test results.

Table 3 shows the antenna parameters when the radiator patch is missing the "U"-shaped parasitic elements and the ground plane. It also shows the change in antenna behavior if the patch remains unslotted. All the parameters are compared with the free space. In all the scenarios, the resonant point deviates from the desired 60 GHz. However, the original design produces more optimized gain and efficiency while keeping the resonant point at 60 GHz.

4.1. Comparison. The table given below summarizes the results of all the parametric studies done above. The results were compared in terms of gains, efficiencies, bandwidths, and return losses. The above parametric study produces

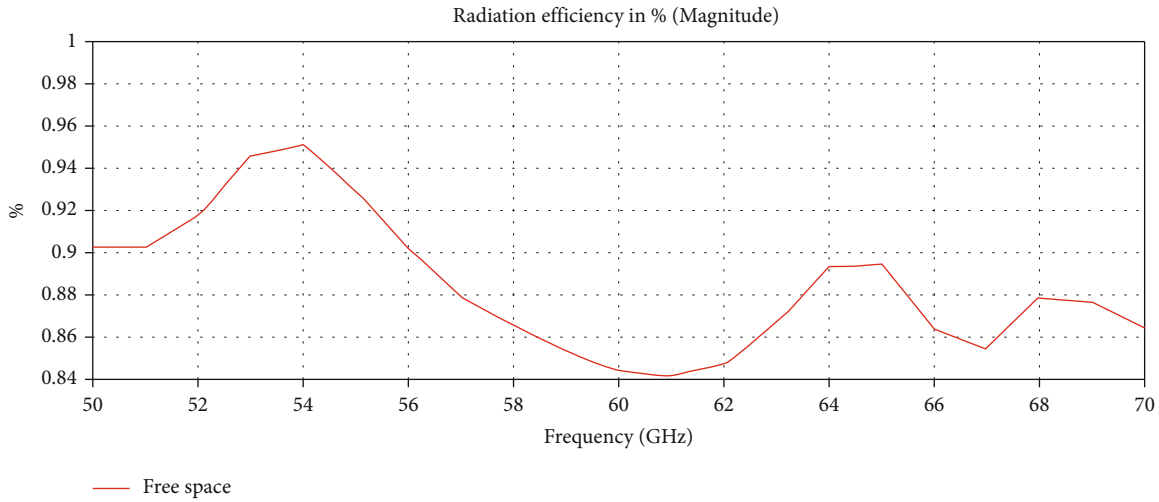

Figure 8: Efficiency vs. frequency.

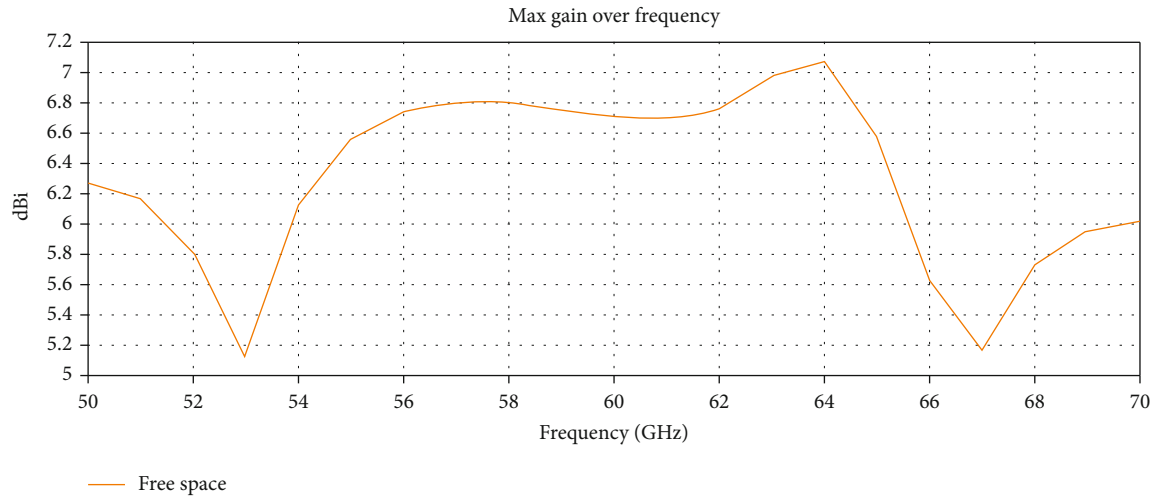

Figure 9: Maximum gain vs. frequency.

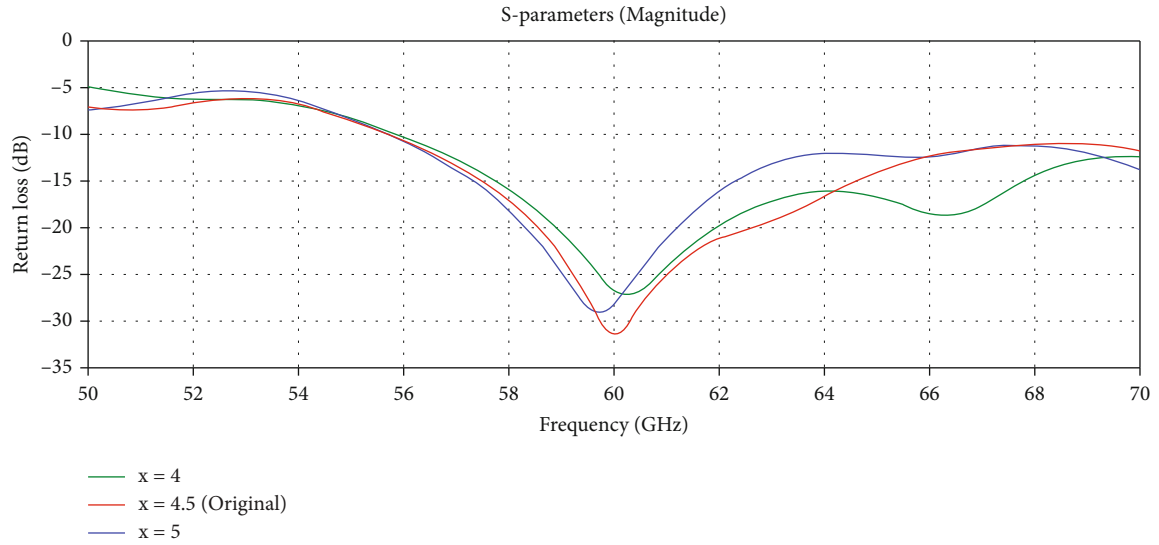

Figure 10: Comparison of return loss for various x values.

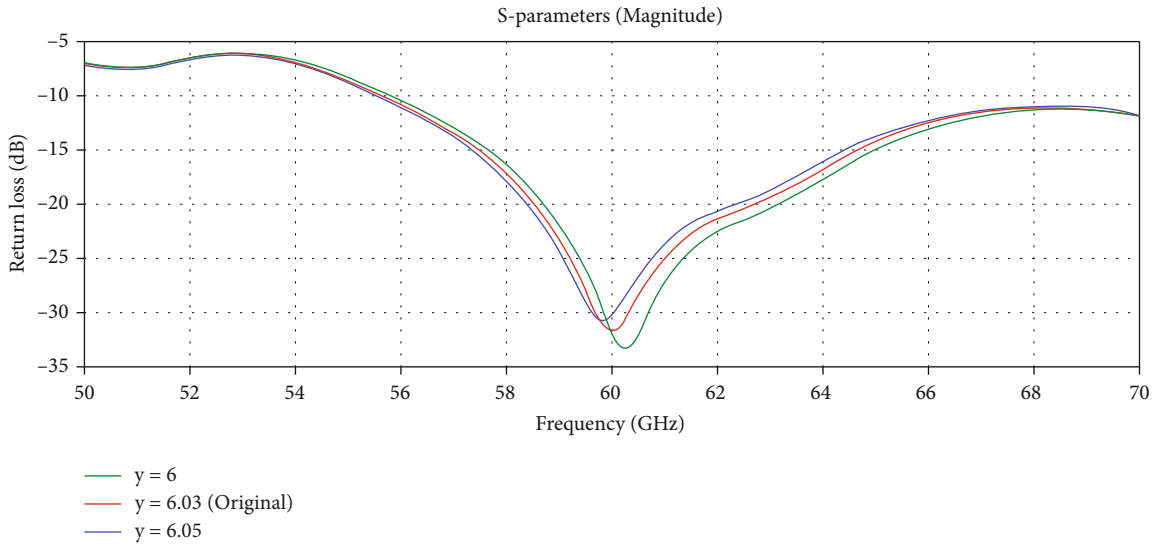

Figure 11: Return loss comparison with different y values.

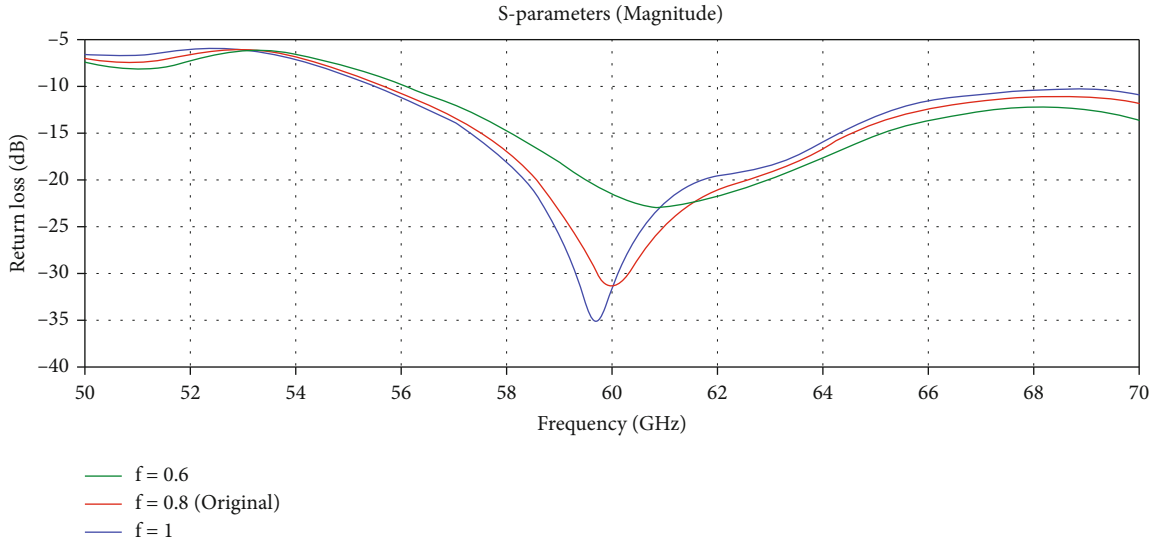

Figure 12: Return loss comparison with different "f" values.

Table 3: Justification of the basic model.

Parameter	Original design	Without parasitic elements	Without slot (solid patch)	Without ground plane
Center frequency (GHz)	60	61.52	59	70
Bandwidth (GHz)	—	—	—	—
Gain (dBi)	6.712	5.081	7.958	6.566
Radiation efficiency (%)	84.48	86.10	87.85	92.02

the results shown in Table 4. The results are compared with the free space simulation findings. In the case of changing the substrate dimensions, it could not produce better results than the original design. In one case, the feed width modification made the return loss lower than the original but shifted the resonant frequency from the desired point. Therefore, the original design produces more appropriate and acceptable results for the 60 GHz frequency.

Table 4: Analytical study.

Parameters	Free-space	$x = 4$	$x = 5$	$y = 6$	$y = 6.05$	$f = 0.6$	$f = 1$
Return loss (dB)	-31.45	-26.63	-28.18	-31.47	-30.10	-21.56	-31.77
Bandwidth (GHz)	—	—	—	—	—	—	—
Gain (dBi)	6.712	6.675	7.006	6.744	6.690	6.806	6.644
Radiation efficiency (%)	84.48	87.57	84.97	84.64	84.50	84.24	85.09

Table 5: Torso phantom dimension values.

Parameter	Length (mm)	Width (mm)	Thickness (mm)	Relative permittivity	Conductivity (S/m)
Skin	12	10	2	7.9753	36.397
Fat	12	10	3	3.1324	2.8152
Muscle	12	10	4	12.856	52.825

5. On-Body Performance Test

The antenna was tested on a computer-generated, three-dimensional human torso phantom because it is meant to be used in a WBAN. The muscles, fat, and skin that make up the human body's top three layers made up the phantom. Three layers are layered on top of each other; the muscle layer is the thickest, measuring 4 millimeters in thickness. The fat layer, with a thickness of 3 millimeters, is next put between the muscle and the skin. The skin is the outermost layer, positioned above the muscle. This is the thinnest layer among the others. The average layer thickness of the human body was used to choose these thicknesses at random. They are created by taking use of the layers' electromagnetic properties. These three layers together form the torso phantom, which measures 12 mm in length and 10 mm in width. The torso is depicted graphically in Figure 10. Then, the torso phantom was mounted with the novel antenna design that was previously shown, and its performance was evaluated by duplicating all of the findings. The results were next contrasted with those found in a free-space simulation. The dimensions and electromagnetic properties of the torso phantom's three levels are presented in the table below. In Table 5, the dimensions of the different layers are given one by one. The relative permittivity of the materials used for skin, fat, and the muscle layers is 7.96, 3.13, and 12.86, respectively. The conductivity of the material is also given in siemens per meter.

Figure 13 depicts the side view of the virtually created human torso model where the three different layers of skin, fat, and muscle are shown.

5.1. Overbody Return Loss. The antenna's on-body return loss is depicted in Figure 14 in the figure above. A 4-millimeter distance to the body was taken into account to replicate this. The bandwidth and return loss have both decreased as a result of the human body effect, although the RL value is still significantly below -10 dB. The on-body bandwidth was found to be around 10 dB for a distance of 4 mm.

5.2. On-Body VSWR. The antenna's on-body voltage standing wave ratio is shown in Figure 15, while the antenna is kept 4 mm away from the torso. The VSWR value at the desired 60 GHz frequency was found to be below 1.7 for the on-body simulation, which stays in the acceptable region as long as it is below 2.

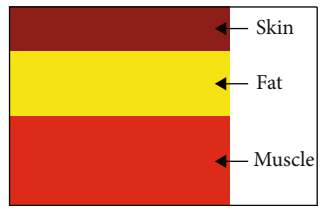

Figure 13: Torso phantom.

5.3. Pattern of On-Body Radiation. The original model for the antenna's on-body performance used 4 mm as the standard distance from the human torso. Figure 16 shows a simulated 3D far-field radiation pattern with and without the structure when the proposed antenna is placed 4 mm from the torso phantom. The maximum increase on the x-axis was measured at 6.67 dBi.

5.4. On-Body 2D Radiation Patterns. In Figure 17, 2D radiation patterns of the antenna are presented when the antenna is placed 4 mm close to the human torso phantom. Figure 17(a) is the pattern on the XY plane, where the on-body radiation pattern looks very much similar to the free space pattern. There is almost no change in lobe directions and gains. In Figure 17(b), the on-body pattern was slightly deviated from the free space result which is expected.

6. Distance-Based Study

To further understand the antenna's performance on the human body, it was put over the torso at five different distances and simulated to see how its performance changed. The torso phantom is separated by 2 mm, 4 mm, 6 mm, 8 mm, and 10 mm.

Figure 18 shows the antenna's placement above the chest at different heights. Antenna parameters were investigated for each distance using different simulations, and they were

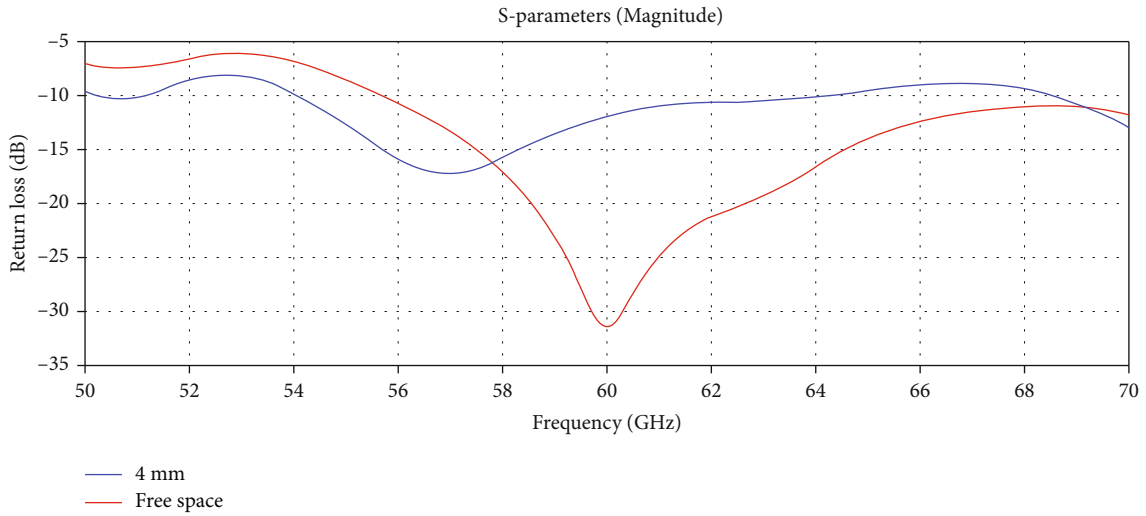

Figure 14: S-parameters comparison between free space and on-body.

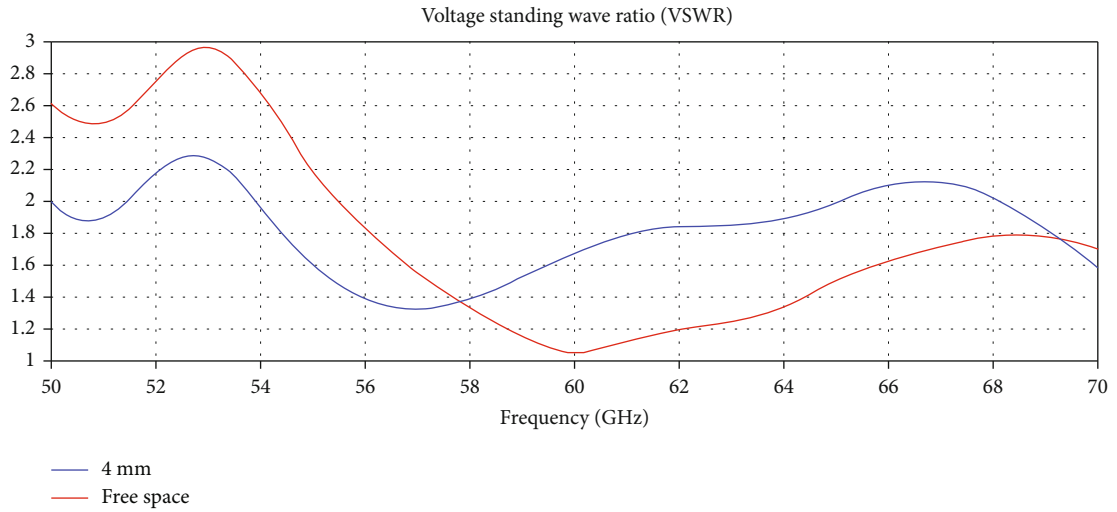

Figure 15: Free-space and on-body VSWR comparison.

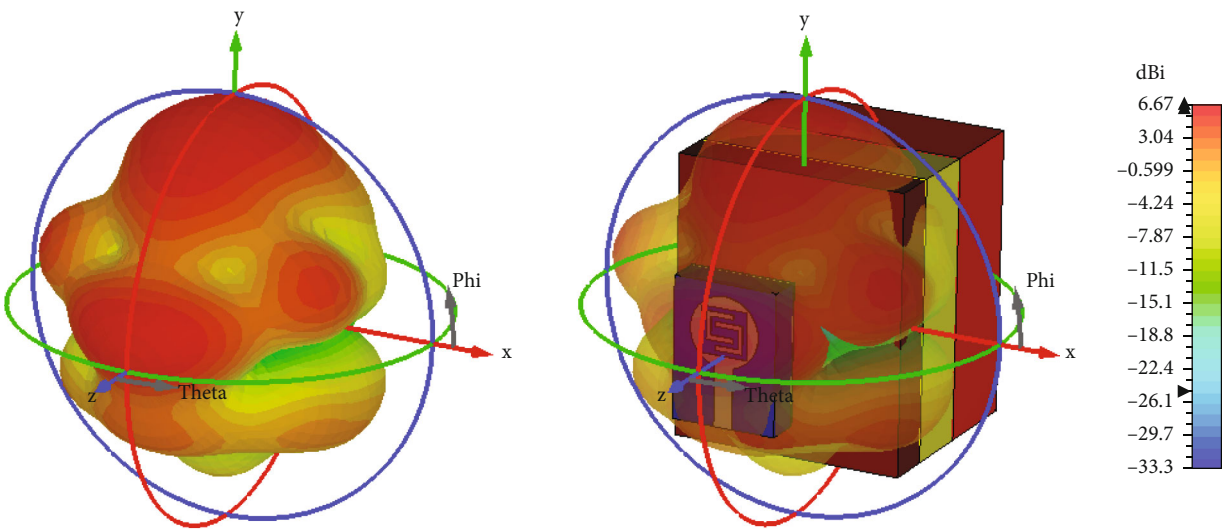

Figure 16: Far-field 3D view on-body 4 mm far without and with structure at 60 GHz.

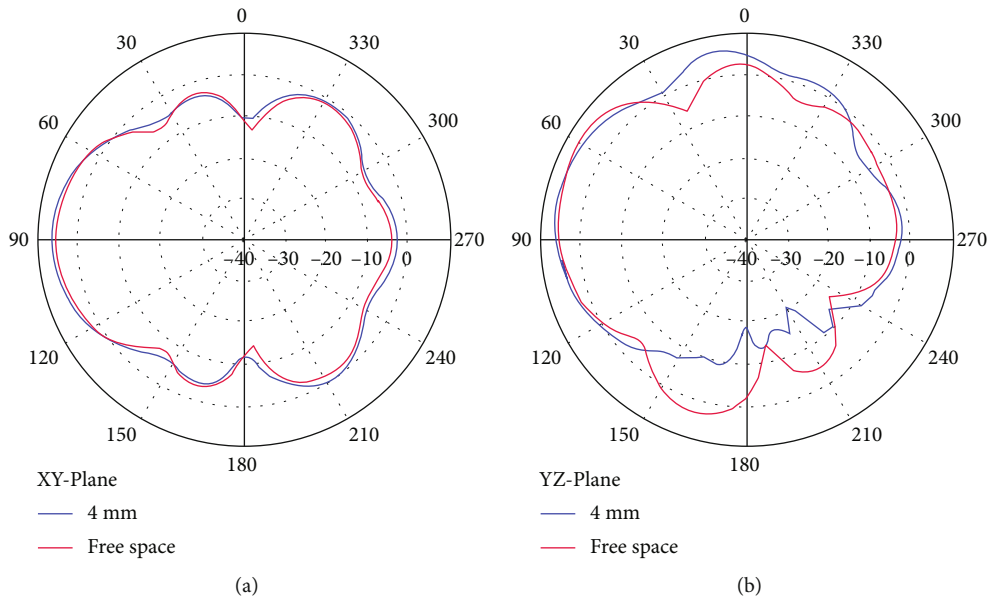

Figure 17: Comparison of the free-space and on-body 2D radiation patterns at 4 mm (a) on the XY plane and (b) on the YZ plane.

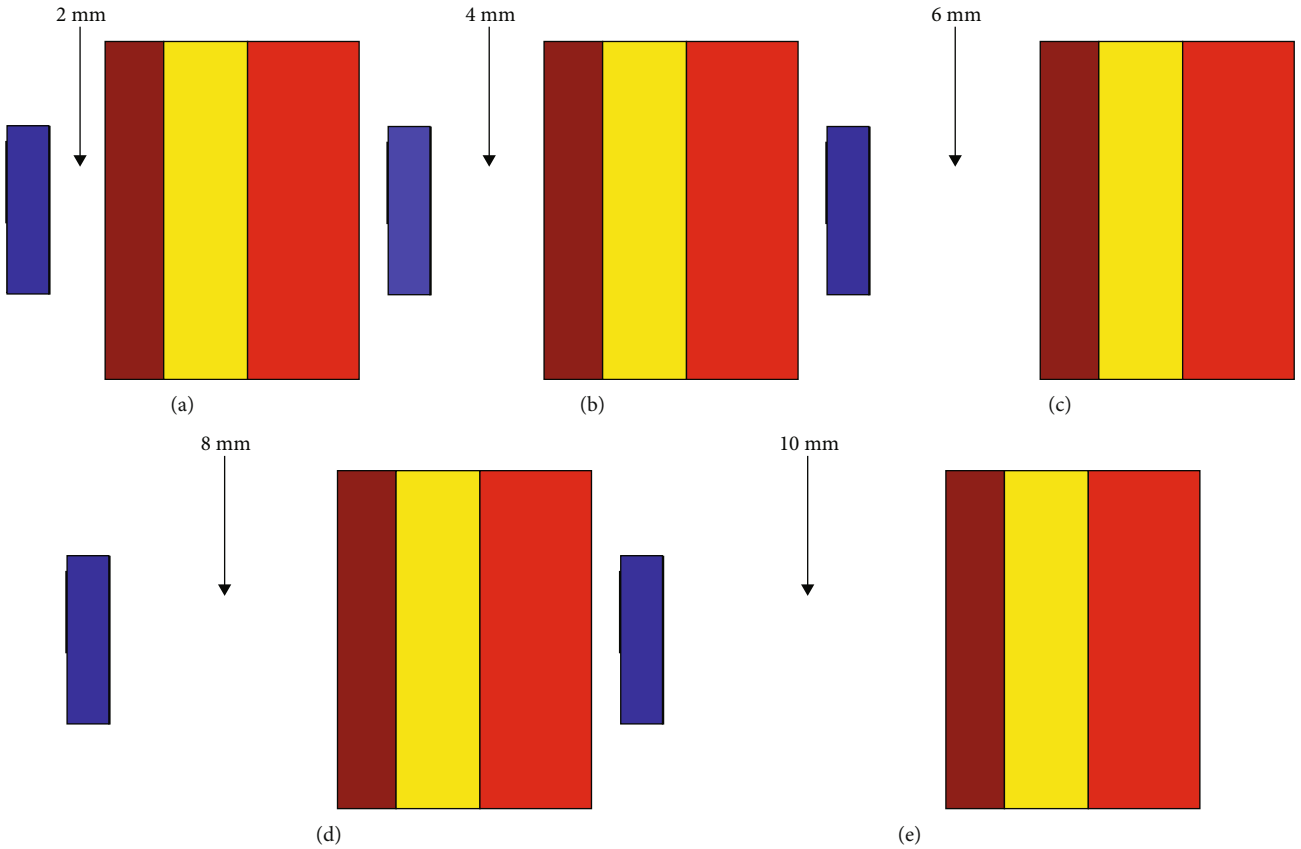

Figure 18: Views looking to the right showing placements of on-body antennas at various distances, including (a) from 2 mm, (b) from 4 mm, (c) from 6 mm, (d) from 8 mm, and (e) from 10 mm.

then compared with one another and the results from the earlier simulations of empty space.

For the return loss results, an antenna kept 8 mm apart from the human body exhibits the lowest return loss, which is slightly below-13 dB. For all the other cases, the return loss value oscillates between -12 dB and -14 dB, which can be seen in the Return Loss comparison plot displayed above (Figure 19). Bandwidths stay almost similar for all the

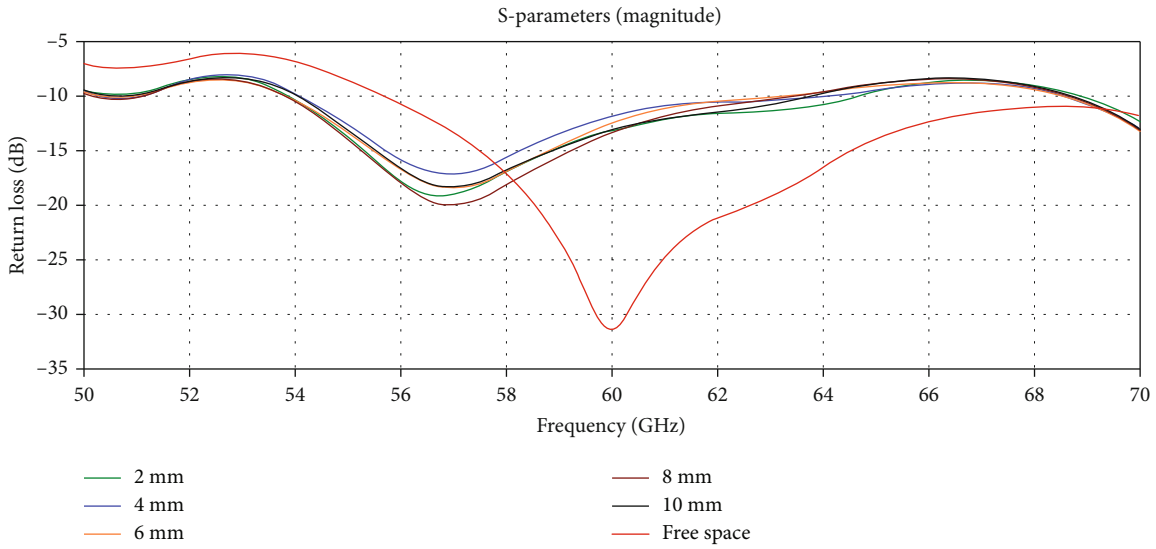

Figure 19: *S*-parameter comparison for varying on-body distances.

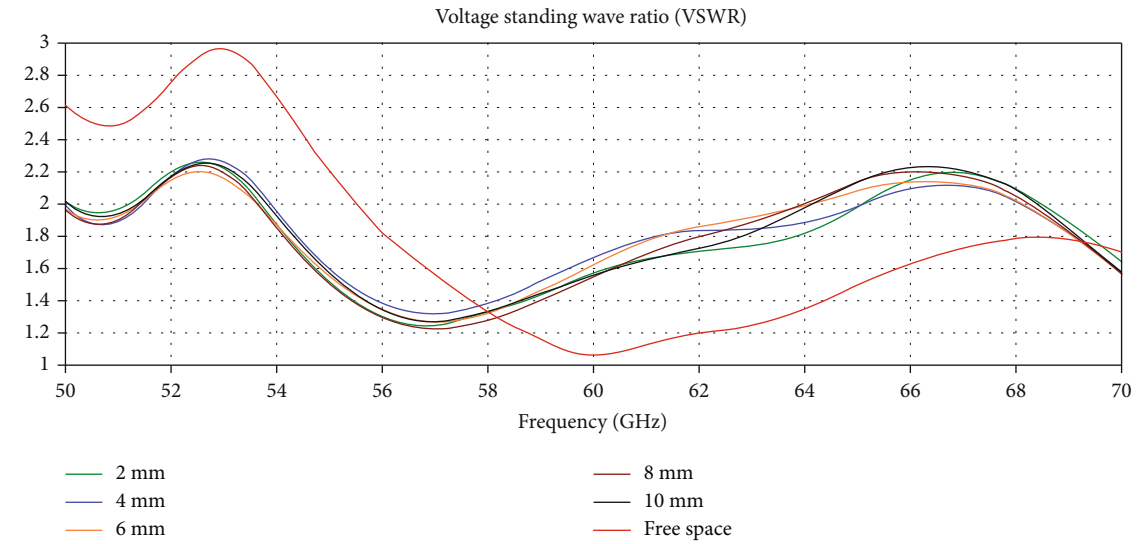

Figure 20: VSWR comparison for various distance on-body.

different on-body simulation scenarios, which vary from 9 GHz to 11 GHz (2 mm). Though the on-body return loss curves show performance differently compared to the free space S11 plot, antenna parameters are still good enough to perform in a body-centric network.

In Figure 20, voltage standing wave ratios were compared for on-body placements of the antenna at different distances. For different distances, on-body VSWR curves show very similar results, but the changes are noticeable when compared to the free-space data. However, for all scenarios, VSWR stayed within 1.5 to 1.7.

Figure 21 depicts how the radiation patterns change as the antenna's distance from the human body increases. In terms of primary lobes, maximum gains, and lobe orientations, it is obvious that the radiation patterns are extremely similar. Figure 19(a) shows the 2D radiation patterns (on the XY plane) of the antenna when it is placed in close proximity to the human torso phantom by varying the distance between them. Patterns are very consistent, even when the on-body distances are varied. Lobe directions remained almost identical while maximum gain values were changed a little bit. Figure 19(b), on the other hand, shows the patterns for YZ planes, which deviate from free space in some specific orientations.

Table 6 contrasts simulations conducted in free-space and on-body. In several on-body simulations, the antenna is positioned at distances of 2 mm, 4 mm, 6 mm, 8 mm, and 10 mm from the torso phantom. Return loss, gain, radiation efficiency, and bandwidth are all taken into account in the comparison. For the return loss comparison, a 2 mm distance from the torso phantom produces a minimum return loss of -44.9 dB. A -32 dB RL was found when the antenna was 6 mm away from the torso, which is the second closest value to the free space simulation. The highest gain was

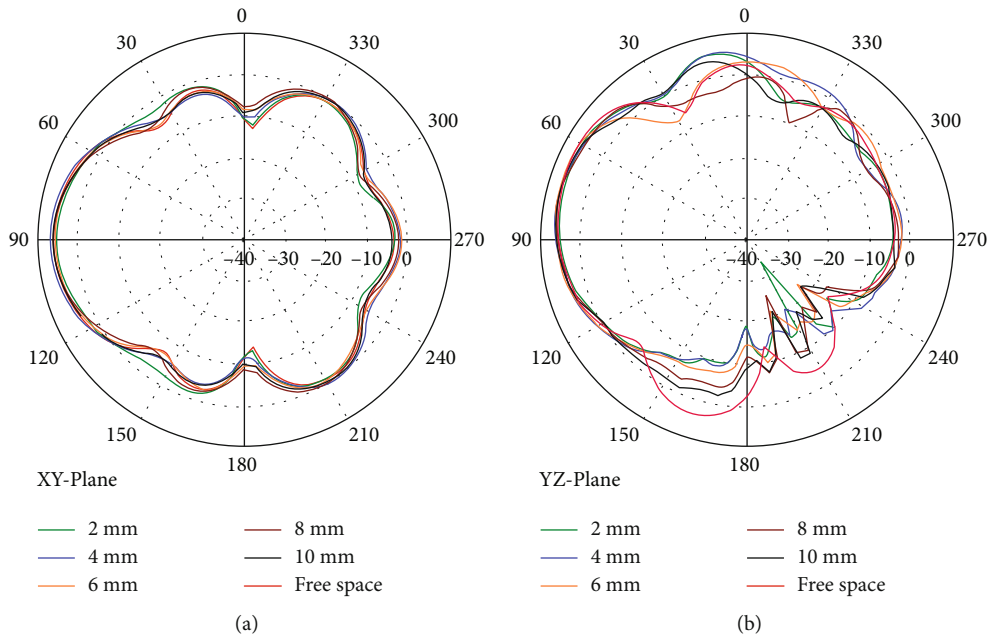

Figure 21: Comparison of the 2D radiation pattern for different on-body distances on the XY plane (a) and the YZ plane (b).

Table 6: Comparison parameters and results.

Parameters	Free-space	On-body 2 mm	On-body 4 mm	On-body 6 mm	On-body 8 mm	On-body 10 m
Return loss(dB)	-31.45	-13.15	-11.99	-12.48	-13.35	-13.17
Bandwidth (GHz)	—	10.77	10.23	9.33	9.54	9.72
Gain (dBi)	6.712	6.293	6.674	6.743	6.400	6.677
Radiation efficiency (%)	84.48	73.78	77.51	76.92	77.41	79.54

Table 7: Comparison with other designs.

	Physical dimension (mm^2)	Return loss (dB)	Gain (dB)	Efficiency	Bandwidth (GHz)	Applied design method	Design complexity
Design 1 [43]	14×12.9	-24	8.66	67.79%	30.068	Slotted patch antenna with partial ground	Q-shaped slot
Design 2 [6]	5.12×8	-32.42	6.071	62.12%	55≤	Multislot Patch antenna	Parasitic element
Design 3 [1]*	3.06×2.28	-13.89	7.13	93%	1.16	Multislot Patch antenna	Multi-dimensional slot
Design 4 [44]	24×17	-14**	4.4	62%	5.8	Substrate-integrated waveguide (SIW) horn antenna	Parallel plate horn
Design 5 (proposed)	6.03×4.5	-12	6.674	77.51%	10.23	Self-complementary patch antenna	Parasitic elements

*Resonant frequency is 60.8 GHz. **Approximate value.

achieved when the antenna was placed at a distance of 6 mm from the body model. Radiation efficiencies increase gradually as the antenna is taken far from the human body. The widest bandwidth was found at a 2 mm distance.

7. Comparison with Other Designs

Here is the comparison table comparing the presented antenna's on-body performance with a few similar antennas designed for BAN/BCN applications operating at 60 GHz. For comparison purposes, a standard 4 mm distance was measured from the human body torso phantom.

In Table 7, the parameters of the proposed antenna for on-body testing were compared with some similar antenna designs. Design 1 presents a partial ground plane and a narrow 'Q'-shaped slot and has a wide bandwidth. Design 2 is a quasiself-complementary antenna with parasitic elements and multiple rectangular slots. For on-body simulations,

both designs used a normal 4 mm spacing from the human body. Design 1 and 2 have used FR4 in their substrates while other designs used RT Duroids (substrate material of design 3 undetermined with a dielectric constant of 2.2). It is clearly visible that the proposed antenna has better radiation efficiency than the other models, except for design3, which has its resonant point slightly above the 60 GHz. However, the presented antenna has a larger bandwidth than designs 3 and 4. Also, from the other parameters, it can be said that the antenna shows better results than average designs.

8. Conclusion

A novel design and study of a self-complimentary miniaturized millimeter wave antenna for wearable applications has been presented. While the proposed antenna design performed significantly well in free-space simulations, the on-body performance of the antenna was good, too. The notable quality of the antenna is that it shows very consistent results for the on-body tests, even though the distances vary, which makes it a potential candidate for the body-centric network (BCN) or wireless body area network (WBAN). Many existing antennas fail to sustain better radiation efficiency while in the near field of a human body, whereas this proposed antenna's recorded minimum on-body efficiency was around 74% for the closest distance. In addition to this, the on-body gain of the antenna shows much wider bandwidths, which is greater than 10 GHz with a gain of -6.674 dB. Aside from that, the antenna performed well in free space simulations, with a gain of more than 6.7 dB and an efficiency of more than 84 percent. All the simulations indicate excellent performance of the antenna throughout the simulation.

This research work is actually based on simulations done in virtual environments due to a lack of opportunities. Simulations done in the CST studio suite have a good reputation in terms of accuracy, which was proven by the countless research done worldwide. Though the antenna was, further parametric improvements could be made in the future by making smaller order arrays with this design.

Data Availability

The data used to support the findings of this study are freely available at http://niremf.ifac.cnr.it/tissprop/

Conflicts of Interest

The authors declare that they have no conflicts of interest to report regarding the present study.

Acknowledgments

This work was funded by the Deanship of Scientific Research at Jouf University under grant No (DSR-2021-02-0390)

References

[1] U. Farooq and G. M. Rather, "A miniaturised Ka/V dual band millimeter wave antenna for 5G body centric network applications," *Alexandria Engineering Journal*, vol. 61, pp. 8089–8096, 2022.

[2] M. Alibakhshikenari, E. M. Ali, M. Soruri et al., "A comprehensive survey on antennas on-chip based on metamaterial, metasurface, and substrate integrated waveguide principles for millimeter-waves and terahertz integrated circuits and systems," *IEEE Access*, vol. 10, pp. 3668–3692, 2022.

[3] K. Neophytou, M. Steeg, A. Stöhr, and M. A. Antoniades, "Compact fixed-beam leaky-wave antenna for 5G millimeter-wave applications," in *2019 13th European Conference on Antennas and Propagation (EuCAP)*, pp. 1–4, Krakow, Poland, 2019.

[4] A. Sebak, "High gain millimeter wave antennas for 5G wireless and security imaging systems," in *2016 33rd National Radio Science Conference (NRSC)*, pp. 2–2, Aswan, Egypt, 2016.

[5] G. Chittimoju and U. Devi, "A comprehensive review on millimeter waves applications and antennas," *Journal of Physics: Conference Series*, vol. 1804, no. 1, article 012205, 2021.

[6] H. M. A. Rahman, M. M. Khan, M. Baz, M. Masud, and M. A. AlZain, "Novel compact design and investigation of a super wideband millimeter wave antenna for body-centric communications," *International Journal of Antennas and Propagation*, vol. 2021, Article ID 8725263, 15 pages, 2021.

[7] A. Ahmed, H. M. Arifur Rahman, and M. M. Khan, "Design and analysis of a compact wideband V-band and W-band antenna for healthcare applications," in *2022 IEEE 12th Annual Computing and Communication Workshop and Conference (CCWC)*, pp. 1043–1048, Las Vegas, NV, USA, 2022.

[8] A. Stohr, C. C. Renaud, D. Rogers et al., "Millimeter-wave photonic components for broadband wireless systems," *IEEE Transactions on Microwave Theory and Techniques*, vol. 58, no. 11, pp. 3071–3082, 2010.

[9] P. Kumar, "Antennas and arrays for 60 GHz high data rate wireless applications," *International Journal on Communications Antenna and Propagation (IRECAP)*, vol. 9, no. 4, pp. 255–262, 2019.

[10] B. Bosco, R. Emrick, S. Franson, J. Holmes, and S. Rockwell, "Emerging commercial applications using the 60 GHz unlicensed band: opportunities and challenges," in *2006 IEEE Annual Wireless and Microwave Technology Conference*, pp. 1–4, Clearwater Beach, FL, USA, 2006.

[11] N. Guo, R. C. Qiu, S. S. Mo, and K. Takahashi, "60-GHz millimeter-wave radio: principle, technology, and new results," *EURASIP Journal on Wireless Communications and Networking*, vol. 2007, no. 1, Article ID 068253, 2006.

[12] B. Yang, Z. Yu, Y. Dong, J. Zhou, and W. Hong, "Compact tapered slot antenna array for 5G millimeter-wave massive MIMO systems," *IEEE Transactions on Antennas and Propagation*, vol. 65, no. 12, pp. 6721–6727, 2017.

[13] B. Kibret, A. K. Teshome, and D. T. H. Lai, "Human body as antenna and its effect on human body communications," *Progress In Electromagnetics Research*, vol. 148, pp. 193–207, 2014.

[14] S. Chowdhury and K. Ali, "Effects of human body on antenna performance: a quantitative study," in *2016 19th International Conference on Computer and Information Technology (ICCIT)*, pp. 108–112, Dhaka, Bangladesh, 2016.

[15] Y. Hao, "Antennas and propagation for body centric wireless communications," in *2011 IEEE International Conference on Microwave Technology & Computational Electromagnetics*, p. 3, Beijing, China, 2011.

[16] K. Fujii, K. Ito, and S. Tajima, "A study on the receiving signal level in relation with the location of electrodes for wearable devices using human body as a transmission channel," in *IEEE Antennas and Propagation Society International Symposium. Digest. Held in conjunction with: USNC/CNC/URSI North American Radio Sci. Meeting (Cat. No.03CH37450)*, Columbus, OH, USA, 2003.

[17] T. G. Zimmerman, "Personal area networks: near-field intrabody communication," *IBM Systems Journal*, vol. 35, no. 3.4, pp. 609–617, 1996.

[18] T. G. Zimmerman, J. R. Smith, J. A. Paradiso, D. Allport, and N. Gershenfeld, "Applying electric field sensing to human-computer interfaces," in *Proceedings of the SIGCHI conference on Human factors in computing systems - CHI '95*, pp. 280–287, Denver, Colorado, USA, May 1995.

[19] W. Wu, Y.-B. Li, R.-Y. Wu, C.-B. Shi, and T.-J. Cui, "Band-notched UWB antenna with switchable and tunable performance," *International Journal of Antennas and Propagation*, vol. 2016, Article ID 9612987, 6 pages, 2016.

[20] H. Rahman and M. Khan, "Design and analysis of a compact band notch UWB antenna for body area network," *Journal of Electromagnetic Analysis and Applications*, vol. 10, no. 9, pp. 157–169, 2018.

[21] V. Kumar and B. Gupta, "Design aspects of body-worn UWB antenna for body-centric communication: a review," *Wireless Personal Communications.*, vol. 97, no. 4, pp. 5865–5895, 2017.

[22] T. Kumpuniemi, M. Hamalainen, K. Y. Yazdandoost, and J. Iinatti, "CATEGORIZED UWB on-body radio channel modeling for WBANS," *Progress In Electromagnetics Research B*, vol. 67, pp. 1–16, 2016.

[23] E. Miralles, C. Andreu, M. Cabedo-Fabrés, M. Ferrando-Bataller, and J. F. Monserrat, "UWB on-body slotted patch antennas for in-body communications," in *2017 11th European Conference on Antennas and Propagation (EUCAP)*, pp. 167–171, Paris, France, 2017.

[24] A. Alomainy, A. Sani, A. Rahman, J. G. Santas, and Y. Hao, "Transient characteristics of wearable antennas and radio propagation channels for ultrawideband body-centric wireless communications," *IEEE Transactions on Antennas and Propagation*, vol. 57, no. 4, pp. 875–884, 2009.

[25] M. Ur-Rehman, N. A. Malik, X. Yang, Q. H. Abbasi, Z. Zhang, and N. Zhao, "A low profile antenna for millimeter-wave body-centric applications," *IEEE Transactions on Antennas and Propagation*, vol. 65, no. 12, pp. 6329–6337, 2017.

[26] N. Chahat, M. Zhadobov, and R. Sauleau, "Antennas for body centric wireless communications at millimeter wave frequencies," in *Progress in Compact Antennas*, IntechOpen, London, UK, 2014.

[27] J. Puskely, M. Pokorny, J. Lacik, and Z. Raida, "Wearable disc-like antenna for body-centric communications at 61 GHz," *IEEE Antennas and Wireless Propagation Letters*, vol. 14, pp. 1490–1493, 2015.

[28] V. S. Ubale and O. S. Lamba, "Flexible wearable antennas for body area network," *International Journal of Engineering Science*, vol. 8, no. 5, pp. 1561–1565, 2020.

[29] Z. H. Jiang, Z. Cui, T. Yue, Y. Zhu, and D. H. Werner, "Compact, highly efficient, and fully flexible circularly polarized antenna enabled by silver nanowires for wireless body-area networks," *IEEE Transactions on Biomedical Circuits and Systems*, vol. 11, no. 4, pp. 920–932, 2017.

[30] A. Brizzi, A. Pellegrini, L. Zhang, and Y. Hao, "Woodpile EBG-based antennas for body area networks at 60GHz," in *2012 4th International High Speed Intelligent Communication Forum*, pp. 1–4, Nanjing, China, 2012.

[31] M. Alibakhshikenari, B. S. Virdee, S. Salekzamankhani et al., "High-isolation antenna array using SIW and realized with a graphene layer for sub-terahertz wireless applications," *Scientific Reports*, vol. 11, no. 1, article 10218, 2021.

[32] M. Alibakhshikenari, B. S. Virdee, A. A. Althuwayb et al., "Study on on-chip antenna design based on metamaterial-inspired and substrate-integrated waveguide properties for millimetre-wave and THz integrated-circuit applications," *J Infrared MilliTerahz Waves*, vol. 42, no. 1, pp. 17–28, 2021.

[33] M. Alibakhshikenari, B. S. Virdee, C. H. See, R. A. Abd-Alhameed, F. Falcone, and E. Limiti, "High-isolation leaky-wave array antenna based on CRLH-metamaterial implemented on SIW with ±30o frequency beam-scanning capability at millimetre-waves," *Electronics*, vol. 8, no. 6, p. 642, 2019.

[34] M. Alibakhshikenari, B. S. Virdee, C. H. See, R. A. Abd-Alhameed, F. Falcone, and E. Limiti, "Super-wide impedance bandwidth planar antenna for microwave and millimeter-wave applications," *Sensors (Basel).*, vol. 19, no. 10, p. 2306, 2019, Published 2019 May 19.

[35] M. Alibakhshikenari, B. S. Virdee, C. See et al., "Beam-scanning leaky-wave antenna based on CRLH-metamaterial for millimetre- wave applications," *IET Microwaves, Antennas & Propagation*, vol. 13, no. 8, pp. 1129–1133, 2019.

[36] M. Alibakhshikenari, B. S. Virdee, L. Azpilicueta et al., "A comprehensive survey of "metamaterial transmission-line based antennas: design, challenges, and applications"," *IEEE Access*, vol. 8, pp. 144778–144808, 2020.

[37] M. Ur-Rehman, M. Adekanye, and H. T. Chattha, "Tri-band millimetre-wave antenna for body-centric networks," *Nano Communication Networks*, vol. 18, pp. 72–81, 2018.

[38] H. Shawkey and D. Elsheakh, "Multiband dual-meander line antenna for body-centric networks' biomedical applications by using UMC 180 nm," *Electronics*, vol. 9, no. 9, p. 1350, 2020.

[39] X. Y. Wu, Y. Nechayev, and P. S. Hall, "Antenna design and channel measurements for on-body communications at 60 GHz," in *2011 XXXth URSI General Assembly and Scientific Symposium*, pp. 1–4, Istanbul, Turkey, 2011.

[40] T. Ramachandran, M. R. I. Faruque, and M. T. Islam, "A dual-band polarization-independent left-handed symmetrical metamaterial for communication system application," *Journal of Materials Research and Technology*, vol. 15, pp. 731–744, 2021.

[41] P. Kumar, T. Ali, and A. Sharma, "Flexible substrate based printed wearable antennas for wireless body area networks medical applications (review)," *Radioelectron.Commun.Syst.*, vol. 64, no. 7, pp. 337–350, 2021.

[42] S. G. Kirtania, A. W. Elger, M. R. Hasan et al., "Flexible antennas: a review," *Micromachines*, vol. 11, no. 9, p. 847, 2020.

[43] M. M. Khan, K. Islam, M. N. A. Shovon, M. Baz, and M. Masud, "Design of a novel 60 GHz millimeter wave Q-slot antenna for body-centric communications," *International Journal of Antennas and Propagation*, vol. 2021, Article ID 9795959, 12 pages, 2021.

[44] S. Razafimahatratra, J. Sarrazin, A. Benlarbi-Delai et al., "On-body propagation characterization with an H-plane substrate integrated waveguide (SIW) horn antenna at 60 GHz," in *2015 European Microwave Conference (EuMC)*, pp. 211–214, Paris, France, 2015.

Hindawi
Wireless Communications and Mobile Computing
Volume 2022, Article ID 2697303, 15 pages
https://doi.org/10.1155/2022/2697303

Research Article

A Machine Learning-Based Model for Stability Prediction of Decentralized Power Grid Linked with Renewable Energy Resources

Muhammad Ibrar,[1] Muhammad Awais Hassan,[1] Kamran Shaukat,[2,3] Talha Mahboob Alam,[4] Khaldoon Syed Khurshid,[1] Ibrahim A. Hameed,[5] Hanan Aljuaid,[6] and Suhuai Luo[2]

[1]*Department of Computer Science, University of Engineering and Technology, Lahore 58590, Pakistan*
[2]*School of Information and Physical Sciences, The University of Newcastle, Callaghan, NSW 2308, Australia*
[3]*Department of Data Science, University of the Punjab, Lahore 54890, Pakistan*
[4]*Department of Computer Science and Information Technology, Virtual University of Pakistan, Lahore 58590, Pakistan*
[5]*Department of ICT and Natural Sciences, Norwegian University of Science and Technology, Trondheim, Norway*
[6]*Computer Sciences Department, College of Computer and Information Sciences, Princess Nourah Bint Abdulrahman University (PNU), P.O. Box 84428, Riyadh 11671, Saudi Arabia*

Correspondence should be addressed to Kamran Shaukat; kamran.shaukat@uon.edu.au, Talha Mahboob Alam; talhamahboob95@gmail.com, and Ibrahim A. Hameed; ibib@ntnu.no

Received 6 June 2022; Revised 6 July 2022; Accepted 28 July 2022; Published 23 August 2022

Academic Editor: Farman Ullah

A decentralized power grid is a modern system that implements demand response without requiring major infrastructure changes. In decentralization, the consumers regulate their electricity demand autonomously based on the grid frequency. With cheap equipment (i.e., smart meters), the grid frequency can be easily measured anywhere. Electrical grids need to be stable to balance electricity supply and demand to ensure economically and dynamically viable grid operation. The volumes of electricity consumed/produced (p) by each grid participant, cost-sensitivity (g), and grid participants' response times (tau) to changing grid conditions affect the stability of the grid. Renewable energy resources are volatile on varying time scales. Due to the volatile nature of these renewable energy resources, there are more frequent fluctuations in decentralized grids integrating renewable energy resources. The decentralized grid is designed by linking real-time electricity rates to the grid frequency over a few seconds to provide demand-side control. In this study, a model has been proposed to predict the stability of a decentralized power grid. The simulated data obtained from the online machine learning repository has been employed. Data normalization has been employed to reduce the biased behavior among attributes. Various data level resampling techniques have been used to address the issue of data imbalance. The results showed that a balanced dataset outperformed an imbalanced dataset regarding classifiers' performance. It has also been observed that oversampling techniques proved better than undersampling techniques and imbalanced datasets. Overall, the XGBoost algorithm outperformed all other machine learning algorithms based on performance. XGBoost has been given an accuracy of 94.7%, but while combining XGBoost with random oversampling, its accuracy prediction has been improved to 96.8%. This model can better predict frequency fluctuations in decentralized power grids and the volatile nature of renewable energy resources resulting in better utilization. This prediction may contribute to the stability of a decentralized power grid for better distribution and management of electricity.

1. Introduction

The majority of the global energy supplies for electricity generation are nonrenewables (oil, gas, coal, etc.) [1]. These nonrenewable energy resources are depleting quickly. They are polluting the environment and causing global warming due to the emission of various greenhouse gasses [2]. Due to these limitations of nonrenewable resources, the world's energy policies are shifting towards renewable resources for clean and sustainable energy [3]. Globally, the current share of renewable energy in electricity generation is 24%, which is expected to grow by 44% by 2030 [4, 5]. Pakistan has enormous potential for renewable energy generation due to long sunshine hours, and its coastal belt has promising wind speeds. According to the Alternate and Renewable Energy Policy 2019 approved by Pakistan, the country has planned to grow its share of renewable energy in electricity generation from 4% to 30% by 2030, excluding hydropower [5]. However, the volatile nature of many renewable energy sources is a well-known challenge [6, 7]. A more flexible approach is required to balance energy demand and supply linked with renewable energy resources since renewable energy resources are more susceptible to fluctuations than nonrenewable energy resources [8, 9]. Various approaches to managing supply and demand have been presented for such a fluctuating power grid. The various smart grid concepts' core idea is to manage consumer demand which is a significant paradigm shift from current grid operating schemes [7].

A decentralized approach means a resource is self-dispatched with rubrics that can be defined in isolation of other resources or in coordination with them. In decentralization, the consumers regulate their electricity demand autonomously based on the grid frequency [6, 10]. The decentralized grid approach was first suggested a few years ago but only recently received much attention by implementing demand response without major infrastructural changes. Electrical grids need to be stable to balance energy supply and demand to ensure economically and dynamically viable grid operation [11]. During periods of excess power, the frequency increases but decreases during periods of underproduction. Grid frequency monitoring is a low-cost and easy way to determine grid stability. The grid's frequency changes when there is an undersupply or oversupply of electricity in the grid [12]. With cheap equipment (i.e., smart meters), consumers can easily measure the grid frequency anywhere.

ML techniques have widely used in the domain of education [13, 14], software measurement [15–17], decision support system [18, 19], social sciences [20, 21], healthcare [22–24], and disease diagnosis [9, 25]. Numerous computational methods were used in the renewable energy domain [26–30]. These include the prediction of the decentralized grid using a decision tree (DT) [11] and Hybrid Kernel Ridge Regression-Extreme Gradient Boosting (KRR-XGBoost) for distributed power systems [31]. The artificial neural network (ANN), support vector regression (SVR), and regression trees (RT) were used for the power output of photovoltaic (PV) systems [32]. For electricity load prediction, ehanced multilayer perceptron (MLP), enhanced support vector machine (SVM), and enhanced logistic regression (LR) were used [33]. Gradient boosted decision tree (GBDT), LR, random forest (RF), and MLP classifier were applied for smart grid stability prediction [34]. ANN, RF, and SVM were used for voltage stability forecasting in transmission systems [35]. ANN, linear discriminant analysis (LDA), and Naïve Bayes (NB) predicted solar power ramp events [36]. Ensemble diverse-extreme learning machine was applied [37] by sampling key variables over a broad feasible solution space. All these studies were not able to achieve effective results. Few studies utilized a large number of features [32, 35, 37] and employed a limited amount of data for modelling purposes [33, 37]. Previous research did not work on class imbalance which caused insufficient results.

Resampling techniques have been used in this study in combination with ML algorithms to predict the stability of a decentralized electricity grid. This study tests the hypothesis that ML algorithms combined with resampling techniques can provide highly accurate predictions for the stability of decentralized electricity grids. ML algorithms can detect trends and anomalies in datasets and thus help grid system operators to make real-time decisions for better distribution of available electricity [38]. Different approaches were used for the stability prediction of power grids, but effective results were not achieved [11, 31–37]. To the best of our knowledge, the available literature concluded that resampling techniques were not used to balance the data for grid stability prediction. Furthermore, only accuracy was used as an evaluation metric in previous studies, but other important metrics like precision, recall, and receiver operating characteristic (ROC) curve were not evaluated.

Contributions were as follows: this research possesses various contributions to decentralized power grid stability prediction.

(1) Latest dataset from the University of California Irvine (UCI) Machine Learning repository has been used to build a ML model for decentralized power grid stability prediction

(2) The data imbalance issue has been explored by comparing the different resampling techniques and evaluating the performance that which resampling technique has given efficient results with a ML classifier

(3) Lastly, our proposed model may help better prediction of the stability of a decentralized electricity grid, which may ultimately help in better distribution. Frequency fluctuations in the decentralized grid due to renewable energy resources can be predicted with the proposed model for better utilization of these renewable energy resources. To test the effectiveness of our proposed technique, it has been verified on the Electricity Grid Dataset. It can be applied to any real-time dataset related to decentralized grid frequency

The rest of the paper is structured as follows:

The existing techniques for grid stability prediction are analyzed in Section 2. Section 3 includes the proposed

solution. The evaluation metrics are described in Section 4. The results of our study have been discussed and analyzed in Section 5. The research is summed up, and the problem definition is restated in Section 6. The study's conclusion, challenges, and limitations are described, and suggestions for future improvements are discussed in section 7.

2. Literature Review

Previous studies have mostly worked on conventional centralized grids with few frequency fluctuations [33]. However, decentralized power grids connected with renewable energy resources involve strong fluctuations on varying time scales, including seasonal, intraday, and short-time fluctuations [7]. The previous studies used imbalanced data to predict the grid stability [11, 31–37]. Abu Al-Haija et al. [39] proposed a system using various ML models to classify stability records in smart grid networks. Seven machine learning architectures are specifically examined, including SVM, DT, LR, NBC, LDC, and GBDT. A recent and substantial dataset for the stability of smart grid networks (SGN Stab2018) was also used to test the system's performance, and it received high marks for classification. Breviglieri et al. [40] studied deep learning models to solve fixed inputs and equality issues in decentralize smart grid control (DSGC) system. By removing those constrictive assumptions on input values, they examined the DSGC system using several optimized deep learning models to forecast smart grid stability.

Massaoudi et al. [41] proposed an accurate stacking ensemble classifier (SEC) for decentralizing smart grid control stability prediction. Using a supervised learning approach, the presented method showed a fantastic ability to categorize the grid instabilities accurately. Numerical findings validate the excellent effectiveness of the suggested model. Arzamasov et al. [11] predicted the results of decentralized grid stability using a DT algorithm. To determine the stability/instability of the grid, they solved a numerical optimization problem called the characteristics roots equation. Positive real numbers indicated instability, and negative real numbers indicated a stable grid state. Yin et al. [31] developed a KRR-XGBoost model to forecast the stability of distributed power systems and provide effective design guidelines and cost optimization for these systems. The grid stability index, the grid stability predictor (stable/unstable), and the factors affecting the grid's stable state covered the data input components. Ali et al. [8] proposed an optimization-based method to smooth voltage. To extend the lifespan of the electric vehicle (EV) battery, EV power fluctuations and their minimum preset state of charge (SOC) are considered in the proposed optimization model.

Different ML models were applied to test their ability to forecast PV power output by Theocharides et al. [32]. SVR, ANN, and RT were explored, each with its own hyperparameters and features. Each model's output power prediction performance was evaluated on real-world PV generation data for one year and compared to a developed persistence model. The basic purpose was to build an association between the input features and their output. Bano et al. [33] utilized ML techniques, i.e., enhanced MLP, enhanced SVM, and enhanced LR, to forecast the electricity load. To forecast New York City's load and price, they used hourly data from 2016 to 2017. Classification and regression tree and recursive feature elimination were used for feature selection. Singular Value Decomposition was used to extract the features. Moldovan and Salomie [34] presented a feature extraction-based ML approach to predict the stability of a smart grid using the Python tsfresh package. They used ML and statistical methods to detect sources of instability and made feature selection before applying classifiers. Their study used four classifiers: LR, GBDT, RF, and MLP. Ali et al. [29] proposed an optimization approach to determine microgrids' optimal locations and sizes of photovoltaic and wind generation systems. They created a bilevel metaheuristic-based method to solve the planning model. Various simulations and study cases are run to evaluate the viability of the proposed model.

Malbasa at el. [35] predicted voltage stability in transmission systems using active machine learning. Their key contribution is applying pool-based active learning techniques to power system measurements like synchrophasor data, a tool for determining voltage stability. Experiments on synthetic data obtained from a complex power system simulation model are used to test their method. The experiments focused on margins of voltage stability prediction in a transmission network using ML techniques. Abuella et al. [36] predicted solar power ramp events to handle high renewable generation ramp rates, energy storage systems, energy management, and voltage regulator settings on distributed generation feeders. They used LDA, ANN, and NB to forecast solar power ramp events. Baltas et al. [37] proposed a response-based model to forecast a benchmark system's stability following a serious disturbance. They used ensemble-based multiple classifiers. Simulated data generated through Spider IDE was used. For the ensemble's final output, three separate approaches were considered. They used a majority voting scheme in their first method. In the second method, a variant of the boosting technique was considered that uses the weight factor and a constant. Finally, in the third approach, an all-or-nothing technique was considered. Ali et al. [30] presented an interval optimization method to schedule EV optimally. The goal was to reduce network active power losses and overall voltage magnitude deviation while considering system-wide restrictions. The best day-ahead scheduling of EV was done using the proposed method on a 33-bus distribution system. Various case studies were conducted to evaluate the viability of the suggested approach. The summary of techniques of related articles is presented Table 1.

3. Methodology

The proposed framework for decentralized grid stability prediction is presented in Figure 1. Our methodology is comprised of the following major steps: (1) dataset selection, (2) data normalization, (3) data resampling, (4) modeling, and (5) evaluation. The data has been pre-processed to obtain effective results. Various resampling techniques have been used to tackle data imbalance issues to get the best

Table 1: A summary of techniques cast-off in related articles.

Reference	Year	ML techniques	Undersampling techniques	Oversampling techniques
[39]	2021	✓	✗	✗
[40]	2021	✓	✗	✗
[41]	2021	✓	✗	✗
[33]	2020	✓	✗	✗
[31]	2019	✓	✗	✗
[34]	2019	✓	✗	✗
[36]	2018	✓	✗	✗
[37]	2018	✓	✗	✗
[11]	2018	✓	✗	✗
[35]	2018	✓	✗	✗
[32]	2018	✓	✗	✗
Proposed model	**2022**	✓	✓	✓

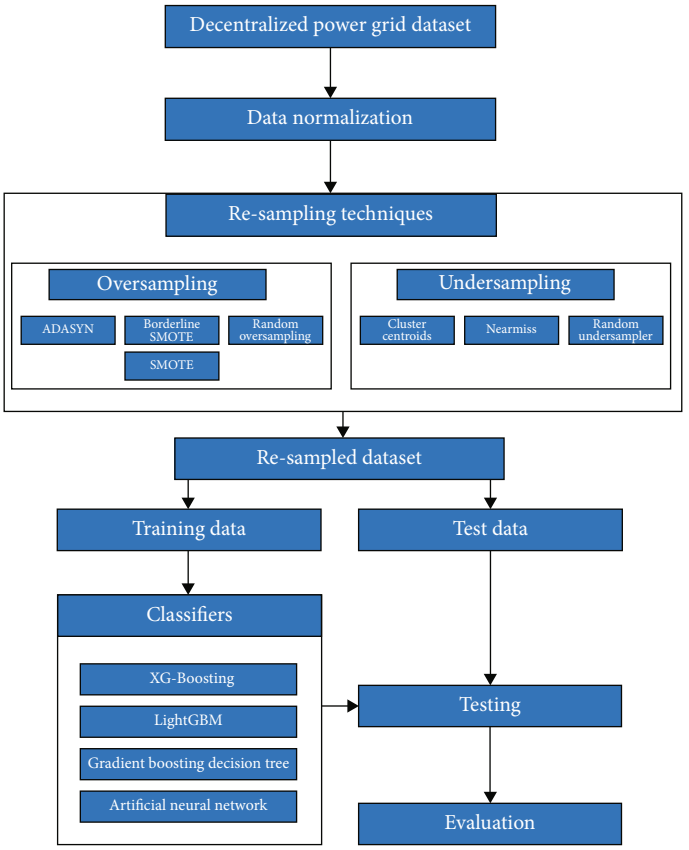

Figure 1: Proposed methodology.

results. After data preprocessing, different ML models were used, and their results were compared.

3.1. Dataset. In this study, the Electricity Grid Simulated Dataset was employed and obtained from the UCI repository. The dataset includes 10,000 instances and 14 features in which 3620 were stable and 6380 were unstable. The dataset has also observed class imbalance issues because unstable instances are far more than stable instances. The dataset contains the reaction time of participants (tau1, tau2, tau3, tau4), nominal power produced/consumed (p1, p2, p3, p4), and gamma coefficient, i.e., price elasticity features (g1, g2, g3, g4) as shown in Table 2. Price elasticity is the measurement of the change in consumption of electricity in response to a change in its price, expressed mathematically as

$$\text{Formula to calculate price elasticity} = \frac{\%\text{Change in electricity quantity demanded}}{\%\text{Change in price}}. \quad (1)$$

Table 2: Feature description used in the dataset.

Feature name	Feature description
tau1	Electricity producer's reaction time in response to price change
tau2	First consumers' reaction time in response to price change
tau3	Second consumer's reaction time in response to price change
tau4	Third consumer's reaction time in response to price change
p1	Nominal power (positive real) produced by the producer (amount of electricity produced)
p2	Nominal power (negative real) consumed by the first consumer (amount of electricity consumed by the first consumer)
p3	Nominal power (negative real) consumed by the second consumer (amount of electricity consumed by the second consumer)
p4	Nominal power (negative real) consumed by the third consumer (amount of electricity consumed by the third consumer)
g1	(Gamma coefficient) proportional to price elasticity of producer
g2	(Gamma coefficient) proportional to the price elasticity of the first consumer
g3	(Gamma coefficient) proportional to the price elasticity of the second consumer
g4	(Gamma coefficient) proportional to the price elasticity of the third consumer
Stab	Target class value real, positive shows instability or negative shows stability
Stabf	Target class label (categorical), i.e., stable or unstable

A numerical optimization problem known as the characteristics roots equation determines the target class value (stab). Positive real numbers indicated instability, and negative real numbers showed the grid's stability. The stability/instability of the system is labeled as stabf (categorical).

3.2. Data normalization. The major issue with various features is that each numerical feature/attribute is represented differently. So, data normalization is an effective data preprocessing technique for tabular data to make comparisons between measurements more accessible while constructing a model. It rescales feature values to confront the standard normal distribution to form new inputs. The maximum and minimum values of various features often vary significantly, like the reaction time of different participants ranges from 0.5 to 0.99, power values of producers range from 1.58 to 5.86, power values of different consumers range from -1.99 to -0.5, and gamma values, i.e., price elasticity of demand of all participants ranges from 0.05 to 0.99. The target variable values resulted from optimizing characteristics roots equations, ranging from -0.08 to 0.10. The Z-score normalization technique has been employed to bring all these features into a specified range. All numerical values have been scaled within the specified range (-1.73 to +1.73). The formula of the Z-score technique is given in equation (2).

$$z = \frac{X - \bar{X}}{S}, \tag{2}$$

where z is the standard score, S is the standard deviation of a sample, X represents each value in the dataset, and $\bar{X}$ is the mean of all values in the dataset. It has been observed that Z-score normalization outperformed other data normalization techniques [42–44].

3.3. Undersampling Techniques. Undersampling is one of the simplest methods for dealing with imbalanced data. This technique undersamples the majority class to balance it with the minority class [45]. The undersampling method can be applied if a sufficient amount of data is collected. This study used three undersampling techniques: near miss, cluster centroid, and random undersampling.

3.3.1. Random Undersampling. This approach is aimed at picking and removing samples from the majority class randomly. Hence, the number of majority class examples is reduced. Due to undersampling, the data set is transformed, with fewer examples in the majority class. This procedure can be replicated until each class has an equal number of examples. This approach proves effective when the minority class has sufficient examples despite the great imbalance. On the other hand, it is always important to consider the risk of losing important data. We remove them randomly from our dataset because we have no means of identifying or maintaining the examples in the majority class rich in information. This method also significantly reduces the size of the training data. As a consequence, it is the most naive method of data undersampling.

3.3.2. Near Miss. This technique was proposed by Mani and Zhang [46] to achieve an equal distribution of classes by removing majority class examples at random. Only the majority class examples in the overlapping region nearest to the minority class examples are retained. When instances of two distinct classes are too close to one another, the majority of class instances are removed to increase the space between these two classes, and this aids in the process of classification. The first process, "NearMiss-1," picks samples from the majority class closest to those from the minority class. This process picks majority class samples with the smallest average distances to the three nearest minority class samples. The second "NearMiss-2" approach picks majority

class samples with the smallest average distances to the three farthest minority class samples. For each minority class sample, the third process, "NearMiss-3," takes a fixed number of the nearest majority class samples. Finally, the fourth method, "Most distant" approach, chooses the majority class samples with the highest average distances to the three nearest minority class samples.

3.3.3. Cluster Centroid. One of the main disadvantages of undersampling is that valuable information from the majority class may be lost, resulting in misclassifying samples after classification. This cannot be afforded to build a solid model. As a result, the cluster centroid method was proposed by Yen and Lee [47] to solve this problem. This technique undersamples the majority class instances by replacing majority class instances from clusters with a cluster of centroids by considering the ratio of majority class samples to minority class samples. Undersampling is accomplished using this approach, generating centroids using k-means clustering methods. The data have been grouped based on similarity. The data is equipped with a K-means algorithm, and the level of undersampling determines the number of clusters (k). The sets of cluster centroids from K-means then entirely substitutes for most cluster samples. The most representative combinations of the majority class will be visualized in the middle of the cluster of centroids. This problem was attempted to be solved by under fitting and overfitting the data and their combination. While under fitting the dataset, only the cluster centroids were considered, adapted from [47].

3.4. Oversampling Techniques. When the number of instances in each class is not equal, any dataset can be called imbalanced. Resampling methods add a bias typically to make the dataset balanced. While classifiers may learn from imbalanced datasets, balanced datasets have more efficient results. All resampling techniques resample data until it reaches the required ratio. It also helps compare various resampling methods in the final training set for a given proportion of majority and minority class data points. The data level resampling method (oversampling and undersampling) is the optimal solution for dealing with class imbalance problems. In this study, various resampling techniques have been employed. By replicating or making new minority class samples, oversampling increases the minority class weight. Different oversampling methods are available in the literature. [48]. Four oversampling techniques have been applied in this study: random oversampling (ROS), adaptive synthetic (ADASYN), synthetic minority oversampling technique (SMOTE), and borderline-SMOTE.

3.4.1. Random Oversampling. ROS replicates minority classes randomly, that replication is content identical to the source, and no new contextual variation is added. To balance the classes, this approach creates a minority class set based on the size of the majority class. Overfitting and increased training time may occur when all the training examples are very close, and the classifier correctly classifies them. If a testing example differs marginally from the training examples, the classifier would be unable to correctly classify it, resulting in misclassification for the new examples. This technique is prone to overfitting, but other oversampling methods are also developed based on ROS.

3.4.2. Synthetic Minority Oversampling Technique. Compared to ROS, the SMOTE is a more advanced approach. Chawla et al. [48] state that it oversamples data by generating synthetic examples. New minority instances are synthesized between existing minority instances in SMOTE. It selects the minority class at random and calculates the K -nearest neighbor for that specific point. Finally, it adds synthetic points between that chosen point and its neighbors. The instance of the x_i minority class is chosen as the foundation for creating new synthetic data points. Several nearest neighbors of the same class are selected from the training set based on a distance metric. Finally, a randomized interpolation has been carried out to obtain new instances. An integer value of oversampling total amount N is determined, which can be set up to achieve a 1 : 1 class distribution or discovered using a wrapper method [49]. After that, a multistep iterative process is carried out, which works as below: first, a minority class instance is chosen randomly from the training set. Next, the K-nearest neighbors are then collected. Finally, N of these K instances are randomly selected to calculate new instances via interpolation. To complete this task, the difference between the feature vector (sample) under consideration and each of the selected neighbors is taken. After that, a random number between 0 and 1 is multiplied by the difference and added to the previous feature vector. As a result, a random point along the "line segment" between the features is selected. If there is a case of nominal attributes, one of the two values is chosen randomly.

Consider the sample $(6, 4)$ and its nearest neighbour $(4, 3)$. The sample for which k-nearest neighbors are being identified is $(6, 4)$, and one of its k-nearest neighbors is $(4, 3)$.

$$\begin{aligned} &\text{Let}: a_{11} = 6, a_{21} = 4, a_{21} - a_{11} = -2, \\ &a_{12} = 4, a_{22} = 3, a_{22} - a_{12} = -1. \end{aligned} \tag{3}$$

The newly generated samples will be as given in equation (4). ran $d(0-1)$ creates two random numbers vectors ranging from 0 to 1.

$$a_1', a_2' = (6, 4) + \text{ran } d(0-1) \times (-2,-1). \tag{4}$$

3.4.3. Adaptive Synthetic. ADASYN works similar to SMOTE. However, weighting the distance and the linear function creates more minority class synthetic examples. According to He et al. [50], ADASYN concentrates on minority class examples based on their level of learning difficulty. The basic idea behind ADASYN is to use a weighted distribution as a criterion for various minority classes to determine how many synthetic samples are required for each minority class [50]. Equation Equation (5) is used to calculate the weight.

$$W = \frac{\Delta}{K}. \tag{5}$$

The value of W varies between 0 to 1, and Δ is the number of examples in a minority class's K-nearest neighbors, which are members of the majority class.

3.4.4. Borderline-SMOTE. Borderline-SMOTE is a more advanced type of SMOTE that aims to generate synthetic samples by interpolating the k-nearest neighbors of the minority instances close to the border [51]. Since these border instances are more relevant for classification, this technique only extracts synthetic instances for minority samples near the boundary of two classes. At the same time, SMOTE produces new instances for each minority sample. Possible misclassified minority class instances will undergo more training in borderline-SMOTE [52]. It first identifies borderline minority instances; then, it uses them to generate synthetic instances with their chosen k-nearest neighbors. Rather than simply replicating the existing samples, SMOTE creates new synthetic samples along the line between the minority samples and their selected nearest neighbors. However, this increases overlapping between classes since synthetic samples are generated without considering neighboring samples. Many modified techniques have been proposed to solve this constraint, with borderline-SMOTE proving the most effective in most cases. Since samples close or on the borderline are more likely to be misclassified than those farther away, borderline-SMOTE just oversamples and enhances these difficult-to-learn samples.

For clear presentation, considering a given training dataset D, we define subsets $D_{\min} \subset D$ and $D_{\text{maj}} \subset D$, where $D_{\min}$ and D_{maj} are the set of minority and majority class samples in D, and the set of m nearest neighbors are determined for each $x_i \in D_{\min}$ called $D_{i:m-\text{NN}}$. Then, calculate how many of x_i nearest neighbors are members of the majority class, i.e., $|D_{i:m-\text{NN}} \cap D_{maj}|$.Then, select the number of neighbours of x_i to form the set "DANGER", which satisfies

$$\frac{m}{2} \leq \left|D_{i:m-\text{NN}} \cap D_{\text{maj}}\right| < m. \tag{6}$$

Only those in "DANGER" having more majority class neighbors than minority class neighbors are suggested in equation (6). This means that they represent samples from the borderline minority classes, which are the most likely to be misclassified. It is worth noting that other x_i are not operating in the next step. Finally, for each sample x_j in the "DANGER" set, select one of the K-nearest neighbors of x_j at random that have the smallest Euclidian distance to it, multiply the corresponding feature vector difference with a random number between [0,1], and this vector difference is added to x_j

$$x_{\text{new}} = x_j + \delta \times \left(\widehat{x}_j - x_j\right), \tag{7}$$

where x_j is the selected minority samples in the "DANGER" set, $\widehat{x} \in D_{\min}$ is one of $x_j{}'sK$-nearest neighbors, and $\delta \in [0, 1]$ is a random number. The resulting synthetic sample is, therefore, one point in the line segment between x_j and $\widehat{x}_j$ according to equation (7). The newly generated samples are appended to the original set and used to train the classifier. The dataset class distribution before and after applying resampling techniques is presented in Table 3.

3.5. XGBoost. It is a GBDT extension introduced by Chen and Guestrin [53]. It is a boosting algorithm and belongs to the supervised learning algorithms. Boosting is an ensemble technique of sequential learning. In boosting, different models are trained one after another. XGBoosting first creates a base model. We take the average number as the first prediction of the base model (also called model zero M0). Next, model M1 is fitted to minimize errors (the difference between the actual and predicted values). Until this, the procedure is the same as gradient boosting. XGBoost uses regularization parameters to avoid overfitting, and it also uses auto pruning to avoid trees not growing beyond a certain level and handles missing values. It has been used to solve various classification problems in many fields. The XGBoost algorithm assigns various levels of importance to features before deciding the weighted distance for the K-means algorithm. It combines predictions from "weak" classifiers (tree model) to get a "strong" classifier (tree model). It speeds up the learning process allowing for quicker modeling using distributed and parallel computing.

A new tree is generated along the direction of the negative gradient of the loss function. As the number of tree models increases, the loss becomes smaller and smaller. The XGBoost computational process started from equation (8):

$$\widehat{y}_i^{(t)} = \sum_{k=1}^{t} f_k(x_i) = \widehat{y}_i^{t-1} + f_t(x_i), \tag{8}$$

where $\widehat{y}_i^{t-1}$ is the previously generated tree model, $f_t(x_i)$ is the newly generated tree model, $\widehat{y}_i^{(t)}$ is the final tree model, and t is the total number of base tree models. Both depths of the tree and the number of trees are essential parameters for the XGBoost algorithm. The problem of determining the best algorithm was changed to finding a new classifier capable of reducing the loss function, with the target loss function given in equation (9).

$$\text{obj}^{(t)} = \sum_{i=1}^{t} (L\left(y_i, \widehat{y}_i^{(t)}\right) + \sum_{i=1}^{t} \Omega(f_i), \tag{9}$$

where y_i is the actual value; $\widehat{y}_i^{(t)}$ is the predicted value; $L(y_i, \widehat{y}_i^{(t)})$ is the loss function, and $\Omega(f_i)$ is the regularization term.

Equation (10) could be obtained by substituting equation (8) into equation (9) and then following some deduction steps.

$$\text{obj}^{(t)} = \sum_{i=1}^{t} L(y_i, \widehat{y}_i^{(t-1)} + f_t(x_i) + \Omega(f_t) + \text{constant}. \tag{10}$$

Table 3: Dataset class distribution: before and after applying resampling techniques.

	Electricity Grid Simulated Dataset		
	Total instances	Stable instances	Instable instances
Imbalanced dataset			
Imbalanced dataset	10000	3620	6380
Oversampled dataset			
ROS	12760	6380	6380
ADASYN	12760	6380	6380
SMOTE	12760	6380	6380
Borderline-SMOTE	12760	6380	6380
Undersampled data			
Near miss	7240	3620	3620
Cluster centroids	7240	3620	3620
Random undersampling	7240	3620	3620

After that, the final target loss function was transformed to equation (11), used to train the model.

$$obj^{(t)} = \sum_{i=1}^{t}\left[g_i f_t(x_i) + \frac{1}{2}h_i f_t^2(x_i)\right] + \Omega(f_t), \quad (11)$$

where $g_i = \partial_{y_i(t-1)} l(y_i, y_i^{(t-1)})$ and $h_i = \partial^2_{y_i(t-1)} l(y_i, y_i^{(t-1)})$ are the loss function's first and second-order gradient statistics. Equation (12) calculates the regularization term $\Omega(f_t)$ to reduce the model's complexity and increase its applicability to other datasets.

$$\Omega(f) = \gamma T + \frac{1}{2}\lambda\|\omega\|^2, \quad (12)$$

where λ and γ are coefficients with default values set as $\lambda = 1, \gamma = 0$, ω is the weight of the leaves, and T is the number of leaves. Both continuous and discrete variables can be used as inputs to the XGBoost algorithm, but the output variable must be discrete, excluding binary variables.

4. Evaluation Metrics

In every predictive modelling task, model evaluation is critical. It becomes more critical in predictive ensemble modeling, where diversity and models' relative performance must be evaluated thoroughly. Each of the evaluation metrics is based on one of 4 classifications. These classifications are true positives (TP), true negatives (TN), false positives (FP), and false negatives (FN). With the aid of the confusion matrix, accuracy is typically used to measure the efficiency of a model [54, 55]. Equation (13) has been used to calculate the model's accuracy.

$$\text{Accuracy} = \frac{\text{TP} + \text{TN}}{\text{TP} + \text{TN} + \text{FP} + \text{FN}}. \quad (13)$$

Precision is about out of the total predicted positives, how many of them are true positives. It means precision measures how many positive instances the classifier said were positive. The model's precision has been calculated using equation (14).

$$\text{Precision} = \frac{\text{TP}}{\text{TP} + \text{FP}}. \quad (14)$$

A recall is about out of the total actual positives, how many of them are true positives. Equation Equation (15) has been used to calculate the model's recall.

$$\text{Recall} = \frac{\text{TP}}{\text{TP} + \text{FN}}. \quad (15)$$

F-measure is the harmonic mean of precision and recall. Precision and recall are mutually exclusive: Low recall is usually associated with higher precision. Equation Equation (16) has been used to calculate the model's F-measure.

$$F - \text{measure} = \frac{2 \times \text{precision} \times \text{recall}}{\text{Precision} + \text{recall}}. \quad (16)$$

ROC curve plot is another commonly used metric for evaluating a classifier's efficiency. ROC graph shows the performance of a classification model at all classification thresholds. It plots the false positive rate (x-axis) versus the true positive rate (y-axis) for different candidate threshold values between 0.0 and 1.0. It is used to interpret the prediction of probabilities for binary classification problems.

5. Results

Various classifiers have been employed to evaluate the performance of an imbalanced Electricity Grid Simulated Dataset, as shown in Table 4. The train-test split technique has been used to assess the performance of ML algorithms. The dataset has been split into two subsets, with 70% for training and 30% for testing purposes. The first subset is the training dataset used to fit the model. The second subset is not used to train the model; instead, the model is provided with the dataset's input element. Then, predictions are made, and the results are compared to the expected results.

Table 4: Performance of ML models on imbalanced dataset.

Models	Accuracy (%)	Precision (%)	Recall (%)	*F*-measure (%)	ROC (%)
ANN	93.4	97.7	92	94.8	98.7
Averaged perceptron	81.5	84.6	87.5	86	88.9
Bayes point machine	81.3	83.2	89.2	86.1	88.7
Decision forest	89.8	91.9	92.4	92.2	95
Decision jungle	89.5	89.7	94.8	92.2	96
GBDT	94.1	95.2	95.8	95.5	98.8
LightGBM	94.6	94.6	97	95.8	98.9
Locally deep SVM	91.9	93.6	93.9	93.8	97.4
LR	81.5	84.4	87.7	86	89
SVM	80.9	84.3	86.6	85.5	88.5
XGBoost	94.7	94.9	96.9	95.9	98.9

This second dataset is called the test dataset. The performance of the XGBoost method has also been compared with other ML models. The XGBoost outperformed other ML models on an imbalanced dataset. XGBoost algorithm was run in Jupyter Notebook. Table 4 shows the results, with the XGBoost model predicting the highest accuracy of 94.7% on the imbalanced Electricity Grid Simulated Dataset. Tuning parameters is a critical step in improving the efficiency of any ML algorithm. It involves determining a grid with all possible parameters and checking them to find the values that maximize classification performance. The default values are used for the parameters whose values are not defined. Various parameters are listed below:

(i) Eta: It is the learning rate of the model. The default value of eta is 0.3; however, the optimal value of eta used in our experiment is 0.4. The feature weights are shrunk by eta to make the boosting procedure more prudent. Its range is from 0 to 1

(ii) Subsample: It controls the number of samples (observations) supplied to a tree. The default value of the subsample is 1. The optimal value used in our experiment is 0.8. Its range is from 0 to 1

(iii) colsample_bytree: It controls the number of features (variables) supplied to a tree. Its default value is 1, ranging from 0 to 1. The optimal value used in our experiment is 0.9

(iv) N-estimator: The number of trees (or rounds) in an XGBoost model is defined in the n_estimators. 100 is the default value for the n-estimator. Its range is from 1 to infinity. The optimal value used in our experiment is 200

To assess the performance of machine learning algorithms, various classifiers were used on undersampled datasets, as shown in Table 5. ANN proved to be the best algorithm. Classifiers were applied to three undersampled datasets. The results are shown in Table 5, in which random undersampling in combination with ANN has predicted the best accuracy of 94.5%. The random undersampling technique outperformed all other undersampling techniques based on accuracy. Other models have also shown effective results on the undersampled dataset. Further, the performance of classifiers was also better on the cluster centroids based on undersampled datasets than near miss.

Oversampling techniques (ADASYN, borderline-SMOTE, ROS, and SMOTE) have also been employed to improve the performance of the classifiers. Various models were applied to oversampled datasets, as shown in Table 6. The results are presented in Table 6, in which the ROS method in combination with XGBoost has predicted the best accuracy of 96.8%. XGBoost, in combination with borderline-SMOTE and SMOTE, has shown promising results with an accuracy of 96.5% and 96.1%, respectively. ADASYN predicted an outcome of 95.9% with the GBDT. The results showed that the XGBoost outperformed other ML models based on imbalanced and oversampled datasets. XGBoost was tuned further by adjusting the values of a few parameters to improve the results. However, ANN proved to be best on an undersampled dataset. The results of the imbalanced dataset have also been compared with undersampling and oversampling techniques. Results showed that ROS-based methods outperformed all other oversampling and undersampling techniques used—the performance of the XGBoost model, along with other models. The proposed model has outperformed previous studies significantly, as shown in Table 7.

The XGBoost, in combination with ROS, outperformed all other models predicting the best accuracy of 96.8%. However, the accuracy was 94.7% on an imbalanced dataset, as shown in Figure 2. The *F*-measure and ROC have also shown better results with ROS as 96.7% and 99.6%, respectively, compared to *F*-measure and ROC on the imbalanced dataset, which showed 95.6% and 98.9%, respectively.

6. Discussion

Effective demand response management and control in decentralized power grids are complex. Because grid participants' consumption and production behaviors are influenced by price signals issued and responded on a seconds scale, key variables influencing the grid's stability are the volumes of electricity consumed/produced (p) by each grid

Table 5: Performance of ML models on an undersampled dataset.

Undersampling technique	Models	Accuracy (%)	Precision (%)	Recall (%)	*F*-measure (%)	ROC
Cluster centroids	ANN	94.4	94.6	94.1	94.4	98.7
	Averaged perceptron	79.1	79.5	78.6	79	88.1
	Bayes point machine	79.1	79.4	78.7	79	88.1
	Decision forest	91.1	93.3	88.6	90.9	97.1
	Decision jungle	88.9	88.8	89.1	88.9	95.8
	GBDT	94.2	94.4	94.1	94.2	98.9
	LightGBM	93.6	94.2	92.8	93.5	98.4
	Locally deep SVM	90.9	91.1	90.6	90.9	97.2
	LR	79.1	79.6	78.4	79	88.1
	SVM	78.5	78.9	77.9	78.4	87.5
	XGBoost	93.7	94.1	93.3	93.7	98.7
Near miss	ANN	92	73.2	89.8	91.9	98.1
	Averaged perceptron	75.2	74	77.9	75.9	83.1
	Bayes point machine	75.1	74.1	77.5	75.7	83
	Decision forest	91.1	93.3	88.6	90.9	97.1
	Decision jungle	85.3	83.7	87.7	85.7	93.1
	GBDT	92.1	90.6	94	92.3	98.3
	LightGBM	91.8	90.6	93.2	91.9	97.9
	Locally deep SVM	88.3	88.3	88.3	88.3	94.6
	LR	75.2	73.9	78	75.9	83
	SVM	74.6	73.2	77.6	75.3	82.3
	XGBoost	92.6	92.1	93.1	92.6	98.8
Random undersampling	ANN	94.5	97.8	91	94.3	99
	Averaged perceptron	80.2	80.1	80.4	80.3	88.9
	Bayes point machine	79.7	79.7	79.9	79.8	88.8
	Decision forest	89	89.1	89	89	95.9
	Decision jungle	89.2	87.8	91.1	89.4	95.9
	GBDT	94.1	94.5	93.7	94.1	98.8
	LightGBM	92.7	93.1	92.1	92.6	98.3
	Locally deep SVM	90	89.8	90.2	90	96.6
	LR	79.8	79.7	80	79.9	88.7
	SVM	80.3	80	80.9	80.4	89
	XGBoost	93.4	93.6	93.1	93.3	98.7

participant and the cost-sensitivity (g), i.e., price elasticity and reaction time (tau) to price signals of the grid participants. A simulation of a decentralized grid applied to a four-node star grid.

In combination with resampling techniques, ML techniques have been used in our study to improve the decentralized grid stability prediction. The simulated four-star node dataset used in this study reflects a simple configuration of a decentralized grid. Here in this study, the grid participants are four and work have been performed on a four-node star architecture grid. The twelve independent variables have been imposed constraints of maximum and minimum values, and an absolute value of power production and consumption has been taken for simulation. As designed, this method successfully explores the feasible solution space with an evaluation of 10,000 cases. However, there are likely stronger correlations between the grid participants in decentralized grids. It has been discovered that the classifier's accuracy is related to class balance. The accuracy increases when the number of minority samples increases in the dataset. As the number of instances increases, the classifier has a greater chance of learning the patterns that differentiate binary classes. The XGBoost model predicted the best accuracy with the ROS method (96.8%), followed by XGBoost with borderline-SMOTE (96.5%). Other combinations predicted slightly lesser accuracy, such as XGBoost with SMOTE-oversampling gave 96.1%, GDBT with ADASYN-oversampling 95.9%, and XGBoost with imbalanced dataset 94.7%. As shown in Table 7, our study outperformed other studies. This can help to avoid power outages and improve grid performance significantly.

Table 6: Performance of ML models on oversample dataset.

Oversampling technique	Models	Accuracy (%)	Precision (%)	Recall (%)	*F*-measure (%)	ROC (%)
ADASYN	ANN	95.4	97.5	93.4	95.4	99
	Averaged perceptron	79.2	78.6	81.3	79.9	87.7
	Bayes point machine	79.1	78.4	81.3	79.8	87.8
	Decision forest	91.2	93.7	88.8	91.2	97.2
	Decision jungle	89.5	89.7	89.7	89.7	96.4
	GBDT	95.9	96.5	95.4	96	99.4
	LightGBM	94.7	96.5	94	94.8	99.1
	Locally deep SVM	91.5	91.7	91.6	91.6	97.4
	LR	79.1	78.3	81.5	79.9	87.8
	SVM	78.8	78.5	80.6	79.5	87.6
	XGBoost	95.7	96.4	95	95.7	99.4
Borderline-SMOTE	ANN	95.1	95.8	94.4	95.1	99
	Averaged perceptron	76.9	77.5	75.9	76.7	86.1
	Bayes point machine	76.9	77.4	76.2	76.8	86.1
	Decision forest	90.8	93.5	87.6	90.5	96.8
	Decision jungle	89.3	91.2	87.1	89.1	96
	GBDT	95.4	96.9	93.7	95.3	99.3
	LightGBM	94.5	95.9	92.7	94.3	99
	Locally deep SVM	90.8	92.4	88.8	90.6	97.2
	LR	76.8	77.4	75.8	76.6	86.1
	SVM	76.8	77.6	75.6	76.6	85.9
	XGBoost	96.5	97.7	95.1	96.4	99.5
ROS	ANN	95.7	97.9	93.4	95.6	99.2
	Averaged perceptron	79.2	79.4	78.9	79.2	88.3
	Bayes point machine	79.4	79.7	79.2	79.4	88.4
	Decision forest	91.8	94.9	88.4	91.6	97.7
	Decision jungle	90.5	92	88.8	90.4	97
	GBDT	95.7	96.8	94.4	95.6	99.4
	LightGBM	95.7	97.2	93.9	95.5	99.4
	Locally deep SVM	90.8	92.4	88.8	90.6	97.2
	LR	79.4	79.5	79.3	79.4	88.4
	SVM	78.8	79.1	78.4	78.8	88.1
	XGBoost	96.8	97.5	95.9	96.7	99.6
SMOTE	ANN	95.6	97.8	93.4	95.5	99.3
	Averaged perceptron	80.1	80.7	79.3	80	89
	Bayes point machine	91.1	933	88.6	90.9	97.1
	Decision forest	95.9	97	94.7	95.8	99.3
	Decision jungle	90.4	90.3	90.7	90.5	96.5
	GBDT	80.3	80.9	79.5	80.2	89
	LightGBM	90	90.8	89.2	90	96.8
	Locally deep SVM	94.9	95.8	93.6	94.7	99.2
	LR	80.2	80.8	79.4	80.1	89
	SVM	79.8	80.6	78.5	79.6	88.9
	XGBoost	96.1	96.5	95.5	96	99.4

The different classification techniques on Electricity Grid Dataset showed different performances to identify improvement in grid stability. XGBoost has an accuracy of 94.7%, but when combining XGBoost with ROS, its accuracy improved to 96.8%. LightGBM has an accuracy of 94.6%, but when combined with ROS, its accuracy improved to 95.7%. Similarly, ANN has an accuracy of 93.4%, but when combining it with ROS, its accuracy improved to 95.7%.

Table 7: Grid stability prediction: a comparison of previous work.

Reference	Year	Dataset	Number of features	Number of instances	Results (accuracy)
[33]	2020	New York Independent System Operator Data	9	2832	Enhanced MLP = 65.01% Enhanced SVM = 70.40% Enhanced LR = 67.78%
[31]	2019	Electrical Grid Stability (Simulated Dataset)	14	10,000	KRR – XGBoost hybrid = 91.40%
[34]	2019	Electrical Grid Stability (Simulated Dataset)	14	10,000	MLP = 93.8% GBDT = 88.8 LR = 66.3% RF = 87.8%
[36]	2018	Australian PV Solar Power Data	12	3828	ANN = 85% NB = 83% LDA = 86%
[37]	2018	Simulated Data generated through Spider IDE	4	3000	Ensemble diverse ELM = 94.13%
[11]	2018	Electrical Grid Stability (Simulated Dataset)	14	10,000	DT = 80%
[35]	2018	Dynamic simulation-based power system data	5	10147	RF = 90.01% ANN = 89.73% SVM = 86.7%

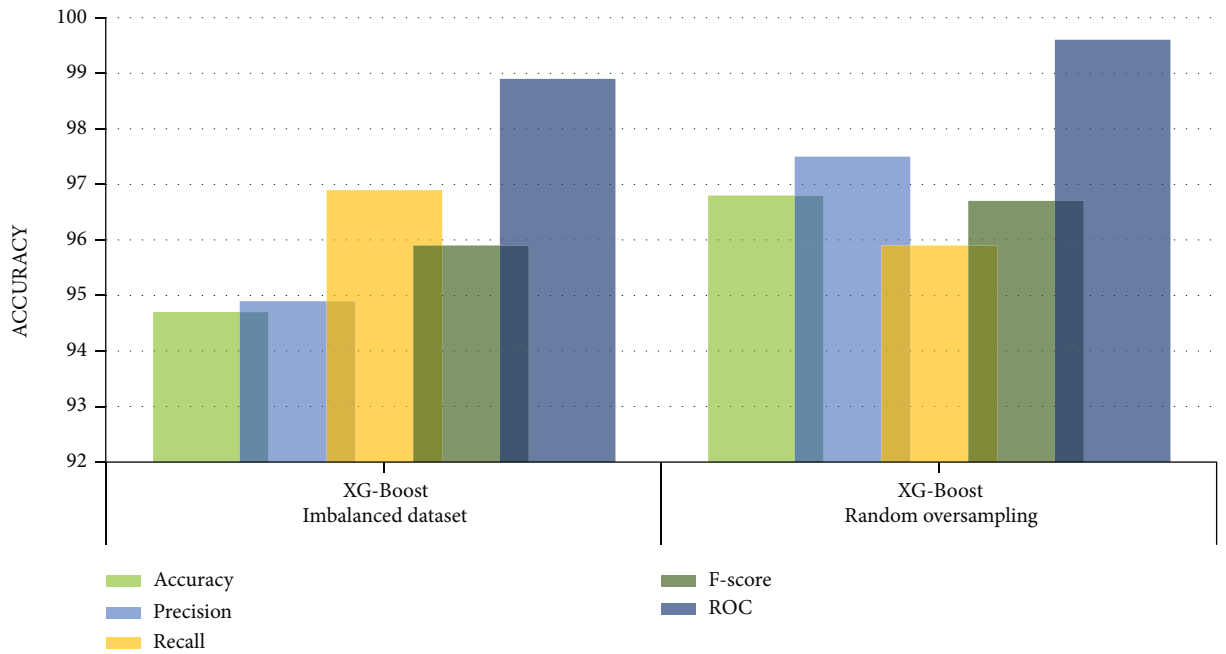

Figure 2: The performance comparison of the proposed framework on imbalance and oversample dataset.

The fourth algorithm, GBDT, gave an accuracy of 94.1%, but while combining it with SMOTE-oversampling and ADASYN-oversampling, its results were improved to 95.9%, as shown in Table 6.

On the contrary, undersampling techniques predicted less accuracy than the oversampling and imbalanced dataset. The ANN with random undersampling gave results of 94.5%, ANN with cluster centroid undersampling gave 94.4%, and XGBoost with near miss undersampling has given results of 92.6%, as shown in Table 5. This model may help better predict the stability of a decentralized electricity grid, which may help better distribute and manage electricity. To test the effectiveness of our proposed technique, it is verified using the Electricity Grid Dataset. It

can be used to evaluate any real-time dataset. LightGBM has never been used to predict grid stability to our knowledge. Rather than employing algorithmic level data resampling techniques, only data level resampling techniques have been employed in this research, limiting our work. A detailed comparison of different studies has been shown in Table 7 below for grid stability prediction.

7. Conclusion

A stable power grid is necessary to overcome power outages and a constant electricity supply. There must be a balance between power supply and demand for a grid to remain stable. Due to the volatile nature of renewable energy resources, the decentralized grid often destabilizes. Various ML algorithms were applied in this study to predict the stability of a decentralized power grid. Key input variables influencing the grid stability were the power production or consumption by the grid participants (p), price elasticity, i.e., the cost sensitivity of the grid participants (g) and participants' reaction time against price changes (tau). The simulated data from the UCI machine learning repository predicts the decentralized grid stability. Balanced data predicts better results than imbalanced data; so, different resampling techniques have been used to address the class imbalance issue and obtain better results. Four oversampling techniques (ROS, ADASYN, SMOTE, and borderline-SMOTE) and three undersampling techniques (random undersampling, near miss, and cluster centroid) were used to balance the class distribution in the dataset. After preprocessing the data, different ML models were used for results prediction, and the results were compared. Oversampling techniques predicted the best results in our experiments.

In contrast, undersampling techniques were less accurate than oversampling and imbalanced datasets. It may also imply that if the number of instances increases, the classifier has a greater chance of learning the patterns that differentiate binary classes. The XGBoost algorithm outperformed all other ML algorithms to predict the decentralized electricity grid. XGBoost predicted accuracy of 94.7%, but while combining it with ROS, its accuracy prediction was improved to 96.8%. To boost the model's accuracy, four tuning parameters were applied. More complex decentralized grids can also be explored with more than four grid participants involving multiple prosumers and different grid architectures, i.e., circular and multibranched configurations, to explore the proposed model's performance further.

Data Availability

The data used to support the findings of this study are available from the corresponding authors upon request

Conflicts of Interest

The authors declare that they have no conflicts of interest

Acknowledgments

Princess Nourah Bint Abdulrahman University Researchers Supporting Project number (PNURSP2022R54), Princess Nourah Bint Abdulrahman University, Riyadh, Saudi Arabia.

References

[1] M. Usman and M. Radulescu, "Examining the role of nuclear and renewable energy in reducing carbon footprint: does the role of technological innovation really create some difference?," *Science of The Total Environment*, vol. 841, article 156662, 2022.

[2] T. T. Teo, T. Logenthiran, and W. L. Woo, "Forecasting of photovoltaic power using extreme learning machine," in *2015 IEEE Innovative Smart Grid Technologies - Asia (ISGT ASIA),*, pp. 1–6, Bangkok, Thailand, 2015.

[3] B. Schäfer, M. Matthiae, M. Timme, and D. Witthaut, "Decentral smart grid control," *New Journal of Physics*, vol. 17, no. 1, article 015002, 2015.

[4] International Renewable Energy Agency, "A renewable energy roadmap 2030," 2021, http://www.irena.org/-/media/Files/IRENA/Agency/Publication/2014/IRENA_REmap_summary_findings_2014.pdf.

[5] Alternate Energy Development Board Government of Pakistan, "Alternate and renewable energy policy," 2019, http://www.aedb.org/images/Draft_ARE_Policy_2019_-_Version_2_July_21_2019.pdf.

[6] M. Younas, S. Shafique, A. Hafeez, F. Javed, and F. Rehman, "An overview of hydrogen production: current status, potential, and challenges," *Fuel*, vol. 316, article 123317, 2022.

[7] B. Schäfer, C. Grabow, S. Auer, J. Kurths, D. Witthaut, and M. Timme, "Taming instabilities in power grid networks by decentralized control," *The European Physical Journal Special Topics*, vol. 225, no. 3, pp. 569–582, 2016.

[8] A. Ali, D. Raisz, and K. Mahmoud, "Voltage fluctuation smoothing in distribution systems with RES considering degradation and charging plan of EV batteries," *Electric Power Systems Research*, vol. 176, article 105933, 2019.

[9] M. Khushi, K. Shaukat, T. M. Alam et al., "A comparative performance analysis of data resampling methods on imbalance medical data," *IEEE Access*, vol. 9, pp. 109960–109975, 2021.

[10] B. N. Alhasnawi, B. H. Jasim, B. E. Sedhom, E. Hossain, and J. M. Guerrero, "A new decentralized control strategy of microgrids in the internet of energy paradigm," *Energies*, vol. 14, no. 8, p. 2183, 2021.

[11] V. Arzamasov, K. Böhm, and P. Jochem, "Towards concise models of grid stability," in *2018 IEEE International Conference on Communications, Control, and Computing Technologies for Smart Grids (SmartGridComm)*, pp. 1–6, Aalborg, Denmark, 2018.

[12] M. Timme, L. Kocarev, and D. Witthaut, "Focus on networks, energy and the economy," *New Journal of Physics*, vol. 17, no. 11, article 110201, 2015.

[13] A. Wahab, T. M. Alam, and M. M. Raza, "Usability evaluation of FinTech mobile applications: a statistical approach," in *2021 International Conference on Innovative Computing (ICIC)*, pp. 1–10, Lahore, Pakistan, 2021.

[14] K. Shaukat, S. Luo, N. Abbas, T. Mahboob Alam, M. Ehtesham Tahir, and I. A. Hameed, "An analysis of blessed Friday sale at

a retail store using classification models," in *2021 The 4th International Conference on Software Engineering and Information Management*, pp. 193–198, Yokohama Japan, 2021.

[15] A. Tariq, M. J. Awan, J. Alshudukhi, T. M. Alam, K. T. Alhamazani, and Z. Meraf, "Software measurement by using artificial intelligence," *Journal of Nanomaterials*, vol. 2022, 10 pages, 2022.

[16] T. I. Baig, T. M. Alam, T. Anjum et al., "Classification of human face: Asian and non-Asian people," in *2019 International Conference on Innovative Computing (ICIC)*, pp. 1–6, Lahore, Pakistan, 2019.

[17] K. Shaukat, T. M. Alam, S. Luo et al., "A review of time-series anomaly detection techniques: a step to future perspectives," in *Advances in Information and Communication. FICC 2021*, K. Arai, Ed., vol. 1363 of Advances in Intelligent Systems and Computing, pp. 865–877, Springer, Cham, 2021.

[18] T. M. Alam, K. Shaukat, A. Khelifi et al., "A fuzzy inference-based decision support system for disease diagnosis," *The Computer Journal*.

[19] T. M. Alam, K. Shaukat, A. Khelifi et al., "Disease diagnosis system using IoT empowered with fuzzy inference system," *Computers, Materials and Continua*, vol. 70, no. 3, pp. 5305–5319, 2022.

[20] K. Shaukat, T. M. Alam, M. Ahmed et al., "A model to enhance governance issues through opinion extraction," in *2020 11th IEEE Annual Information Technology, Electronics and Mobile Communication Conference (IEMCON)*, pp. 511–516, Vancouver, BC, Canada, 2020.

[21] T. M. Alam and M. J. Awan, "Domain analysis of information extraction techniques," *International Journal Of Multidisciplinary Sciences And Engineering*, vol. 9, no. 6.

[22] Y. Ali, A. Farooq, T. M. Alam, M. S. Farooq, M. J. Awan, and T. I. Baig, "Detection of schistosomiasis factors using association rule mining," *IEEE Access*, vol. 7, pp. 186108–186114, 2019.

[23] T. I. Baig, Y. D. Khan, T. M. Alam, B. Biswal, H. Aljuaid, and D. Q. Gillani, "Ilipo-pseaac: identification of lipoylation sites using statistical moments and general pseaac," *Computers, Materials and Continua*, vol. 71, no. 1, pp. 215–230, 2022.

[24] K. Shaukat, T. M. Alam, I. A. Hameed et al., "A comprehensive dataset for bibliometric analysis of SARS and coronavirus impact on social sciences," *Data in Brief*, vol. 33, article 106520, 2020.

[25] M. Z. Latif, K. Shaukat, S. Luo, I. A. Hameed, F. Iqbal, and T. M. Alam, "Risk factors identification of malignant mesothelioma: a data mining based approach," in *2020 International Conference on Electrical, Communication, and Computer Engineering (ICECCE)*, pp. 1–6, Istanbul, Turkey, 2020.

[26] S. Farah, N. Humaira, Z. Aneela, and E. Steffen, "Short-term multi-hour ahead country-wide wind power prediction for Germany using gated recurrent unit deep learning," *Renewable and Sustainable Energy Reviews*, vol. 167, article 112700, 2022.

[27] A. K. Bashir, S. Khan, B. Prabadevi et al., "Comparative analysis of machine learning algorithms for prediction of smart grid stability†," *International Transactions on Electrical Energy Systems*, vol. 31, no. 9, article e12706, 2021.

[28] A. Ali, K. Mahmoud, and M. Lehtonen, "Optimal planning of inverter-based renewable energy sources towards autonomous microgrids accommodating electric vehicle charging stations," *IET Generation, Transmission & Distribution*, vol. 16, no. 2, pp. 219–232, 2022.

[29] A. Ali, K. Mahmoud, and M. Lehtonen, "Optimization of photovoltaic and wind generation systems for autonomous microgrids with PEV-parking lots," *IEEE Systems Journal*, vol. 16, no. 2, pp. 3260–3271, 2022.

[30] A. Ali, D. Raisz, and K. Mahmoud, "Optimal scheduling of electric vehicles considering uncertain RES generation using interval optimization," *Electrical Engineering*, vol. 100, no. 3, pp. 1675–1687, 2018.

[31] D. Yin, Y. Yang, M. Yang, Z. Yang, C. Li, and L. Li, "A new distributed power system for stability prediction and analysis," in *2019 IEEE 10th International Conference on Software Engineering and Service Science (ICSESS)*, pp. 1–4, Beijing, China, 2019.

[32] S. Theocharides, G. Makrides, G. E. Georghiou, and A. Kyprianou, "Machine learning algorithms for photovoltaic system power output prediction," in *2018 IEEE International Energy Conference (ENERGYCON)*, pp. 1–6, Limassol, Cyprus, 2018.

[33] H. Bano, A. Tahir, I. Ali, A. Haseeb, and N. Javaid, "Electricity load and price forecasting using enhanced machine learning techniques," in *Innovative Mobile and Internet Services in Ubiquitous Computing. IMIS 2019*, L. Barolli, F. Xhafa, and O. Hussain, Eds., vol. 994 of Advances in Intelligent Systems and Computing, pp. 255–267, Springer, Cham, 2020.

[34] D. Moldovan and I. Salomie, "Detection of sources of instability in smart grids using machine learning techniques," in *2019 IEEE 15th International Conference on Intelligent Computer Communication and Processing (ICCP),*, pp. 175–182, Cluj-Napoca, Romania, 2019.

[35] V. Malbasa, C. Zheng, P.-C. Chen, T. Popovic, and M. Kezunovic, "Voltage stability prediction using active machine learning," *IEEE Transactions on Smart Grid*, vol. 8, no. 6, pp. 3117–3124, 2017.

[36] M. Abuella and B. Chowdhury, "Forecasting solar power ramp events using machine learning classification techniques," in *2018 9th IEEE International Symposium on Power Electronics for Distributed Generation Systems (PEDG)*, pp. 1–6, Charlotte, NC, USA, 2018.

[37] G. N. Baltas, C. Perales-González, P. Mazidi, F. Fernandez, and P. Rodríguez, "A novel ensemble approach for solving the transient stability classification problem," in *2018 7th International Conference on Renewable Energy Research and Applications (ICRERA)*, pp. 1282–1286, Paris, France, 2018.

[38] D. A. Wood, "Predicting stability of a decentralized power grid linking electricity price formulation to grid frequency applying an optimized data-matching learning network to simulated data," *Technology and Economics of Smart Grids and Sustainable Energy*, vol. 5, no. 1, 2020.

[39] Q. Abu Al-Haija, A. A. Smadi, and M. F. Allehyani, "Meticulously intelligent identification system for smart grid network stability to optimize risk management," *Energies*, vol. 14, no. 21, p. 6935, 2021.

[40] P. Breviglieri, T. Erdem, and S. Eken, "Predicting smart grid stability with optimized deep models," *SN Computer Science*, vol. 2, no. 2, pp. 1–12, 2021.

[41] M. Massaoudi, H. Abu-Rub, S. S. Refaat, I. Chihi, and F. S. Oueslati, "An effective ensemble learning approach-based grid stability assessment and classification," in *2021 IEEE Kansas Power and Energy Conference (KPEC)*, pp. 1–6, Manhattan, KS, USA, 2021.

[42] S. Shabbir, M. S. Asif, T. M. Alam, and Z. Ramzan, "Early prediction of malignant mesothelioma: an approach towards non-

invasive method," *Current Bioinformatics*, vol. 16, no. 10, pp. 1257–1277, 2021.

[43] T. M. Alam, M. Mushtaq, K. Shaukat, I. A. Hameed, M. Umer Sarwar, and S. Luo, "A novel method for performance measurement of public educational institutions using machine learning models," *Applied Sciences*, vol. 11, no. 19, p. 9296, 2021.

[44] T. M. Alam, K. Shaukat, I. A. Hameed et al., "An investigation of credit card default prediction in the imbalanced datasets," *IEEE Access*, vol. 8, pp. 201173–201198, 2020.

[45] T. M. Alam, M. M. A. Khan, M. A. Iqbal, W. Abdul, and M. Mushtaq, "Cervical cancer prediction through different screening methods using data mining," *International Journal of Advanced Computer Science and Applications*, vol. 10, 2019.

[46] I. Mani and I. Zhang, "kNN approach to unbalanced data distributions: a case study involving information extraction," in *Proceedings of workshop on learning from imbalanced datasets*, Washington DC, 2003.

[47] S.-J. Yen and Y.-S. Lee, "Cluster-based under-sampling approaches for imbalanced data distributions," *Expert Systems with Applications*, vol. 36, no. 3, pp. 5718–5727, 2009.

[48] N. V. Chawla, K. W. Bowyer, L. O. Hall, and W. P. Kegelmeyer, "SMOTE: synthetic minority over-sampling technique," *Journal of Artificial Intelligence Research*, vol. 16, pp. 321–357, 2002.

[49] A. Fernández, S. Garcia, F. Herrera, and N. V. Chawla, "SMOTE for learning from imbalanced data: progress and challenges, marking the 15-year anniversary," *Journal of Artificial Intelligence Research*, vol. 61, pp. 863–905, 2018.

[50] H. He, Y. Bai, E. A. Garcia, and S. Li, "ADASYN: adaptive synthetic sampling approach for imbalanced learning," in *2008 IEEE International Joint Conference on Neural Networks (IEEE World Congress on Computational Intelligence)*, pp. 1322–1328, Hong Kong, 2008.

[51] H. Wang and B. Raj, "On the origin of deep learning," 2017, https://arxiv.org/abs/1702.07800.

[52] T. M. Alam, K. Shaukat, I. A. Hameed et al., "A novel framework for prognostic factors identification of malignant mesothelioma through association rule mining," *Biomedical Signal Processing and Control*, vol. 68, article 102726, 2021.

[53] T. Chen and C. Guestrin, "Xgboost: a scalable tree boosting system," in *Proceedings of the 22nd ACM SIGKDD International Conference on Knowledge Discovery and Data Mining*, pp. 785–794, San Francisco California, USA, 2016.

[54] T. M. Alam, M. A. Iqbal, Y. Ali et al., "A model for early prediction of diabetes," *Informatics in Medicine Unlocked*, vol. 16, article 100204, 2019.

[55] T. M. Alam, K. Shaukat, M. Mushtaq et al., "Corporate bankruptcy prediction: an approach towards better corporate world," *The Computer Journal*, vol. 64, no. 11, pp. 1731–1746, 2021.

Hindawi
Wireless Communications and Mobile Computing
Volume 2022, Article ID 7761150, 10 pages
https://doi.org/10.1155/2022/7761150

Research Article

A Low-Profile Compact Meander Line Telemetry Antenna with Low SAR for Medical Applications

N. H. Sulaiman,[1] **Muhammad Inam Abbasi**,[2] **N. A. Samsuri**,[3] **M. K. A. Rahim**,[3] **and F. C. Seman**[4]

[1]*School of Electrical Engineering and Artificial Intelligence, Xiamen University Malaysia, Sepang, Selangor, Malaysia*
[2]*Centre for Telecommunication Research & Innovation (CETRI), Faculty of Electrical and Electronic Engineering Technology (FTKEE), Universiti Teknikal Malaysia Melaka (UTeM), Melaka 76100, Malaysia*
[3]*School of Electrical, Faculty of Engineering, Universiti Teknologi Malaysia, 81310 Johor Bharu, Malaysia*
[4]*Fakulti Kejuruteraan Elektrik Dan Elektronik, Universiti Tun Hussein Onn Malaysia, 86400 Parit Raja, Batu Pahat, Johor, Malaysia*

Correspondence should be addressed to Muhammad Inam Abbasi; muhammad_inamabbasi@yahoo.com

Received 26 March 2022; Revised 26 July 2022; Accepted 30 July 2022; Published 12 August 2022

Academic Editor: Farman Ullah

A low-profile Compact Meander Line Telemetry Antenna (CMLTA) operating at 402.5 MHz for the Medical Implant Communication System (MICS) band medical applications is introduced. The proposed antenna focuses specifically on pacemaker telemetry applications. The meander line technique with an open loop configuration and simple transmission line feeding mechanism has been used for achieving the compact design. Based on the theory of surface current distribution, the proposed technique provides the opportunity to increase the electrical dimensions while decreasing the physical dimensions of the antenna. Further design optimization is carried out to optimize the overall antenna size to a maximum volume of 4080 mm^3. By introducing CMLTA, the size of the antenna is reduced by 79% as compared to the previous work. The proposed antenna demonstrated satisfactory performance with 10 dB bandwidth of 6.17%, a maximum gain of -22 dBi and an EIRP of -25.28 dBi. The analysis of Specific Absorption Rate under premise use of 1 W input power provided the maximum 1 g and averaged 10 g SAR of 74.7 W/kg and 17.7 W/kg, respectively, demonstrating a satisfactory level according to the IEEE standard safety guidelines. Fabrication and measurements are carried out where measured results are found to be in good agreement with the simulated results. With the optimized dimensions, satisfactory gain, EIRP, and SAR performance, the proposed CMLTA is deemed suitable for pacemaker telemetry applications for effective communication.

1. Introduction

The microstrip patch antennas are proposed by different researchers in various forms because of their compact size and high-performance capabilities. Many applications require high gain antennas, and hence, microstrip arrays are required for these applications [1–6], while other applications demand electrically small and compact antennas [7, 8]. The implantable antenna is one of its kind, which has been receiving immense attention nowadays [9–14]. Recent research works have shown that implantable antenna needs to be designed with broadband performance in order to reduce the shift in resonant frequency due to nonhomogenous human tissues [15]. The antenna size is one of the main issues in designing an implantable antenna. Besides that, maintaining good performance in different environments is indeed a challenging task. Some solutions have been suggested in the past, such as loading the ground plane with slots [16]. However, slotted ground design is confined to those applications without a conductor under the ground plane. Two more types of low-profile implantable antennas were introduced in [17], where spiral and PIFA structures were proposed to obtain a small size for implantable antennas. The radiation efficiency of PIFA was observed to be

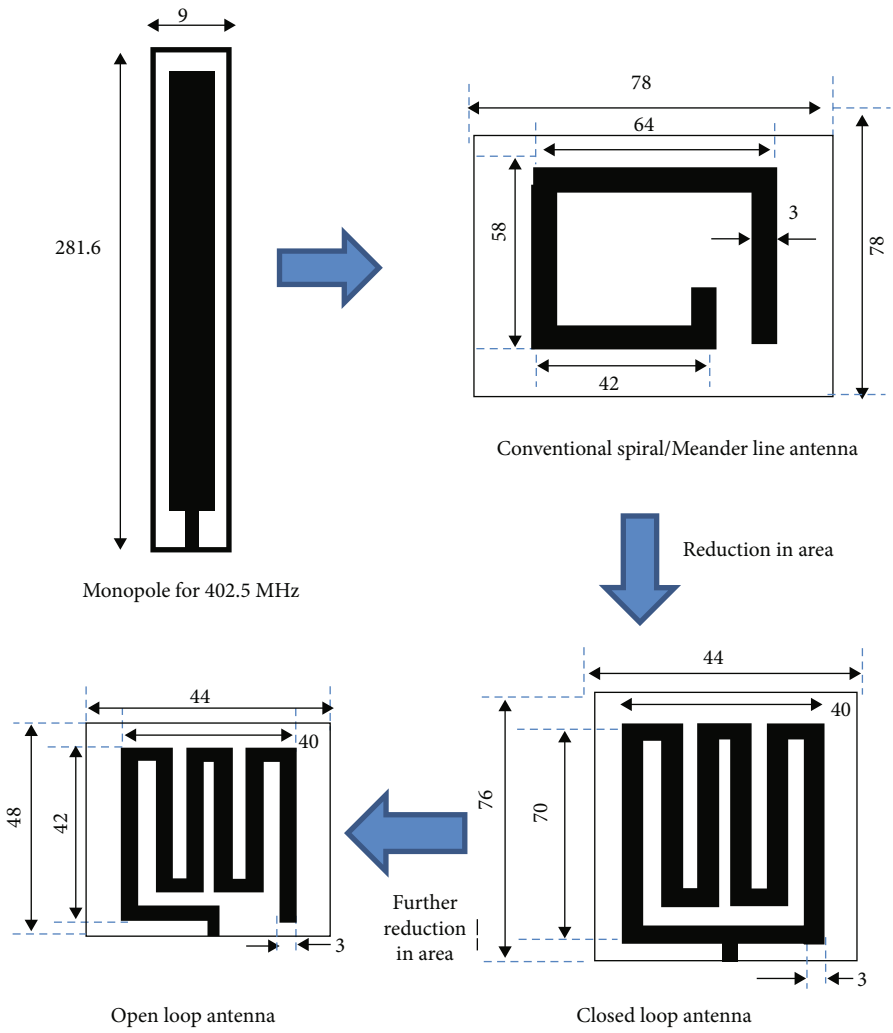

Figure 1: Detail design process and configuration of the proposed CMLTA (open loop) (all dimensions are in mm).

higher than that of the microstrip antenna. However, PIFA in [17] used high dielectric permittivity material to obtain a smaller size. In another work [18], an implantable antenna for pacemaker applications with dimensions of $42 \times 43.6 \times 11$ mm was proposed, and the investigations were carried out by implanting the antenna inside the pig. However, the accuracy of measured results and antenna size still remains the major issue to be resolved in implantable antenna design.

Since an implantable antenna has to be embedded in the human body, therefore, safety considerations have to be taken into account while designing such antennas. Moreover, the design process of biomedical systems involves Electromagnetic (EM) radiating structures like antennas, which might harm the human body by excessive exposure to radiation or thermal heating. Effective Isotropic Radiated Power (EIRP) is one of the factors that can be used to characterize and limit the radiated power from the antenna. The thermal heating of the tissues can be classified by the Specific Absorption Rate (SAR) [19, 20]. In order to preserve patient safety, the standard SAR guidelines need to be carefully addressed. The antenna is required to be designed with accuracy and carefulness, considering it is surrounded by a complicated tissue environment [21, 22]. Generally, for implantable antenna measurements and analysis, there are two approaches used to mimic the human body, which are the one-layer skin tissues model (homogenous phantom) and three-layer model (non-homogenous phantom) consisting of skin, fat, and muscle [23, 24]. In [25], two tissue models were compared, and the results showed that there is no significant discrepancy between the reflection coefficient of the antenna, while a slight resonant frequency shift was observed. In another work, the implantable antenna was also analyzed in the human body by using Gustav Voxel model, which is available in CST MWS [9]. This technique can also be useful, particularly for determining the antenna performance according to the safety limit for EIRP and SAR.

In this research work, an improved design of a low-profile implantable antenna based on the Compact Meander Line Telemetry Antenna (CMLTA) operating at 402.5 MHz for the Medical Implant Communication System (MICS) band medical applications is proposed. The antenna size has been reduced based on the optimization of the electrical length of the antenna, while the EIRP and SAR have been governed to follow the safety standards by the effective use

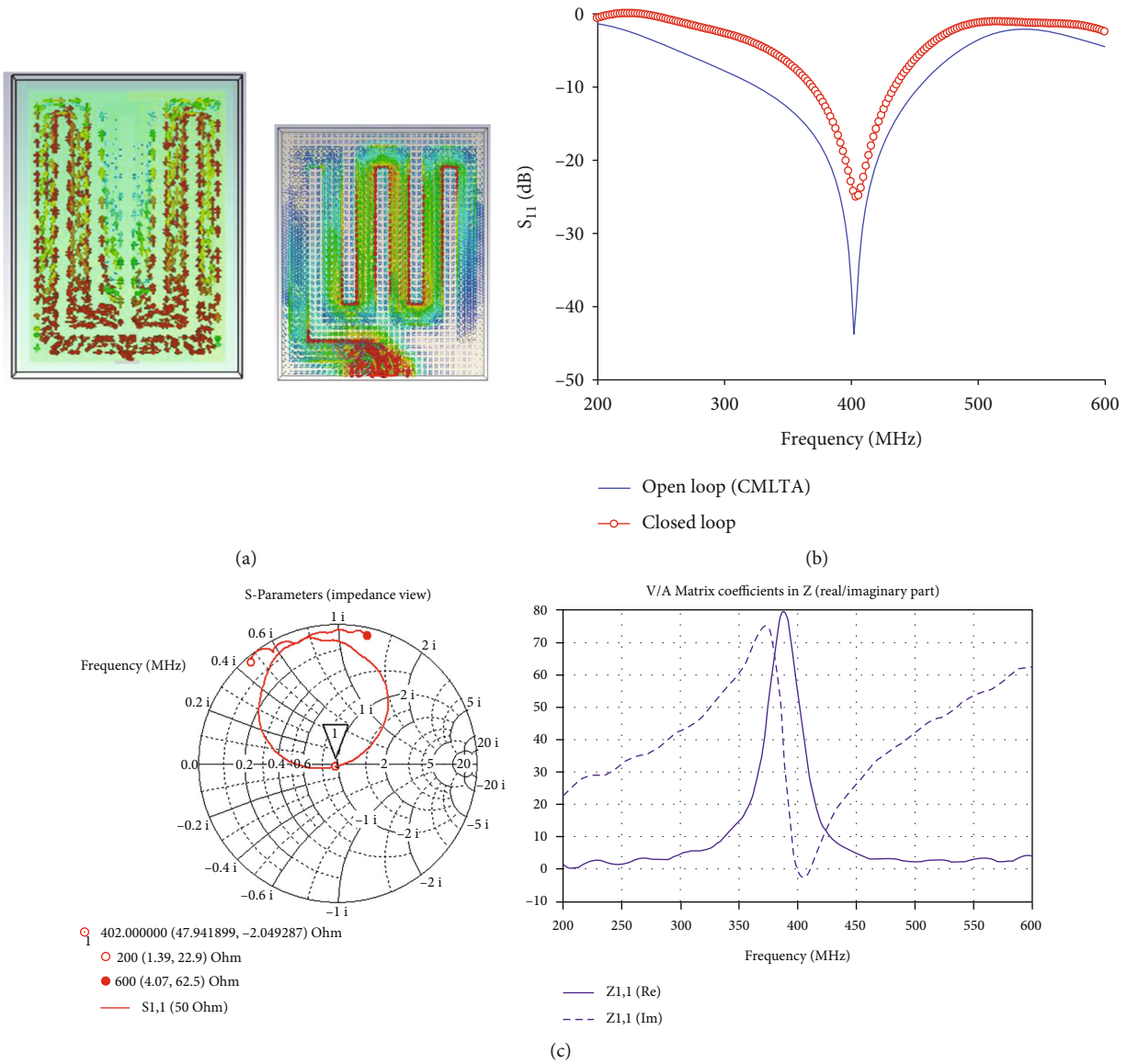

Figure 2: Comparison between closed loop and open loop (CMLTA): (a) surface current distribution; (b) simulated return loss performance; (c) wave impedance of the proposed CMLTA.

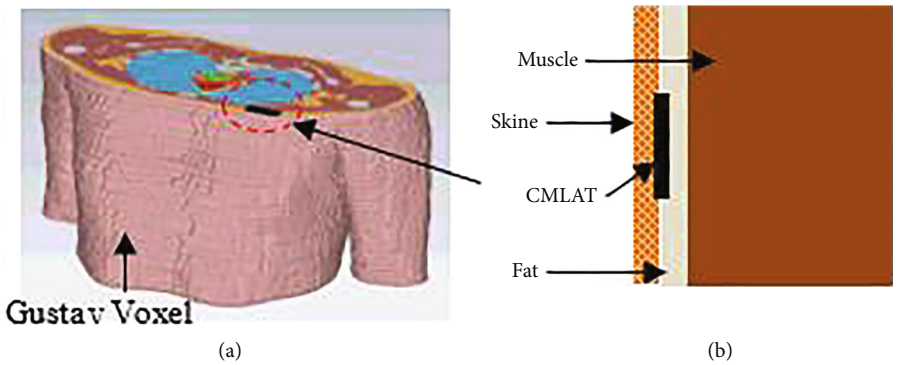

Figure 3: Simulations and measurements setup of the proposed antenna. (a) Simulation setup of the CMLTA in voxel body and (b) nonhomogenous phantom.

Table 1: Size comparison between the proposed antenna and previous work.

Ref.	References		Proposed CMLTA		Percentage reduction
	Design technique/material	Volume (mm^3)	Design technique	Volume (mm^3)	
[12]	PIFA/ Taconic CER-10 ($\varepsilon_r = 10$)	20143			79%
[11]	Microstrip Spiral/Rogers 3010 ($\varepsilon_r = 10.2$)	10240	Microstrip Meander Line/ ($FR\,4 = 4.7$ and $\tan\delta = 0.025$)	4080	60%
[11]	PIFA/Rogers 3010 ($\varepsilon_r = 10.2$)	6144			34%

of substrate and superstrate. The analysis is based on the measured results obtained using the developed single-layer homogeneous phantom model. The proposed CMLTA could be a suitable telemetry antenna to be implanted together with an artificial pacemaker.

2. Antenna Design and Optimization

The proposed antenna is designed at 402.5 MHz by means of commercially available CST Microwave Studio (CST MWS). Miniaturization of the implantable antenna is achieved by the optimization of the meander line technique as detailed in [26, 27]. Furthermore, open loop meander and closed loop meander line are also considered in the miniaturization process. The full ground plane configuration has been used, keeping in mind the requirements and sensitivity of the pacemaker telemetry applications. On the other hand, by introducing open loop configurations, the length and width of the substrate have been successfully reduced by 36.84% and 40%, respectively, as compared to the closed loop configuration. Design optimization of the antenna is carried out in order to achieve the optimum size and obtain efficient performance by comparing closed loop and open loop CMLTA, as shown in Figure 1.

The comparison between the surface current distribution and reflection coefficient performance of closed loop and open loop CMLTA antennas is shown in Figure 2(a). It can be observed from the figure that by implementing an open loop configuration, the surface current covers a longer distance, and hence, the electrical dimensions of the antenna are enlarged. This provides an opportunity to reduce the physical dimensions of the antenna. Figure 2(b) shows a comparison between the simulated return loss performance of open loop and closed loop meander line antennas. It has been demonstrated that open loop configuration offers higher bandwidth performance as compared to the closed loop configuration. Therefore, open loop configuration is chosen for further investigation in this work and annotated as Compact Meander Line Telemetry Antenna (CMLTA). Figure 2(c) shows the wave impedance of the proposed antenna, which was observed to be well matched at 402.5 MHz as in [28].

For further evaluation, the proposed CMLTA is also simulated in in-body environment. In this case, the CMLTA is added with the superstrate layer which is capable of protecting neighbouring body tissues surrounding the proposed

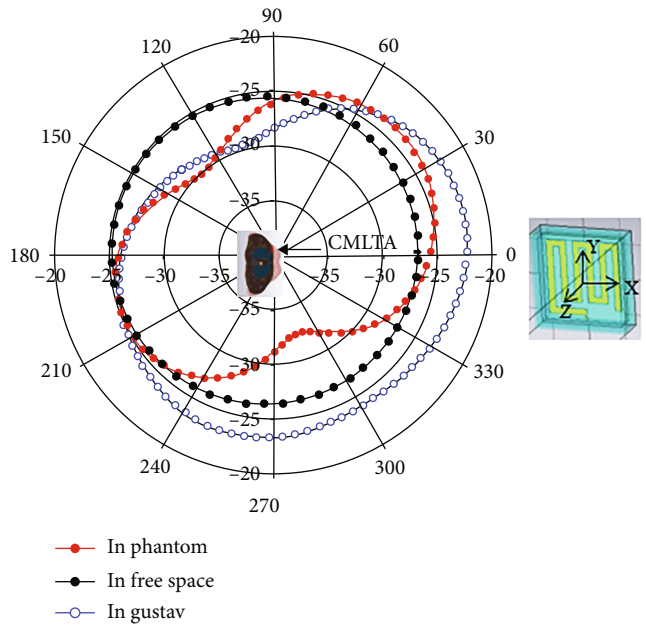

Figure 4: Simulated radiation patterns for CMLTA in phantom (nonhomogenous), Gustav voxel, and free space.

Table 2: G ain and EIRP of the proposed CMLTA.

Simulation environment	Peak gain (dBi)	Power (mW)	EIRP (dBm)
Homogeneous phantom	-24	0.745	-25.28
Nonhomogenous phantom	-29.9	0.110	-39.49
Gustav voxel	-22	0.085	-32.71

antenna. The superstrate layer acts as a buffer between the metal radiator and human tissues by reducing Radio Frequency (RF) power at the locations of lossy human tissues [29]. Therefore, for the proposed design, the superstrate and substrate have been used. In order to obtain a low profile antenna, FR-4 substrate has been chosen due to the low cost and easy fabrication. Based on the investigations carried out for different available thicknesses of FR4, 3.2 mm is observed to provide good matching, optimum size and better bandwidth performance as compared to other thicknesses of the superstrate. The complete assembly of the proposed antenna consists of a substrate with the full ground

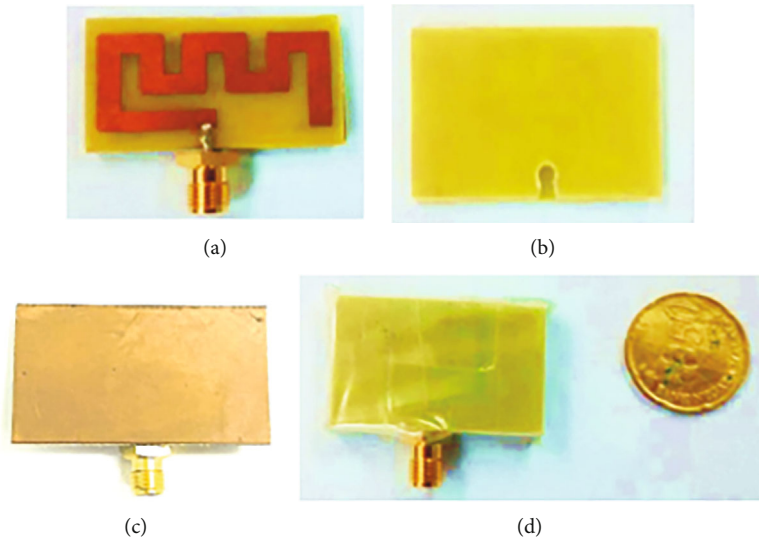

Figure 5: Fabricated antenna. (a) CMLTA on the substrate, (b) superstrate, (c) ground plane, and (d) CMLTA wrapped in plastic.

on one side and a radiating element on the other side. The radiating meander line is covered with the superstrate, and the antenna is placed inside the plastic casing. Different materials for the casing were investigated, which include plastic, aluminium, and tin, while the optimum desired performance was achieved by using plastic casing, as demonstrated in [30].

In order to investigate the performance of the proposed antenna inside the human body, simulations have been carried out in a nonhomogenous model as well as the Gustav body model made available by CST MWS as shown in Figure 3.

For the nonhomogenous model, the CMLTA is embedded under the skin and above fat and muscle layers. As in [31], the skin thickness is varied between 1 mm to 5 mm in order to observe its effect on the antenna performance. The size of the proposed antenna has been optimized by implanting the antenna inside the human body environment. However, for measurement purposes, the CMLTA has also been simulated in a homogenous phantom ($\varepsilon_r = 59.95$, $\tan\delta = 0.622$). The size comparison of the proposed antenna with previous work is shown in Table 1, while the radiation pattern of the antenna is shown in Figure 4.

It can be observed that a good monopole-like far-field pattern can be achieved by the proposed antenna design. The maximum realized gains at 402.5 MHz in nonhomogenous phantom and Gustav voxel are -24 dBi and -22 dBi, respectively, which are considered suitable for pacemaker telemetry applications. Based on the IEEE guidelines for safety, the EIRP of the implantable antenna should be lesser than -16 dBm [31]. The EIRP of the proposed design is -25.28 dBm and -32.71 dBm for homogeneous phantom and Gustav voxel, as shown in Table 2.

3. Fabrication and Measurements

The Compact Meander Line Telemetry Antenna (CMLTA) has been fabricated using 3.2 mm thick FR-4 ($\varepsilon_r = 4.7$, $\tan\delta = 0.025$) dielectric substrate (both for substrate and superstrate). The width (Ws) and length (Ls) of the substrate are 30 mm and 21.25 mm, respectively. As discussed in a previous work [32], the implantable antenna has to be protected using a casing in order to avoid direct contact with the developed phantom. The proposed antenna has to be wrapped in plastic for measurement purposes so that the radiating element can be covered and direct contact with the liquid phantom can be avoided. If the wrapping is not proper, it will affect the RF signal; hence, the CMLTA performance will be degraded. The fabricated sample of the proposed CMLTA is shown in Figure 5.

For measurement purposes, the homogenous liquid phantom has been successfully developed using the composition of water (51.3%), sugar (47.3%), and salt (1.4%) to achieve phantom properties at 402.5 MHz. Various composite samples of

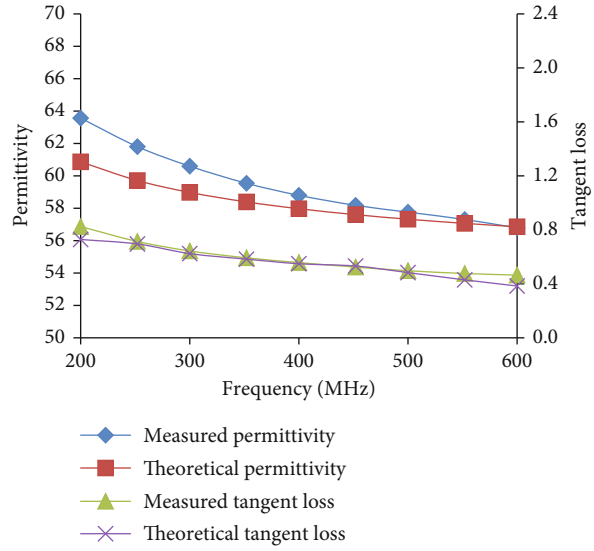

Figure 6: Comparison between measured and theoretical material properties of the developed phantom.

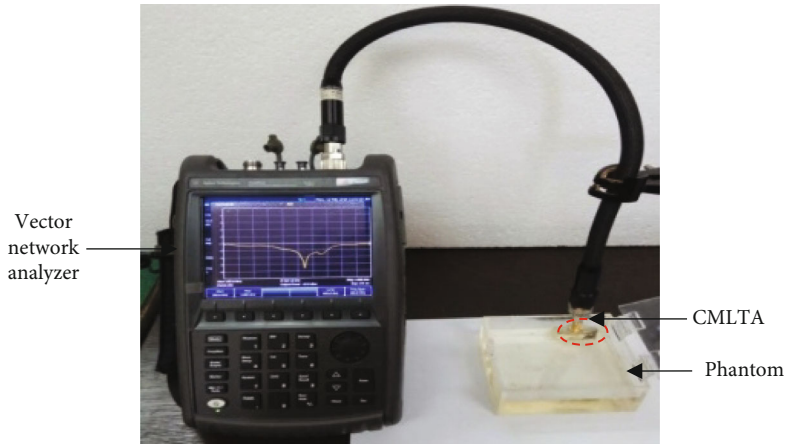

Figure 7: Measurement setup of CMLTA in a homogeneous phantom.

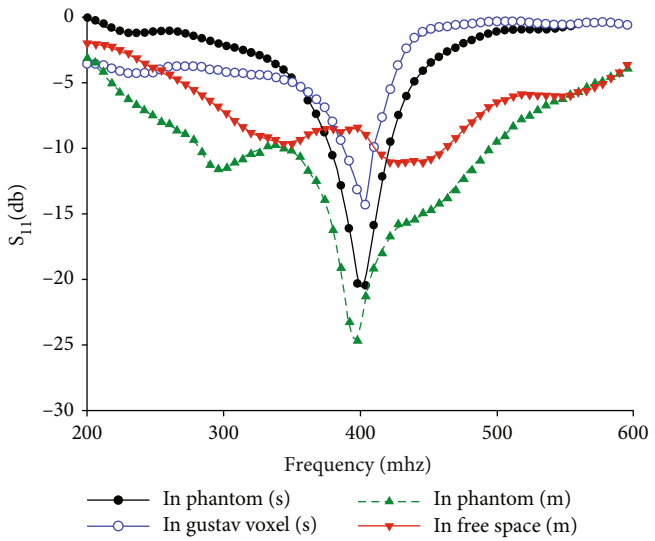

Figure 8: Simulated (s) and measured (m) CMLTA performances.It can be observed that the measured results are in good agreement with the simulated results, especially in the case of the phantom model. It can also be noted that the proposed implantable antenna worked well within the MICS band (402 MHz-405 MHz). The antenna in free space demonstrated a shift in resonant frequency as expected as the proposed antenna is purposely designed to be utilized in an in-body environment.

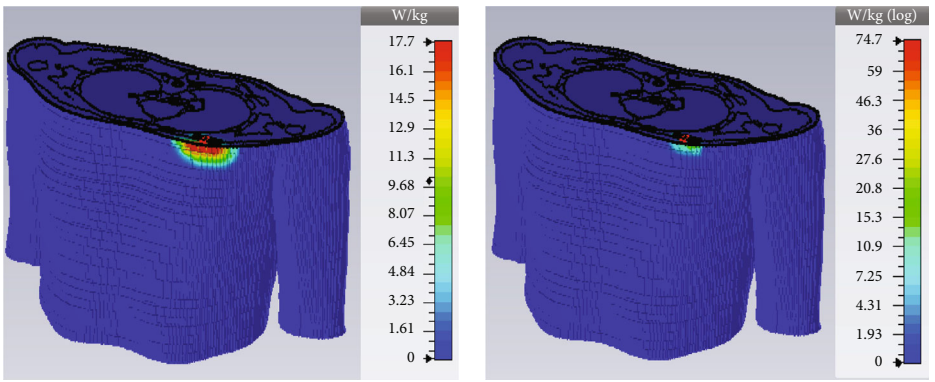

(a) 10 g (b) 1 g

Figure 9: SAR distribution in Gustav model at 402.5 MHz (1 W input power).

Table 3: SAR of CMLTA.

Standard	Maximum SAR (W/kg)	Maximum input power (mW)
C95.1-1999 (1 g-avg)	74.7	8.31
C95.1-2005 (10 g-avg)	17.7	55.20

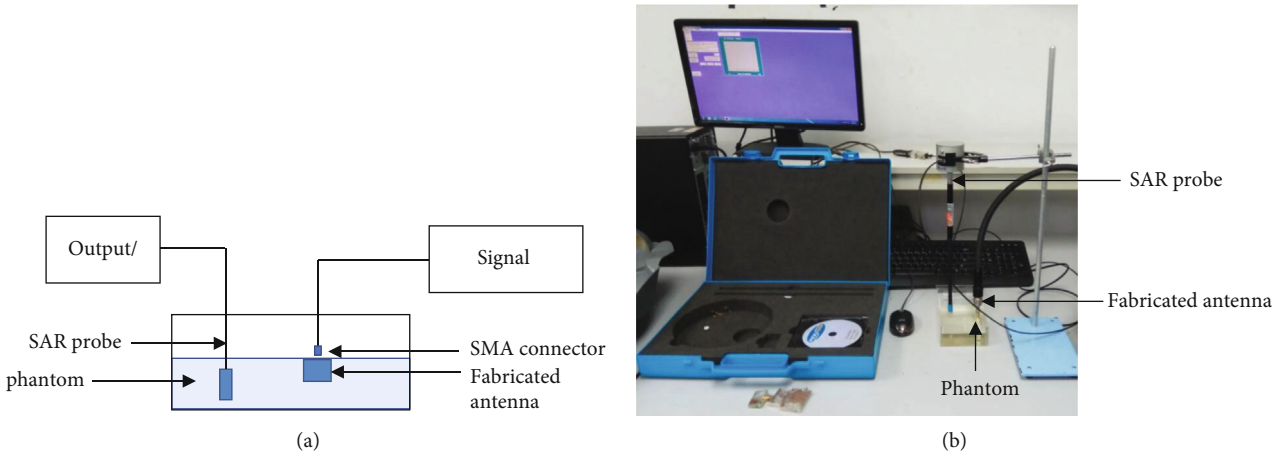

Figure 10: SAR measurements: (a) general measurement setup; (b) SAR measurements using liquid phantom.

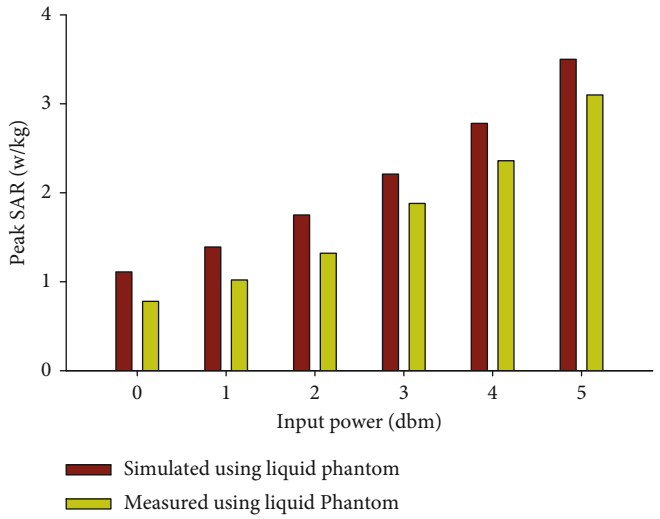

Figure 11: Simulated and measured SAR using liquid phantom.

Table 4: Performance comparisons of the proposed antenna and other implantable antennas.

Ref.	10 dB-BW (%)	Implantation tissue	Peak gain (dBi)	1 g-avg max SAR (W/kg)
[36]	8.37	Skin	—	294
[37]	5.17	Muscle	—	274.9
[38]	6.09	Skin	-33.2	606
CMLTA	6.17	Voxel body	-22	74.7

the solution have been developed to characterize material properties for comparison with the theoretical properties at 402.5 MHz [17]. Figure 6 shows the optimum dielectric properties achieved from the developed solution. The measured dielectric properties of the proposed solution have good agreement with theoretical values provided by FCC, with a maximum discrepancy of 0.43% in permittivity and 11.11% in conductivity. The obtained measured results are much closer to the FCC [33] values as compared to the results provided in the previously proposed phantom [34].

By using the developed phantom $S_{11,}$ measurements of the CMLTA have been carried out with a Vector Network

Analyzer (VNA). The measurement setup is shown in Figure 7.

As depicted in Figure 7, the CMLTA, wrapped in plastic, has been completely immersed in the developed liquid phantom. Moreover, it has been assured that the SMA connector is not having any contact with the phantom, which can modify the input impedance and hence can provide improper measured results. The comparison between the measured and simulated results is shown in Figure 8.

4. Specific Absorption Rate Analysis

In the simulation, the CMLTA is placed inside the Gustav body model, which consists of multiple layers of tissues such as muscle, skin, and fat. The CMLTA is implanted in between the skin tissue and muscle. The input power of 1 W is used, and the SAR distribution is as shown in Figure 9.

The maximum SAR is observed near the skin. No further penetration is observed as the CMLTA is equipped with a superstrate layer that protects the adjacent body tissue. Based on the previous studies, SAR investigations have also been carried out using 1 W as input power [35]. Under the premise of 1 W input power, the maximum of 10 g and 1 g average of SAR is 74.7 W/kg and 17.7 W/kg, respectively. Hence, to meet the 1 g and 10 g IEEE standards, the allowed input power of the CMLTA should be limited to 8.31 mW and 55.20 mW, respectively. The tabulated SAR results are shown in Table 3. In addition, the results are also recorded for different input power ranging from 0 dBm to 5 dBm (as the range of power is considered in [20]).

In order to validate the simulations, measurements are conducted, and the measurement setup for SAR is shown in Figure 10. The SAR probe from INDEXSAR is used to measure SAR using the *CheckSar* software interface. The fabricated CMLTA is connected to the signal generator. The CMLTA is immersed in the developed liquid phantom, and the input power is varied as in the simulation. The graphical results for SAR measurements and comparison with simulations for variable input power are shown in Figure 11.

It can be observed from Figure 11 that by varying input power from 0 dBm to 5 dBm, peak SAR has increased from 1.11 W/kg to 3.50 W/kg. The increment of peak SAR follows the theoretical trend of SAR, where a higher SAR level is distributed with higher excited power due to more absorption of energy by the human body.

Table 4 outlines the performance comparison of the proposed CMLTA to different implantable antennas. It can be seen that the CMLTA offers 6.17% of bandwidth performance, which is in the same range as previous works. Moreover, in this work, peak gain and SAR performance have also been compared between voxel body and phantom muscles demonstrating much better SAR performance.

5. Conclusions

A Compact Meander Line Antenna (CMLTA) has been designed and developed for implantable medical applications. By employing the meander line technique, a CMLTA has been proposed where the overall dimensions have provided a 79% reduction as compared to the antenna designs provided by the previous researchers. Moreover, CMLTA is easier to fabricate and has a low-cost antenna. A homogenous phantom has also been developed for validation through measurements. The reflection coefficient or S_{11} is successfully investigated by using a developed phantom, and a peak gain of -22 dBi with an EIRP of -25.28 dBi is demonstrated. Moreover, SAR analysis of the proposed antenna is carried out where the maximum SAR value is observed to be 74.7 W/kg which satisfies the IEEE standard safety guidelines. In the future, the antenna will be further used for In-Vivo measurements in order to demonstrate its applicability in implantable medical applications.

Data Availability

Data can be obtained by contacting the corresponding author.

Conflicts of Interest

The authors declare no conflict of interest.

Acknowledgments

This research was funded by MyBrain15 and Universiti Teknologi Malaysia (UTM) grant numbers 12H08 and 4F883. The authors are also thankful to the Centre for Research and Innovation Management (CRIM), Universiti Teknikal Malaysia Melaka (UTeM), for the financial support of this work.

References

[1] M. Alibakhshikenari, B. S. Virdee, P. Shukla et al., "Metamaterial-Inspired antenna array for application in microwave breast imaging systems for tumor detection," *IEEE Access*, vol. 8, pp. 174667–174678, 2020.

[2] M. Alibakhshikenari, B. S. Virdee, and E. Limiti, "Study on isolation and radiation behaviours of a 34×34 array-antennas based on SIW and metasurface properties for applications in terahertz band over 125-300 GHz," *Optik*, vol. 206, article 163222, 2020.

[3] M. Alibakhshikenari, B. S. Virdee, A. A. Althuwayb et al., "Study on on-chip antenna design based on metamaterial-inspired and substrate-integrated waveguide properties for millimetre-wave and THz integrated-circuit applications," *Journal of Infrared, Millimeter, and Terahertz Waves*, vol. 42, no. 1, pp. 17–28, 2021.

[4] A. Y. I. Ashyap, S. Alamri, S. H. Dahlan et al., "Triple-band metamaterial inspired antenna for future terahertz (THz) applications," *Computers, Materials & Continua*, vol. 72, no. 1, pp. 1071–1087, 2022.

[5] M. Inam, M. H. Dahri, M. H. Jamaluddin, N. Seman, M. R. Kamarudin, and N. H. Sulaiman, "Design and characterization of millimeter wave planar reflectarray antenna for 5G communication systems," *Engineering*, vol. 29, no. 9, article e21804, 2019.

[6] M. Inam and M. Y. Ismail, "Integration of PIN diodes with slot embedded patch elements for active reflectarray antenna

design," in *2012 International Symposium on Telecommunication Technologies*, Kuala Lumpur, Malaysia, 2012.

[7] R. Patel and T. Upadhyaya, "Electrically small inverted L planar patch antenna for wireless application," *Microwave and Optical Technology Letters*, vol. 60, no. 10, pp. 2351–2357, 2018.

[8] R. Patel and T. Upadhyaya, "An electrically small antenna for nearfield biomedical applications," *Microwave and Optical Technology Letters*, vol. 60, no. 3, pp. 556–561, 2018.

[9] L. Berkelmann and D. Manteuffel, "Antenna parameters for on-body communications with wearable and implantable antennas," *IEEE Transactions on Antennas and Propagation*, vol. 69, no. 9, pp. 5377–5387, 2021.

[10] Y. Feng, Y. Li, L. Li, B. Ma, H. Hao, and L. Li, "Design and system verification of reconfigurable matching circuits for implantable antennas in tissues with broad permittivity range," *IEEE Transactions on Antennas and Propagation*, vol. 68, no. 6, pp. 4955–4960, 2020.

[11] F. Faisal, M. Zada, A. Ejaz, Y. Amin, S. Ullah, and H. Yoo, "A miniaturized dual-band implantable antenna system for medical applications," *IEEE Transactions on Antennas and Propagation*, vol. 68, no. 2, pp. 1161–1165, 2020.

[12] C. Liu, Y. Zhang, and X. Liu, "Circularly polarized implantable antenna for 915 MHz ISM-band far-field wireless power transmission," *IEEE Antennas and Wireless Propagation Letters*, vol. 17, no. 3, pp. 373–376, 2018.

[13] H. Li, B. Wang, L. Guo, and J. Xiong, "Efficient and wideband implantable antenna based on magnetic structures," *IEEE Transactions on Antennas and Propagation*, vol. 67, no. 12, pp. 7242–7251, 2019.

[14] I. A. Shah, M. Zada, and H. Yoo, "Design and analysis of a compact-sized multiband spiral-shaped implantable antenna for scalp implantable and leadless pacemaker systems," *IEEE Transactions on Antennas and Propagation*, vol. 67, no. 6, pp. 4230–4234, 2019.

[15] O. H. Murphy, A. Borghi, M. R. Bahmanyar et al., "RF communication with implantable wireless device: effects of beating heart on performance of miniature antenna," *Healthcare Technology Letters*, vol. 1, no. 2, pp. 51–55, 2014.

[16] C. Liu, S. Member, Y. Guo, S. Member, and S. Xiao, "A hybrid patch/slot implantable antenna for biotelemetry devices," *IEEE Antennas and Wireless Propagation Letters*, vol. 11, pp. 1646–1649, 2013.

[17] J. Kim and Y. Rahmat-Samii, "Implanted antennas inside a human body: simulations, designs, and characterizations," *IEEE Transactions on Microwave Theory and Techniques*, vol. 52, no. 8, pp. 1934–1943, 2004.

[18] U. Kim and J. Choi, "An implantable antenna for wireless body area network application," *Journal of Electromagnetic Engineering and Science*, vol. 10, no. 4, pp. 206–211, 2010.

[19] K. Agarwal and Y. Guo, "Interaction of electromagnetic waves with humans in wearable and biomedical implant antennas," in *2015 Asia-Pacific Symposium on Electromagnetic Compatibility (APEMC)*, pp. 154–157, Taipei, Taiwan, 2015.

[20] A. Kiourti and K. S. Nikita, "Detuning issues and performance of a novel implantable antenna for telemetry applications," in *2012 6th European Conference on Antennas and Propagation (EUCAP)*, pp. 746–749, Prague, Czech Republic, 2011.

[21] C. Liu, S. Member, Y. Guo, S. Member, and H. Sun, "Design and safety considerations of an implantable rectenna for far-field wireless power transfer," *IEEE Transactions on Antennas and Propagation*, vol. 62, no. 11, pp. 5798–5806, 2014.

[22] N. Othman, N. Asmawati, and N. Akma, "Evaluation of specific absorption rate due to medical implant in near-field exposure," *Jurnal Teknologi*, vol. 64, no. 3, pp. 23–27, 2013.

[23] N. A. Samsuri and J. A. Flint, "A study on the effect of loop-like jewellery items worn on human hand on Specific Absorption Rate (SAR) at 1900 MHZ," in *2008 Loughborough Antennas and Propagation Conference*, pp. 297–300, Loughborough, UK, 2008.

[24] E. Rajo-iglesias, "A review of implantable patch antennas for biomedical telemetry: challenges and solutions [wireless corner]," *IEEE Antennas and Propagation Magazine*, vol. 54, no. 3, pp. 210–228, 2012.

[25] A. Kiourti and K. S. Nikita, "Accelerated design of optimized implantable antennas for medical telemetry," *IEEE Antennas and Wireless Propagation Letters*, vol. 11, pp. 1655–1658, 2012.

[26] N. H. Sulaiman, N. A. Samsuri, M. K. A. Rahim, F. C. Seman, and M. Inam, "Compact meander line telemetry antenna for implantable pacemaker applications," *Indonesian Journal of Electrical Engineering and Computer Science*, vol. 10, no. 3, p. 883, 2018.

[27] N. H. Sulaiman, N. A. Samsuri, M. K. A. Rahim, F. C. Seman, and M. Inam, "Design and analysis of optimum performance pacemaker telemetry antenna," *Telekomnika*, vol. 15, no. 2, p. 877, 2017.

[28] I. Kim, S.-G. Lee, Y.-H. Nam, and J.-H. Lee, "Investigation on wireless link for medical telemetry including impedance matching of implanted antennas," *Sensors*, vol. 21, no. 4, article 1431, 2021.

[29] H. Li, Y. X. Guo, C. Liu, S. Xiao, and L. Li, "A miniature-implantable antenna for medradio-band biomedical telemetry," *IEEE Antennas and Wireless Propagation Letters*, vol. 14, pp. 1176–1179, 2015.

[30] E. Hanada, Y. Antoku, S. Tani et al., "Electromagnetic interference on medical equipment by low-power mobile telecommunication systems," *IEEE Transactions on Electromagnetic Compatibility*, vol. 42, no. 4, pp. 470–476, 2000.

[31] Z. Duan, Y. X. Guo, M. Je, and D. L. Kwong, "Design and in vitro test of a differentially fed dual-band implantable antenna operating at MICS and ISM bands," *IEEE Transactions on Antennas and Propagation*, vol. 62, no. 5, pp. 2430–2439, 2014.

[32] A. M. A. Waddah, N. R. Khairun, and M. S. Abdirahman, "Performance of ultra-wideband wearable antenna under severe environmental conditions and specific absorption rate (Sar) study at near distances," *ARPN Journal of Engineering and Applied Science*, vol. 10, no. 4, pp. 1613–1622, 2015.

[33] FC Commission, D. L. Means, and K. W. Chan, *Evaluating compliance with FCC guidelines for human exposure to radio-frequency electromagnetic fields supplement C, edition 01-01-OET bulletin 65, edition 97-01*, Federal Communications Commission, Washington, D. C., 2001.

[34] C. Liu, Y. X. Guo, and S. Xiao, "Compact dual-band antenna for implantable devices," *IEEE Antennas and Wireless Propagation Letters*, vol. 11, pp. 1508–1511, 2012.

[35] S. Sabrin, K. P. Esselle, and K. M. Morshed, "A compact implantable antenna for bio-telemetry," in *2015 International Symposium on Antennas and Propagation (ISAP)*, pp. 2–5, Hobart, TAS, Australia, 2015.

[36] J. Kim and Y. Rahmat-samii, "Planar inverted-F antennas on implantable medical devices: meandered type versus spiral type," *Microwave and Optical Technology Letters*, vol. 48, no. 3, pp. 567–572, 2006.

[37] W. Huang and A. A. Kishk, "Embedded spiral microstrip implantable antenna," *International Journal of Antennas and Propagation*, vol. 2011, Article ID 919821, 6 pages, 2011.

[38] R. Li and S. Xiao, "Compact slotted semi-circular antenna for implantable medical devices," *Electronics Letters*, vol. 50, no. 23, pp. 1675–1677, 2014.

Hindawi
Wireless Communications and Mobile Computing
Volume 2022, Article ID 3712859, 10 pages
https://doi.org/10.1155/2022/3712859

Research Article

On Computational Offloading in Massive MIMO-Enabled Next-Generation Mobile Edge Computing

Saad AlJubayrin,[1] Muhammad Arslan Khan,[2] Rehan Ali Khan,[3] Javed Khan,[3] Kalim Ullah,[3] and Md Yeakub Ali[4]

[1]*Department of Computer Science, College of Computing and Information Technology, Shaqra University, Saudi Arabia*
[2]*Department of Computer Science & Engineering, HITEC University, Museum Road, Taxila, Pakistan*
[3]*Department of Electrical Engineering, University of Science & Technology Bannu, 28100, Pakistan*
[4]*Department of Electronics and Telecommunication Engineering, Rajshahi University of Engineering & Technology (RUET), Rajshahi 6204, Bangladesh*

Correspondence should be addressed to Md Yeakub Ali; yeakub@ete.ruet.ac.bd

Received 13 June 2022; Revised 13 July 2022; Accepted 21 July 2022; Published 9 August 2022

Academic Editor: Fawad Zaman

Next-generation wireless communication networks are expected to support massive connectivity with high data rate, low power consumption, and computational latency. However, it can significantly enhance the existing network complexity, which results in high latency. To ease this situation, mobile edge cloud and massive multiple input and multiple output (MIMO) have recently emerged as the effective solutions. Mobile edge cloud has the ability to overcome the constraints of low power and finite computational resources in next-generation communication systems by allowing devices to offload their extensive computation to maximize the computation rate. On the other hand, MIMO can enhance network spectral efficiency by using large number of antenna elements. The integration of mobile edge cloud with massive MIMO also helps to increase the energy efficiency of the devices; as a result, more bits are computed with minimal energy consumption. In this work, a mathematical model is formulated by considering the devices' energy constraint, which is nonconvex in nature. Following that, to overcome this, we transformed the original optimization problem using the first approximation method and solved the partial offloading schemes. Results reveal that the proposed scheme outperforms the others by considering computational rate as a performance matrix.

1. Introduction

Future wireless communication networks are expected to connect massive devices to the Internet [1]. These devices would be intelligent, cost-effective, and energy efficient [2]. Moreover, such devices will provide diverse quality of services [3]. Some promising technologies for these networks are artificial intelligence/machine learning [4], autonomous vehicles [5], reflecting intelligent surfaces [6], backscatter communication system [7], unmanned aerial vehicles [8], nonorthogonal multiple access [9], and high frequencies such as millimeter wave, terahertz, and visible light communications [10]. However, there exist several challenges in the development of these networks [11]. The most critical issue is the spectral efficiency due to the limited spectrum resources [12]. Another issue is the allocation of existing resources in efficient way [13]. Furthermore, security is also a big issue in both physical and network layers [14].

Recent advancements in the Internet of Things (IoT) and applications such as augmented reality [15], self-driving vehicles, smart cities [16], smart grids, and home automation have resulted in the concept of the Internet of Everything (IoE) [17], where a large number of computing and communication capable devices (e.g., sensors) are deployed [18]. The primary purpose of these sensor nodes is to collect a large amount of data generated from real-time applications and use it to manage traffic control systems [19], security [20], surveillance [21], and noise pollution control [22], as well as to assist existing

infrastructure. Similarly, the amount of data generated grows exponentially as IoT devices such as sensors, actuators, and smartphones become more widely used [23, 24]. These devices collect data from various applications, such as health care, monitoring, and security [25, 26]. In addition, these devices are small in size and have limited computing power and finite battery life [27]. However, the processing of the huge amounts of data that are produced by real-time applications must take place in an extremely condensed amount of time [28]. Due to their limited computational capabilities, these devices are unable to handle large amounts of data [29]. As a result, their quality of service (QoS) is highly compromised [30, 31]. Because of this, the need for a lot of computing power shows that users are moving away from traditional ways of communicating and toward computers [32, 33].

1.1. Related Work. In the last few decades, central clouds have been used to get around the problem of having too many computers. These central clouds enable on-demand access to massive storage and extensive computation [33–36]. In addition to this, these clouds are situated too far away from these devices, and as a result, they bring latency into the system [37]. As a result of this, relying on central clouds is insufficient [38]. However, to overcome the latency constraint imposed by central clouds, the mobile edge cloud (MEC) emerges as a practical solution, providing high computational capabilities in close proximity to these devices. The MEC enables these devices to offload their extensive computations in one of two ways: binary offloading or partial offloading. Within the framework of a binary offloading approach, the task in its entirety is computed either locally or at the MEC. In contrast, the task is divided in to two distinct segments within the framework of the partial offloading system [39]. A component of the task is carried out locally, while the remaining portion is offloaded to MEC so that it can be processed on a much larger scale. Thus, the perfect match of MEC with IoT attracted much attention from academia and industry and was identified as a critical technology beyond 5G/6G wireless networks [27, 40–43].

Recent work has focused on overcoming finite battery life constraints and limited computational capabilities by using either a partial or binary offloading scheme. The author of [15] investigates the concept of wireless power mobile edge cloud using a partial offloading scheme and maximizes end-user energy efficiency by optimally allocating the resources such as transmitted power and local chip computation and transmitting time using a mesh adaptive direct search algorithm. In [44], the author optimizes resource allocation and implements a partial offloading scheme to reduce the energy consumption of orthogonal frequency division multiple access-based mobile edge cloud networks. Simultaneously, the author describes task placement in [45] as a stochastic optimization problem, which will eventually lead to a deterministic approach for minimizing energy consumption via the dynamic offloading algorithm. In [46], the author investigates a binary offloading scheme based on optimal resource allocation over a stochastic wireless channel in order to reduce the MEC's energy consumption, whereas in [47], the author optimizes the end-computation user's rate by allocating resources such as transmission time, chip computational capabilities, and mode selection variables that specify whether the task is computed locally or offloaded to MEC for further processing.

The literature shows that offloading tasks minimize energy consumption, either partial or binary offloading schemes. However, latency is also a critical performance metric for evaluating the MEC network's performance. As a result, considerable research has been conducted in the literature to address the time-sensitive application. In [48], an author formulates the latency minimization problem for single and multiple device scenarios by partially offloading the task to MEC and investigates the role of the intelligent reflecting surface in MEC. Simultaneously, the author formulates the mutual communication and computational resource allocation problem in [49] in order to minimize the weighted sum latency of all devices. Additionally, some work has been conducted that takes into account both energy consumption and latency constraints for time-sensitive applications [50, 51]. The authors in [51] formulate the multiobjective constraint optimization problem and investigate the trade-off between energy consumption and latency in this joint formulation. Simultaneously, the author of [51] investigates the weighted sum of the task's execution time and computational energy consumption while taking the transmission power constraint into account via a partial offloading scheme.

Furthermore, the researcher contributed significantly to the field by integrating orthogonal frequency division multiple access with MEC in order to further optimize communication resource utilization by considering profit [52, 53], latency [54], and energy efficiency [55] as performance metrics. In [52], the authors consider the price of computation and optimize end-users and MEC resources using the game theory approach. Simultaneously, the author in [53] considers the objective of mobile network profit maximization while taking the end-user's quality of service constraints into account by optimizing computational and communication resources jointly. As illustrated above, successive offloading to MEC reduces energy consumption and latency. In comparison, the success of the MEC network is mainly dependent on the performance of the communication links. Thus, its performance can be enhanced by integrating it with cutting-edge wireless communication technologies such as massive MIMO. Massive MIMO, as a critical technology for the 5th generation of communication systems, supports a large number of users while increasing spectral efficiency, system capacity, robustness, and energy efficiency.

Getting inspired by massive MIMO's advantage, some researchers started considering its integration with MEC. In [56], authors consider the concept of cell-free massive MIMO which enables mobile edge cloud and uses stochastic and queuing theory to analyze the impact of computational probability on energy consumption. In [57], a low complexity algorithm is designed to optimize the communication and computational resources by considering energy consumption as a performance metric for massive MIMO-enabled MEC. The above discussion shows that MEC can

overcome finite battery life constraints, but their performance mainly depends on the communication link. Simultaneously, massive MIMO is a cutting-edge technology of wireless communication that increases spectral efficiency. Integrating it with the MEC will dramatically increase the transmission rate, which directly leads to a higher computational rate.

1.2. Motivation and Contribution. The concept of smart cities includes a significant number of Internet of Things devices. IoT is an abbreviation for the Internet of Things, which refers to low-power devices that are used to manage or aid the infrastructure of smart cities, such as traffic control, security aspects, surveillance, and pollution control. These real-time applications on these devices are generating a significant amount of data, which is being collected by these devices. On the other hand, the processing capabilities of these devices are insufficient to process the huge amount of data detected by these low-power sensors, which demand massive computation in a short amount of time. To overcome the limitations mentioned earlier, MEC emerges as a practical solution that allows these devices to offload their extensive computation. In comparison, MEC's performance can be increased by integrating it with the cutting-edge wireless communication technology called massive MIMO. Integration of massive MIMO and MEC will increase the performance of the MEC network and increase the spectral efficiency provided by massive MIMO. Specifically, massive MIMO's increased spectral and energy efficiencies can yield higher transmission rates and lower energy consumption for offloading in MEC. Moreover, the more significant number of users supported by massive MIMO can enable more parties to offload simultaneously, thus reducing queuing delays. Motivated by these facts, we aim to show the benefits of applying massive MIMO to MEC networks as given below:

(1) A mathematical model is formulated for optimal allocation of resources like channel estimation time, transmission power, computational resources, and task offloading decision parameter to maximize the cumulative computation rate of the network with subject to latency and energy constraint

(2) A fundamental trade-off between offloading and local computation is analyzed. It reveals that as the number of computational cycles requirement increases, devices start offloading their extensive task to maintain the quality of service requirements

(3) Comparative analysis of partial offloading, binary offloading, edge computation, and local computation scheme is done. Results demonstrate that the partial offloading scheme outperforms the other by considering cumulative computational rate as a performance metric

The rest of the paper is organized as follows: Section 1 represents the mathematical model of massive MIMO-enabled mobile edge cloud, whereas algorithms and simulations results are discussed in Section 3. Similarly, Section 4 concludes the work.

2. System Model

In this work, we consider the concept of massive MIMO-enabled MEC. As illustrated in Figure 1, an access point (AP) such as a base station equipped with K of antennas and a mobile edge cloud, also known as a MEC, is used to offer N number connected Internet of Things devices access to communication and computational resources. These IoT devices, such as sensor nodes, are deployed in smart cities to collect real-time data for the purpose of managing or assisting the smart city's existing infrastructure. Similarly, data generated by real-time applications is time-sensitive and must be processed in a minimal amount of time. In addition, Internet of Things devices have limited processing resources, which are insufficient to carry out operations that need large computations in a short period of time. As a result, IoT devices add latency to the system in which they are used. To overcome the constraint imposed by IoT devices' limited computational capability, the mobile edge cloud emerges as a practical solution capable of providing extensive computation to low-power IoT devices on-demand. IoT devices can offload computations that require massive amounts of computation in a short period of time.

Similarly, frame-based transmission is carried out over the same frequency band and flat fading channel. For ease of simplicity, we consider the case of perfect CSI, which means the channel is known at AP. Furthermore, for extensive computation, all users simultaneously transmit a portion of the computation task to the MEC located at the AP via space-division multiple access (SDMA) methods. Because of simultaneous transmission, AP uses the linear detector to detect each user information as represented by the matrix $\mathcal{Q}$ between n-th user and K antennas. In addition, we take into consideration a partial offloading approach for the placement of the task at the MEC. In this particular scheme, the task is broken up into two portions. The remaining part of the work is sent to the MEC to be processed, while the first part of the task is computed locally.

2.1. Task Offloading Model. Low-power Internet of Things devices are used in smart cities to collect huge amounts of raw data from real-time applications. These applications require considerable computation to be completed in a short amount of time. Latency is a problem that arises within the system as a result of the limited computational capacity of the components. As a result, quality of service (QoS) and quality of experience (QoE) are greatly compromised. Therefore, to meet the QoS and QoE requirements, these devices start offloading their tasks using a partial offloading scheme. Similarly, the number of bits offloaded by n-th to MEC located at AP in time t is represented as

$$\mathcal{R}_n^E = \mathrm{B}\log_2(1 + \chi_n)t. \tag{1}$$

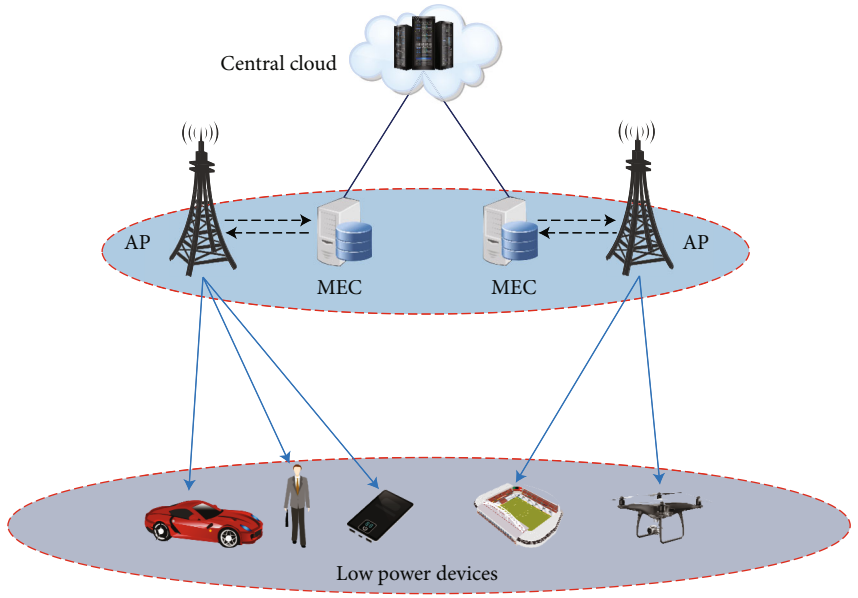

Figure 1: System model of mobile edge cloud system.

In Equation (1), B represents the system bandwidth, and χ_n represents the signal to interference plus noise ratio given by

$$\chi_n = \frac{\xi_n \left| q_n^H h_n \right|^2}{\Phi_n + \left| q_n^H q_n \right| \sigma^2}. \tag{2}$$

Similarly in (2), h_n represent the channel coefficient column matrix between n-th user and K number of antennas, ξ_n represents the uplink transmission power, and q_n represents the linear detector coefficient, whereas $\Phi_n = \sum_{i=1, i\neq k}^{N} \xi_i \left| q_n^H h_i \right|^2$ represents the interference imposed on n -th users from others and σ^2 represents the Gaussian noise factor. Simultaneously, energy consumption while offloading the number of bits to MEC for extensive computation is given by

$$\Psi_n^E = \xi_n t + \xi_r t. \tag{3}$$

In Equation (3), ξ_r signifies the constant circuit energy required for signal processing, which is static across all devices.

2.2. Local Computation. In conjunction with the computation that is taking place at MEC, a piece of the task is carried out locally by making use of the limited processing resources that are accessible on the devices. The number of cycles that must pass through the devices before one bit of data may be computed denoted by the notation $\mathscr{C}_n$. In order to complete the computation on a local scale, devices use the entire $\mathscr{T}$ time frame. As a consequence of this, the following is how the number of bits is determined locally:

$$\lambda^k = \frac{\Psi_n \mathscr{T}}{\mathscr{C}_n}. \tag{4}$$

In Equation (4), the symbol Ψ_n denotes the proportion of computational resources that the n-th device has designated to be used by itself in order to carry out the task locally. While simultaneously computing the task locally by the n-th user, the energy computation is expressed as follows:

$$\chi^k = \kappa_n \Psi_n^3 \mathscr{T}. \tag{5}$$

In Equation (5), κ_k represents the computational energy efficiency of the IoT devices.

2.3. Problem Formulation. Within the scope of this work, we investigate the idea of massive MIMO-enabled MEC. This work was aimed at improving the device's computational rate by optimizing transmission power ξ, edge computational time t, local computational resources Ψ, and task segmentation y_n^E. Following that, mathematically, optimization problems can be formulated as follows:

$$\mathbf{P1}: \max_{t, \xi_n, \Psi_n, y_n^E} \sum_{n=1}^{N} \left(w_n^L \frac{y_n^L \xi \mathscr{T}}{\mathscr{C}_n} + w_n^E \frac{y_n^E t}{\nu} B \log_2 (1 + \chi_n) \right) \tag{6a}$$

$$C_1: y_n^L \kappa_k \Psi_n^3 \mathscr{T} + y_k^E (\xi_n t + p_r \tau) \leq \mathscr{E}_{\max}, \forall n \tag{6b}$$

$$C_2: 0 \leq \Psi \leq \Psi_{\max}, \forall n \tag{6c}$$

$$C_3: y_k \in (0, 1), \xi_n \geq 0, \forall n. \tag{6d}$$

The fundamental goal of this work is to maximize the computational rate of low-power devices that are connected

1 **input:** $N \longleftarrow$ sensor nodes, $\mathscr{C} \longleftarrow$ cycles requirement, $\mathscr{E}_{\max} \longleftarrow$ Maximum battery life, $\Psi \longleftarrow$ Maximum computational capability of devices, $[t^{lower}, \xi_n{}^{lower}, \Psi_n{}^{lower}, y_n^{E^{lower}}, \mathscr{F}_n{}^{lower}]$ lower bound of Decision variables, $[t^{upper}, \xi_n{}^{upper}, \Psi_n{}^{upper}, y_n^{E^{upper}}, \mathscr{F}_n{}^{upper}]$ upper bound of Decision variables,
2 **Initialization:** Number of decision variables
3 $\mathfrak{A} \longleftarrow 4N + 1$, Generate Population.
4 **Execution:**
5 **while** $error \leq \epsilon$
6 **foreach** $p \in Population$ **do**
7 $\Omega \longleftarrow$ *solve* (8)
8 **end**
9 // *Sort* Ω *in Descending order, and select best Population*
10 //*Base on best population, calculate mean* $\mathscr{M}$ *and standard deviation* $\mathscr{SD}$. **foreach** $p \in Population$ **do**
11 $\Omega \longleftarrow$ *solve* (8)
12 **end**
13 **end**
14

Algorithm 1: Convex Optimization Algorithm.

to the MEC at the AP while simultaneously taking into consideration a number of constraints. In (6a), (6b), (6c), and (6d), the overhead at the MEC due to successive offloading is denoted by ν, whereas w_n^L and w_n^E are the weighting coefficients used to prioritize the users according to their quality of service requirements, such that $w_n^L + w_n^E = 1$. Simultaneously, y_n^L and y_n^E are chosen in such a way that $y_n^E = 1 - y_n^L$ indicates the part of the task that was executed either locally or at the MEC. Following that, constraint C_1 specifies that the task is computed locally or offloaded to MEC. In both cases, the energy consumption should be less than the maximum amount of power that the gadgets can draw from their batteries, as represented by $E_{\max}$.

3. Results and Discussion

3.1. Optimal Resource Allocation. The objective function specified in (6a), (6b), (6c), and (6d) is nonlinear and nonconvex in nature due to logarithmic nature of rate equation. Following that, it is analytically challenging to solve and get the optimal results. To overcome this limitation, we introduce a slag variable $\mathscr{F}$ and transform an optimization problem P1 as follows:

$$\mathbf{P2}: \max_{t,\xi_n,\Psi_n,y_n^E,\mathscr{F}_n} \sum_{n=1}^{N} \left(w_n^L \frac{y_n^L \xi \mathscr{T}}{\mathscr{C}_n} + w_n^E \frac{y_n^E t}{\nu} \mathscr{F}_n \right) \tag{7a}$$

$$C_1: B\log_2\left(1 + \frac{\xi_n \left|q_n^H h_n\right|^2}{\Phi_n + \left|q_n^H q_n\right|\sigma^2}\right) \geq \mathscr{F}_n, \forall n \tag{7b}$$

$$\text{s.t.Equations (6b) to (6d).} \tag{7c}$$

The objective function specified in (7a), (7b), and (7c) is convex by definition. Additionally, the constraint mentioned in (7b) is not convex in nature. To overcome this, we use the first-order approximation method and further transform the objective function as follows:

$$\mathbf{P3}: \max_{t,\xi_n,\Psi_n,y_n^E,\mathscr{F}_n} \sum_{n=1}^{N} \left(w_n^L \frac{y_n^L \xi \mathscr{T}}{\mathscr{C}_n} + w_n^E \frac{y_n^E t}{\nu} \mathscr{F}_n \right) \tag{8a}$$

$$C_1: \log\left(\mathfrak{F}_n\right) \geq \frac{\log(2)\mathscr{F}_n}{B} + \log\left(\Phi_n + \left|q_n^H q_n\right|\right), \forall n \tag{8b}$$

$$\text{s.t.Equations (6b) to (6d).} \tag{8c}$$

In Equation (8b), $\mathfrak{F}_n = \Phi_n + |q_n^H q_n|\sigma^2 + \xi_n |q_n^H h_n|^2$. Following that, the constraints and objection function of (8a), (8b), and (8c) is convex in nature and can be solve easily using the convex optimization Algorithm 1.

3.2. Discussion. In the concept of smart cities, these low-power devices are used to collect the real-time data used to make decisions for further action or planning. Data collected from real-time applications needs extensive computation that can be computed locally using device computational resources or placed as a whole in MEC for further processing. Figure 2 is a comparative study of the local computational scheme and the edge computational scheme through the use of varied amounts of computational cycles C_K from 10 K-cycles to 100 K-cycles. The computational rate is used as a performance metric, and this number refers to the number of bits that are computed in $T = 1$ seconds. The effectiveness of the model that has been proposed is evaluated using this metric. Simulations were carried out using Algorithm 1 by setting a number of devices $K = 50$. Results reveal that local computation, in which the whole task is computed locally using device computational resources, outperforms the edge computation scheme, where the whole task is to be placed on the MEC server for extensive computation. This behavior is because of successive offloading, and it leads to congestion at MEC and thus introduces overhead. As a result, it takes more time to compute the task. As a result, the computation rate is low using the edge computational scheme as compared to the local computation scheme. On

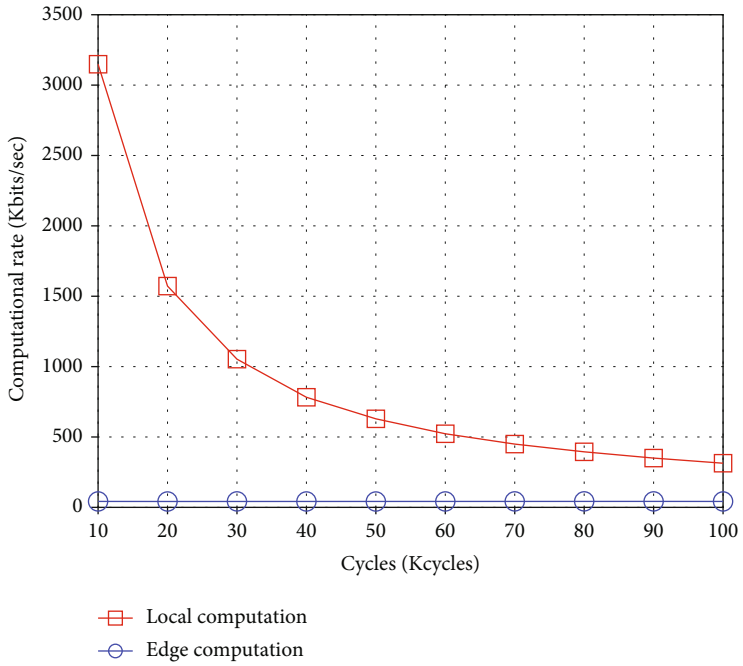

Figure 2: Comparison of local and edge computation scheme.

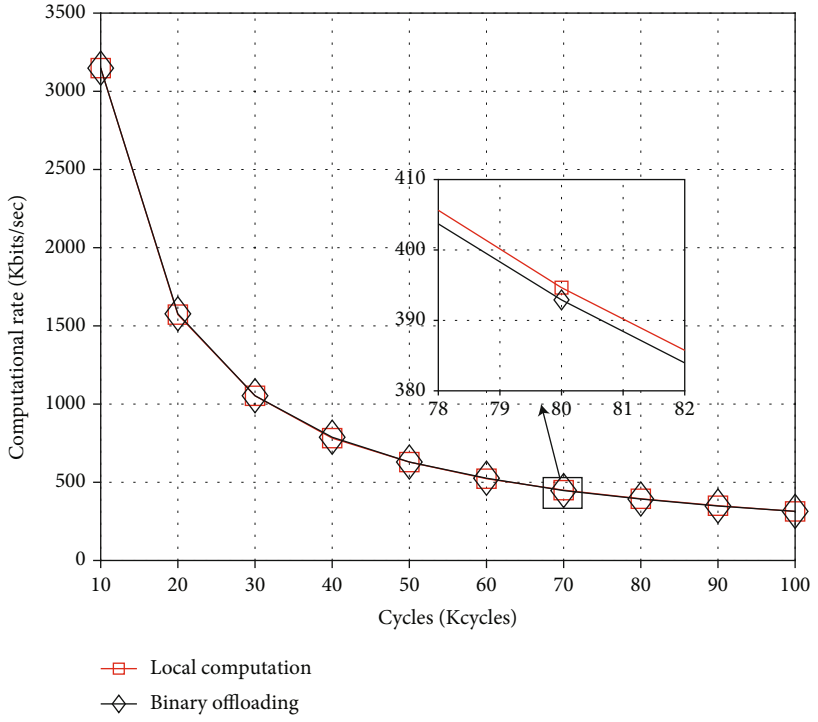

Figure 3: Comparison of local computation and binary offloading scheme.

the other hand, as the computational cycle requirements increase, the performance of the local computational scheme is going to decrease because of the finite computational capability of the devices. Thus, the quality of service requirements is highly compromised.

As is evident from the above discussion, successive offloading results in congestion at the MEC servers; thus, it introduces overhead. In order to prevent congestion, MEC gives devices the ability to offload their computation by utilizing a binary offloading method. In a binary offloading strategy, some devices offload their tasks to MEC, where the rest compute locally using their finite computational resources. Figure 3 shows a comparative analysis of the binary offloading method and the local computation by

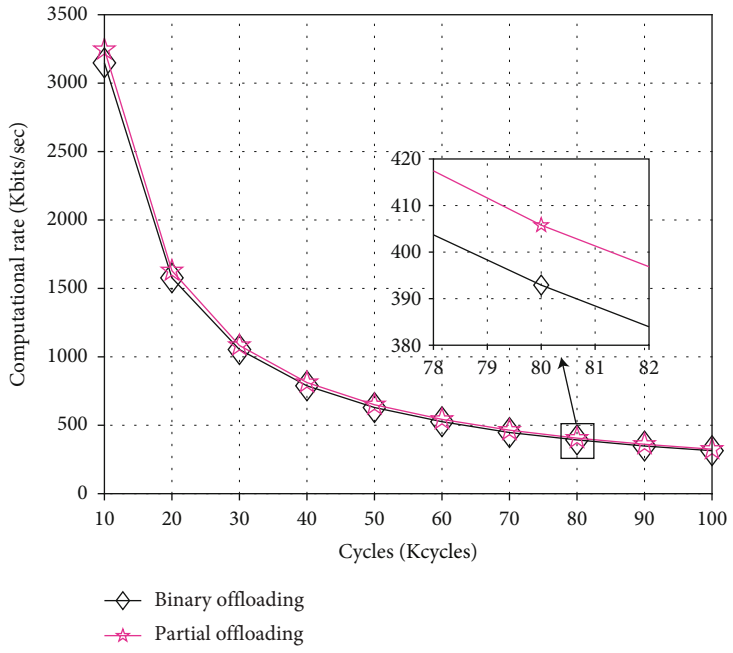

Figure 4: Comparison of binary and partial offloading scheme.

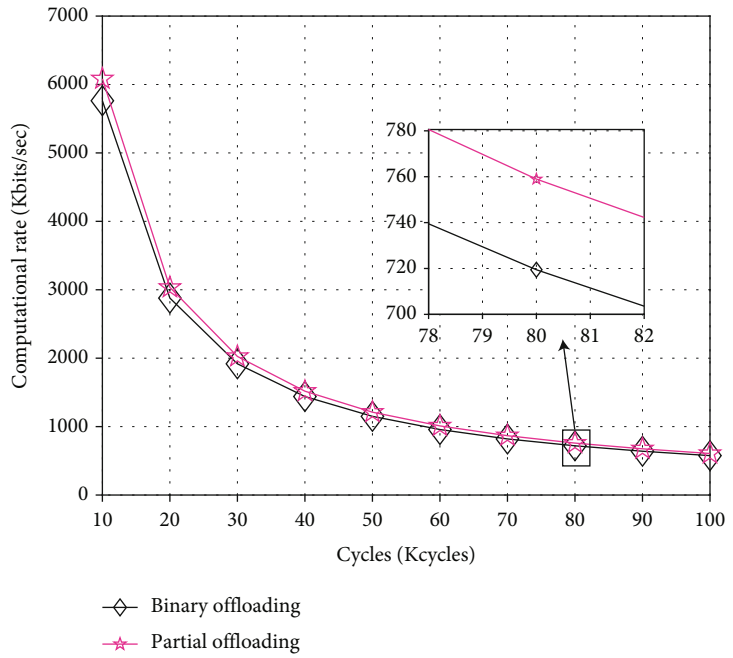

Figure 5: Comparison of binary and partial offloading scheme with multiple users.

taking the computational rate into consideration as a performance parameter across numerous needs for the computational cycle. Results reveal that, for the low number of computational cycles required, the performance of both schemes is the same. On the other hand, as the number of computational cycle requirements increases, the binary offloading scheme starts performing better than the local computation scheme. This trend is because, in the local computation scheme, the finite computational capability of the devices is not enough to handle a large number of computational cycle requirements. Therefore, as a result, to maintain the quality of service requirements, they started offloading their whole task to the MEC server located at the AP for extensive computation. To overcome the latency constraint, binary offloading is an effective solution that allows some of the devices to start offloading their extensive computation; thus, the commutative computation rate of the network increases.

In the binary offloading scheme, some devices are offloading their task to MEC, whereas the rest of the devices are computing their task locally using finite computational resources. In contrast, a second offloading technique known as the partial offloading scheme delegates a portion of the work to MEC from each of the devices. In the partial offloading technique, the work is divided into two halves; one component is computed locally, and the other portion is offloaded to MEC for additional processing. Both portions of the task are computed in parallel. Figure 4 represents the comparative analysis of the partial and binary offloading scheme. An extensive simulation was carried out, and average results were produced. The results reveal that the partial offloading scheme's performance is much better than the binary offloading scheme, even for the small number of computational cycle requirements. This trend is because, in the binary offloading scheme, the task as a whole is offloaded to MEC; thus, it requires more computational energy and time, whereas in the partial offloading scheme, only a portion of the task is offloaded, and as compared to the whole task, it also consumes less energy and requires minimal time. This tremendous effect can be seen more effectively by increasing the number of users from 50 to 100, as shown in Figure 5. The effectiveness of this proposed model can be utilized in the future generation communication system, where a large number of devices are used to collect data for making a future decisions like in smart cities to manage traffic, and pollution control, make better use of infrastructure, and keep citizens safe and clean.

4. Conclusion

In this work, we considered the massive MIMO-enabled mobile edge cloud to provide the computational resources to the low-power devices to maintain the quality of service requirements. This work is aimed at maximizing the computational rate by optimal allocation of computational resources, computational and channel estimation time, and transmission powers. A comparative analysis of the local computation scheme, edge computational scheme, binary offloading scheme, and partial offloading scheme were carried out in order to validate the proposed system. The results of these analyses revealed the fundamental trade-off that exists between offloading and local computations. The findings demonstrate that the limited computing capabilities of devices are insufficient to manage substantial computation when the required number of computational cycles grows. In contrast, a partial offloading strategy performs significantly better than the other offloading strategies used for comparison in the scenario described above.

Data Availability

This article does not meet the criteria for data sharing since no data sets were generated or analyzed.

Conflicts of Interest

The authors declare that there are no conflicts of interest regarding the publication of this paper.

References

[1] J. Liu, M. Ahmed, M. A. Mirza et al., "RL/DRL meets vehicular task offloading using edge and vehicular cloudlet: a survey," *IEEE Internet of Things Journal*, vol. 9, no. 11, pp. 8315–8338, 2022.

[2] D. Shome, O. Waqar, and W. U. Khan, "Federated learning and next generation wireless communications: a survey on bidirectional relationship," *Transactions on Emerging Telecommunications Technologies*, no. article e4458, 2021.

[3] W. U. Khan, M. A. Jamshed, E. Lagunas, S. Chatzinotas, X. Li, and B. Ottersten, "Energy efficiency optimization for backscatter enhanced NOMA cooperative V2X communications under imperfect CSI," *IEEE Transactions on Intelligent Transportation Systems*, pp. 1–12, 2022.

[4] F. Jameel, W. U. Khan, S. T. Shah, and T. Ristaniemi, "Towards intelligent IoT networks: reinforcement learning for reliable backscatter communications," in *In 2019 IEEE Globecom workshops (GC Wkshps). IEEE*, pp. 1–6, Waikoloa, HI, USA, 2019.

[5] M. Ahmed, S. Raza, M. A. Mirza et al., "A survey on vehicular task offloading: classification, issues, and challenges," *Journal of King Saud University-Computer and Information Sciences*, 2022.

[6] W. U. Khan, E. Lagunas, Z. Ali, S. Chatzinotas, and B. Ottersten, "Integration of NOMA with reflecting intelligent surfaces: a multi-cell optimization with sic decoding errors," 2022, http://arxiv.org/abs/2205.03248.

[7] F. Jameel, W. U. Khan, M. A. Jamshed, H. Pervaiz, Q. Abbasi, and R. Jäntti, "Reinforcement learning for scalable and reliable power allocation in SDN-based backscatter heterogeneous network," in *In IEEE INFOCOM 2020-IEEE Conference on Computer Communications Workshops (INFOCOM WKSHPS). IEEE*, pp. 1069–1074, Toronto, ON, Canada, 2020.

[8] W. U. Khan, E. Lagunas, Z. Ali et al., "Opportunities for physical layer security in UAV communication enhanced with intelligent reflective surfaces," 2022, http://arxiv.org/abs/2203.16907.

[9] A. Ihsan, W. Chen, and W. U. Khan, "Energy-efficient backscatter aided uplink NOMA roadside sensor communications under channel estimation errors," 2021, http://arxiv.org/abs/2109.05341.

[10] S. Raza, S. Wang, M. Ahmed, M. R. Anwar, M. A. Mirza, and W. U. Khan, "Task offloading and resource allocation for IoV using 5G NRV2X communication," *IEEE Internet of Things Journal*, vol. 9, no. 13, 2022.

[11] I. Tomkos, D. Klonidis, E. Pikasis, and S. Theodoridis, "Toward the 6G network era: opportunities and challenges," *IT Professional*, vol. 22, no. 1, pp. 34–38, 2020.

[12] W. U. Khan, F. Jameel, X. Li, M. Bilal, and T. A. Tsiftsis, "Joint spectrum and energy optimization of NOMA-enabled small-cell networks with QoS guarantee," *IEEE Transactions on Vehicular Technology*, vol. 70, no. 8, pp. 8337–8342, 2021.

[13] A. Ihsan, W. Chen, M. Asif, W. U. Khan, and J. Li, "Energy-efficient IRS-aided NOMA beamforming for 6G wireless communications," 2022, http://arxiv.org/abs/2203.16099.

[14] F. Jameel, S. Wyne, G. Kaddoum, and T. Q. Duong, "A comprehensive survey on cooperative relaying and jamming strategies for physical layer security," *IEEE Communications Surveys & Tutorials*, vol. 21, no. 3, pp. 2734–2771, 2018.

[15] A. Mahmood, A. Ahmed, M. Naeem, and Y. Hong, "Partial offloading in energy harvested mobile edge computing: a direct search approach," *IEEE Access*, vol. 8, pp. 36 757–36 763, 2020.

[16] M. Sheng, Y. Wang, X. Wang, and J. Li, "Energy-efficient multiuser partial computation offloading with collaboration of terminals, radio access network, and edge server," *IEEE Transactions on Communications*, vol. 68, no. 3, pp. 1524–1537, 2019.

[17] F. Jameel, S. Zeb, W. U. Khan, S. A. Hassan, Z. Chang, and J. Liu, "NOMA-enabled backscatter communications: toward battery-free IoT networks," *IEEE Internet of Things Magazine*, vol. 3, no. 4, pp. 95–101, 2020.

[18] M. K. Ehsan, "Performance analysis of the probabilistic models of ism data traffic in cognitive radio enabled radio environments," *IEEE Access*, vol. 8, pp. 140–150, 2019.

[19] H. Ju and R. Zhang, "Throughput maximization in wireless powered communication networks," *IEEE Transactions on Wireless Communications*, vol. 13, no. 1, pp. 418–428, 2014.

[20] A. Mahmood, Y. Hong, M. K. Ehsan, and S. Mumtaz, "Optimal resource allocation and task segmentation in IoT enabled mobile edge cloud," *IEEE Transactions on Vehicular Technology*, vol. 70, no. 12, pp. 13 294–13 303, 2021.

[21] I. Qadeer and M. K. Ehsan, "Improved channel reciprocity for secure communication in next generation wireless systems," *Cmccomputers Materials & Continua*, vol. 67, no. 2, pp. 2619–2630, 2021.

[22] W. U. Khan, J. Liu, F. Jameel, V. Sharma, R. Jäntti, and Z. Han, "Spectral efficiency optimization for next generation NOMA-enabled IoT networks," *IEEE Transactions on Vehicular Technology*, vol. 69, no. 12, pp. 15 284–15 297, 2020.

[23] S.-W. Ko, K. Han, and K. Huang, "Wireless networks for mobile edge computing: spatial modeling and latency analysis," *IEEE Transactions on Wireless Communications*, vol. 17, no. 8, pp. 5225–5240, 2018.

[24] M. Ahmed, W. U. Khan, A. Ihsan, X. Li, J. Li, and T. A. Tsiftsis, "Backscatter sensors communication for 6G low-powered NOMA-enabled IoT networks under imperfect SIC," 2021, http://arxiv.org/abs/2109.12711.

[25] J. H. Anajemba, T. Yue, C. Iwendi, M. Alenezi, and M. Mittal, "Optimal cooperative offloading scheme for energy efficient multi-access edge computation," *IEEE Access*, vol. 8, pp. 53 931–53 941, 2020.

[26] M. Shabbir, A. Shabbir, C. Iwendi et al., "Enhancing security of health information using modular encryption standard in mobile cloud computing," *IEEE Access*, vol. 9, pp. 8820–8834, 2021.

[27] Y. Zhang, B. Di, P. Wang, J. Lin, and L. Song, "HetMEC: heterogeneous multi-layer mobile edge computing in the 6 G era," *IEEE Transactions on Vehicular Technology*, vol. 69, no. 4, pp. 4388–4400, 2020.

[28] M. K. Ehsan, A. A. Shah, M. R. Amirzada et al., "Characterization of sparse WLAN data traffic in opportunistic indoor environments as a prior for coexistence scenarios of modern wireless technologies," *Alexandria Engineering Journal*, vol. 60, no. 1, pp. 347–355, 2021.

[29] W. U. Khan, A. Ihsan, T. N. Nguyen, M. A. Javed, and Z. Ali, "NOMA-enabled backscatter communications for green transportation in automotive-industry 5.0," *IEEE Transactions on Industrial Informatics*, p. 1, 2022.

[30] U. Masud, M. R. Amirzada, H. Elahi et al., "Design of two-mode spectroscopic sensor for biomedical applications: analysis and measurement of relative intensity noise through control mechanism," *Applied Sciences*, vol. 12, no. 4, p. 1856, 2022.

[31] M. K. Ehsan, *Statistical Modeling of Indoor Data Traffic in the 2.4 Ghzism Band for Cognitive Radio Systems*, Kassel University Press, 2017.

[32] M. K. Ehsan and D. Dahlhaus, "A framework for statistical characterization of indoor data traffic for efficient dynamic spectrum access in the 2.4 ghz ism band," *International Journal of Digital Information and Wireless Communications (IJDIWC)*, vol. 5, no. 4, pp. 210–220, 2015.

[33] A. Mahmood, A. Ahmed, M. Naeem, M. R. Amirzada, and A. Al-Dweik, "Weighted utility aware computational overhead minimization of wireless power mobile edge cloud," *Computer Communications*, vol. 190, pp. 178–189, 2022.

[34] M. K. Ehsan and D. Dahlhaus, "Statistical modeling of ism data traffic in indoor environments for cognitive radio systems," in *In 2015 Third International Conference on Digital Information, Networking, and Wireless Communications (DINWC). IEEE*, pp. 88–93, Moscow, Russia, 2015.

[35] A. A. Shah, M. K. Ehsan, K. Ishaq, Z. Ali, and M. S. Farooq, "An efficient hybrid classifier model for anomaly intrusion detection system," *IJCSNS*, vol. 18, no. 11, p. 127, 2018.

[36] N. Naz, M. K. Ehsan, M. R. Amirzada, M. Y. Ali, and M. A. Qureshi, "Intelligence of autonomous vehicles: a concise revisit," *Journal of Sensors*, vol. 2022, 11 pages, 2022.

[37] J. H. Anajemba, T. Yue, C. Iwendi, P. Chatterjee, D. Ngabo, and W. S. Alnumay, "A secure multiuser privacy technique for wireless IoT networks using stochastic privacy optimization," *IEEE Internet of Things Journal*, vol. 9, no. 4, pp. 2566–2577, 2021.

[38] N. Abbas, Y. Zhang, A. Taherkordi, and T. Skeie, "Mobile edge computing: a survey," *IEEE Internet of Things Journal*, vol. 5, no. 1, pp. 450–465, 2018.

[39] H. Shafique, A. A. Shah, M. A. Qureshi, M. K. Ehsan, and M. R. Amirzada, "Machine learning empowered efficient intrusion detection framework," *VFAST Transactions on Software Engineering*, vol. 10, no. 2, 2022.

[40] Y. Wang, M. Sheng, X. Wang, L. Wang, and J. Li, "Mobile-edge computing: partial computation offloading using dynamic voltage scaling," *IEEE Transactions on Communications*, vol. 64, no. 10, pp. 4268–4282, 2016.

[41] M. R. Amirzada, Y. Khan, M. K. Ehsan, A. U. Rehman, A. A. Jamali, and A. R. Khatri, "Prediction of surface roughness as a function of temperature for SiO_2 thin-film in PECVD process," *Micromachines*, vol. 13, no. 2, p. 314, 2022.

[42] W. U. Khan, E. Lagunas, A. Mahmood, S. Chatzinotas, and B. Ottersten, "Integration of backscatter communication with multi-cell NOMA: a spectral efficiency optimization under imperfect SIC," 2021, http://arxiv.org/abs/2109.11509.

[43] M. A. Qureshi, M. Asif, M. F. Hassan et al., "A novel auto-annotation technique for aspect level sentiment analysis," *Computers, Materials and Continua*, vol. 70, no. 3, pp. 4987–5004, 2022.

[44] M. Zhao, J.-J. Yu, W.-T. Li et al., "Energy-aware offloading in time-sensitive networks with mobile edge computing," 2020, http://arxiv.org/abs/2003.12719.

[45] Y. Chen, N. Zhang, Y. Zhang, X. Chen, W. Wu, and X. S. Shen, "Dynamic computation offloading in edge computing for Internet of Things," *IEEE Transactions on Cloud Computing*, vol. 6, no. 3, pp. 4242–4251, 2019.

[46] W. Zhang, Y. Wen, K. Guan, D. Kilper, H. Luo, and D. O. Wu, "Energy-optimal mobile cloud computing under stochastic wireless channel," *IEEE Transactions on Wireless Communications*, vol. 12, no. 9, pp. 4569–4581, 2013.

[47] S. Bi and Y. J. Zhang, "Computation rate maximization for wireless powered mobile-edge computing with binary computation offloading," *IEEE Transactions on Wireless Communications*, vol. 17, no. 6, pp. 4177–4190, 2018.

[48] T. Bai, C. Pan, Y. Deng, M. Elkashlan, A. Nallanathan, and L. Hanzo, "Latency minimization for intelligent reflecting surface aided mobile edge computing," *IEEE Journal on Selected Areas in Communications*, vol. 38, no. 11, pp. 2666–2682, 2020.

[49] J. Ren, G. Yu, Y. He, and G. Y. Li, "Collaborative cloud and edge computing for latency minimization," *IEEE Transactions on Vehicular Technology*, vol. 68, no. 5, pp. 5031–5044, 2019.

[50] L. Cui, C. Xu, S. Yang et al., "Joint optimization of energy consumption and latency in mobile edge computing for Internet of Things," *IEEE Internet of Things Journal*, vol. 6, no. 3, pp. 4791–4803, 2018.

[51] Z. Kuang, L. Li, J. Gao, L. Zhao, and A. Liu, "Partial offloading scheduling and power allocation for mobile edge computing systems," *IEEE Internet of Things Journal*, vol. 6, no. 4, pp. 6774–6785, 2019.

[52] S.-H. Kim, S. Park, M. Chen, and C.-H. Youn, "An optimal pricing scheme for the energy-efficient mobile edge computation offloading with OFDMA," *IEEE Communications Letters*, vol. 22, no. 9, pp. 1922–1925, 2018.

[53] P. Paymard, N. Mokari, and M. Orooji, "Task scheduling based on priority and resource allocation in multi-user multi-task mobile edge computing system," in *In 2019 IEEE 30th Annual International Symposium on Personal, Indoor and Mobile Radio Communications (PIMRC). IEEE*, pp. 1–7, Istanbul, Turkey, 2019.

[54] M. Li, S. Yang, Z. Zhang, J. Ren, and G. Yu, "Joint subcarrier and power allocation for OFDMA based mobile edge computing system," in *In 2017 IEEE 28th Annual International Symposium on Personal, Indoor, and Mobile Radio Communications (PIMRC). IEEE*, pp. 1–6, Montreal, QC, Canada, 2017.

[55] Y. Wu, Y. Wang, F. Zhou, and R. Q. Hu, "Computation efficiency maximization in OFDMA-based mobile edge computing networks," *IEEE Communications Letters*, vol. 24, no. 1, pp. 159–163, 2019.

[56] S. Mukherjee and J. Lee, "Edge computing-enabled cell-free massive MIMO systems," *IEEE Transactions on Wireless Communications*, vol. 19, no. 4, pp. 2884–2899, 2020.

[57] Y. Hao, Q. Ni, H. Li, and S. Hou, "Energy-efficient multi-user mobileedge computation offloading in massive MIMO enabled HetNets," in *In ICC 2019-2019 IEEE International Conference on Communications (ICC). IEEE*, pp. 1–6, Shanghai, China, 2019.

Hindawi
Wireless Communications and Mobile Computing
Volume 2022, Article ID 7281872, 15 pages
https://doi.org/10.1155/2022/7281872

Research Article

Exploiting Blockchain and RMCV-Based Malicious Node Detection in ETD-LEACH for Wireless Sensor Networks

Asad Ullah Khan,[1,2] Maimoona Bint E. Sajid,[1] Abdul Rauf,[3] Malik Najmus Saqib,[4] Fawad Zaman,[5] and Nadeem Javaid[1,6]

[1]*Department of Computer Science, COMSATS University Islamabad, Islamabad 44000, Pakistan*
[2]*Department of Computer Science, Federal Urdu University, Islamabad 44000, Pakistan*
[3]*Hamdard University, Islamabad 44000, Pakistan*
[4]*Department of Cybersecurity, College of Computer Science and Engineering, University of Jeddah, Jeddah 21959, Saudi Arabia*
[5]*Department of Electrical and Computer Engineering, COMSATS University Islamabad, Islamabad 44000, Pakistan*
[6]*School of Computer Science, University of Technology Sydney, Ultimo, NSW 2007, Australia*

Correspondence should be addressed to Nadeem Javaid; nadeemjavaidqau@gmail.com

Received 5 March 2022; Revised 1 July 2022; Accepted 8 July 2022; Published 2 August 2022

Academic Editor: A.H. Alamoodi

In this paper, a routing protocol based on energy temperature degree-low energy-adaptive clustering hierarchy (ETD-LEACH) is proposed. In the protocol, nodes consume less energy when transmitting data, which improves the network lifetime. The proposed protocol selects the cluster heads (CHs) on the bases of degree, temperature, and energy to perform routing. Moreover, for solving the issue of a single point of failure, the blockchain is utilized. The data transactions are also housed in the blockchain, which is deployed on the CHs and BSs, as, in blockchain, multiple nodes take part. Therefore, to perform a consensus between them, a proof-of-authority (PoA) consensus mechanism is used in the underlying work. In the blockchain, the secure hashing algorithm-256 (SHA-256) is used for secure hashing of data transactions. Furthermore, malicious nodes are detected during the routing using the real-time message content validation (RMCV) scheme in the ETD-LEACH protocol. The proposed model is evaluated under the denial-of-service (DoS) attack, the man-in-the-middle (MITM) attack, and the smart contract analysis performed by the Oyente tool. The performance of the proposed model is evaluated through simulations. The ETD-LEACH and energy threshold-low energy-adaptive clustering hierarchy (ETH-LEACH) protocols are compared using different parameters like number of alive nodes, energy consumption, throughput, and delay. ETD-LEACH consumes less energy and has a better network lifetime as compared to ETH-LEACH. In addition, the RMCV-ETD-LEACH network performance is better than that of both DoS-ETD-LEACH and MITM-ETD-LEACH. Moreover, PoA transaction cost is less than that of proof of work. Also, the execution time of SHA-256 is less than the execution time of SHA-512. Moreover, the value of the packet delivery ratio (PDR) is found to be 89.9% and 99.9% with and without the malicious nodes, respectively.

1. Introduction

In the past few years, the wireless sensor networks (WSNs) have been globally used in different fields of life like the military, transportation, health applications, etc. [1, 2]. The WSN consists of compact-sized sensors that are deployed in the targeted environment. The sensors are used for tracking and monitoring purposes. In tracking purposes, sensors track enemies, animals, road traffic, etc., while in the monitoring process, sensors monitor the environment, patients' health, malicious activities, etc. [3, 4].

Unfortunately, WSNs have high security threats. The attackers attack the network and affect the network performance. Malicious nodes take part and tamper or misroute the data packets [5, 6]. Moreover, sensors are resource-constrained devices and have limited storage for storing the sensed data, while the base station (BS) is a centralized entity that causes a high chance of a single point of failure.

Therefore, blockchain is used in the WSNs to store data and provide security.

The blockchain is a decentralized, distributed, transparent, and tamper-proof ledger. In the blockchain, data transactions of the networks are stored in blocks. All blocks are chronologically connected with each other using hashes. The block structure consists of a block header and body. In the block header, there is a nonce, hash, timestamp, and Merkle tree, as shown in Figure 1, while all transactional informational is stored in the body. The nonce contains a 32-bit value that shows that the block is generated correctly. It is used in the block-mining process. Proof of work (PoW), proof of authority (PoA), and proof of stake are some of the prominent consensus mechanisms that are used to perform mining in blockchain networks. Besides, the hash is of two types: block hash and Merkle root hash. The hash is generated by the secure hashing algorithm-256 (SHA-256). Moreover, the timestamp shows the time when a new block is generated. In the Merkle tree, the hashes of all the transactions are stored in the root, and it provides security to the transactions. Therefore, it is difficult for a third party to tamper with the transactions.

Moreover, once the data transaction is added to the block, it is difficult to tamper. Therefore, blockchain is used to avoid a single point of failure. Furthermore, in the WSNs, the blockchain uses double SHA-256 for security that consumes high computational power. Furthermore, the PoW consensus mechanism is used, which incurs high transaction costs. Moreover, in WSNs, CHs are resource constrained, and their energy is drained at an early stage. Therefore, all nodes die early, which affects the network lifetime [3, 5, 7]. Moreover, in the WSNs, malicious nodes attack the network while performing routing to tamper with the data packets [8–10].

In this paper, we focus on the efficient selection of cluster heads (CHs), malicious nodes' detection, and secure routing data. The CHs are efficiently selected using the energy threshold-low energy-adaptive clustering hierarchy (ETD-LEACH), while the malicious nodes are detected using real-time message content validation (RMCV). Furthermore, the PoA consensus mechanism is used to perform consensus between the network nodes while SHA-256 is used for secure hashing the routing data. Moving ahead, the robustness and resilience of the proposed model is checked by evaluating it against denial-of-service (DoS) and man-in-the-middle (MITM) attacks. The smart contract is also assessed against different vulnerabilities using Oyente.

The major contributions made in the proposed work are as follows.

(1) ETD-LEACH and RMCV are used for efficient clustering and malicious nodes' detection, respectively

(2) PoA consensus mechanism is used for consensus while SHA-256 is used for secure hashing of the routing data

(3) The proposed model is evaluated against DoS and MITM attacks, while Oyente tool is employed to check the smart contract's resilience against different vulnerabilities

The organization of the remaining manuscript is as follows. The related work is provided in Section 2 while Section 3 comprises the explanation of the proposed system model. The validation of the proposed work is performed through simulations, the results of which are discussed in Section 4. Furthermore, the resilience of the smart contract against different vulnerabilities is discussed in Section 5, while Section 6 presents the conclusion. Table 1 presents the list of acronyms.

2. Related Work

The Internet of Things (IoTs) is a subdomain of WSN. In IoTs, multiple nodes communicated with each other via wireless connectivity. To disturb the communication, the nodes are attacked both internally and externally. When attacked internally (referred to as internal attack), malicious nodes tamper the data, while when attacked externally (referred to as external attack), malicious nodes attack the whole network, which is more damaging than the damage caused by an internal attack. Therefore, malicious nodes' detection is the main issue nowadays [11]. In [12], the authors work on localization issues in WSN. However, malicious nodes tamper the location of unknown nodes; therefore, nodes' energy is consumed. The high energy consumption affects the network lifetime [13].

In the WSN [1], authentication of the nodes is not efficient. However, a third party performs authentication, which has a high chance of performing maliciously. In [14], while performing routing, detection of the data-tampering nodes is performed. Furthermore, in [7], IoTs generate a large amount of data; therefore, security risks in terms of tampering data and unauthorized devices accessing the data are increased. However, malicious nodes' presence affects the customer's trust.

The sensors sense the data and forward it to the destination [9]. A WSN is mostly used in military wars, education, healthcare, etc. The security issue arises in the WSN while sending a data packet from source to destination. The security issues involve the malicious nodes attacking the data packet or a legitimate node acting selfishly. Moreover, a malicious node creates a black hole attack in the network. The data packets are not being forwarded to the destination and are dropped on their way to the destination due to the malicious nodes. Therefore, to resolve the above-mentioned security issues, the authors propose a central management routing protocol in which the intermediary node acts as a gateway and third party [9]. However, central authority or third party does not provide a fair secure model. Malicious nodes attack the central authority. Furthermore, in routing, a loop routing issue also arises. Malicious nodes broadcast false routing information; therefore, the data packet does not reach the destination and continuously moves in the loop [15, 16].

IoTs are used worldwide for every field of life [17]. However, IoTs have less memory and computational power and a

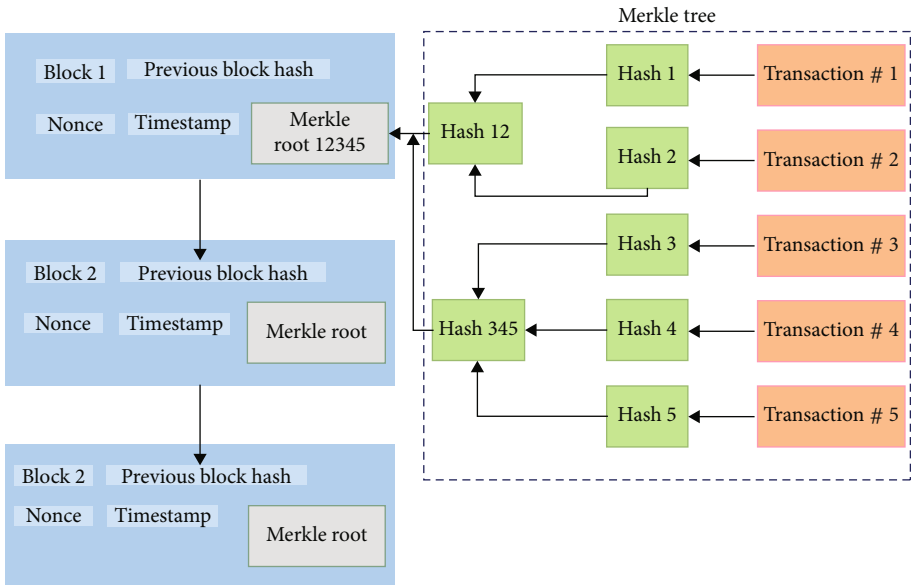

Figure 1: Block's structure.

high rate of security threats. Furthermore, the blockchain is widely used in WSN [18]; however, the consensus used in blockchain takes much time in mining data and is not suitable for smart health.

In [19], it is mentioned that WSNs are used in each field of life. However, sensors are not secured, and customers are not satisfied because of the lack of trust in terms of packet drop, delay, and energy consumption [20, 21]. In [22], the blockchain is widely used in each application for data storage and security. However, the number of users increases with the increase in applications; therefore, the PoW consensus mechanism incurs a large computational cost. Moreover, no consensus mechanism is scalable; therefore, a scalability issue also arises.

In [23], the authors highlight the issue of the centralized database. IoTs are used everywhere like smart cities, healthcare, e-commerce, etc. Large data is accessed and stored on the fog layer, which is centralized and not secure. In [24], the authors highlight the issue of security, in which a third party is involved in the communication of two parties. However, the third party is not trustworthy. In the past, authors resolve this issue by using a central authority (CA) that communicates with both parties. However, in CA, there is an issue of a single point of failure. Therefore, in the communication of IoTs, the main challenges are the single point of failure and connectivity between the increasing number of devices in IoT networks.

In [25], the authors discuss the issue of localization in WSNs. In the past, authors propose localization algorithms [26]; however, the algorithms are not secure, consume high computational resources of BS, and do not provide an accurate location of sensors. Therefore, securing sensor nodes' localization remains a challenge. The authors face the issue of security in smart cities, fog, and cloud in [27]. There is another issue of trustworthiness among nodes and privacy of data. The data is not secure against unauthorized users. Moreover, smart cities are scalable; however, there is an issue of data traceability.

In [28], authors highlight the issues related to a centralized entity and nodes' malicious behavior. In traditional models, authors use centralized servers that process and store the data in a centralized manner. Therefore, there is a high chance that unauthorized nodes access the data and tamper or misuse the data. Furthermore, in the centralized system, there is a chance of a single point of failure. In [29, 30], IoTs share the data both intranetwork and internetwork. The data is shared on a large scale; however, data is not secured because users are not authorized. Traditional models use CA, digital signature, etc. However, these all are centralized and not secure.

3. System Model

3.1. Network Deployment. In the proposed system model, we deploy ordinary nodes (ONs) in the network, select the cluster heads (CHs) from ONs, and perform routing. The CHs' selection and routing are performed using the ETD-LEACH protocol. The ETD-LEACH is used for reactive networks. In these networks, sudden changes occur in the environment like change in temperature, humidity, etc., and nodes sense the data immediately. The ONs sense data from the surroundings and forward it to the CHs, which have more energy than ONs. Afterwards, CHs forward energy to the BSs. The ETD-LEACH protocol is divided into two phases that are mentioned as follows.

(1) Cluster formation

(2) Data transmission

3.1.1. Cluster Formation. At the initial stage, nodes are deployed with energy $E_O = 1.5$. When the sensors sense the same type of data, they are grouped in one cluster. After

Table 1: List of acronyms.

Acronyms	Description
BS	Base station
CA	Central authority
CHs	Cluster heads
CV	Current value
DoS	Denial of service
ETD-LEACH	Energy temperature degree-low energy-adaptive clustering hierarchy
ETH-LEACH	Energy threshold-low energy-adaptive clustering hierarchy
HT	Hard threshold
IoTs	Internet of things
MITM	Man-in-the-middle
ONs	Ordinary nodes
PDR	Packet delivery ratio
PoA	Proof of authority
PoW	Proof of work
RMCV	Real-time message content validation
SHA-256	Secure hashing algorithm-256
ST	Soft threshold
WSNs	Wireless sensor networks
Con	Conflict
e	Exponential function
etype	Type of message
G	Group of ONs
info	Information
loc_i	Location of sender
loc_q	Location of receiver
P	Probability of ONs
n	Nodes
CV	Current sensed value

clusters' formation, CHs are created from ONs based on energy, temperature, and degree, in which those ONs are selected as CHs, which have high energy and degree. These CHs sense the temperature value within the given range that gives the current sensing value (CV), as provided in Equation (1).

3.1.2. Data Transmission. In the ETD-LEACH protocol, data is transmitted hierarchically [31]. The ONs sense the data and forward it to the CHs, which further transmit the data to the BS. In this protocol, data is transmitted to the BS when sensed data values meet the given thresholds. The following two types of thresholds are used in the proposed work.

(a) *Hard threshold (HT)*: in the HT, when ONs sense the data and data values are found to be greater than or equal to HT, then ONs transmit the sensed data towards the CHs. The sensed data is calculated in the following equation.

$$\text{CV} = \text{temp}i \sum (\text{temp}f - \text{temp}i) * \text{rand}\,(1, 1), \quad (1)$$

where CV is the current sensed value and temp$i$ and temp$f$ are the minimum and maximum ranges of temperature, respectively. The rand is a random function.

(b) *Soft threshold (ST)*: in the ST, ONs transmit data only in the condition when the difference of CV and the previously sensed value is greater than or equal to the given ST

Therefore, the ETD-LEACH network lifetime is better because less energy is consumed when data is transmitted in the low range. Moreover, only that data is transmitted to BS that meets the thresholds.

3.2. Blockchain Deployment. After the deployment of the WSN, the blockchain is deployed on CHs and BS. Blockchain is the decentralized ledger in which data hashes are stored on CHs and data is transmitted to BS. The private blockchain is utilized, and the PoA consensus mechanism is used for mining new blocks. In the blockchain, the SHA-256 hashing algorithm is used to secure data. In SHA-256 [32, 33], data is converted into ciphertext, and a hash of 256 bits is generated, which is difficult to tamper. The size of the generated hash is the same for one letter, one paragraph, and one word. The block size is 512 bits, and the padding length is 10 bits. Moreover, extra data can be added at the end of the message, as shown in Figure 2.

3.3. Malicious Nodes' Detection. Malicious nodes are present in the network, which act as legitimate nodes and send the data packets during routing. Malicious nodes are detected using the real-time message content validation (RMCV) scheme. In this scheme [34], malicious nodes are detected by validating the message content. Data packets are divided into clusters; same types of data packets are gathered in one cluster while different types of data packets are grouped in different clusters. Then, data packet validation is performed in intraclustering to find false and true data packets. In this manner, malicious nodes are detected. Figure 3 put forwards the overview of malicious nodes' detection process. The format of the data packet is given in the following equation.

$$\text{DataPacket} = \text{Msg}\left(\text{loc}_q, \text{loc}_{\text{int}}, \text{etype}, \text{info}, \text{te}, \text{mpath}\right), \quad (2)$$

where loc_q is the location of the receiver, loc_{int} is the location of the sender, and etype is the message type like temperature conditions, e.g., rainy and sunny. The info is the information that the message contains like temperature is an event and its info is sunny, rainy, and cloudy. te is the time in which a message is received by the receiver. The mpath shows the path from where the data packet

```
1: Deployment of nodes and BS
2: Degree of nodes
3: For i = 1 : nodes do
4:   For j = 1 : nodes do
5:     If i ≠ j then
6:       Find distance of the nodes
7:       If distance < = 20 then
8:         Add index of the nodes
9:       End if
10:    End if
11:  End for
12: End for
13: For i = 1 : nodes do
14:   For j = 1 : nodes do
15:     Check the nodes, neighbors
16:     If neighbor == 0 then
17:       A(i, j) = 0
18:     Else
19:       A(i, j) = 1
20:     End if
21:   End for
22: End for
23: For r = 1 : rounds do
24:   For i = 1 : n do
25:     If energy < = 0 then
26:       Then all nodes will die
27:     End if
28:     If dead == 1 then
29:       First node dies
30:     End if
31:     If dead==0.5∗nodes then
32:       Half nodes die
33:     End if
34:     If dead == nodes then
35:       Full nodes die
36:     End if
37:   End for
38:   For i = 1 : nodes do
39:     On the basis of degree, CHs are selected
40:     If current sensed value = temperature initial +
    (temperature initial + temperature final) ∗ rand (1, 1) then
41:       If sensed value > = hard threshold then
42:         Test = current value − sensed value
43:         If test > = soft threshold then
44:           Perform CHs' selection
45:           Send data packets
46:         End if
47:       End if
48:     End if
49:   End for
50: End for
```

Algorithm 1: ETD-LEACH protocol.

is transmitted. After sending data packets to the destination, trustworthiness of data packets is calculated using Equation (3).

$$\text{Trust}(c) = \frac{\left(e^{\xi} - e^{\xi}.\text{Con}_c\right)\text{Support}'(c)}{e^{\xi} - 1}. \tag{3}$$

In Equation (3), e is the exponential function with ξ, which is a positive number. The e^{ξ} increases with the increase in Con_c conflicts in data packets' content. Conflict is either true or false. The $\text{Support}'(c)$ is the function that shows the path from where the data packet is sent. When the same paths are used for data packet transmission, then there is a high chance of a false data packet being

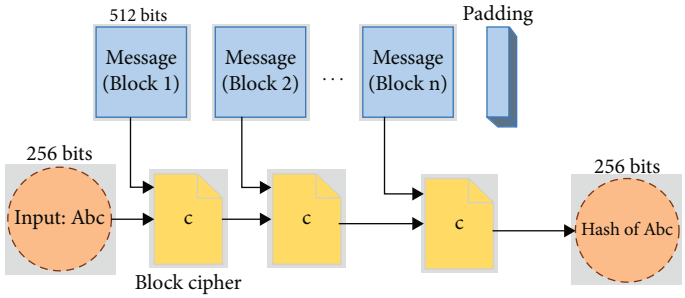

Figure 2: SHA-256.

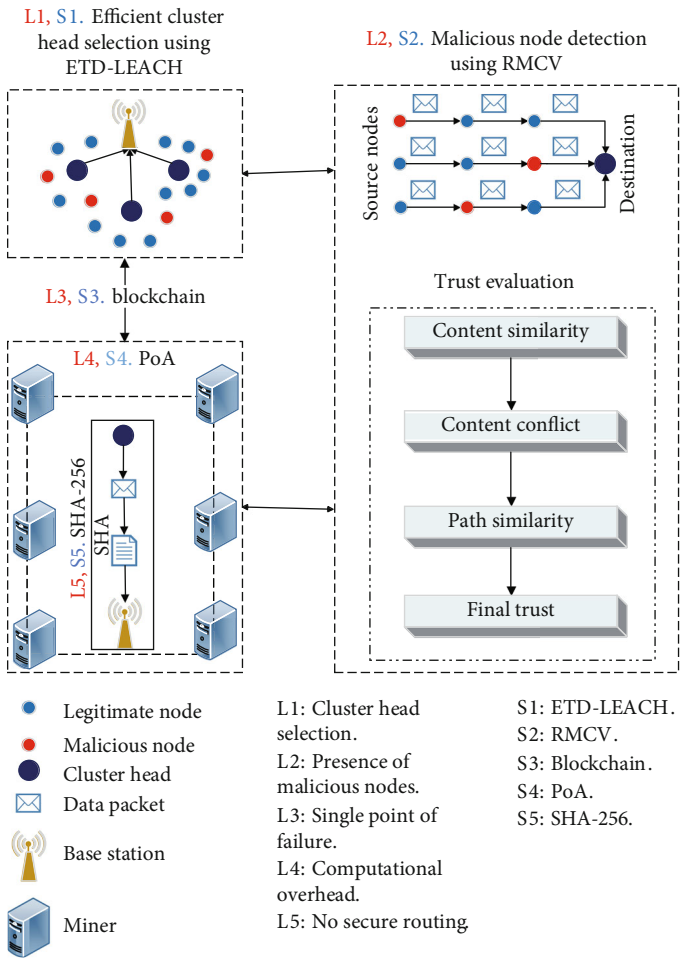

Figure 3: RMCV-based malicious nodes' detection in ETD-LEACH with blockchain in WSN.

transmitted. Therefore, Support$'(c)$ finds independent paths. The message tampering rate is low when the data packet is sent over independent paths. After calculation of trust of each message, we come to know that these nodes send less trustworthy data packets and are considered as malicious. For performing secure routing and successfully sending all the packets to the destination, malicious nodes are detected and revoked from the network [35].

The identified limitations are mapped with their proposed solutions and validations in Table 2. The first limitation (L1) is inefficient CHs' selection because CHs consume high energy and have minimum network lifetime. The limitation is solved through ETD-LEACH in which CHs are selected on the bases of energy, degree, and temperature. The selected CHs have less energy and high network lifetime. The second limitation (L2) is the presence of malicious nodes that is solved through the RMCV technique. Through this technique, 35% of malicious nodes are detected. Furthermore, in limitation three (L3), a single point of failure issue arises that is solved through decentralized blockchain. Limitation four (L4) is consuming high computational power while mining using the PoW

```
1: Deployment of nodes and BS
2: Degree of nodes
3: For i = 1 : nodes do
4:   For j = 1 : nodes do
5:     If i ≠ j then
6:       Find distance of the nodes
7:       If distance < = 20 then
8:         Add index of the nodes
9:       End if
10:    End if
11:  End for
12: End for
13: For i = 1 : nodes do
14:   For j = 1 : nodes do
15:     Check the nodes' neighbors
16:     If neighbor == 0 then
17:       A(i, j) = 0
18:     Else
19:       A(i, j) = 1
20:     End if
21:   End for
22: End for
23: For r = 1 : rounds do
24:   For i = 1 : n do
25:     If energy < = 0 then
26:       All nodes will die
27:     End if
28:     If dead == 1 then
29:       First node dies
30:     End if
31:     If dead == 0.5 ∗ nodes then
32:       Half nodes die
33:     End if
34:     If dead == nodes then
35:       Full nodes die
36:     End if
37:   End for
38:   For i = 1 : nodes do
39:     On the basis of nodes' degree, CHs are selected
40:     If current sensed value = temperature initial +
    (temperature initial + temperature final) ∗ rand (1, 1) then
41:       If sensed value > = hard threshold then
42:         Test = current value − sensed value
43:         If test > = soft threshold then
44:           Perform CHs' selection
45:           Send data packets
46:         End if
47:       End if
48:     End if
49:   End for
50:   Calculate content similarity of data packets using Equation (2)
51:   Calculate content conflict using Equation (3)
52:   Calculate path similarity using Equation (3)
53:   Calculate final trust using Equation (3)
54: End for
```

Algorithm 2: RMCV-ETD-LEACH protocol.

consensus mechanism. This issue is solved through the PoA consensus mechanism that consumes less computational power. Limitation five (L5) is that the XOR hashing function is not secure for hashing of routing data. In the proposed model, SHA-256 is used for securely hashing the routing data while storing it in the blockchain.

Table 2: Identified limitations' mapping with proposed solutions and validations.

Identified limitations	Proposed solutions	Performed validations
L1: inefficient CHs' selection	S1: ETD-LEACH	V1: dead nodes, delay, energy consumption, and throughput, as shown in Figures 4, 5, 6, and 7, respectively
L2: presence of malicious nodes	S2: RMCV	V2: PDR, number of alive nodes, and energy consumption, as shown in Figures 8, 9, and 10, respectively
L3: single point of failure	S3: blockchain	V3, V4: transaction cost shown in Figure 11
L4: PoW utilizes high computational power	S4: PoA	
L5: no secure routing using XOR	S5: SHA-256	V5: execution time shown in Figure 12

4. Simulation Results and Discussions

4.1. Simulation Parameters. In this section, we evaluated the performance of the proposed system model by implementing and comparing the routing protocols and schemes. The WSN consists of 100 nodes that are randomly deployed in an area of 100 m × 100 m, and each node has 1.5 J energy. The data packets are delivered to the destination through the source node. Here, it is to be noted that the data packet size is 4000 bits. The simulation parameters are provided in Table 3.

The routing protocols use 10,000 rounds. The ETD-LEACH is used for routing, and RMCV is used for the malicious nodes' detection during routing. The blockchain is deployed on BS and CHs. The SHA-256 is used in the blockchain for data hashing.

4.2. Comparison of ETD-LEACH and ETH-LEACH. The ETD-LEACH protocol is used for clustering and routing. The ETD-LEACH performance is better than that of ETH-LEACH because ETD-LEACH has high energy as compared to ETH-LEACH. In ETH-LEACH, CHs are selected on the basis of energy threshold, which is equal to 0.85 J, whereas, in ETD-LEACH, CHs are selected on the bases of high degree, energy, and temperature-sensing value. Moreover, in ETH-LEACH, the energy threshold is fixed. In ETD-LEACH, the node that has high energy is selected as a CH. This is the reason that in ETH-LEACH, nodes' energy dissipates early as compared to ETD-LEACH.

In Figure 4 and Table 4, it is seen that in ETD-LEACH, the first node dies at the 4000th round while all nodes die at the 9500th round, whereas, in ETH-LEACH, the first node dies at the 3000th round while all nodes die at the 7500th round. Therefore, network lifetime of ETD-LEACH is better than that of ETH-LEACH.

In Figure 5, it is seen that ETH-LEACH has less delay as compared to ETD-LEACH. The ETD-LEACH has high delay because of HT and ST. In ETD-LEACH, data is transmitted after meeting the thresholds due to which the delay occurs while sending data to the BS. In ETH-LEACH, data is frequently sent to the BS without meeting any thresholds; therefore, delay does not occur.

In the routing protocols, high energy is consumed when data is sensed and transmitted from nodes to CHs and CHs to BS. As shown in Figure 6 and Table 5, the ETD-LEACH consumes less energy as compared to ETH-LEACH because ETD-LEACH uses thresholds while transmitting the data.

Table 3: Simulation parameters.

Parameters	Value of parameters
Network interface	Wireless
Sensing area	100 × 100 m^2
Deployment	Random
Total nodes	100
Initial energy of nodes	1.5 J
Data packet size	4000 bps
Protocol	ETD-LEACH
Rounds	10,000
Malicious node detection	RMCV
Consensus	PoA
Hashing algorithm	SHA-256

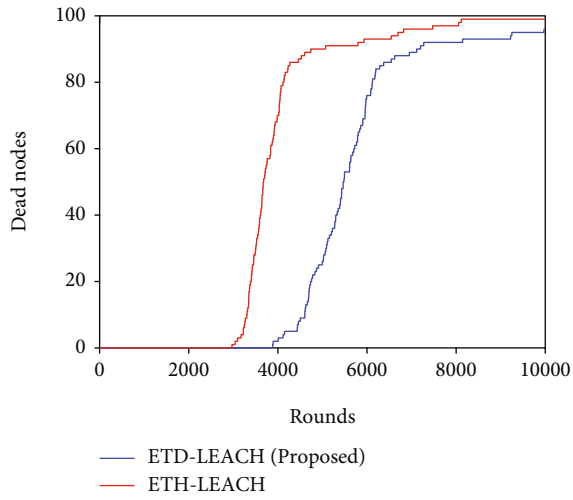

Figure 4: Comparison of dead nodes between ETD-LEACH and ETH-LEACH.

Table 4: Performance analysis of ETD-LEACH and ETH-LEACH.

Protocols	First node dies	Last node dies
ETD-LEACH	4000th round	9500th round
ETH-LEACH	3000th round	7500th round

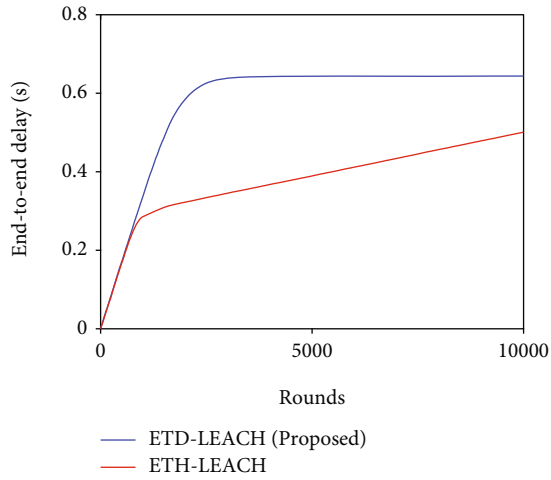

Figure 5: Comparison of delay between ETD-LEACH and ETH-LEACH.

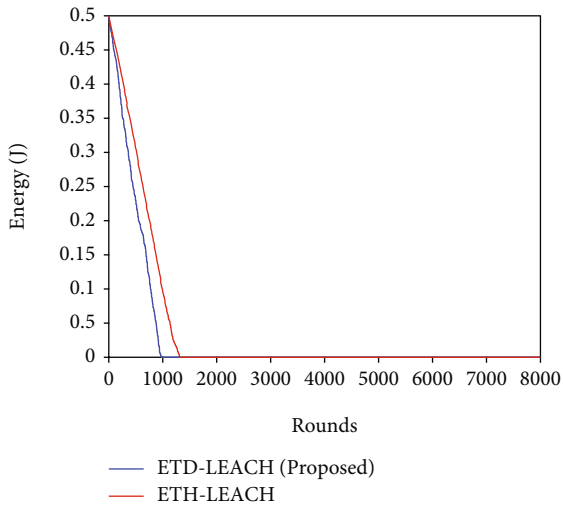

Figure 6: Comparison of energy between ETD-LEACH and ETH-LEACH.

Table 5: Performance analysis of energy consumption in ETD-LEACH and ETH-LEACH.

Protocols	Energy consumption
ETD-LEACH	0.1 J
ETH-LEACH	1.3 J

When sensed data meets the HT, then data is transmitted towards the CHs. In the next iteration, when new data is sensed, which is different from the saved sensed data and equal to or greater than ST, then it is transmitted, whereas, in ETH-LEACH, data packets are transmitted repeatedly. Therefore, nodes' energy dissipates early, and they die rapidly.

In Figure 7, it is shown that the data packets are sent from CHs to BS. In ETD-LEACH, fewer data packets are

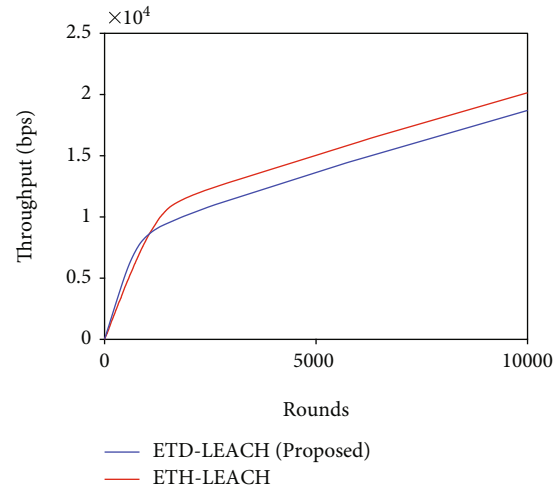

Figure 7: Comparison of throughput between ETD-LEACH and ETH-LEACH.

sent to the BS as compared to ETH-LEACH. The data packet sending rate is less in ETD-LEACH because only that data is sent to the BS, which meets the thresholds. In ETH-LEACH, there is no threshold to send the sensed data towards the BS; therefore, the throughput rate is high.

4.3. Malicious Nodes' Detection Using RMCV. Routing is performed by the ETD-LEACH protocol. We performed routing in which 89.9% of data packets are received at the destination while the remaining 10.1% of data packets are dropped that shows the presence of malicious nodes. These nodes are detected by the RMCV scheme. In this scheme, malicious nodes are detected by data packets' content. Moreover, the scheme checks the trust of each data packet and marks the packet as either honest or fake. Afterwards, nodes that send the fake data packets are detected. Based on the nature of data packets, 35% of malicious nodes are detected. After detection, routing is performed again. 99.9% of data packets are received while 0.1% of data packets are dropped, as shown in Figure 8 and Table 6.

The RMCV-ETD-LEACH performs better than ETD-LEACH because nodes remain alive for a long period in the absence of malicious nodes. As given in Figure 9 and Table 7, in RMCV-ETD-LEACH, the last node is alive till the 4800th round while in ETD-LEACH, the last node is alive till the 3900th round. In ETD-LEACH, nodes die early as compared to RMCV-ETD-LEACH because in ETD-LEACH, nodes act maliciously by sending wrong data packets. As a result, correct data packets are to be resent. Moreover, high energy is consumed while sending accurate data packets again.

In Figure 10 and Table 8, ETD-LEACH consumes high energy as compared to RMCV-ETD-LEACH because of corrupted data packets' delivery in ETD-LEACH. 31% of malicious nodes are present in the ETD-LEACH. These nodes are revoked from the network using RMCV-ETD-LEACH. It means that the number of nodes in RMCV-ETD-LEACH is less as compared to ETD-LEACH and that is why less energy is consumed.

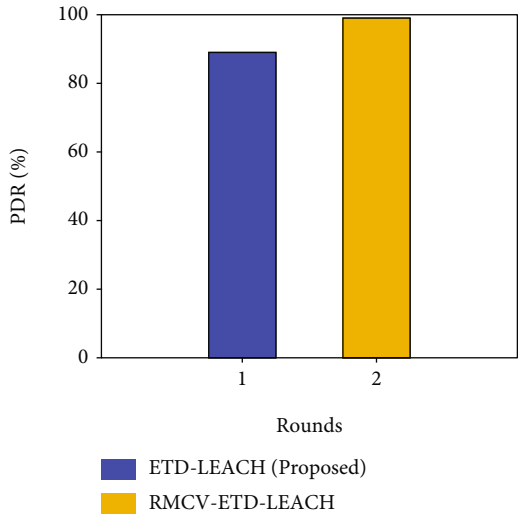

Figure 8: Comparison of PDR in ETD-LEACH and RMCV-ETD-LEACH.

Table 6: Performance analysis of PDR in ETD-LEACH and RMCV-ETD-LEACH.

Protocols	PDR
ETD-LEACH	89.9%
RMCV-ETD-LEACH	99.9%

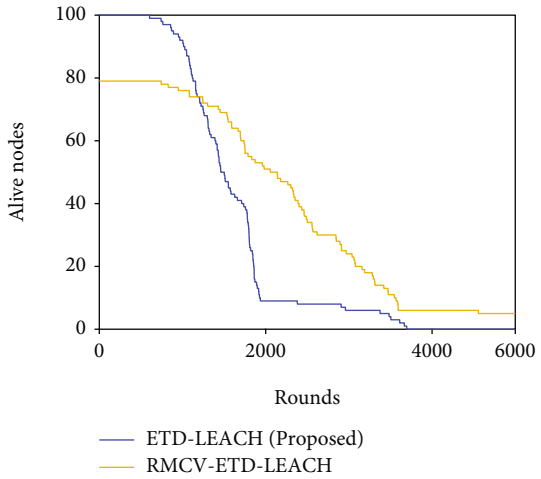

Figure 9: Comparison of number of alive nodes in ETD-LEACH and RMCV-ETD-LEACH.

Table 7: Performance analysis of alive nodes in ETD-LEACH and RMCV-ETD-LEACH.

Protocols	First node alive	Last node alive
ETD-LEACH	1000th round	3900th round
RMCV-ETD-LEACH	1100th round	4800th round

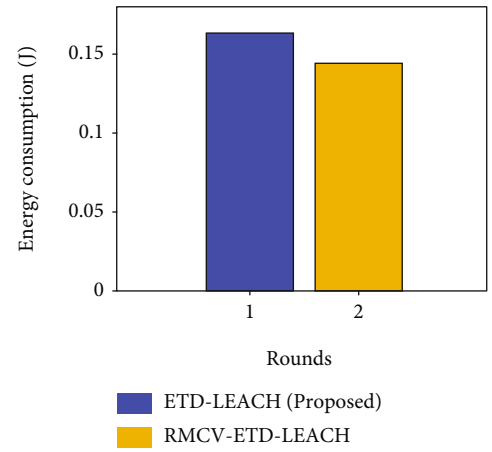

Figure 10: Comparison of energy consumption between ETD-LEACH and RMCV-ETD-LEACH.

Table 8: Performance analysis of energy consumption in ETD-LEACH and RMCV-ETD-LEACH.

Protocols	Energy consumption
ETD-LEACH	0.16 J
RMCV-ETD-LEACH	0.14 J

4.4. SHA-256 in Blockchain. The blockchain is implemented on CHs and BS. In the blockchain, the PoA consensus mechanism is used because its transaction cost is less than that of PoW. In the PoW, miners first solve a complex mathematical puzzle and then add a new block to the blockchain, which incurs a high transaction cost. In the PoA, preselected miners have the authority to add new blocks without solving a complex mathematical puzzle. Therefore, PoA outperforms PoW in terms of transaction cost, as shown in Figure 11.

The routing data is stored on BS and is encrypted by SHA-256. The data hashes are stored in the blockchain. The SHA-256 is used because it is more secure than SHA-1 and has less execution time than SHA-512. In the SHA-1, 164 bits are used for hashing the data. Therefore, it is less secure because 164 bits can be tampered easily and quickly. In the SHA-512, 512 bits are used for hashing, which makes it more secure than SHA-1 and SHA-256. However, execution time is maximum in it because of 512-bit hashing. Therefore, SHA-256 is used for hashing because it is more secure than SHA-1, and its execution time is less than that of SHA-512, as shown in Figure 12.

4.5. Formal Security Analysis. The security analysis is performed on the proposed ETD-LEACH protocol. The attacks discussed below are induced in our proposed model. Attacks are evaluated using different performance metrics: PDR, dead nodes, energy consumption, and delay.

The DoS and MITM attacks are induced in ETD-LEACH. In the DoS, malicious nodes send extensive unnecessary data packets towards the destination and create heavy

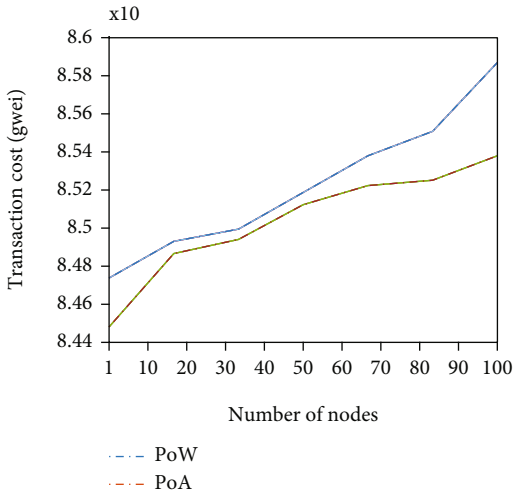

Figure 11: Comparison of transaction cost between PoA and PoW.

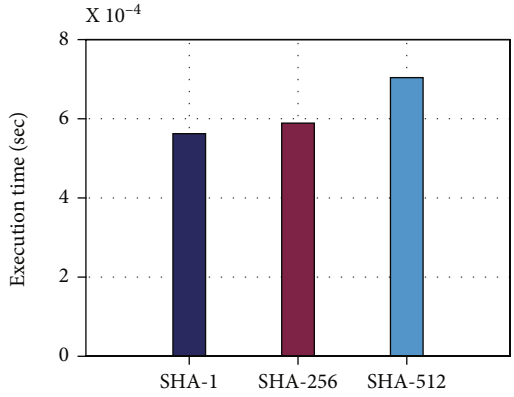

Figure 12: Comparison of execution time of SHA-1, SHA-256, and SHA-512.

traffic. Therefore, due to heavy traffic during routing, large bandwidth is occupied that minimizes the network performance. The fake data packets are received at the destination that are not required. Therefore, under DoS, 82% of legitimate data packets are received at destination, and the remaining 18% of data packets are considered malicious. In the MITM attack, malicious nodes become part of the network that eavesdrop and tamper the data packets. In this attack, tampered data packets are sent towards destinations. In the MITM attack, PDR is 79% because in this attack, tampered data packets are received at the destination. This attack has lower PDR as compared to DoS because this attack steals the victim node's IP address and also gateway IP address. Therefore, malicious nodes in the MITM attack easily get routing information and tamper the data packets without any limit. It is because malicious nodes get access to the data packets without the knowledge of the legitimate source and destination nodes. Furthermore, both attacks are prevented by the RMCV scheme that detects the malicious nodes present in the network. The scheme evaluates the trust of each data packet once the data packets are successfully received at the destination. Afterwards, malicious and legitimate data packets are detected and checked. Based on malicious and legitimate data packets, 35% of malicious nodes are detected. The RMCV scheme detects the malicious nodes because clusters are formed and the trust is calculated on the basis of trust of the malicious node. In the same way, malicious nodes are detected. The data required at destination is sent by maximum nodes; however, a minimum number of nodes send tampered data and they have low trust. Therefore, malicious nodes are detected through RMCV. After the malicious nodes' detection, PDR is increased to 99%, which shows that all legitimate data packets are received by the destination, as shown in Figure 13 and Table 9.

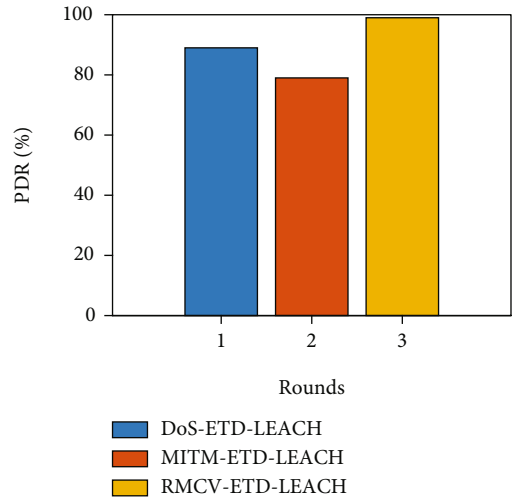

Figure 13: Comparison of PDR in DoS-ETD-LEACH, MITM-ETD-LEACH, and RMCV-ETD-LEACH.

Table 9: Performance analysis of ETD-LEACH under DoS and MITM attacks and RMCV scheme.

Protocols	PDR
DoS-ETD-LEACH	89.9%
MITM-ETD-LEACH	79.9%
RMCV-ETD-LEACH	99.9%

Figure 14 and Table 10 show that RMCV-ETD-LEACH has high network lifetime because all nodes are dead after 3900 rounds, and all such nodes that behave maliciously are removed from the network. Therefore, only legitimate nodes perform routing, and the network consumes low energy, whereas, in the presence of DoS and MITM attacks, all nodes are dead at the 2300th and 1400th rounds, respectively. In the DoS attack, malicious nodes send a large number of data packets towards the destination node that consume a large amount of resources. As a result, the energy is drained, and the nodes die early. Moreover, in the MITM attack, all nodes die early as compared to the DoS attack. In this attack, malicious nodes act as legitimate nodes, and legal nodes perform routing using malicious nodes as intermediary nodes. Upon receiving the data packets, the malicious

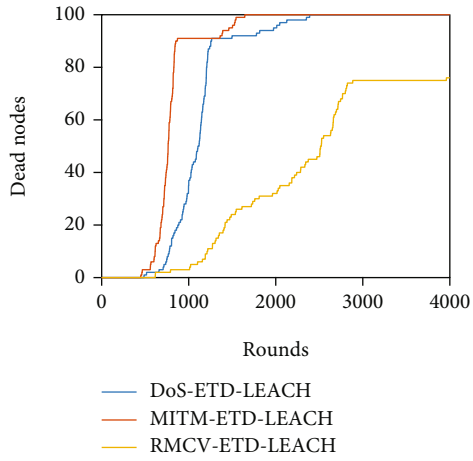

Figure 14: Comparison of dead nodes in DoS-ETD-LEACH, MITM-ETD-LEACH, and RMCV-ETD-LEACH.

Table 10: Performance analysis of ETD-LEACH under DoS and MITM attacks and RMCV scheme.

Protocols	First node dead	Last node dead
DoS-ETD-LEACH	500th round	2300th round
MITM-ETD-LEACH	400th round	1400th round
RMCV-ETD-LEACH	700th round	3900th round

nodes behave maliciously and corrupt the data packets before forwarding them to the destination. All the received data packets are tampered; therefore, destination nodes again send the request for the legitimate data packets. Consequently, nodes' energy depletes, and they die at the 1400th round.

The ETD-LEACH performance depends on the energy consumed by the nodes. As shown in Figure 15, the MITM attack consumes high energy as compared to the DoS attack and the proposed scheme RMCV-ETD-LEACH. The legitimate nodes perform routing for the sake of sending legitimate data packets. Furthermore, in the DoS attack, malicious nodes target a legitimate node and send heavy traffic that makes the legitimate node busy, and it does not receive legitimate data packets. After receiving a large number of malicious data packets, its energy is depleted. Moreover, in RMCV-ETD-LEACH, malicious nodes are not part of the network, and only the legitimate nodes are part of the network. They do not perform any malicious activity and consume less energy. Consequently, the RMCV-ETD-LEACH network performance is better than that of both DoS-ETD-LEACH and MITM-ETD-LEACH.

DoS-ETD-LEACH has high delay as compared to both MITM-ETD-LEACH and RMCV-ETD-LEACH, as shown in Figure 16. In the DoS attack, the destination node receives a large number of data packets resulting in high congestion. The legitimate data packets have to wait for routing that increases the delay. The MITM attack has less delay because the delay occurs only when the data packets are being tampered by the malicious nodes. These corrupted data packets are then sent to the destination node. Furthermore, in RMCV-ETD-LEACH, delay is the least, and it occurs only when checking the presence of malicious nodes in the routing path.

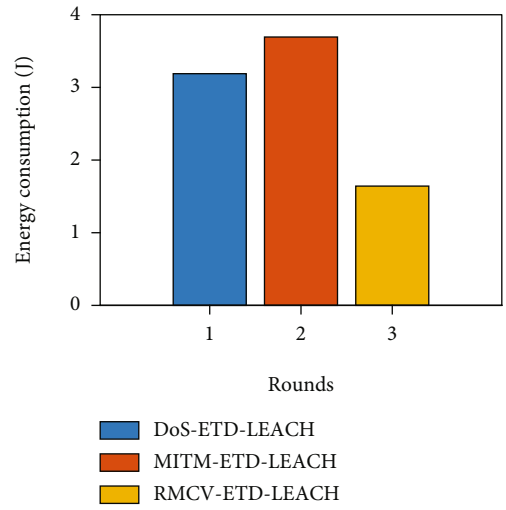

Figure 15: Comparison of energy consumption in DoS-ETD-LEACH, MITM-ETD-LEACH, and RMCV-ETD-LEACH.

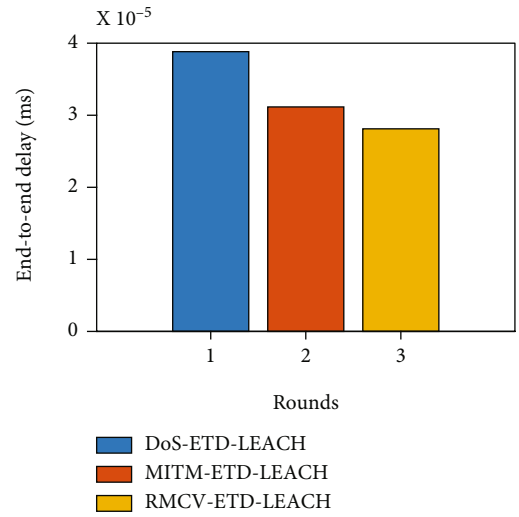

Figure 16: Comparison of end-to-end delay in DoS-ETD-LEACH, MITM-ETD-LEACH, and RMCV-ETD-LEACH.

(1) *Impersonation attack*: the registration of nodes at the blockchain secures the network against this attack. Moreover, it is ensured that malicious node cannot make a duplicate ID of a legitimate node

(2) *Spoofing attack*: the malicious node acts as a legitimate node using its ID. This attack is not possible because it is difficult to steal a legitimate ID from the blockchain

```
root@68c239632c96:/oyente/oyente# python oyente.py -s reg-storage.sol
WARNING:root:You are using evm version 1.8.2. The supported version is 1.7.3
WARNING:root:You are using solc version 0.4.21. The latest supported version
0.4.19
INFO:root:contract reg-storage.sol:reg-storage:
INFO:symExec:          ========== Results ==========
INFO:symExec:             EVM Code Coverage:                       99.5%
INFO:symExec:             Integer Underflow:                       False
INFO:symExec:             Integer Overflow:                        False
INFO:symExec:             Parity Multisig Bug 2:                   False
INFO:symExec:             Callstack Depth Attack Vulnerability:    False
INFO:symExec:             Transaction Ordering Dependence (TOD):   False
INFO:symExec:             Timestamp Dependency:                    False
INFO:symExec:             Re-Entrancy Vulnerability:               False
INFO:symExec:          ===== Analysis Completed =====
root@68c239632c96:/oyente/oyente# python
```

Figure 17: Security analysis using Oyente tool.

5. Smart Contract Analysis

The blockchain is used around the globe for data security. However, malicious entities perform attacks on the smart contract to make it vulnerable and to tamper the data. Therefore, the security analysis of the proposed smart contract through which CHs are registered and authorized, and routing data is stored, is performed. Furthermore, the registration of those CHs is canceled from the smart contracts that are detected as malicious by the RMCV scheme. The security analysis is performed through the Oyente tool that detects the attacks, which is possible on the smart contract, as shown in Figure 17. The attacks are discussed as follows [35].

5.1. Integer Underflow and Overflow. In the smart contract, the maximum size of the integer is 256 bits. The error arises when an attacker changes the integer value by subceeding and exceeding the lower and upper boundaries of the smart contract.

5.2. Parity Multisig Bug 2. Multiple fake accounts are created, and transactions are performed by an attacker in this attack. The smart contract stops working when multiple fake accounts are detected. From Figure 17, it is inferred that the proposed smart contract is not affected by this attack.

5.3. Callstack Depth Attack Vulnerability. The call function depth limit is taken to be 1023 frames. If the limit exceeds 1024 frames, the execution of new instructions fails. The attacker intentionally makes the frames to exceed, so the execution of new information fails. In the proposed smart contract, this attack is not possible because only authorized nodes call the functions.

5.4. Transaction Ordering Dependence. The functions involved in the smart contract consumes gas during execution. Malicious nodes manipulate the gas price to execute transactions maliciously. In this smart contract, this attack is not possible because there is no transaction-ordering function.

5.5. Timestamp Dependency. In this attack, the attacker changes the timestamp. When the mining time of the transaction is changed from a block, then the mining time of all transactions is changed. In our smart contract, this attack is not possible because there is no timestamp dependency function.

5.6. Reentrancy Vulnerability. The attacker calls the same function again and again that interrupts its execution. In the proposed smart contract, this attack is not possible because only authorized nodes are allowed to call the functions.

6. Conclusion

In this paper, we focus on efficient clustering using ETD-LEACH that consumes less energy and has better network lifetime. Moreover, blockchain is deployed on the WSNs for achieving security and SHA-256 is used for secure hashing. Furthermore, RMCV is used to find the trustworthiness of data packets. Based on the trustworthiness, malicious nodes are detected during routing. The efficiency of the proposed model is evaluated through simulations. The ETD-LEACH network lifetime is found to be better than that of ETH-LEACH. Moreover, in ETD-LEACH, energy consumption is less than ETH-LEACH. Moreover, the PoA transaction cost is less than that of PoW, and the SHA-256 execution time is less than that of SHA-512. The PDR is calculated to be 89.9% and 99.9% with and without the malicious nodes, respectively. Furthermore, the proposed model's resilience is tested by inducing DoS and MITM attacks and performing security analysis. Smart contract analysis is also performed using the Oyente tool, which shows the robustness of the proposed smart contract.

Data Availability

No dataset is used in this article.

Conflicts of Interest

The authors declare that they have no conflicts of interest.

References

[1] Z. Cui, X. U. E. Fei, S. Zhang et al., "A hybrid blockchain-based identity authentication scheme for multi-WSN," *IEEE Transactions on Services Computing*, vol. 13, no. 2, pp. 241–251, 2020.

[2] K. Latif, N. Javaid, I. Ullah, Z. Kaleem, Z. A. Malik, and L. D. Nguyen, "DIEER: delay-intolerant energy-efficient routing with sink mobility in underwater wireless sensor networks," *Sensors*, vol. 20, no. 12, p. 3467, 2020.

[3] J. Yick, B. Mukherjee, and D. Ghosal, "Wireless sensor network survey," *Computer Networks*, vol. 52, no. 12, pp. 2292–2330, 2008.

[4] Z. A. Khan, G. Latif, A. Sher et al., "Efficient routing for corona based underwater wireless sensor networks," *Computing*, vol. 101, no. 7, pp. 831–856, 2019.

[5] K. Haseeb, N. Islam, A. Almogren, and I. U. Din, "Intrusion prevention framework for secure routing in WSN-based mobile Internet of Things," *IEEE Access*, vol. 7, pp. 185496–185505, 2019.

[6] Z. Noshad, N. Javaid, T. Saba et al., "Fault detection in wireless sensor networks through the random forest classifier," *Sensors*, vol. 19, no. 7, p. 1568, 2019.

[7] M. P. Barua and M. S. Indora, "Overview of security threats in WSN," *International Journal of Computer Science and Mobile Computing*, vol. 2, pp. 422–426, 2013.

[8] N. Javaid, U. Shakeel, A. Ahmad et al., "DRADS: depth and reliability aware delay sensitive cooperative routing for underwater wireless sensor networks," *Wireless Networks*, vol. 25, no. 2, pp. 777–789, 2019.

[9] P. K. Chithaluru, M. S. Khan, M. Kumar, and T. Stephan, "ETH-LEACH: an energy enhanced threshold routing protocol for WSNs," *International Journal of Communication Systems*, vol. 34, no. 12, article e4881, 2021.

[10] A. Javaid, N. Javaid, Z. Wadud et al., "Machine learning algorithms and fault detection for improved belief function based decision fusion in wireless sensor networks," *Sensors*, vol. 19, no. 6, p. 1334, 2019.

[11] B. Jia, T. Zhou, W. Li, Z. Liu, and J. Zhang, "A blockchain-based location privacy protection incentive mechanism in crowd sensing networks," *Sensors*, vol. 18, no. 11, p. 3894, 2018.

[12] P. K. Sharma and J. H. Park, "Blockchain based hybrid network architecture for the smart city," *Future Generation Computer Systems*, vol. 86, pp. 650–655, 2018.

[13] S. Tabatabaei, "A novel fault tolerance energy-aware clustering method via social spider optimization (SSO) and fuzzy logic and mobile sink in wireless sensor networks (WSNs)," *Computer Systems Science and Engineering*, vol. 35, no. 6, pp. 477–494, 2020.

[14] J. Yang, S. He, X. Yang, L. Chen, and J. Ren, "A trusted routing scheme using blockchain and reinforcement learning for wireless sensor networks," *Sensors*, vol. 19, no. 4, p. 970, 2019.

[15] J. Wang, Y. Gao, C. Zhou, S. Sherratt, and L. Wang, "Optimal coverage multi-path scheduling scheme with multiple mobile sinks for WSNs," *Computers, Materials & Continua*, vol. 62, no. 2, pp. 695–711, 2020.

[16] J. Wang, H. Han, H. Li, S. He, P. K. Sharma, and L. Chen, "Multiple strategies differential privacy on sparse tensor factorization for network traffic analysis in 5G," *IEEE Transactions on Industrial Informatics*, vol. 18, no. 3, pp. 1939–1948, 2022.

[17] W. She, Q. Liu, Z. Tian, J. S. Chen, B. Wang, and W. Liu, "Blockchain trust model for malicious node detection in wireless sensor networks," *IEEE Access*, vol. 7, pp. 38947–38956, 2019.

[18] T. H. Kim, R. Goyat, M. K. Rai et al., "A novel trust evaluation process for secure localization using a decentralized blockchain in wireless sensor networks," *IEEE Access*, vol. 7, pp. 184133–184144, 2019.

[19] G. Ramezan and C. Leung, "A blockchain-based contractual routing protocol for the Internet of Things using smart contracts," *Wireless Communications and Mobile Computing*, vol. 2018, 14 pages, 2018.

[20] J. Wang, J. Chunwei, Y. Gao, A. K. Sangaiah, and G.-j. Kim, "A PSO based energy efficient coverage control algorithm for wireless sensor networks," *Computers, Materials & Continua*, vol. 56, no. 3, pp. 433–446, 2018.

[21] J. Wang, Y. Gao, X. Yin, F. Li, and H.-J. Kim, "An enhanced PEGASIS algorithm with mobile sink support for wireless sensor networks," *Wireless Communications and Mobile Computing*, vol. 2018, 9 pages, 2018.

[22] S. Hong, "P2P networking based internet of things (IoT) sensor node authentication by Blockchain," *Peer-to-Peer Networking and Applications*, vol. 13, no. 2, pp. 579–589, 2020.

[23] A. Rovira-Sugranes and A. Razi, "Optimizing the age of information for blockchain technology with applications to IoT sensors," *IEEE Communications Letters*, vol. 24, no. 1, pp. 183–187, 2020.

[24] M. Revanesh and V. Sridhar, "A trusted distributed routing scheme for wireless sensor networks using blockchain and meta-heuristics-based deep learning technique," *Transactions on Emerging Telecommunications Technologies*, vol. 32, no. 9, pp. 42–59, 2021.

[25] L.-E. Wang, Y. Bai, Q. Jiang, V. C. M. Leung, W. Cai, and X. Li, "Beh-Raft-Chain: a behavior-based fast blockchain protocol for complex networks," *IEEE Transactions on Network Science and Engineering*, vol. 8, no. 2, pp. 1154–1166, 2020.

[26] J. Wang, X. Qiu, and T. Yuanfei, "An improved MDS-MAP localization algorithm based on weighted clustering and heuristic merging for anisotropic wireless networks with energy holes," *Computers, Materials & Continua*, vol. 60, no. 1, pp. 227–244, 2019.

[27] N. Shi, L. Tan, C. Yang et al., "BacS: a blockchain-based access control scheme in distributed internet of things," *Peer-to-peer networking and applications*, vol. 14, no. 5, pp. 2585–2599, 2021.

[28] S. Hameed, S. A. Shah, Q. S. Saeed et al., "A scalable key and trust management solution for IoT sensors using SDN and blockchain technology," *IEEE Sensors Journal*, vol. 21, no. 6, pp. 8716–8733, 2021.

[29] R. Goyat, G. Kumar, M. Alazab et al., "A secure localization scheme based on trust assessment for WSNs using blockchain technology," *Future Generation Computer Systems*, vol. 125, pp. 221–231, 2021.

[30] P. Kumar, G. P. Gupta, and R. Tripathi, "TP2SF: a trustworthy privacy-preserving secured framework for sustainable smart cities by leveraging blockchain and machine learning," *Journal of Systems Architecture*, vol. 115, pp. 101954–101954, 2021.

[31] D. Liao, H. Li, W. Wang, X. Wang, M. Zhang, and X. Chen, "Achieving IoT data security based blockchain," *Peer-to-Peer Networking and Applications*, vol. 14, no. 5, pp. 2694–2707, 2021.

[32] A. Mubarakali, "An efficient authentication scheme using blockchain technology for wireless sensor networks," *Wireless Personal Communications*, pp. 1–15, 2021.

[33] T. Samant, P. Mukherjee, A. Mukherjee, and A. Datta, "TEEN–V: a solution for intra-cluster cooperative communication in wireless sensor network," in *2017 International Conference on I-SMAC (IoT in Social, Mobile, Analytics and Cloud)(I-SMAC)*, pp. 209–213, IEEE, 2017.

[34] A. Almasri and K. A. Darabkh, "A comparative analysis for WSNs clustering algorithms," in *2020 Fifth International Conference on Fog and Mobile Edge Computing (FMEC)*, pp. 263–269, IEEE, 2020.

[35] M. B. E. Sajid, S. Ullah, N. Javaid, I. Ullah, A. M. Qamar, and F. Zaman, "Exploiting machine learning to detect malicious nodes in intelligent sensor-based systems using blockchain," *Wireless Communications and Mobile Computing*, vol. 2022, 16 pages, 2022.

Hindawi
Wireless Communications and Mobile Computing
Volume 2022, Article ID 7095528, 13 pages
https://doi.org/10.1155/2022/7095528

Research Article

Diabetic Retinopathy Detection Using Genetic Algorithm-Based CNN Features and Error Correction Output Code SVM Framework Classification Model

Najib Ullah,[1] Muhammad Ismail Mohmand,[1] Kifayat Ullah,[2] Mohammed S. M. Gismalla,[3] Liaqat Ali,[4] Shafqat Ullah Khan,[5] and Niamat Ullah[6]

[1]*Department of Computer Science, The Brains Institute Peshawar, Pakistan*
[2]*Department of Computer and Software Technology, University of Swat, Pakistan*
[3]*Department of Electronic and Electrical Engineering, Faculty of Engineering, International University of Africa, Khartoum, Sudan*
[4]*Department of Electrical Engineering, University of Science and Technology Bannu, Pakistan*
[5]*Department of Electronics, University of Buner, Pakistan*
[6]*Department of Computer Science, University of Buner, Pakistan*

Correspondence should be addressed to Mohammed S. M. Gismalla; mohsalih@iua.edu.sd

Received 9 March 2022; Revised 25 April 2022; Accepted 22 June 2022; Published 25 July 2022

Academic Editor: Abdul Basit

Diabetic retinopathy (DR) is a type of eye disease that may be caused in individuals suffering from diabetes which results in vision loss. DR identification and routine diagnosis is a challenging task and may need several screenings. Early identification of DR has the potential to prevent or delay vision loss. For real-time applications, an automated DR identification approach is required to assist and reduce possible human mistakes. In this research work, we propose a deep neural network and genetic algorithm-based feature selection approach. Five advanced convolutional neural network architectures are used to extract features from the fundus images, i.e., AlexNet, NASNet-Large, VGG-19, Inception V3, and ShuffleNet, followed by genetic algorithm for feature selection and ranking features into high rank (optimal) and lower rank (unsatisfactory). The nonoptimal feature attributes from the training and validation feature vectors are then dropped. Support vector machine- (SVM-) based classification model is used to develop diabetic retinopathy recognition model. The model performance is evaluated using accuracy, precision, recall, and F1 score. The proposed model is tested on three different datasets: the Kaggle dataset, a self-generated custom dataset, and an enhanced custom dataset with 97.9%, 94.76%, and 96.4% accuracy, respectively. In the enhanced custom dataset, data augmentation has been performed due to the smaller size of the dataset and to eliminate the noise in fundus images.

1. Introduction

In telemedicine, automatic classification of ophthalmologic diseases using retinal image analysis has become a routine. Manual segmentation was previously used, but it was difficult, tedious, labor driven, and observer oriented and needed a high skill level. In contrast, computer-assisted detection of ocular disorders is comparatively less expensive, achievable, and purpose oriented and does not require a highly skilled clinician to grade the images. For on time identification and real-time classification of eye illnesses, the advancement of screening system is required and may be very helpful in the treatment process. There are a number of eye diseases and their causes may also be different. Diabetes is an illness that has become more frequent in recent years, and diabetes may cause eye abnormalities that may result in vision loss. Diabetes is a common disease nowadays, and it may harm the eyes and may result in vision loss [1].

Based on data from the International Diabetes Federation, reported in 9th edition stated that in 2019, diabetes affected around 19 million people in Pakistan which is 148 times higher than their previous report. It is putting them

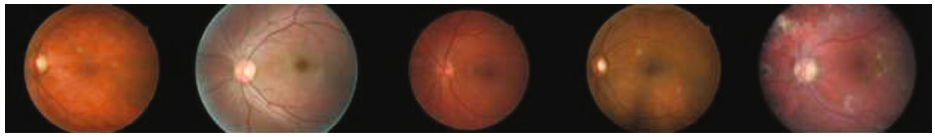

Figure 1: DR classification.

Table 1: Stages of diabetic retinopathy [2].

Status	Normal	Nonproliferative diabetic retinopathy			Proliferative diabetic retinopathy
Type of DR	Not seen	Mild DR	Moderate DR	Severe DR	High-risk DR
Retina condition	Healthy	Several little blood vessel swells	The cholesterol is stored as tiny chunk in the veins with visible regions of blood leakage	Blood leakage area may large. Unpredictable beading in the veins. At the optic circle, new blood vessels are formed. Occlusion of a vein	There is a lot of bleeding and fresh blood is forming in the retina. Complete and total blindness

at high risk of life-affecting complications. 8.5 million of these 19 million are still undiagnosed, and they must be vulnerable. Around the globe, approximately 463 million persons are suffering from diabetes. People living with diabetes are always at high risk for diseases associated with diabetes, such as diabetic retinopathy (DR), diabetic macular edema (DME), and glaucoma. Diabetic retinopathy is the most prevalent of all diseases, and it is caused by the damage of blood vessels in the eye retina. Microaneurysms, vitreous hemorrhage, hard exudates, and retinal detachment are only a few of the signs and symptoms of DR, but there might be others.

In Figure 1, we demonstrated different retina images with various diabetic retinopathy levels. The disease begins with minor alterations in the eyes' blood vessels, which is named mild DR. In this case, the patient may be able to overcome the disease and recover completely. If this disease's condition is not managed, it will develop to moderate DR. In the case of moderate DR, blood vessel leakage may start. In the next case, if the disease progresses, it can develop into severe and proliferative DR, which can result in total visual loss.

By 2030, it is estimated that 13 million people in the United States will have DR [1]. If DR is not detected early enough, it can result in a variety of vision problems, including blindness. As a result, a diabetic patient should see an experienced ophthalmologist for an annual or biannual eye checkup and screening.

In addition to identifying DR, its severity degree must be determined in order to be able to cure it. The two primary types of DR are NPDR (nonproliferative DR) and PDR (proliferative DR) [1]. The nonproliferative DR is divided into three phases, which are stated below: The mildest form of DR is mild NPDR, which is followed by moderate and severe NPDR. PDR refers to the most advanced stage of diabetic retinopathy. No DR, mild DR, moderate DR, severe DR, and proliferating DR are the five stages of DR severity as demonstrated in Table 1. Lesions on fundus photographs that look as little circular shaped red particles at the terminals of the blood vessels are an early indicator of diabetic retinopathy. Microaneurysms, hemorrhages, and/or transudes are signs of moderate DR. In proliferative DR stage, the formation of new blood vessels is occurring, as well as the anomalies mentioned above [3]. Color fundus photographs of a normal retina, as well as varying degrees of DR severity, are shown in Figure 1. A primary challenge with DR recognition is the complication of diagnosing symptoms early on in the course of DR owing to the visual resemblances found among normal fundus photo, moderate DR, and occasionally considerable DR. If diabetic retinopathy developed to an advanced phase, this may cause a loss in vision. To aid medical professionals by identifying DR in real-time, in the literature, several computer-based techniques have been created. Lesions are automatically detected and graded for DR screening, and grading has received a lot of interest from researchers, in these ways to imitate human experts. Blood vessel detection and segmentation in retinal images were created. Since the advent of deep learning algorithms, particularly convolutional neural networks (CNNs), is still a relatively new field of study, several academic communities have already used CNNs for a variety of purposes, including recognizing DR [1]. In the research community, deep learning is widely used for the image classification purpose as it employs neural networks to calculate thousands of mathematical equations with many parameters. Recent DR detection research has generally focused on developing new algorithms for typical fundus images that are predominantly affected by occlusion, refraction, lighting fluctuations, and blur. In this study, we developed a custom dataset and proposed a deep learning approach which works on large dataset and gives better performance.

2. Review of the Previous Work

Various methods to detect DR have been proposed. For multiclass classification, this section focuses on deep learning and neural network algorithms. Fundus images have been divided into two groups by some researchers: diabetic, which encompasses moderate to severe NPDR, and nondiabetic, which signifies the individual does not have DR [4]. Using one primary classifier and backpropagation neural organization processes, the authors suggested a strategy for accurately determining a class where a fundus picture may be classified based on these results. Similarly, a deep learning-based technique for classifying fundus pictures for human ophthalmologist diagnosis has been proposed. Based on Inception V3, the authors developed a Siamese-like CNN binocular model that is able to detect fundus pictures in both the eyes and deliver output from both eyes at the same time [5]. The authors suggested a hybrid strategy for detecting DR [6], in which the deep learning model is aided by histogram (HE) contract limited adaptive histogram (CLACHE). During the diagnosis procedure, the approach uses picture augmentation to bring greater attention and effectiveness. The authors employed five convolutional neural network (CNN) architectures to assess progress indicators for the dataset of diabetic retinopathy patients. Images are divided into three groups depending on the severity of the disease, according to their classification system [7]. The authors presented a novel CNN architecture for diagnosing DR based on ResNet18 in [8]. This method overcomes the issue of significant class imbalance while also generating an area. It is added to the previously mentioned contribution by highlighting semantic areas of the fundus picture to represent the severity degree. The authors developed a strategy for identifying DR based on binary classification, and severity was not a problem. For the datasets under consideration, they used a binary classification system consisting of normal and abnormal photos [2]. The authors of [9] presented a model based on deep learning to categorize a small-scale dataset of diabetic retinopathy images. As an accuracy statistic, they employed Cohen's kappa. In [10], the author designed a CNN-based model and extracted features from a dataset with 30,000 images. While performing preprocessing, they applied denoising techniques and obtained accuracy of 95% and 85% for binary classification and five-class problem of diabetic retinopathy. In [11], a deep learning algorithm has been proposed to grade diabetic retinopathy by modification of GoogLeNet. In the grading process, the authors obtained an accuracy of 81%, while inaccurate prediction achieved 96% accuracy on a custom dataset developed by Jichi Medical University containing 9939 images. In a previous study [12] using 80000 images from the Kaggle dataset, a state-of-the-art DR stage classification technique was constructed. Using complicated DR characteristics such as MAs, HEMs, and exudates on the retina, they employed a CNN architecture with data augmentation to categorize five degrees of DR severity. On a validation set of 5000 samples, a high-end graphical processor unit (GPU) was used, resulting in an accuracy of 75% and a SE of 95%. In the proposed model [13], the authors developed a CNN network for multistage classification on 128000 fundus images with the technical support of professional ophthalmologists. The developed CNN model obtained an accuracy of 97.5% in the classification of DR stages. The authors in [14] developed a one-of-a-kind approach for classifying fundus photos as normal, moderate, severe, and proliferative DR. The images given as input were preprocessed by morphological operations with disc- and diamond-structuring elements. After this process, six features were obtained considering the perimeter and area of pixels. For the classification, an 8 hidden layer single feedforward neural network was used. 6 units were used as input for each feature value mentioned and 4 units as output, one for each DR level. On the Kaggle dataset and a custom dataset developed by the California Health Care Foundation, the authors employed the Inception V3 architecture for automated classification of diabetic retinopathy in [15]. They got an accuracy of 82% for the Kaggle dataset with a batch size of 64 and 88% for the custom dataset with a batch size of 128. The authors used convolutional neural network-based pretrained Inception V3, which was trained on ImageNet, to perform transfer learning [16] while working on fundus pictures to categorize images into five groups. They got 48.2% accuracy on the EyePACS dataset. The authors of [17] suggested a class coding strategy for predicting and target scores using VGG-D architecture to identify diabetic retinopathy. The design was capable to detect diabetic retinopathy with an accuracy of 82%. The EyePACS dataset was utilized by the authors in [18] to demonstrate the effectiveness of Inception V3 in diagnosing diabetic retinopathy. They also tested AlexNet and VGG16 and got 37.43% and 50.03% accuracy, respectively. Working on a CNN-based architecture, [19] employed 35126 images from the EyePACS dataset to diagnose diabetic retinopathy. Noise removal, normalization, and the use of several hyperparameters resulted in a validation accuracy of 83.68% and a specificity of 93.65%. After using transfer learning and hyperparameter tuning, the authors demonstrated the performance of several pretrained CNN models in the classification of diabetic retinopathy, namely, VGGNet, GoogLeNet, AlexNet, and ResNet. All of these models were tested on 35,126 pictures from the EyePACS dataset. VGG outperforms all of these models in this study. In [20], the authors compared the Inception V4 deep learning system's performance to human graders. They have performed an experiment in Thailand in which 25,326 images were used, resulting in the deep learning approach achieving better accuracy than human graders. This experiment demonstrated that deep learning may be used to identify any. This experiment demonstrated that deep learning may be used to identify any disease. Deep learning lowered the rate of false negatives by 23% while significantly increasing the rate of false positives to 2%. In [21], the authors have developed an ensemble-based model of five CNN models, including Inception V3, ResNet-50, Dense 121, Dense 169, and Xception to classify different diabetic retinopathy severity levels. The model shows performance as 69%, 48%, 65%, 84%, and 51%, respectively. The results show that in this particular study, Dense 169 showed better performance as compared to other models. In [22], the authors presented

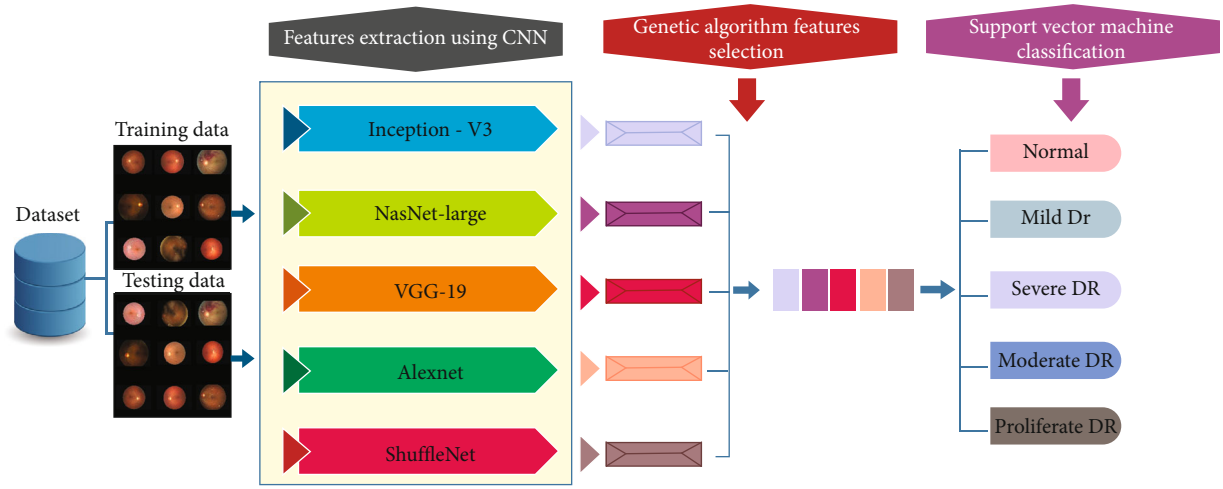

Figure 2: Proposed framework.

an AlexNet-based architecture to characterize the severity degree of diabetic retinopathy using appropriate rectified linear activation Units, Pooling, and SoftMax. The team enhanced accuracy across the board by using the Messidor dataset. Researchers often employ the digital images of retina for vessel extraction (DRIVE) and structured analysis of retina (STARE) to segment the vessel network utilizing local and the global vessel features. Different classifiers are also used like support vector machine and K-neighbor, which provide better accuracy, 86% and 55%, respectively, in [23]. They also used pixel clustering to remove the fundus image mask in [23]. Using a Gaussian mixture model (GMM), visual geometry group network (VGGNet), singular value decomposition (SVD), principal component analysis (PCA), and SoftMax, the authors proposed a symmetrically optimal solution for region segmentation, high dimensional feature extraction, feature selection, and fundus image classification in [24]. According to the authors, the VGG-19 model outperformed AlexNet, and the spatial invariant feature transforms in classification accuracy and processing time (SIFT). For people living with diabetes, their body monitoring is a challenging task. In [25], the authors proposed an IoT-based system in which the system uses wearable sensors that will recommend prescriptions and food for patients. In this article, the combination of type-2 fuzzy logic and the fuzzy ontology enhanced the system accuracy. This may be helpful for patients with diabetes. CNN is widely used these days in many computer vision applications. But there are some problems in this system, one of which is the global optimization of CNN training. Training and fast classification play a significant role in the development of CNN. In [26], to increase the convergence and efficiency of CNN training, the authors use the modified resilient backpropagation (MRPROP) technique. To minimize network overtraining, a tolerance band is created, which is used with the global best idea for weight update criteria to allow the CNN's training algorithm to optimize its weights more quickly and precisely.

In [27], the author proposed a system that is focused on DR stage classification, but to speed up the training and model convergence, they adopted the lowest learnable parameters. The VGG-16, spatial pyramid pooling layer (SPP), and network-in-network (NiN) are layered to create the VGG-NiN model, which is a highly nonlinear, scale-invariant deep model. Because of the SPP layer's virtue, the suggested VGG-NiN model can process a DR picture at any size. In [28], the authors demonstrated a comparison between different pretrained learning methods and ConvNet, and they also focused on their optimization, for the detection of images and classification. To validate their study, the authors also performed some experiments on a skin detection dataset and a public face dataset that may be able to provide some solutions.

3. Methodology

This section is related to mythology adopted in this study and research framework.

3.1. Framework. The proposed framework represented in Figure 2 defines an architecture of a computer-aided diabetic retinopathy diagnosis system. A benchmark dataset of five classes is loaded to the system, partitioning it into two subdatasets, i.e., trainset and validation. For partitioning the dataset, a hold-out cross-validation mechanism is followed that splits the dataset with a percentage of 70/30, where 70% of the images from five classes are selected randomly for model training along with their labels, while the remaining 30% images with their corresponding labels are selected as the validation set which will be used to evaluate the proposed model's performance. Five advanced convolutional neural network architectures are used to extract robust and noninvariant features from the RGB images, i.e., AlexNet, NASNet-Large, VGG-19, Inception V3, and ShuffleNet, that will perform feature extraction from the training set image and validation set images. A CNN model has two parts, i.e., feature extraction and classification; for the purposed system of feature extraction, an image is input to

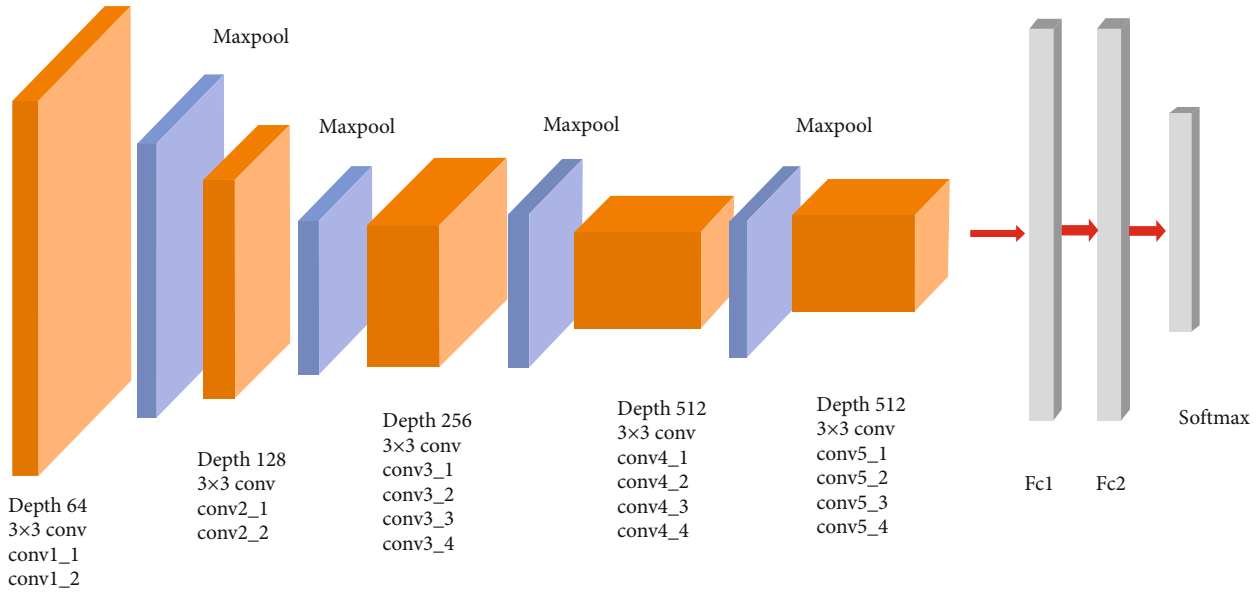

Figure 3: The pretrained architecture of VGG 19.

the CNN model, and from the last fully connected layers, a feature vector of 1000 features is extracted. In the proposed feature extraction block, five CNNs are used which will give an output of 5000 images. Feature selection in machine learning is an unsupervised learning approach used to reduce the dimension of the feature vector. The proposed framework genetic algorithm with tournament selection method is used to rank the features into high rank (optimal) and low ranked (unsatisfactory). The nonoptimal feature attributes from the training and validation feature vectors are dropped. Support vector machine classification model is used to develop diabetic retinopathy recognition model. SVM is a binary classifier capable of classifying two classes of data; the benchmark dataset consists of five classes of data, so an error correction output code framework is applied on the SVM classifier to develop a multiclass classifier that can classify more than two classes of data. The SVM model is trained on the training set feature vector and its labels. Upon completion of the model training, the trained model is tested on the validation set features; the model's predicted labels are compared with the actual labels to create a confusion matrix. Using the information in the confusion matrix, the performance of the model is evaluated using standard classification performance evaluation metrics such as accuracy, precision, recall, and F1 score.

3.2. CNN Architecture. Deep neural networks created on convolutional neural network models are widely used nowadays to deal with challenges in computer vision. In order to distribute the dataset in normal and different categories of diabetic retinopathy patients, CNN-based AlextNet, NASNet-Large, Inception V3, VGG 19, and ShuffleNet models and transfer learning approaches were adopted. The adopted CNN models and the AlexNet, NASNet-Large, Inception V3, VGG 19, and ShuffleNet, along with genetic algorithm for feature selection, are presented systematically in the figure below.

3.2.1. AlexNet. AlexNet is a CNN-based model having approximately 650000 neurons and 60 million parameters. It was introduced by Alex Krizhevsky in 2012. The AlexNet architecture presented in Figure 3 is made up of fully linked layers and one SoftMax tile. Convolutional filters and the ReLU nonlinear transfer function are included in each convolutional layer. A variety of effects may be achieved by blending layers. The input size is changed due to the presence of entirely linked layers. Neural networks include convolutional neural networks, which is a type of neural network. They are made up of neurons that have a weight and bias that can be read. Each neuron receives a number of inputs. It then adds a weight-bearing amount on top of that. Finally, it is transferred by turning, activating, and releasing the device. The figure below demonstrates AlexNet architecture.

3.2.2. Inception V3. Inception, a CNN architecture proposed by Google Inc. in 2014, is used in computer vision and bears a good reputation in this field. The aim of the development of inception deep neural network architecture is to estimate and cover the best local scant formation of a convolutional vision network using complex modules that were already accessible. In December 2015, an improved inception model was proposed by Szegedy that was named Inception V3 presented in Figure 4 which performed better as compared to the benchmark. Inception V3 was used for identification of different objects, human action recognition, classification of video, segmentation, and object tracking. Inception V3 includes smaller convolution factorization, asymmetric convolution factorization, and auxiliary classifiers efficiently reducing the grid size. Inception V3 extends the activate scale of networking filtering before employing maximum or average pooling to avoid a representational bottleneck. Furthermore, deconstruction into smaller convolutions may enhance the network's accessible space of variations,

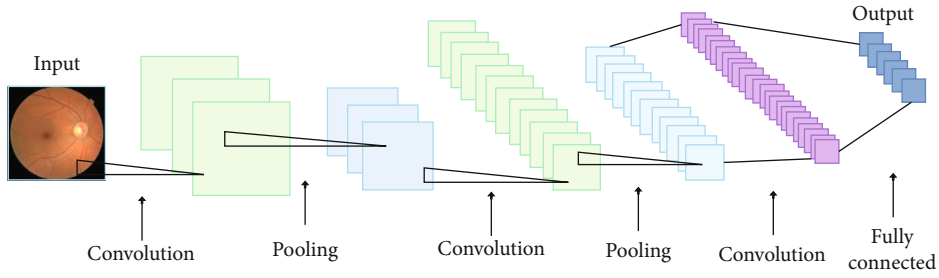

Figure 4: The pretrained architecture of Inception V3.

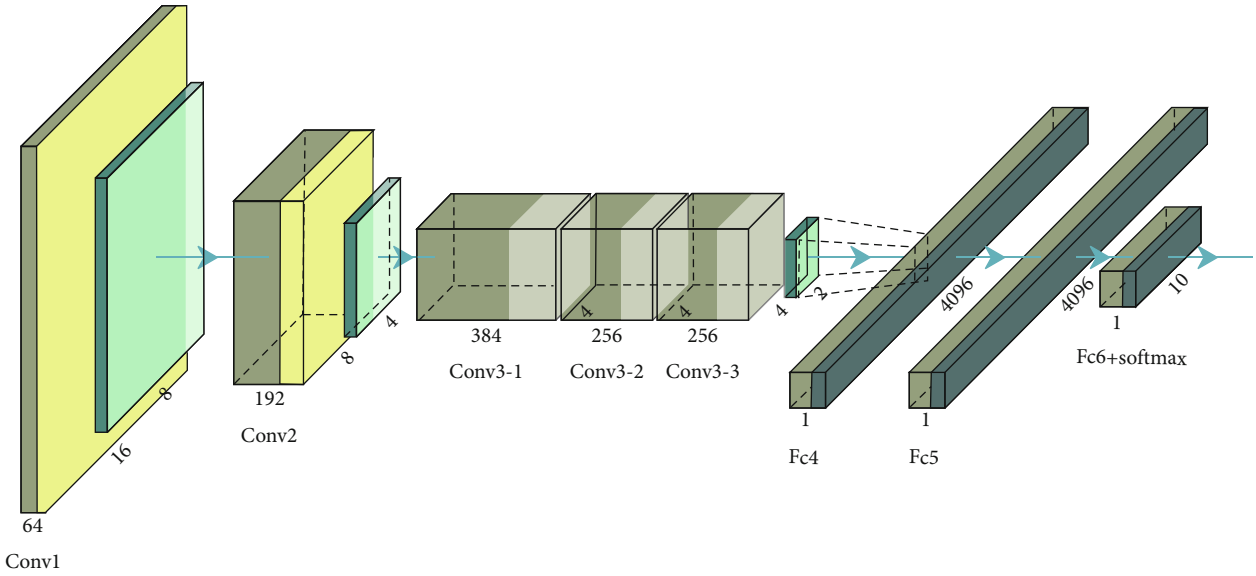

Figure 5: The pretrained architecture of AlexNet.

enabling it to provide insight, while the use of auxiliary classifiers allows the network to be accurate. Inception V3 features a more monolithic design and has a lower computation cost. Using the TensorFlow distributed machine learning framework, the Inception V3 model trained networks with a hypostatical pitch.

3.2.3. VGG 19. VGGNet stands for visual geometry group network and multilayered deep neural network. The VGG is a CNN-based network that is applied to the ImageNet dataset. In Figure 5, we presented that VVG 19 is a very simple network and is very useful due to its simple nature. The 3×3 convolutional layers are placed on the top to extend the depth level. In VGG 19, handle max-pooling stages are employed to minimize volume size. VGG 19 is commonly used in medical imaging studies because of its versatility and simplicity.

3.2.4. NASNet-Large. Although previous ANNs have all provided us with unique and significant insights and have impacted the future of ANN design, their particular architectural design was established by humans, influenced by their experiences and biases. Google launched NASNet-Large presented in Figure 6, which framed finding the ideal CNN architecture as a reinforcement learning problem. NASNet has plenty of computing power. The basic concept was to find the optimal combination of filter sizes, output channels, strides, number of layers, and other characteristics in the specified search space. The accuracy of the searched architecture on the provided dataset was the reward for each search activity in this reinforcement learning environment. NASNet achieves extraordinary better results on ImageNet and also performs well on large datasets.

3.2.5. ShuffleNet. Figure 7 shows the ShuffleNet architecture which is one among computationally efficient CNN architectures that was proposed in 2017 by the member of the research group of Megvii Inc. It was specifically designed for a mobile device with limited computational power, and the ShuffleNet was designed with fewer parameters. ShuffleNet uses two new operations to speed up computations: convolution of points in a group and path shuffling. If we reduce the network size, there will be no loss in the accuracy of the model, but it even performs better.

3.3. Genetic Algorithm-Based Feature Selection. A genetic algorithm is an optimization method used up to the mark in deep learning research. The GA model is an evolutionary search strategy that emulates nature's selection, mutation, and crossover mechanisms. Choosing the most trustworthy

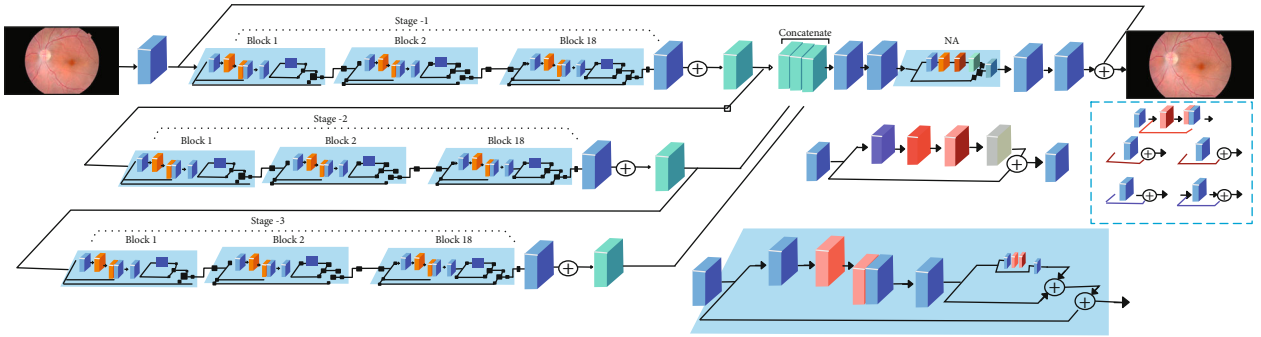

Figure 6: Pretrained architecture of NASNet-Large.

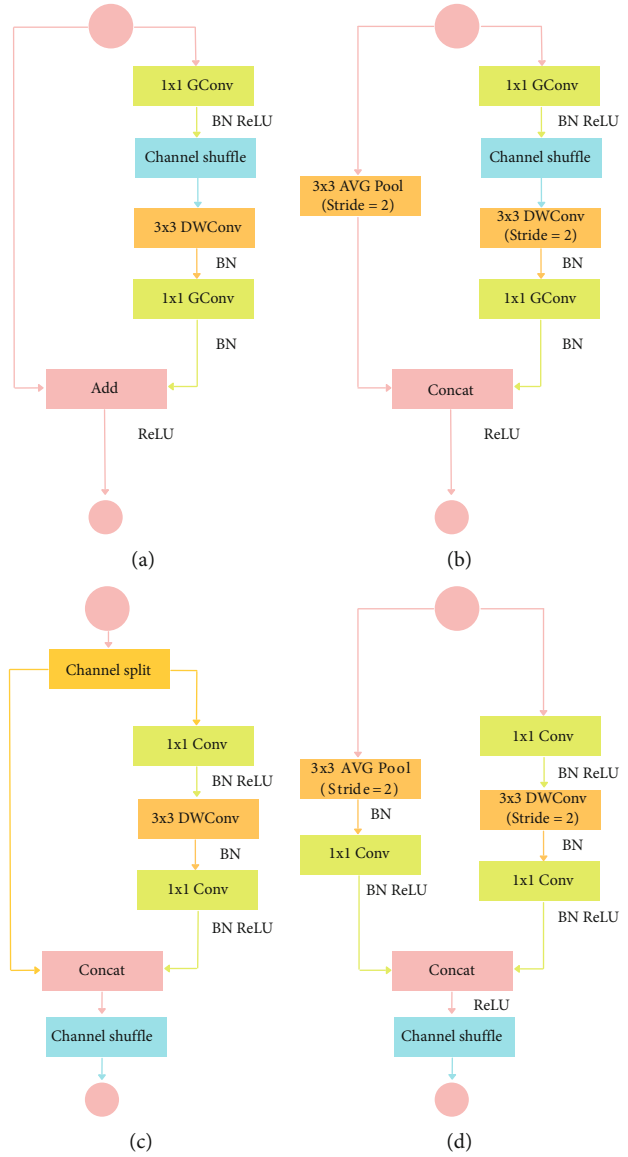

Figure 7: The pretrained ShuffleNet.

and discriminative characteristics that decrease the high dimension of feature space to a minimum is feature selection. GA is a metaheuristic feature selection approach that begins the search and finds many solutions to the problem. GA is an optimizer, which means it will choose the best solution from a list of options. In this particular research case,

```
Z,M Vbest ← ϕ → initialize
P0 ← Gaussian distribution at random with σ =0.3 and μ=0.6
All genes are discretized into binary values.
        {0, Pi < 0.5}
As a result
        {1, otherwise}
While m ≤ M do
m ← m +1.
GA (Pm)
If argmaxm (Pm) ≥ then Vbest ← argmaxm (Pm)
End while
Return best P → Return the most fit one
```

Pseudocode 1: Pseudocode of feature selection method utilizing GA.

5000 features have been extracted in which 800 are optimal, which is indeed a large number that may affect computation cost in terms of module's training time and may affect the classifier accuracy result. It is also possible that due to irrelevant and redundant features, set overfitting maybe found. If that set exists, it is vital to eliminate it. To achieve this goal, we employ an effective genetic algorithm approach as supported by experimental results. In the proposed system, generation of random uniform population is done in the first step. The crossover and probability mutation for every individual generation are 0.5. The model begins by generating a random population. The chromosomes are made up of a number of gene characteristics, each of which has a real number. Below algorithm is the representation of chromosomes. The chromosomal representation is shown in the equation below.

$$Z = \{\sim \mathrm{Hi} | \sim \mathrm{Hi} \in 0, 1]]\} \mathrm{n\,i} = 1. \tag{1}$$

3.4. Multiclass SVMs. VMs have also been successfully used in practice, particularly for classification problems, and are a hot subject in the ML field right now. FVapnik and his colleagues proposed a unique statistical learning theory-based machine learning method. SVMs use structural risk minimization and are different from other risk models which use empirical risk minimization. This is theoretically sound and may be used in various situations. In SVM, the support vectors (a subset of the training points) must be examined to find the best separating hyperplane. SVMs may achieve high classification accuracy by selecting the optimum separation hyperplane even with minimal training sets.

Given a dataset,

$$\{(x_i, y_i), x_i \in R^n\, y_i \in \{-1 + 1\}, i = 1, \cdots .N\}. \tag{2}$$

As mentioned in the expression, the binary classification fundamental issue may be asked.

$$\begin{gathered} \min_{m,q,\epsilon} F = \frac{1}{2} \|m\|2 + C \sum_{i=I}^{N} \epsilon_i, \\ \mathrm{s.t}\, y_i\left(M^T \varnothing(x_i) + q\right) \geq 1 - \varepsilon_i, i = 1, \cdots \cdots N, \\ \varepsilon_i \geq 0, i = \cdots .., N \end{gathered} \tag{3}$$

where $y_i(M^T \varnothing(x_i) + q) \geq 1$ comprises first the given constraints $(M^T \varnothing(x_i) + q) \geq 1$ if $y_i + 1(M^T \varnothing(x_i) + q) \leq 1$ if $y_i = -1$ and ε_i are slack variables in the inequalities set that enable misclassifications; the punishment factor is $C > 0$. Expression (4) states its dual problem.

$$\min_{\partial} \frac{1}{2} \partial^T \varrho \partial - e^T \partial. \tag{4}$$

Subject to $y^T \partial = 0$,

$$0 \leq \partial i \leq C, i = 1, \cdots, i, \tag{5}$$

where e is vector of all ones, ϱ is an l *by* l positive semidefinite matrix, $\varrho_{ij} \equiv y_i y_j K(x_i, x_j)$, and $K((x_i, x_j) \equiv \varnothing(x_i)^T \varnothing(x_j)$ The preparation vectors are transferred into upper level Euclidean space by the function, and the input vector x may be described as in this high-ranking dimensional showcase space. Equation (6) provides the decision function.

$$\mathrm{Sgn}\left(\sum_{i=1}^{l} y_i \partial_i K(x_i, x) + q\right). \tag{6}$$

The aim of the development of support vector machines was a binary classification. It is still a work in progress to figure out how to make it work for multiclass categorization. In most cases, there are a few different techniques to multiclass SVM.

The essential purpose of the development of support vector machines was binary classification. Its extension for multiclass classification is not yet achieved, however still under research. For multiclass SVM, there are a few options.

(i) One vs. all

(ii) One vs. one

(iii) A graph with a direct acyclic path

(iv) ECO codes

3.5. Error-Correcting Output Codes. Error-correcting output code (ECOC) is a technique for breaking down a multiclass classification issue into a set of binary classifier subproblems. Sejnowski and Rosenberg (1987) presented the approach error-correcting output coding in their well-known system NET talk.

We can solve the problem by linking each of the classes with a row of an A ∗ B "Coding Matrix"; we can provide entries in the range from {-1, 0, +1}. Each class will be assigned string *B* that is unique in nature. Here from *B*, we mean the binary classification problem numbers, we are supposed to construct. In the matrix, each column expresses a difference between two classes "1" and "+1," while class "0" will be ignored. The classes having "-1" and "+1" will communicate with our "li:" and "li+," respectively. These strings will be referred to as "Codewords." Then, *B* binary functions are learned for each bit position in these binary strings, one for each bit position. The expected outputs of these *B* binary functions are provided by the codeword for class *i* during training, for example, from class *i*. Each *n* binary function is calculated to yield a *B* binary sequence, which is then used to classify new *X* values. The generated strings are compared to the *K* features, and *X* is assigned to that class whose features are near to the newly generated strings, according to some distance measure. Coding is a crucial subject to take. Two qualities should be included in a suitable ECO code for a problem that belongs to the *K* class: row and column separation. The ability of a code to fix mistakes is proportional to the number of rows separated. If *d* is the least hamming distance, then at least code can be corrected to a single bit error $\lfloor (d-1)/2 \rfloor$.

3.6. Major Contribution. The main contributions of this research study include the following.

(i) Firstly, a new feature extraction block is developed, using five state-of-the-art CNN models to extract features from the fundus images. Genetic algorithm is used for optimal feature selection extracted through developed block

(ii) An error correction output code framework is applied on the SVM classifier to develop a multiclass classifier that can classify more than two classes of data

(iii) A custom dataset is developed by collecting fundus images from a local hospital. The dataset contains five classes of fundus images of healthy persons and those with mild DR, moderate DR, severe DR, and proliferative DR

(iv) Finally, we carry out experiments on three dataset: Kaggle dataset, custom dataset, and augmented custom dataset. The proposed model performed well on the enhanced custom dataset as compared to the Kaggle dataset and the custom dataset

3.7. Performance Matrices. All the already discussed CNN models, genetic algorithm, and SVM classifier are used in our experiment. We consider five indicators to measure the performance of our proposed system. All these values were determined using some basic terms from the confusion matrix, and they are true negative (TN), false negative (FN), true positive (TP), and false positive (FP).

Therefore, the following equations give the indicators values:

$$\text{Accuracy} = \frac{\text{TN} + \text{TP}}{\text{FP} + \text{TN} + \text{TP} + \text{FN}}, \tag{7}$$

$$\text{Recall} = \frac{\text{TP}}{\text{FN} + \text{TP}}, \tag{8}$$

$$\text{Specificity} = \frac{\text{TN}}{\text{FP} + \text{TN}}, \tag{9}$$

$$\text{Precision} = \frac{\text{TP}}{\text{FP} + \text{TP}}, \tag{10}$$

$$\text{F1 Score} = 2 \times \left\{ \frac{\text{Precision.} \times \text{Recall}}{\text{Precision.+Recall}} \right\}. \tag{11}$$

The accuracy of the classification model is determined by several factors, as shown in Equation (7). Furthermore, as shown in Equation (8), the rate of sensitivity reflects a classifier's capacity to build the focused class correctly. Similarly, as indicated in Equation (9), the specificity rate demonstrates a classifier's separation capabilities. The precision rate evaluates the accuracy with which a class is determined as shown in Equation (10).Equation (11) defines F1 score as the harmonic mean sensitivity (recall) and accuracy value. In this study, as a result, all related evaluation parameters for CNNs were calculated. Based on the parameters mentioned above, the results are presented in the next section.

4. Results and Implementation

This section provides the description of the dataset utilized in this study, experimental setup, and obtained results.

4.1. Dataset. In our research work, the performance of our proposed model is evaluated using three datasets; the first dataset is an eight GB labeled dataset taken from the Kaggle repository, while the second dataset is a custom dataset. The custom dataset contains retina fundus images to classify different levels of diabetic retinopathy. The fundus photos for custom dataset development are obtained from local hospital which are captured on digital fundus camera, i.e., Canon CX-1. Both left and right eye samples of the patients are provided. Each sample is scaled with 0 to 4 for each DR class by the ophthalmologist. A level of 0 indicates the healthy case, while ratings 1, 2, 3, and 4 show mild, moderate, severe, and proliferative DR, respectively. These scales are employed as labels in our proposed model.

The proposed approach differs from the existing system, which distributed fundus images based on the clinical and pathological changes in the retina. Furthermore, we consider the clinical practice, which is, we distributed the fundus image of abnormalities and the treatment methods. Pictures are divided and placed in different folders according to their tags. The process of dividing the images into different categories is done under the guidelines of an expert ophthalmologist. After that, the images are cropped, and the key features are separated. A filtering technique is also used to equalize and contrast the image modification. The third dataset in augmented or enhanced custom dataset. Due to less image in custom dataset, data augmentation is performed. Data augmentation is a technique for increasing the range of data available that has been adopted. After that, flipping, cropping, rotating, zooming, and padding are done.

4.2. Experimental Setup. We developed a novel approach by incorporating CNN models, genetic algorithm, and ECOC multiclass SVM to detect diabetic retinopathy. The architectures used for features learning are AlexNet, Inception V3, VGG-19, NASNet-Large, and ShuffleNet. The features from each CNN model are extracted using the last fully connected layer with a dimension of 1×1000 per image. The genetic algorithm is used to select the optimal features. The SVM model hyperparameters (C value, kernel, filter type, and optimizer) are tuned to select the optimal hyperparameters for classifying DR images into their corresponding classes. Therefore, the parameters are defined using the training results for the improvement of performance. We utilized the value of C as 1, kernel type was RBF, and filter type was feature normalization. We used MATLAB deep learning framework for feature extraction. In contrast, the SVM classifier used is part of the CNN models' statistics and machine learning toolbox. All simulations are performed on HP Z440 work with an Intel Xeon processor consisting of 48 GB of RAM and 8 GB of NVIDIA RTX 2070 SUPER GPU.

When conducting experiments, several performance metrics were used to evaluate the performance of the methodology proposed in this paper, including accuracy, precision, recall, and F1 score. An important GA-based feature selection method is also included, which selects the optimal features while also reducing the dimensions of the feature vector and facilitating efficient model training and development. In the experiment, it is necessary to distinguish between three types of datasets: the benchmark dataset, the customized dataset, and the customized enhanced dataset (all of which are customized). The datasets has been divided into two parts: a trainset and a test set, with a 70/30 split between the two parts to make model validation and parameter tuning more straightforward. To train the classifier, it must be fed with information about the trainset's features as well as the labels that have been assigned to them. The classification model is SVM with an error correction output code intended to be used in error correction. Following the completion of model training, the trained model is evaluated against the validation set, which comprises the reduced feature vector containing only optimal features and the actual validation set, as soon as possible after the training is completed. Confusion matrixes are calculated by comparing predicted labels from an SVM classifier to the existing labels vector generated by the SVM classifier to calculate the confusion matrixes (see Figure 1). The confusion matrixes contain the rates of four different classifications, namely, true positive (TP), false positive (FP), false negative (FN), and true negative (TN), which are used to calculate the models' accuracy, precision, recall, and F1 score. The experiments are conducted using three sets of data. One is the benchmark Kaggle dataset, the second is a self-developed customized dataset, and the third is an augmented version of the custom dataset. The proposed model shows better results on the Kaggle dataset. On the custom dataset, due to fewer images, the model performance was comparatively lower. To enhance the model's performance in the custom dataset, we performed augmentation for the custom dataset and applied the model on new data that showed improved results. Figure 8 shows the confusion matrices of the experiments we performed on the three different datasets: the Kaggle dataset, the custom dataset, and the augmented custom dataset. The experimental results showed that the proposed method can effectively classify diabetic retinopathy.

For the comparison of the results of the experiments performed on different datasets, accuracy, precession, recall, receiver operating characteristic (ROC) curves, and the area under the ROC are used. Table 2 presents the accuracy, precession, recall, and F1 score of the model for the three datasets. The model achieves a higher accuracy of 97.9% when trained and tested on the Kaggle dataset. On the self-developed custom dataset, the model achieves comparatively lesser accuracy of 94.76% since there are less photos in the dataset.

The researchers performed data augmentation for the custom dataset and developed another version of the custom dataset, the augmented custom dataset. We trained and tested the model on the augmented custom dataset and achieved a comparatively higher accuracy of 96.4%. The model achieves a higher precision rate on the augmented custom dataset and the custom dataset. It is observed that precision is low on the Kaggle dataset.

Figure 9 shows the ROC curves, and from which, it can be appreciated that the performance of model over Kaggle dataset is better than the other two datasets. It is also observed that the augmented custom dataset performed well as compared to custom dataset. The model performance has been shown in Figure 10 in terms of accuracy, precision, recall and F-measure.

4.3. Discussion. The proposed methodology in this paper was evaluated using five-class datasets, a benchmark dataset, a custom dataset, and an enhanced custom dataset. The dataset was split into two sections: training and validation. Parts use a cross-validation mechanism with a percentage of 70/30; 70% of the images and labels were used for training, while the remaining 30% of mages and labels were used for validation. Five pretrained CNN models were used for feature extraction from the images. We used five CNN models for feature extraction, and we got 5000 images. To make the feature vector's dimension smaller, feature selection was used, and for this purpose, the genetic algorithm with tournament selection methods is

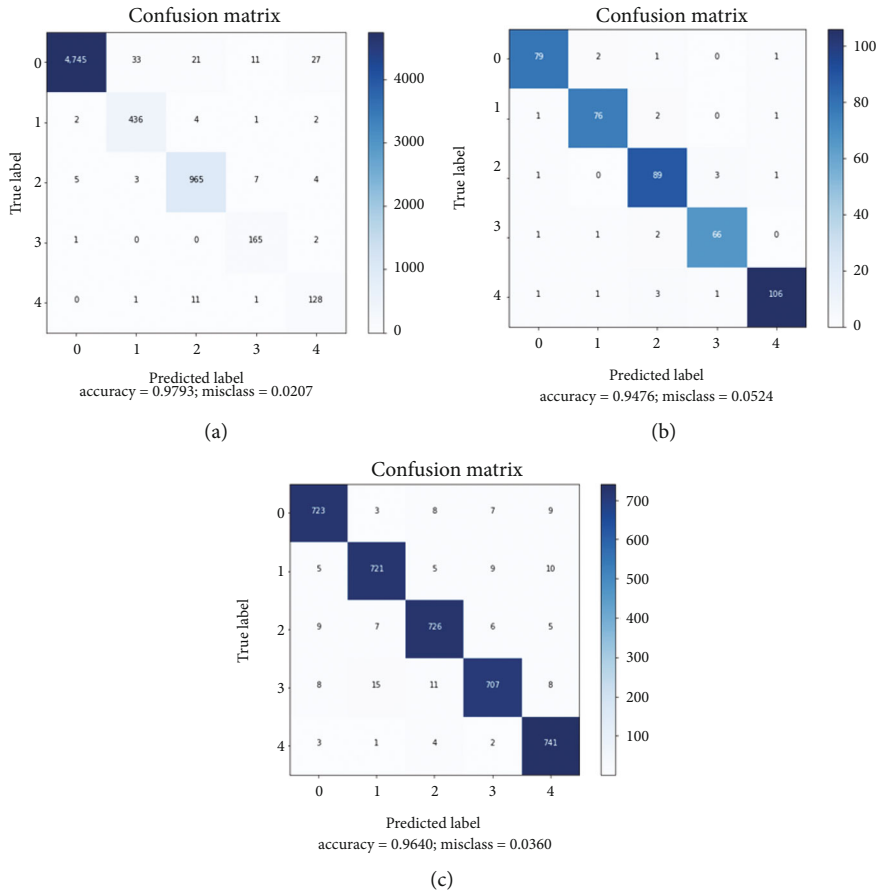

Figure 8: Confusion matrix of the proposed model on different datasets.

Table 2: Results obtained on the proposed model.

DS	Class	Accuracy	Precision	Recall	*F*-measure
Kaggle	Normal class	97.9	0.9983	0.981	0.9896
	Mild DR class		0.9218	0.9796	0.9499
	Moderate DR class		0.964	0.9807	0.9723
	Severe DR class		0.8919	0.9821	0.9348
	Proliferative DR class		0.7853	0.9078	0.8421
Custom	Normal class	94.76	0.9518	0.9518	0.9518
	Mild DR class		0.95	0.95	0.95
	Moderate DR class		0.9175	0.9468	0.9319
	Severe DR class		0.9429	0.9429	0.9429
	Proliferative DR class		0.9725	0.9464	0.9593
Augmented custom	Normal class	96.4	0.9666	0.964	0.9653
	Mild DR class		0.9652	0.9613	0.9633
	Moderate DR class		0.9629	0.9641	0.9635
	Severe DR class		0.9672	0.9439	0.9554
	Proliferative DR class		0.9586	0.9867	0.9724

used to rank the features. Support vector machine classification model is used to classify images in classes. All three datasets, the benchmark dataset, the custom dataset, and the enhanced custom dataset, have file classes, i.e., normal, mild DR, moderate DR, severe DR, and proliferative DR. The method begins with a multiclass dataset being evaluated for accuracy. The average classification accuracy is then evaluated using hold-out cross-validation. Individual

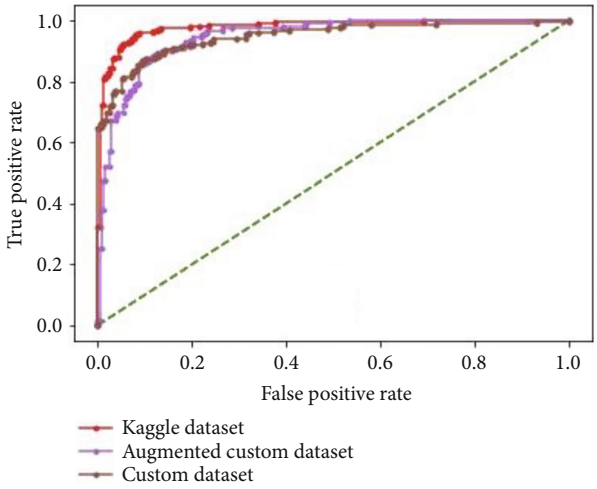

Figure 9: Performance demonstration through ROC.

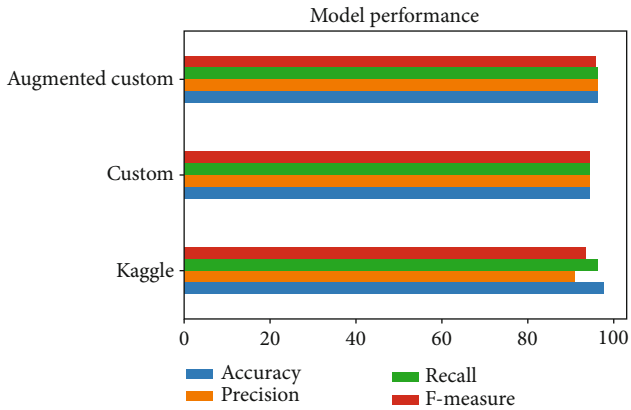

Figure 10: Graphical representation of performance.

accuracy data are used to determine the average accuracy value. The findings show how to use the SVM classification approach to explore CNN features using feature extraction on pretrained CNN networks. The SVM classifies the images and returns a confusion matrix for each severity level of the disease. The most accurate dataset is the Benchmark dataset which achieved an accuracy of 97.9% for normalized training feature vector. The model's accuracy increases by incorporating the evolutionary search method. Our unique data package achieves the highest precision of 0.9641 on the augmented custom dataset and the lowest precision of 0.9122 on the Kaggle dataset. In [28], the author gives a thorough examination of the link between ConvNet and various pretrained learning approaches, as well as the consequences of optimization. These hybrid networks improve on state-of-the-art algorithms for image, audio, text, and video identification, classification, and detection. ConvNet has also been used in computer vision for some task-specific applications. To validate the survey, the authors also performed some experiments on a public face and skin detection dataset to provide an authentic solution.

4.4. Conclusion. The recognition of the five stages of severity level of DR using fundus images is a challenging task. Most of the existing studies worked on only the binary classification of DR with significantly good results. This research has presented a deep learning-based model for feature extraction using five pretrained deep architectures and GA for optimal feature selection. The performance of model is tested on three datasets: the Kaggle dataset, a custom dataset, and enhanced custom dataset. The proposed approached achieved an accuracy of 97.9% on the Kaggle dataset. It achieved 94.76% accuracy on the custom dataset and 96.4% accuracy on the enhanced custom dataset with five classes. Our suggested approach performed better on the Kaggle dataset and had poorer outcomes on the custom dataset across all three datasets. The outcomes of this study can help doctors and researchers make better clinical decisions. There are a few flaws in our research that can be addressed in the future studies. A more thorough examination is required, which requires the collection of more patient data. Future research should focus on distinguishing between individuals with normal symptoms and those with nonproliferative symptoms in terms of accuracy. The nonproliferative symptoms may not be seen at all or may not be visible at all on retina imaging. Another possibility is to expand the scope of the presented approach to larger datasets. Other medical issues, such as cancer and tumors, may be addressed.

Data Availability

Data will be available on request.

Conflicts of Interest

The authors declare that they have no conflicts of interest.

References

[1] R. Gargeya and T. Leng, "Automated identification of diabetic retinopathy using deep learning," *Ophthalmology*, vol. 124, no. 7, pp. 962–969, 2017.

[2] M. Chetoui, M. A. Akhloufi, and M. Kardouchi, "Diabetic retinopathy detection using machine learning and texture features," in *Proceedings of the 2018 IEEE Canadian Conference on Electrical Computer Engineering (CCECE)*, vol. 13–16, pp. 1–4, Quebec, QC, Canada, 2018.

[3] M. Mateen, J. Wen, M. Hassan, N. Nasrullah, S. Sun, and S. Hayat, "Automatic detection of diabetic retinopathy: a review on datasets, methods and evaluation metrics," *IEEE Access*, vol. 8, pp. 48784–48811, 2020.

[4] D. K. Prasad, L. Vibha, and K. R. Venugopal, "Early detection of diabetic retinopathy from digital retinal fundus images," in *Proceedings of the 2015 IEEE Recent Advances in Intelligent Computational Systems (RAICS)*, pp. 240–245, Trivandrum, India, 10–12 December 2015.

[5] X. Zeng, H. Chen, Y. Luo, and W. Ye, "Automated diabetic retinopathy detection based on binocular Siamese-like convolutional neural network," *IEEE Access*, vol. 7, pp. 30744–30753, 2019.

[6] D. J. Hemanth, O. Deperlioglu, and U. Kose, "An enhanced diabetic retinopathy detection and classification approach using deep convolutional neural network," *Neural Computing and Applications*, vol. 32, no. 3, pp. 707–721, 2020.

[7] Z. Gao, J. Li, J. Guo, Y. Chen, Z. Yi, and J. Zhong, "Diagnosis of diabetic retinopathy using deep neural networks," *IEEE Access*, vol. 7, pp. 3360–3370, 2019.

[8] P. Junjun, Y. Zhifan, S. Dong, and Q. Hong, "Diabetic retinopathy detection based on deep convolutional neural networks for localization of discriminative regions," in *Proceedings of the 2018 International Conference on Virtual Reality and Visualization (ICVRV)*, vol. 22–24, pp. 46–52, Qingdao, China, October 2018.

[9] A. Samanta, A. Saha, S. C. Satapathy, S. L. Fernandes, and Y. D. Zhang, "Automated detection of diabetic retinopathy using convolutional neural networks on a small dataset," *Pattern Recognition Letters*, vol. 135, pp. 293–298, 2020.

[10] R. Ghosh, "Automatic detection and classification of diabetic retinopathy stages using CNN," in *Proceedings of the 2017 4th International Conference on Signal Processing and Integrated Networks (SPIN)*, Noida, Delhi-NCR, India, 2–3 February 2017.

[11] H. Takahashi, H. Tampo, Y. Arai, Y. Inoue, and H. Kawashima, "Applying artificial intelligence to disease staging: deep learning for improved staging of diabetic retinopathy," *PLoS One*, vol. 12, no. 6, article e0179790, 2017.

[12] H. Pratt, F. Coenen, D. M. Broadbent, S. P. Harding, and Y. Zheng, "Convolutional neural networks for diabetic retinopathy," *Procedia computer science*, vol. 90, pp. 200–205, 2016.

[13] V. Gulshan, L. Peng, M. Coram et al., "Development and validation of a deep learning algorithm for detection of diabetic retinopathy in retinal fundus photographs," *JAMA*, vol. 316, no. 22, pp. 2402–2410, 2016.

[14] W. L. Yun, U. Rajendra Acharya, Y. Venkatesh, C. Chee, L. C. Min, and E. Ng, "Identification of different stages of diabetic retinopathy using retinal optical images," *Information Sciences*, vol. 178, no. 1, pp. 106–121, 2008.

[15] Y. S. Kanungo, "Detecting diabetic retinopathy using deep learning," in *Proceedings of the 2017 2nd IEEE International Conference on Recent Trends in Electronics, Information & Communication Technology (RTEICT)*, vol. 19–20, pp. 801–804, Bangalore, India, 2017.

[16] S. Masood and T. Luthra, "Identification of Diabetic Retinopathy in Eye Images Using Transfer Learning," in *Proceedings of the 2017 International Conference on Computing, Communication and Automation (ICCCA)*, Greater Noida, India, 5–6 May 2017.

[17] A. Kwasigroch, B. Jarzembinski, and M. Grochowski, "Deep CNN based decision support system for detection and assessing the stage of diabetic retinopathy," in *Proceedings of the 2018 International Interdisciplinary PhD Workshop (IIPhDW)*, Swinoujscie, Poland, 9–12 May 2018.

[18] X. Wang, Y. Lu, Y. Wang, and W. B. Chen, "Diabetic retinopathy stage classification using convolutional neural networks," in *Proceedings of the 2018 IEEE International Conference on Information Reuse and Integration (IRI)*, Salt Lake City, UT, USA, 6–9 July 2018.

[19] G. Garc, J. Gallardo, A. Mauricio, L. Jorge, and C. D. Carpio, "Detection of diabetic retinopathy based on a convolutional neural network using retinal fundus images," in *International Conference on Artificial Neural Networks; Springer*, pp. 1–8, Berlin/Heidelberg, Germany, 2017.

[20] P. Ruamviboonsuk, J. Krause, P. Chotcomwongse et al., "Deep learning versus human graders for classifying diabetic retinopathy severity in a nationwide screening program," *NPJ digital medicine*, vol. 2, no. 1, pp. 1–9, 2019.

[21] S. Qummar, F. G. Khan, S. Shah et al., "A deep learning ensemble approach for diabetic retinopathy detection," *IEEE Access*, vol. 7, pp. 150530–150539, 2019.

[22] I. Ardiyanto, H. A. Nugroho, R. Lestari, and B. Buana, "Deep learning-based diabetic retinopathy assessment on embedded system," in *Proceedings of the 2017 39th Annual International Conference of the IEEE Engineering in Medicine and Biology Society (EMBC)*, pp. 1760–1763, Jeju Island, Korea, 11–15 July 2017.

[23] Grissworld Home Care, "The 4 stages of diabetic retinopathy: what you can expect," 2019. Available online: https://www.http://griswoldhomecare.com/blog/2015/january/the-4-stages-of-diabetic-retinopathy-what-you-ca/ (accessed on13 December 2021).

[24] M. Mateen, J. Wen, S. Song, and Z. Huang, "Fundus image classification using VGG-19 architecture with PCA and SVD," *Symmetry*, vol. 11, no. 1, p. 1, 2019.

[25] F. Ali, S. R. Islam, D. Kwak et al., "Type-2 fuzzy ontology-aided recommendation systems for IoT-based healthcare," *Computer Communications*, vol. 119, pp. 138–155, 2018.

[26] S. U. Rehman, S. Tu, O. U. Rehman, Y. Huang, C. M. S. Magurawalage, and C. C. Chang, "Optimization of CNN through novel training strategy for visual classification problems," *Entropy*, vol. 20, no. 4, p. 290, 2018.

[27] Z. Khan, F. G. Khan, A. Khan et al., "Diabetic retinopathy detection using VGG-NIN a deep learning architecture," *IEEE Access*, vol. 9, pp. 61408–61416, 2021.

[28] S. Rehman, S. Tu, M. Waqas et al., "Unsupervised pre-trained filter learning approach for efficient convolution neural network," *Neurocomputing*, vol. 365, pp. 171–190, 2019.

Hindawi
Wireless Communications and Mobile Computing
Volume 2022, Article ID 1858865, 12 pages
https://doi.org/10.1155/2022/1858865

Research Article

Direction-of-Arrival Estimation Method for Principal Singular Vectors Based on Multiple Toeplitz Matrices

Yaofeng Tang,[1,2] **Kuangang Fan**,[2,3] **Shuang Lei**,[2,3] **and Junfeng Cui**[4]

[1]*School of Mechanical and Electrical Engineering, Jiangxi University of Science and Technology, Ganzhou, Jiangxi 341000, China*
[2]*Key Laboratory of Magnetic Levitation Technology in Jiangxi Province, Ganzhou, Jiangxi 341000, China*
[3]*School of Electrical Engineering and Automation, Jiangxi University of Science and Technology, Ganzhou, Jiangxi 341000, China*
[4]*China Railway Signal & Communication Research & Design Institute Group Company Limited, Beijing 100070, China*

Correspondence should be addressed to Kuangang Fan; kuangangfriend@163.com

Received 16 May 2022; Revised 22 June 2022; Accepted 23 June 2022; Published 8 July 2022

Academic Editor: Fawad Zaman

A principal singular vector based on multiple Toeplitz matrices is proposed to solve the accuracy problem of direction-of-arrival (DOA) estimation for coherent signals. First, the data matrix received by uniform linear array (ULA) is transformed into a Toeplitz matrix. An equivalent covariance matrix is obtained by square weighted summation method using the Toeplitz matrix. Then, a polynomial containing DOA information is constructed because the signal space and the steering matrix have the same column space; the Toeplitz matrix is built using polynomial coefficients. The problem is transformed into solving linear equations by establishing the relationship between the Toeplitz matrix and the signal subspace. Furthermore, the weighted least square method is used to obtain multiple candidates for linear equations. Finally, the maximum likelihood (ML) rule is used to select source signal candidates from multiple candidates. In comparison with currently known algorithm, the proposed algorithm has the characteristics of high estimation accuracy, low-complexity, and strong anti-interference ability and resolution. Even when the signal-to-noise ratio (*SNR*) is low, the snapshot number is small, and multiple signals exist; this method can still provide good estimation performance and resolution, which is more than 90% in most cases. Simulation experiments verify the superiority of the algorithm.

1. Introduction

Array signal processing is a crucial research issue in signal processing and has been extensively used in radar [1, 2], sensor [3, 4], remote sensing [5–7], target detection [8, 9], and wireless communication [10–12].

As one of the most important research contents in array signal processing, direction-of-arrival (DOA) estimation has been the focus of scholars for decades. Scholars have put forward many excellent algorithms. Among them, DOA algorithm based on subspace is the most representative method in DOA estimation, including multiple signal classification (MUSIC) [13], estimation of signal parameters via rotational invariance techniques (ESPRIT) [14], and its variants [15–20]. MUSIC replaces data matrix by constructing sampling covariance matrix and then obtains DOA by spectral peak search, which has high signal source detection resolution. However, due to coherent signals, the performance of the algorithm degrades and DOA cannot be accurately estimated. ESPRIT algorithm uses the rotation invariance between signal subspaces caused by sensor arrays with translational invariance structure; it is used to obtain high-resolution DOA information. Similar to the MUSIC algorithm, the detection accuracy of DOA decreases seriously in the face of coherent signal detection.

Many techniques and algorithms for processing coherent signals, such as forward-only spatial smoothing (FOSS) [21] and forward/backward spatial smoothing (FBSS) [22], have been proposed by scholars to process coherent signals. These methods divide the total array into several subarrays and then use the average value of the subarray covariance matrix to solve the coherent signal direction finding. However, the disadvantage of these methods is that they reduce the array aperture, resulting in reduced resolution of closely spaced

arrivals. In addition, signal subspace fitting (SSF) [23] and maximum likelihood (ML) [24–26] can solve the coherent signal by reducing the multidimensional problem to the 1D problem, without the need for feature decomposition in the process; it is insensitive to the coherence between signals. However, the number of signals greatly influences the estimation accuracy of the algorithm, and more signals indicate greater influence.

Recently, DOA algorithm based on polynomial solution, such as the method of direction estimation (MODE) [27, 28], the enhanced principal-singular-vector utilization for modal analysis (EPUMA) [29], and its variants [30–33], has received remarkable attention from scholars. MODE is similar to ML, but it can process coherent signals without complex computation and has no convergence problems. EPUMA is a low-complexity algorithm; it generates $(P + K)$ DOA candidates for K sources and then selects K to obtain coherent signal DOA information. Scholars have obtained good results by using these algorithms to solve coherent signals. However, in the low *SNR* and small snapshot number, they cannot accurately estimate, because the algorithm cannot accurately obtain sufficient signal information. If the source signal is highly correlated, then this situation will be exacerbated.

In addition, scholars have also proposed other excellent DOA algorithms [34–40]. In [34], a direction-of-arrival estimation algorithm based on low-rank reconstruction of the Toeplitz covariance matrix is proposed by scholars. In order to fully utilize the underlying received information in the presence of missing elements in the difference coarray, interpolation is performed and a dual variable rank minimization problem is formulated. The scholars recast the problem as a multiconvex form and developed an alternative optimization mechanism to solve the problem through cyclic iterations. In [35], a modified scheme based on forward and backward partial Toeplitz matrices reconstruction named as FB-PTMR is proposed. The scholars exploited half rows of the sample covariance matrix (SCM) to reconstruct the data matrix to overcome the performance deterioration of ESPRIT-like algorithm. In [36], the scholars used the existing decoherence algorithm, where the sample covariance matrix of each row is formed into a full-rank Toeplitz matrix to achieve decoherence, and then a new cost function to obtain DOA via a 1-D search. The advantage of the algorithm is that it does not require to know the source number information. In [37], aiming at the fact that conventional algorithms based on the convex relaxation is computationally expensive, the scholars proposed a nonconvex accelerated structured alternating projection-based direction-of-arrival estimation approach without solving semidefinite programming. In [38], the scholars proposed a new real-valued transformation for DOA estimation with arbitrary linear arrays by exploiting the virtual steering of linear arrays, which achieve a better performance in terms of both estimation accuracy and computational complexity. In [39], a DOA algorithm based on correlation matrix rearrangement is proposed. The algorithm can effectively deal with coherent signals in both 1D and 2D. In [40], an algorithm called MTOEP is proposed. MTOEP uses Toeplitz matrix and the observation data of each sensor to calculate a set of correlation matrices and then sums the square weighted of these correlation matrices to form the full-rank equivalent data covariance matrix. However, when multiple related signals and independent signals coexist, the error of this algorithm increases; a higher degree of correlation that exists between signals indicates greater error.

We propose a principal singular vector algorithm based on multi-Toeplitz matrix to eliminate the weakness of the existing algorithm. The proposed algorithm constructs a new covariance matrix and polynomial containing signal information by using the characteristic matrix, where the received data moments and signal space have the same column space as the steering matrix. The estimation problem is transformed into a linear equation problem, and the proposed algorithm has a better resolution effect. This algorithm combines the advantages of Toeplitz matrix and polynomial solution to obtain a high precision estimation algorithm without noise processing and auxiliary matrix. Subsequent experiments prove that the proposed algorithm can process multiple signals with low *SNR*, or the snapshot number is small and still has good performance.

This paper is organized as follows: we introduce the proposed algorithm in Section 2. In Section 3, we perform a series of simulation experiments. Finally, we summarize the study.

1.1. Notations. Superscripts $(\cdot)^{\dagger}$, $(\cdot)^{T}$, $(\cdot)^{H}$, $(\cdot)^{-1}$, and $(\cdot)^{*}$ represent the matrix pseudoinverse, matrix transpose, matrix conjugate transpose, matrix inversion, conjugate, and traces of matrix, respectively. The operator diag $\{\cdot\}$, $\mathrm{E}\{\cdot\}$, vec$\{\cdot\}$, and $\otimes$ indicate diagonalization, expectation, vectorization, and Kronecker product, respectively. I_M and $0_{M\times N}$ denote $M \times M$ identity matrix and $M \times N$ zero matrix, respectively.

2. Proposed Algorithm

2.1. Signal Model. The uniform linear array (ULA) consists of $2\,\mathrm{M}+1$ isotropic sensors, each spaced $d = \lambda/2$ apart, assuming that K narrow band signals impinge on the array in the distance. The received signal is expressed as follows:

$$x(t) = As(t) + n(t), t = -M, \cdots, M, \tag{1}$$

where $A = [\mathbf{a}(\theta_1) \cdots \mathbf{a}(\theta_K)]$ is the steering matrix, $s(t) = [s_1(t) \cdots s_K(t)]^T$ denotes the $K \times 1$ source signal vector, $n(t)$ is Gaussian white noise vector with zero mean and variance σ_n^2, and snapshot number is N. The incident angle of the kth signal is θ_K, and the steering vector due to the kth source is expressed as follows:

$$\mathbf{a}(\theta_k) = \left[e^{-j2\pi M \sin(\theta_k)d/\lambda}, \cdots, 1, \cdots, e^{j2\pi M \sin(\theta_k)d/\lambda}\right]^T, \tag{2}$$

where λ is the carrier wavelength.

2.2. Equivalent Covariance Matrix Is Constructed Based on Toeplitz Matrix of Data Matrix. We use data matrix $x(t)$

to construct $(M+1)\times(M+1)$ Toeplitz matrix, whose expression is as follows:

$$\begin{aligned} R_X(t) &= \begin{bmatrix} x_0(t) & x_1(t) & \cdots & x_M(t) \\ x_{-1}(t) & x_0(t) & \cdots & x_{M-1}(t) \\ \vdots & \vdots & \ddots & \vdots \\ x_{-M}(t) & x_{-M+1}(t) & \cdots & x_0(t) \end{bmatrix} \\ &= R_{As}(t) + R_N(t), \end{aligned} \tag{3}$$

where

$$\begin{aligned} R_{As}(t) &= \begin{bmatrix} y_0(t) & y_1(t) & \cdots & y_M(t) \\ y_{-1}(t) & y_0(t) & \cdots & y_{M-1}(t) \\ \vdots & \vdots & \ddots & \vdots \\ y_{-M}(t) & y_{-M+1}(t) & \cdots & y_0(t) \end{bmatrix}, \\ R_N(t) &= \begin{bmatrix} n_0(t) & n_1(t) & \cdots & n_M(t) \\ n_{-1}(t) & n_0(t) & \cdots & n_{M-1}(t) \\ \vdots & \vdots & \ddots & \vdots \\ n_{-M}(t) & n_{-M+1}(t) & \cdots & n_0(t) \end{bmatrix}, \end{aligned} \tag{4}$$

are the $(M+1)\times(M+1)$ Toeplitz matrix constructed by the $As(t)$ and the noise vector $n(t)$, respectively. Therefore, we can obtain the correlation matrix between Rxi and the ith isotropic sensor output $x_i(t)$, as follows:

$$\begin{aligned} R_{Xi} &= \mathrm{E}[R_X(t)x_i^*(t)] = \mathrm{E}[R_{AS}(t)y_i^*(t)] + \mathrm{E}[R_N(t)n_i^*(t)] \\ &= R_{Asi} + \sigma_n^2\tilde{I}_{(M+1),i}, \end{aligned} \tag{5}$$

where $\tilde{I}_{(M+1),i}$ is an $(M+1)\times(M+1)$ matrix whose elements are zero, except the ith diagonal, which is unity element. We fully use Rxi information to avoid the decrease in the estimation accuracy caused by noise suppression and array output covariance matrix. The advantage of this approach is that the noise term is diagonalized to improve the estimation accuracy without the need for denoising. Then, we have the following:

$$\begin{aligned} \tilde{R} &= \sum_{i=-M}^{M} R_{Yi}R_{Yi}^H \\ &= \sum_{i=-M}^{M}\left[\left(R_{Xi} + \sigma_n^2\tilde{I}_{(M+1),i}\right)\left(R_{Xi} + \sigma_n^2\tilde{I}_{(M+1),i}\right)^H\right] \\ &= \sum_{i=-M}^{M} R_{Xi}R_{Xi}^H + \sum_{i=-M}^{M} R_{Xi}\sigma_n^2\tilde{I}_{(M+1),i}^H + \sum_{i=-M}^{M}\sigma_n^2\tilde{I}_{(M+1),i}R_{Xi}^H \\ &\quad + \sum_{i=-M}^{M}\sigma_n^4\tilde{I}_{(M+1),i}\tilde{I}_{(M+1),i}^H. \end{aligned} \tag{6}$$

According to formula (6), an equivalent covariance matrix can be obtained. In addition, to further improve performance, FBSS technology was used to further optimize the obtained equivalent R, which is expressed as follows:

$$R = \tilde{R} + J\tilde{R}^*J, \tag{7}$$

where J is a $(M+1)\times(M+1)$ matrix with antidiagonal, and the other element is zero. Then, singular value decomposition of R is obtained as follows:

$$\hat{R} = \hat{U}_s\hat{\Lambda}_s\hat{U}_s^H + \hat{U}_n\hat{\Lambda}_n\hat{U}_n^H, \tag{8}$$

where $\hat{R}$, $\hat{U}_s$, $\hat{U}_n$, $\hat{\Lambda}_s$, and $\hat{\Lambda}_n$ represent the estimated values of R, U_s, U_n, Λ_s, and Λ_n; Λ_s contains the signal eigenvalues, and Λ_n contains the noise eigenvalues.

2.3. Toeplitz Matrix Containing DOA Information Is Constructed. U_s and A have the same column space, according to linear prediction (LP) theory; thus, each column of U_s is a sum of P sinusoids. From [41], we obtain the following:

$$z_k^P + \sum_{i=1}^{P} r_i z_k^{P-i} = 0, \tag{9}$$

where $z_k = e^{j2\pi \sin(\theta_k)d/\lambda}$, $k = 1, \cdots, K$, and r_i represents the LP coefficients. According to LP coefficients, Toeplitz matrix $B(r)$ consists of polynomial formula (9) coefficients containing signal information, as follows:

$$\begin{aligned} B(r) &= Toeplitz\left(\left[r_K 0_{M-P-1}^T\right]^T, \left[r_K \cdots r_1 1 0_{M-P-1}^T\right]\right) \\ &= \begin{bmatrix} r_K & r_{K-1} & \cdots & r_0 & 0 & 0 & 0 \\ 0 & r_K & r_{K-1} & \cdots & r_0 & 0 & 0 \\ & \ddots & \ddots & \ddots & \ddots & \ddots & \\ 0 & 0 & 0 & r_K & r_{K-1} & \cdots & r_0 \end{bmatrix}^{\mathrm{H}}. \end{aligned} \tag{10}$$

2.4. Multiple DOA Candidates Were Obtained by Solving Linear Equations. The matrix form of formula (9) is as follows:

$$e_k = F_k r - g_k = 0_{M-P} \tag{11}$$

where

$$F_k = \begin{bmatrix} [\mathbf{u}_k]_P & [\mathbf{u}_k]_{P-1} & \cdots & [\mathbf{u}_k]_1 \\ [\mathbf{u}_k]_{P+1} & [\mathbf{u}_k]_P & \cdots & [\mathbf{u}_k]_2 \\ \vdots & \vdots & & \vdots \\ [\mathbf{u}_k]_{M-1} & [\mathbf{u}_k]_{M-2} & \cdots & [\mathbf{u}_k]_{M-P} \end{bmatrix}, \tag{12}$$

$r = -[r_1 \cdots r_P]^T$, $g_k = -[[\mathbf{u}_k]_{P+1} \cdots [\mathbf{u}_k]_M]^T$, and $[\mathbf{u}_k]_M$ is the mth element in u_k.

Table 1: Implementation steps of the proposed algorithm.

(1) An equivalent $\widehat{R}$ is obtained through calculation of formulas (3), (5), (6), (7) and (8)
(2) The Toeplitz matrix containing DOA information is constructed by using formula (10)
(3) Formulas (14)–(16) were combined to obtain formula (18)
(4) Initialize $B(r)$ by using $\widehat{r}_0$ in formula (21), and utilize the $B(r)$ to construct $\widehat{W}$ via formula (18)
(5) The exact $\widehat{r}$ is obtained through several iterations of formulas (18) and (20)
(6) All DOA candidates were obtained by calculating formula (22)
(7) DOA values were obtained from all DOA candidates via formula (23)

Let $\widehat{F}$ and $\widehat{g}$ become estimates of F and g, and then we have the following:

$$\widehat{F}_k r \approx \widehat{g}_k \tag{13}$$

formula (13) cannot be solved directly due to noise. Therefore, the relationship between Toeplitz matrix $B(r)$ and formula (13) should be established. In the case of noise, we find that

$$vec(B(r)U) = vec(B(r)(U_s + \Delta U_s)) = \mathbf{0}_{(M-P)\times k}. \tag{14}$$

By combining formulas (11) and (14), the following can be obtained:

$$vec(B(r)U) = F_k r - g_k = \mathbf{0}_{(M-P)\times k}. \tag{15}$$

2.5. Weighted Least Square Method Used to Solve the Linear Equation. The weighted least square (WLS) method [42] is used to obtain a more accurate estimate, and the cost function is set as follows:

$$(\widehat{e})^H W \widehat{e}, \tag{16}$$

where $W = (\mathrm{E}[\widehat{e}(\widehat{e})^H])^{-1}$, and $\widehat{e} = \widehat{F}r - \widehat{g}$. Then, the solution of formula (16) is as follows:

$$\widehat{r} = \left((\widehat{F})^H W \widehat{F}\right)^{-1} (\widehat{F})^H W \widehat{g}, \tag{17}$$

where we replace r by $\widehat{r}$. However, we cannot obtain the value of $\widehat{r}$ directly, because W is unavailable. Thus, we obtain an estimate of W by combining formulas (14) and (16), as follows:

$$\widehat{W} = \Gamma \otimes \left(B(r)B^H(r)\right)^{-1}, \tag{18}$$

Table 2: Main step complexity of the proposed algorithm.

Main steps	Complexity
$\widehat{R}$	$\mathcal{O}\left(3M^3 + (N+1)M^2\right)$
EVD of $\widehat{R}$	$\mathcal{O}\left(M^3\right)$
$\widehat{W}^{-1}$	$\mathcal{O}\left((M-P)^3\right)$
$\widehat{r}$	$\mathcal{O}\left(2P^2K(M-P) + 2PK(M-P)^2 + P^3 + PK(M-P)\right)$

where W is replaced by $\widehat{W}$, and

$$\widehat{\Gamma} = \begin{bmatrix} \dfrac{\left(\widehat{\lambda}_1 - \widehat{\sigma}_n^2\right)^2}{\lambda_1} & & \\ & \ddots & \\ & & \dfrac{\left(\widehat{\lambda}_K - \widehat{\sigma}_n^2\right)^2}{\widehat{\lambda}_K} \end{bmatrix}, \tag{19}$$

$$\delta^2 = \frac{1}{M-N} \sum_{i=N+1}^{M} \lambda_i.$$

Then, by plugging formula (18) into formula (17), we have the following:

$$\widehat{r} = \left((\widehat{F})^H \widehat{W} \widehat{F}\right)^{-1} (\widehat{F})^H \widehat{W} \widehat{g}.. \tag{20}$$

2.6. Maximum Likelihood Rule Used to Obtain DOA. Multiple $\widehat{r}$ are iteratively obtained, and then the maximum likelihood rule is used

to obtain the exact DOA. First, the initial value of $\widehat{r}$ is obtained by calculation, which can be obtained from formula (13), as follows:

$$\widehat{r}_0 = (\widehat{F})^{\dagger} \widehat{g}, \tag{21}$$

and then formula (21) is substituted into formula (18) to obtain new $\widehat{W}$. The new $\widehat{W}$ is substituted into formula (20) to obtain $\widehat{r}$. After several iterations, we obtain all the DOA candidates as follows:

$$\widehat{\theta}_i = \sin^{-1}\left(\frac{\lambda \angle \widehat{r}_i}{2\pi d}\right), i = 1, \cdots, k. \tag{22}$$

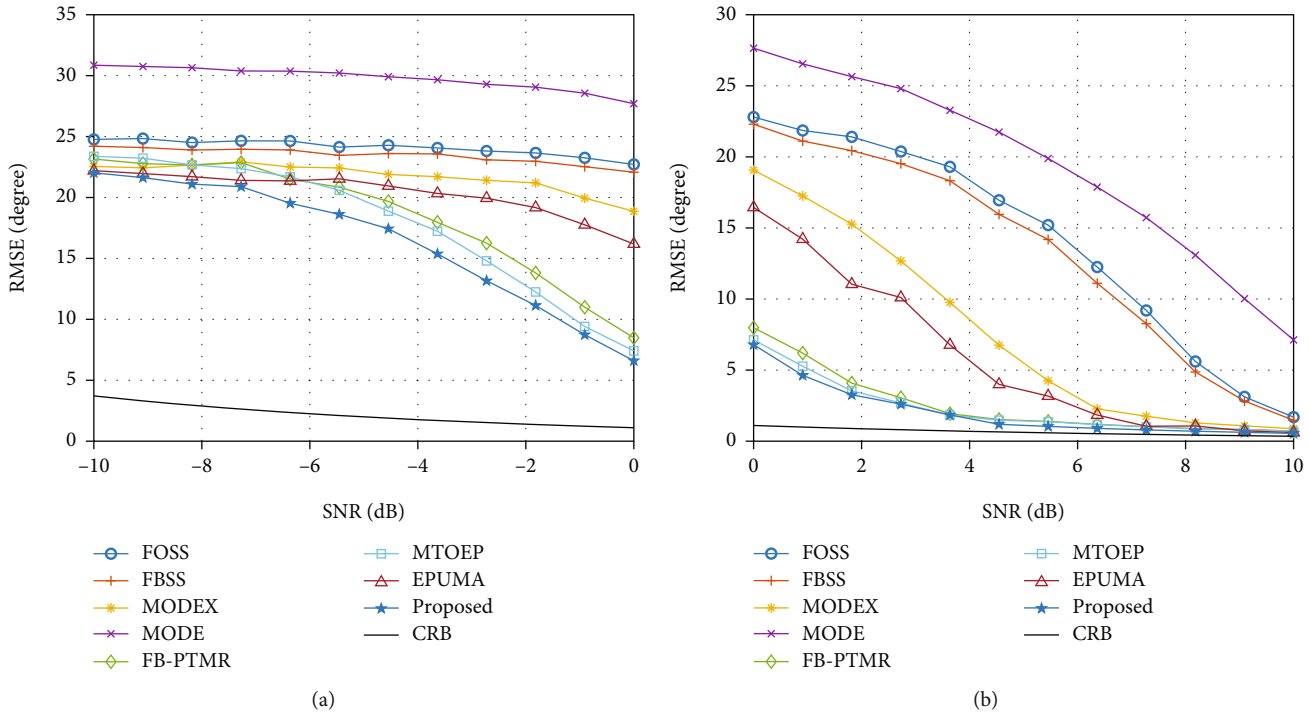

Figure 1: Algorithm RMSE versus *SNR* for two coherent signals and one uncorrelated signal with DOAs being [−5°, 0°, 25°] when $N = 100$. (a) *SNR* increased from −10 dB to 0 dB; (b) *SNR* increased from 0 dB to 10 dB.

Finally, we select estimates from all DOA candidates by maximum likelihood rule, as follows:

$$L(\Theta) = tr\left(\left(I_M - A(\Theta)\left(A^H(\Theta)A(\Theta)\right)^{-1}A^H(\Theta)\right)\widehat{R}\right), \quad (23)$$

where $L(\Theta)$ contains the desired DOA information. The proposed algorithm is summarized in Table 1.

2.7. Complexity Analysis. The main steps of the proposed algorithm are as follows:

(1) Calculation of $\widehat{R}$ and its EVD

(2) Calculation of $\widehat{W}^{-1}$

(3) Calculation of $\hat{r}$

The complexity of the main steps of the proposed algorithm is summarized in Table 2.

The sample covariance matrix and EVD complexity of the proposed algorithm are $\mathcal{O}(3M^3 + (N+1)M^2)$ and $\mathcal{O}(M^3)$, respectively. The computational $\widehat{W}^{-1}$ complexity is mainly caused by $B(r)B^H(r)$, which is about $\mathcal{O}((M-P)^3)$. The complexity of calculating $\hat{r}$ is $\mathcal{O}(2P^2K(M-P) + 2PK(M-P)^2 + P^3 + PK(M-P))$. Finally, the complexity of DOA is obtained by maximum likelihood rule, that is, $\mathcal{O}(G(M^3 + 3MK^2 + K^3))$. Thus, the complexity of the proposed scheme is:

$$\mathcal{O}\left(4M^3 + M^2(N+1) + I\left(M^3 - K^3 - 11MK^2 - 2M^2K + 4K^3M + 4K^2M^2\right) + G\left(M^3 + 3MK^2 + K^3\right)\right), \quad (24)$$

where I is the number of iterations, and $G = (P+K)!/K!P!$. Due to $G \gg I$ and isotropic sensors $M \gg K$, the complexity is reduced to $\mathcal{O}((N+1)M + GM^3)$.

3. Results and Discussion

In this section, we present a series of experiments to verify the superior performance of the proposed algorithm and consider ESPRIT [14], MODE [27], MODEX [31], EPUMA [29], FB-PTMR [35], and MTOEP [40] for comparison. The Cramér–Rao Bound (CRB) is used as a measure of performance in the experiment. In addition, FBSS [21] and FOSS [22] technologies are used to improve the ability of ESPRIT to process coherent signals. During the experiment, we assume that all signals are narrowband signals, and the ULA composed of $M = 10$ sensors is used to receive K signals. In order to demonstrate the advantage of the proposed algorithm in dealing with coherent signals, in the following experiments, coherence coefficient is 1. Furthermore, 3000 Monte Carlo experiments are performed for each experiment to obtain more accurate experimental data. The root mean square error (RMSE) of DOA is as follows:

$$\text{RMSE} = \sqrt{\frac{1}{3000K}\sum_{k=1}^{K}\sum_{i=1}^{3000}\left(\widehat{\theta}_{k,i} - \theta_k\right)^2}, \quad (25)$$

where $\widehat{\theta}_{k,i}$ is the experimental value and θ_k is the true value.

In the first experiment, we study the effect of different *SNR* on the RMSE and resolution of the algorithm. Three signals with DOAs being [−5°, 0°, 25°]are consider (K=3),

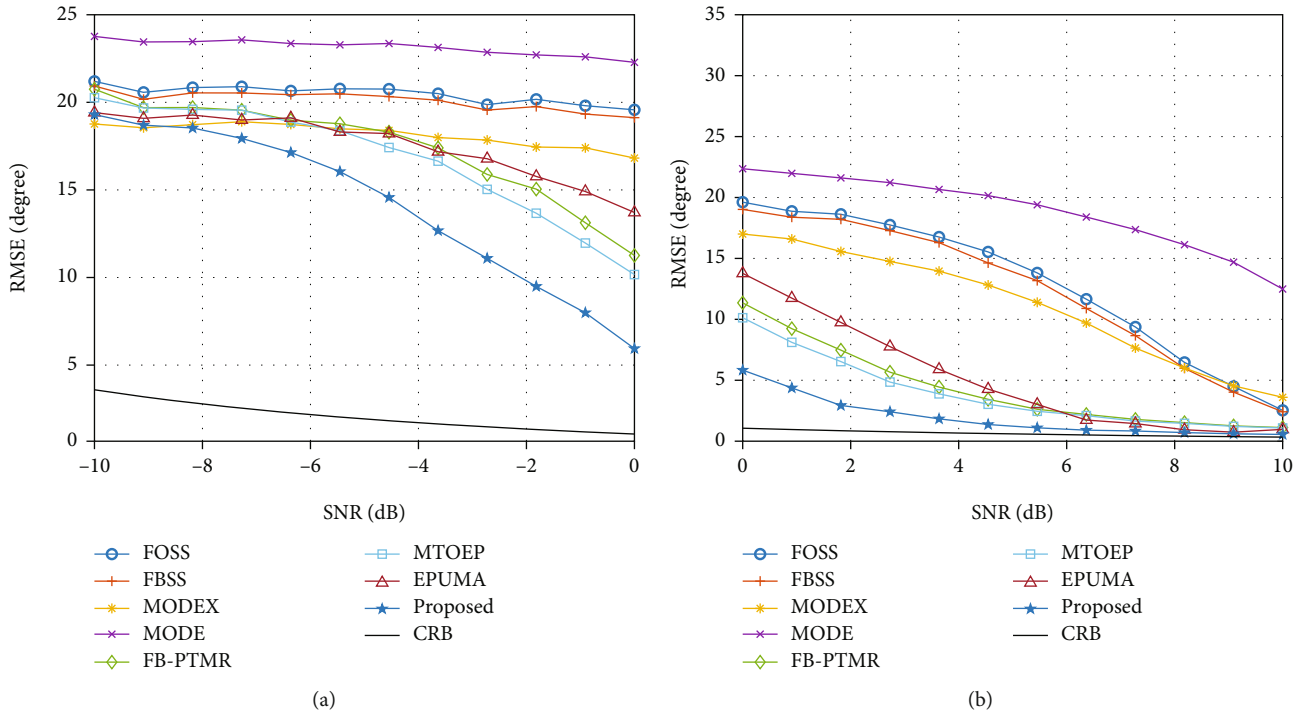

Figure 2: Algorithm RMSE versus *SNR* for two coherent signals and two uncorrelated signals with DOAs being [−5°, 0°, 25°, 31°] when $N = 100$. (a) *SNR* increased from −10 dB to 0 dB; (b) *SNR* increased from 0 dB to 10 dB.

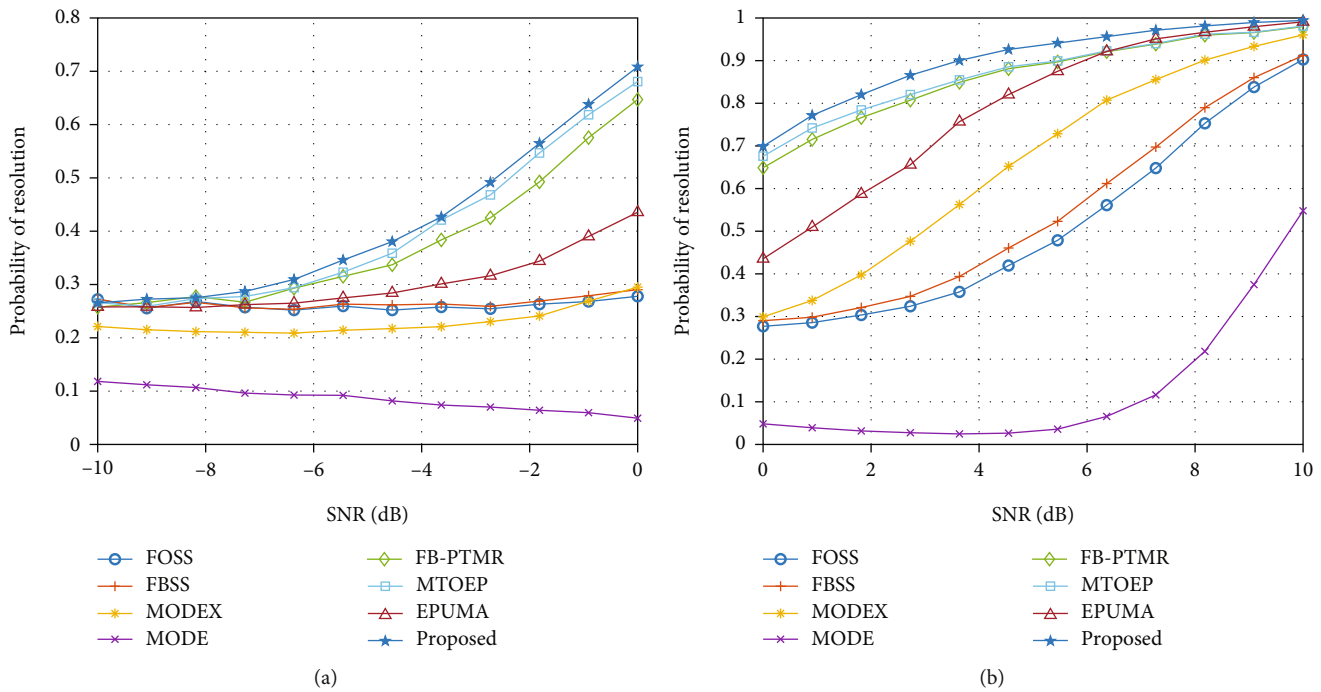

Figure 3: Algorithm probability versus *SNR* for two coherent signals and two uncorrelated signals with DOAs being [−5°, 0°, 25°] when $N = 100$. (a) *SNR* increased from −10 dB to 0 dB; (b) *SNR* increased from 0 dB to 10 dB.

where the first two signals are coherent and uncorrelated with the third one. We can obtain RMSE from (25), and the snapshot number is $N = 100$. As shown in Figure 1, when $SNR < 0$ dB, the RMSE of all algorithms are far from the CRB, FB-PTMR, and MTOEP, and the proposed algorithms are slightly better than the other algorithms. When $SNR > 0$ dB and $K = 3$, the RMSE of all algorithms is reduced, as well as the FB-PTMR, MTOEP, and the proposed converge to the

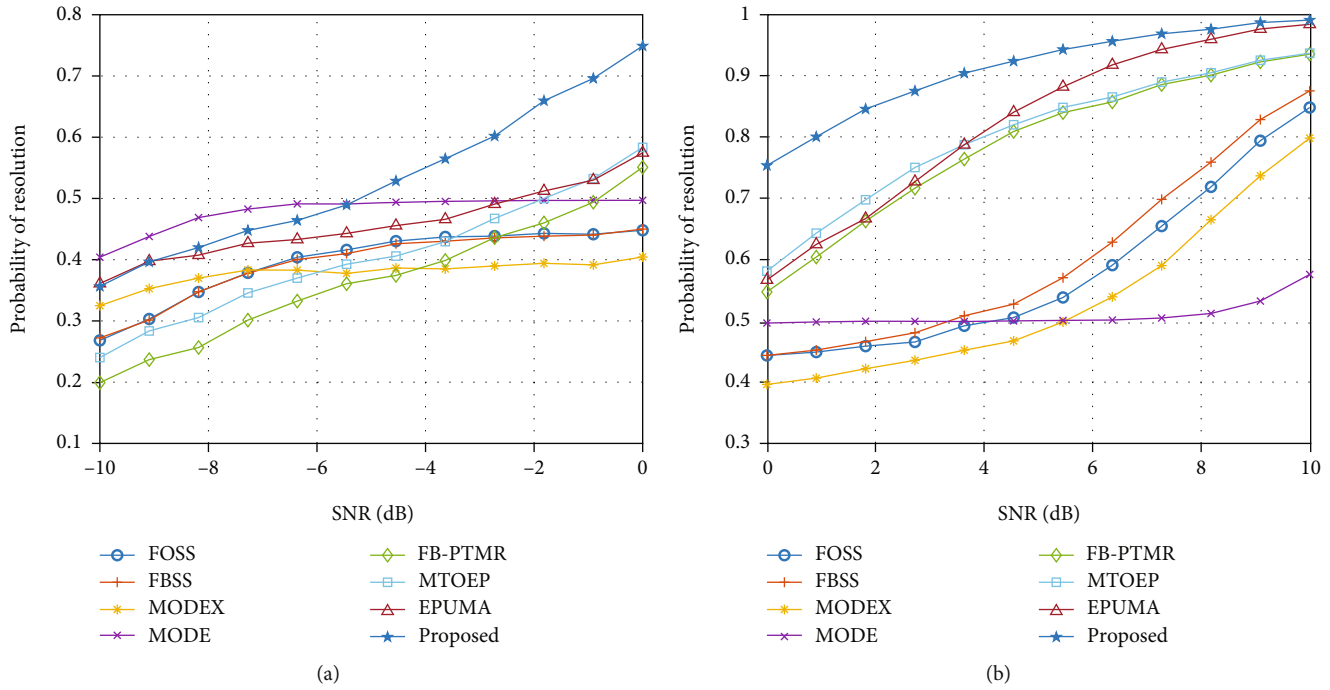

Figure 4: Algorithm probability versus *SNR* for two coherent signals and two uncorrelated signals with DOAs being [−5°, 0°, 25°, 31°] when $N = 100$. (a) *SNR* increased from −10 dB to 0 dB; (b) *SNR* increased from 0 dB to 10 dB.

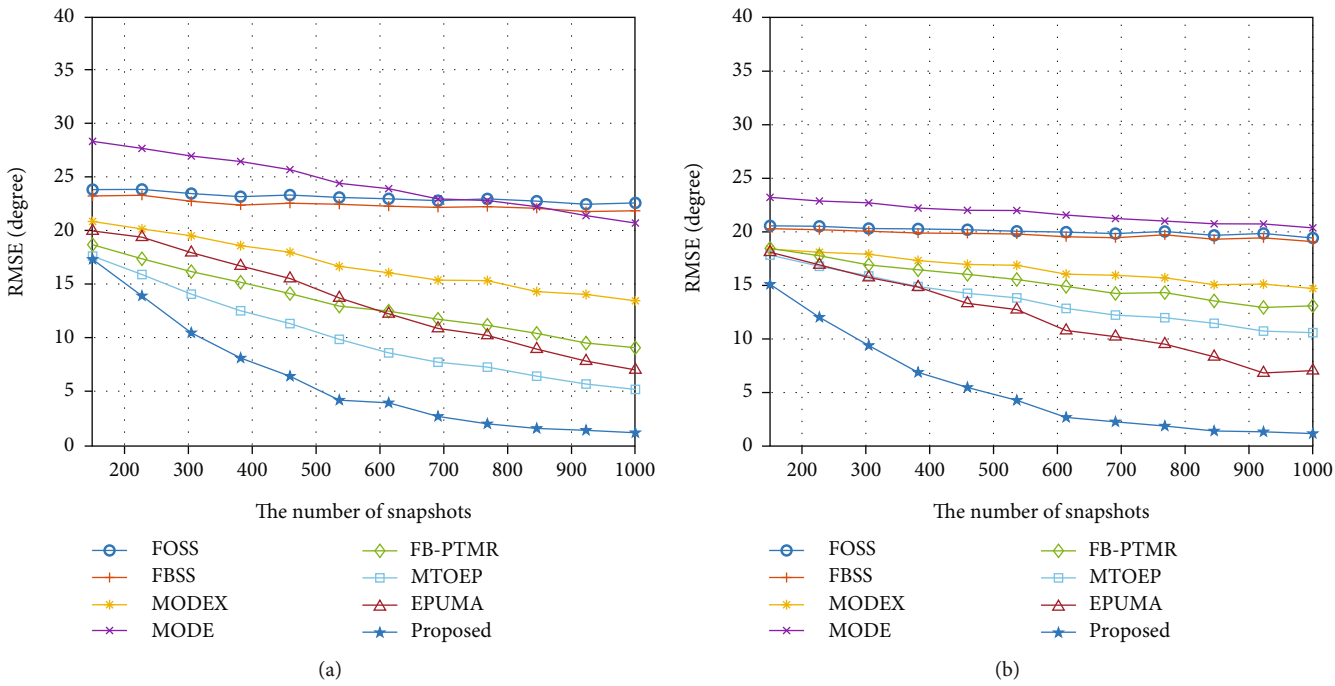

Figure 5: Algorithm RMSE versus snapshot number when $SNR = -5$ dB. (a) Two coherent signals and one uncorrelated signals with DOAs being [−5°, 0°, 25°]; (b) two coherent signals and two uncorrelated signals with DOAs being [−5°, 0°, 25°, 31°].

CRB when $SNR = 5$ dB. Meanwhile, due to the lack of array aperture, although ESPRIT optimized by FOSS and FBSS can process coherent signals, the RMSE of the optimized ESPRIT does not completely converge to the CRB until *SNR* = 10 dB. The performance is the best when using EPUMA and MODEX on $SNR > 6$ dB, MODE always has a large distance from the CRB, and its ability to process coherent signals is poor.

To further verify the performance of the proposed algorithm, an uncorrelated signal ($K = 4$) is added. Figure 2

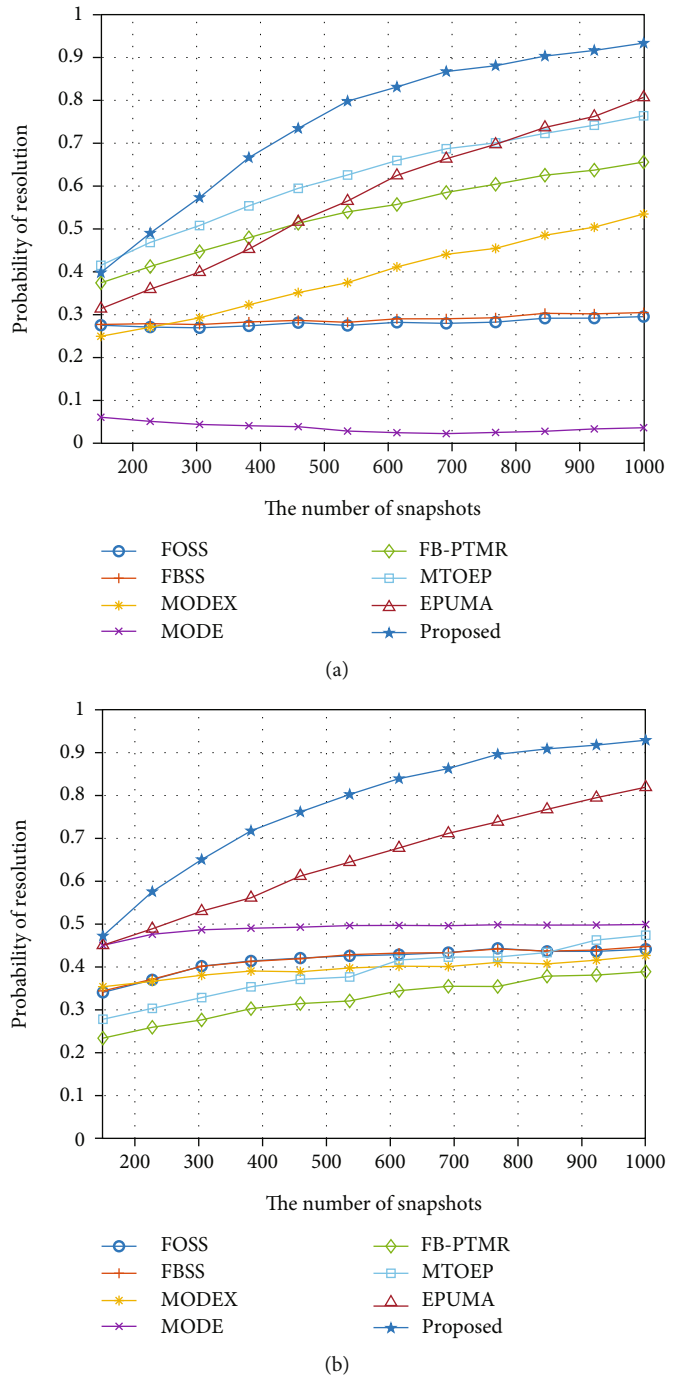

Figure 6: Algorithm probability versus snapshot number when $SNR = -5$ dB. (a) Two coherent signals and one uncorrelated signals with DOAs being $[-5^\circ, 0^\circ, 25^\circ]$; (b) two coherent signals and two uncorrelated signals with DOAs being $[-5^\circ, 0^\circ, 25^\circ, 31^\circ]$.

shows that, similar to $K = 3$, when $SNR < 0$ dB, the RMSE of all algorithms is large and far from the CRB. The RMSE of the proposed algorithm is smaller than that of other algorithms. When $SNR = 6$ dB and $SNR > 8$ dB, the proposed algorithm and EPUMA converge to the CRB, respectively. FB-PTMR and MTOEP still have a gap with the CRB even when $SNR = 10$ dB. Compared with $K = 3$, when $K = 4$, only the proposed algorithm is unaffected by the number of signals, whereas the other algorithms are affected by the number of signals, among which MODEX is the most affected.

The influence of SNR on algorithm resolution is shown in Figures 3 and 4. When $K = 3$, $SNR<0$ dB, the resolution of FB-PTMR, MTOEP, and the proposed algorithm is lower than 80%, whereas other algorithms are lower than 50%. With the increase in SNR, the resolution of all algorithms increases rapidly. Except for MODE, when $SNR = 10$ dB, the performance reached or exceeded 90%. When $K = 4$, $SNR < 0$ dB, the resolution of the proposed algorithm is much higher than that of the other algorithms but lower than 80%. When $SNR = 10$ dB, only the resolution of EPUMA,

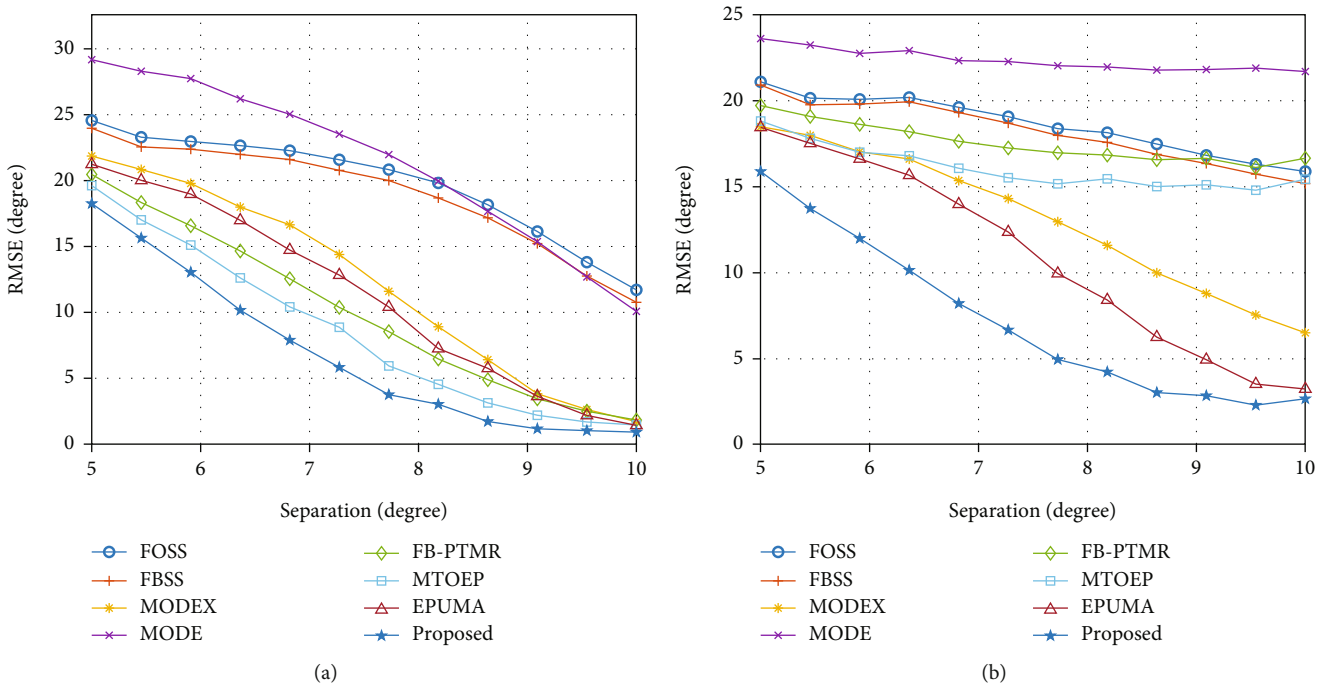

Figure 7: Algorithm RMSE versus $\Delta\theta$ when $SNR = -5$ dB. (a) Two coherent signals and one uncorrelated signal with DOAs being $[-5^\circ, 0^\circ + \Delta\theta, 25^\circ]$; (b) two coherent signals and two uncorrelated signals with DOAs being $[-5^\circ, 0^\circ + \Delta\theta, 25^\circ, 31^\circ]$.

MTOEP, FB-PTMR, and the proposed algorithm reaches or even exceeds 90%, whereas that of the other algorithms is lower than 90%.

This group of experiments verifies that the proposed algorithm has good anti-interference ability and can still effectively process coherent signals when facing multiple signals and different *SNR*, with small error and high resolution, which is unavailable in other algorithms. Under certain conditions, the resolution of the proposed algorithm even reaches 95%, whereas that of other algorithms is greatly affected by the number of signals. In addition, the error increases evidently, and the resolution decreases when processing multiple signals. Furthermore, this group of experiments show the advantage of the proposed algorithm in processing coherent signals at low *SNR*, and the next experiments will further study the ability of the proposed algorithm to handle coherent signals in different situations when $SNR = -5$ dB.

In the second experiment, we study the effect of different snapshot numbers on the RMSE and resolution of the algorithm. The experimental conditions are the same as the first experiment. Figure 5 shows that the performance of the proposed algorithm is better than that of the other algorithms. When $K = 3$, with the increase in snapshot number, the proposed algorithm converges rapidly, and RMSE decreases. Although the RMSE of MODEX, FB-PTMR, MTOEP, and EPUMA is also reduced, it is not as good as the proposed algorithm. However, FOSS, FBSS, and MODE almost remain unchanged, and their errors are much higher than those of the other algorithms, even if the snapshot number is 1000. When $K = 4$, the proposed algorithm still has better processing ability and is unaffected by the number of signals. EPUMA is less affected by the number of affected signals, and RMSE is basically unchanged, but not as good as the proposed algorithm. However, the other algorithms are greatly affected by the number of signals, and the RMSE increases.

Figure 6 shows that when $K = 3$, the resolution of EPUMA and MTOEP can be close to or reaches 80%, whereas when $K = 4$, the resolution of MTOEP decreases seriously and is lower than 50%. Other algorithms have low resolution in any case, but the proposed algorithm can still have a resolution higher than 90% under any condition.

Therefore, compared with other algorithms, the proposed algorithm can effectively use snapshot to detect signal information, and the estimation accuracy is high. It can process multiple signals with a high resolution of more than 90%, whereas other algorithms are inferior to the proposed algorithm with a low resolution.

In the third experiment, we study the effect of different angular separation on the RMSE and resolution of the algorithm. The parameters remained the same as in the first experiment. In Figure 7, when $K = 3$ and separation is 9, the MTOEP and the proposed algorithm reach the optimal state. In addition, the other algorithms are not at their best even when the separation is 10. When $K = 4$, only EPUMA and the proposed algorithm are less affected by the number of signals, with RMSE decreasing significantly as separation increases, whereas the RMSE of the other algorithms decreases but not as much as EPUMA and the proposed algorithm.

As in the previous experiment, we also tested the angular separation impact on algorithm resolution. As shown in Figure 8, when $K = 3$, the resolution of EPUMA and the

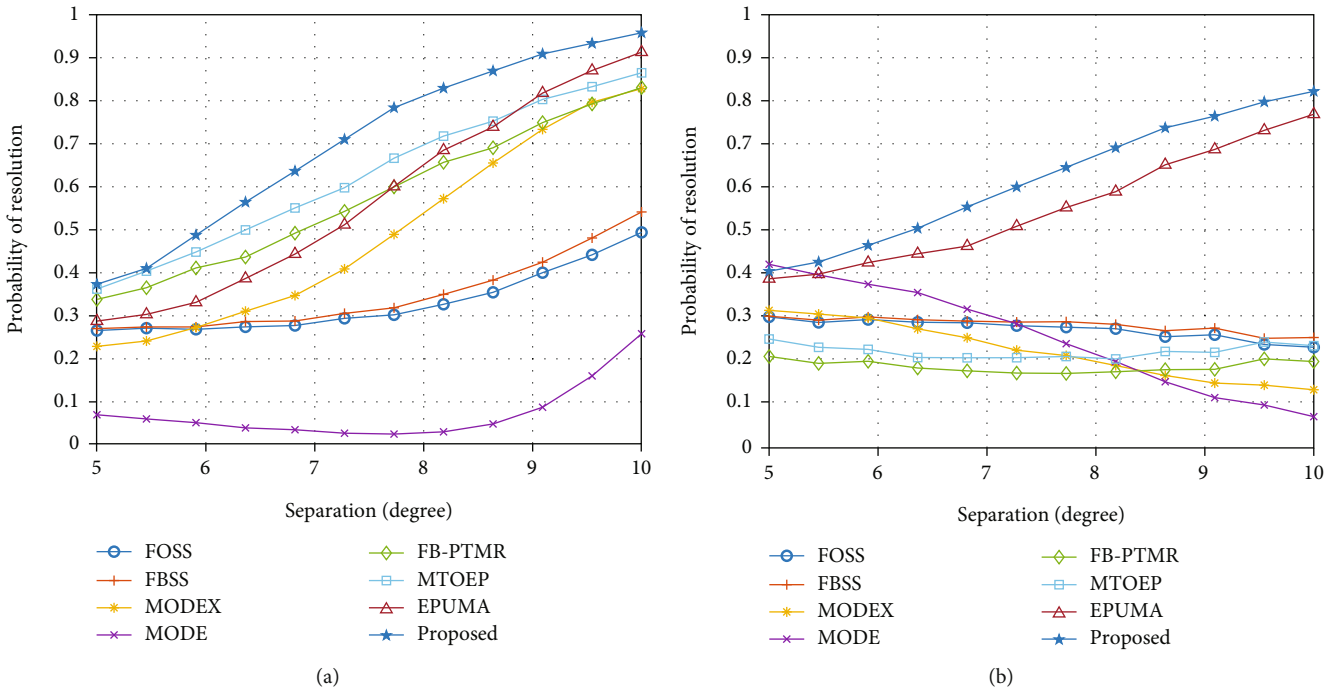

FIGURE 8: Algorithm probability versus $\Delta\theta$ when $SNR = -5$ dB. (a) Two coherent signals and one uncorrelated signals with DOAs being $[-5^\circ, 0^\circ + \Delta\theta, 25^\circ]$; (b) two coherent signals and two uncorrelated signals with DOAs being $[-5^\circ, 0^\circ + \Delta\theta, 25^\circ, 31^\circ]$.

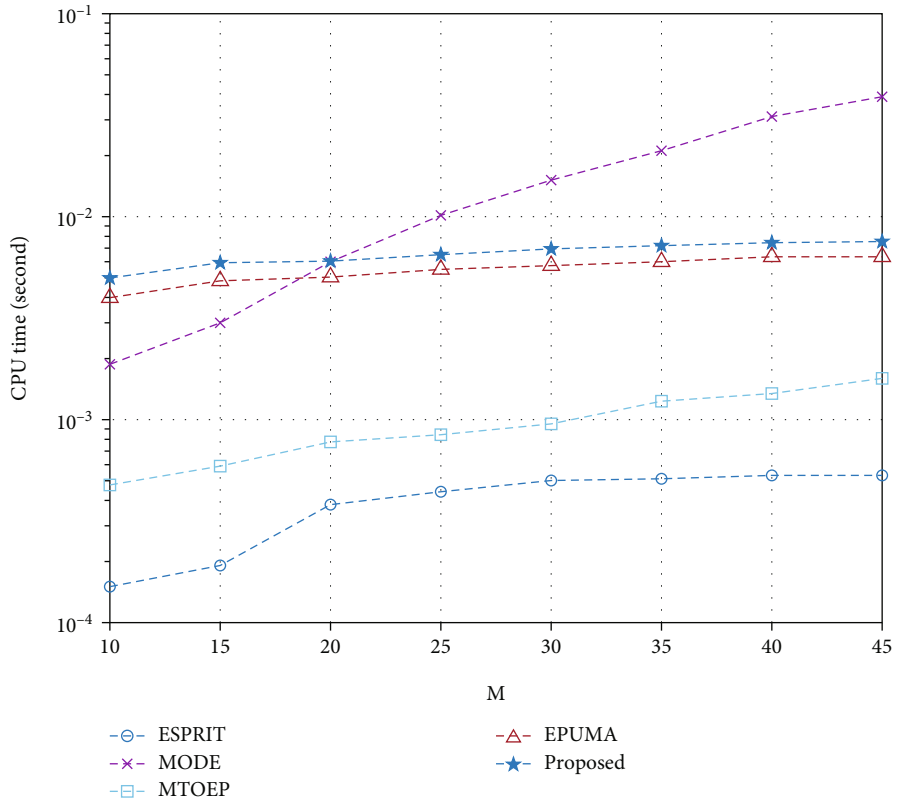

FIGURE 9: CPU time versus M when $K = 3$ and $N = 80$.

proposed algorithm reaches or even exceeds 90%. The resolution of MTOEP, FB-PTMR, and MODEX also exceeds 80%, and that of the remaining algorithms does not exceed 60%. When $K = 4$, the resolution of all algorithms decreases seriously. The performance of EPUMA and the proposed algorithm is reduced from 90% to about 80%,

whereas that of other algorithms is lower than or equal to 30%.

This set of experiments demonstrates that the proposed algorithm is relatively affected when dealing with angular separation variations of multiple coherent signals ($K = 4$), but the resolution is still higher than that of the other algorithms under the same conditions; the resolution of the algorithm reaches 80%. When the number of signals is small ($K = 3$), the resolution of the proposed algorithm can still exceed 90%. The performance of other algorithms is far inferior to that of the proposed algorithm.

Finally, because FB-PTMR, FBSS, and FOSS are all based on ESPRIT algorithm, MODEX complexity is extremely huge, so we compare the complexity of ESPRIT, MODE, MTOEP, EPUMA, and the proposed algorithm. We assume that three signals are available, N is 80, and we vary M from 10 to 45. Through calculation, we obtain that the complexity of ESPRIT, MODE, MTOEP, and EPUMA is $\mathcal{O}(M^2N + M^3)$, $\mathcal{O}((8K^3 + 1)(M - K)^3)$, $\mathcal{O}(4M^3 + (N + 1)M^2)$, and $\mathcal{O}(M^2N + GM^3)$, respectively. Figure 9 shows that ESPRIT has simple computational complexity, whereas the standard MODE is the most computationally intensive method among the six competitors. The computational complexity of the proposed algorithm and EPUMA is similar.

4. Conclusions

An efficient algorithm without auxiliary matrix and noise preprocessing is proposed by combining the advantages of polynomial solving DOA signal and Toeplitz matrix reconstruction. In the face of multiple signals, the performance of other reference algorithms has been greatly affected, whereas the proposed algorithm still has high estimation accuracy. Simulation experiments show that the proposed algorithm has the advantage of processing multiple signals containing coherent signals, and it is less affected by *SNR* and snapshot number, which is an advantage that other reference algorithms do not have. Under certain conditions, the resolution can reach 90% and sometimes exceed 95%. Although the proposed algorithm has many advantages, when angular separation changes and with multiple signals ($K = 4$), the proposed algorithm is affected to some extent, and the resolution is only 80%. However, when $K = 3$, the resolution immediately increases to 95%. In addition, the proposed algorithm has low complexity. This paper provides a signal location method with high estimation accuracy, strong anti-interference ability, and effective processing of multiple signals.

Data Availability

Data are only available upon request due to restrictions regarding, e.g., privacy and ethics. The data presented in this study are available from the corresponding author upon request. The data are not publicly available due to their relation to other ongoing research.

Conflicts of Interest

The authors declare no conflict of interest.

Acknowledgments

This work was supported by the National Natural Science Foundation of China (No. 61763018), the Central Guided Local Science and Technology Funding Project of the Science and Technology Department of Jiangxi Province (Cross-regional Cooperation, 20221ZDH04052), the 03 Special Project and 5G Program of the Science and Technology Department of Jiangxi Province (No. 20193ABC03A058), the China Scholarship Council (CSC, No. 201708360150), the Key Foundation of Education Committee of Jiangxi (Nos. GJJ170493 and GJJ190451), the Program of Qingjiang Excellent Young Talents in Jiangxi University of Science and Technology (JXUSTQJBJ2019004), and the Cultivation Project of the State Key Laboratory of Green Development and High-Value Utilization of Ionic Rare-Earth Resources in Jiangxi Province (20194AFD44003), the Key Research and Development Plan of Ganzhou (industrial field), and the Science and Technology Innovation Talent Project of Ganzhou.

References

[1] A. Norrdine, H. Cetinkaya, and R. Herschel, "Radar wave based positioning of spatially distributed MIMO radar antenna systems for near-field nondestructive testing," *IEEE Sensors Letters*, vol. 4, no. 5, pp. 1–4, 2020.

[2] S. G. Dontamsetti and R. V. R. Kumar, "A distributed MIMO radar with joint optimal transmit and receive signal combining," *IEEE Transactions on Aerospace and Electronic Systems*, vol. 57, no. 1, pp. 623–635, 2021.

[3] X.-h. Sheng and H. Yu-Hen, "Maximum likelihood multiple-source localization using acoustic energy measurements with wireless sensor networks," *IEEE Transactions on Signal Processing*, vol. 53, no. 1, pp. 44–53, 2005.

[4] I. Bekkerman and J. Tabrikian, "Target detection and localization using MIMO radars and sonars," *IEEE Transactions on Signal Processing*, vol. 54, no. 10, pp. 3873–3883, 2006.

[5] X. Chao, C. Fan, and X. Huang, "Time reversal linearly constrained minimum power algorithm for direction of arrival estimation in diffuse multipath environments," *Remote Sensing*, vol. 12, no. 20, p. 3344, 2020.

[6] J. W. Paik, W. Hong, and J.-H. Lee, "Direction-of-Departure and direction-of-arrival estimation algorithm based on compressive sensing: data fitting," *Remote Sensing*, vol. 12, no. 17, p. 2773, 2020.

[7] Y. Quan, R. Zhang, Y. Li, R. Xu, S. Zhu, and M. Xing, "Microwave correlation forward-looking super-resolution imaging based on compressed sensing," *IEEE Transactions on Geoscience and Remote Sensing*, vol. 59, no. 10, pp. 8326–8337, 2021.

[8] H. Zhang, J. Shi, Q. Zhang, B. Zong, and J. Xie, "Antenna selection for target tracking in collocated MIMO radar," *IEEE Transactions on Aerospace and Electronic Systems*, vol. 57, no. 1, pp. 423–436, 2021.

[9] Y. Qian, Z. Yang, and H. Zeng, "Direct position determination for augmented coprime arrays via weighted subspace data fusion method," *Mathematical Problems in Engineering*, vol. 2021, Article ID 2825025, 10 pages, 2021.

[10] K. N. R. S. V. Prasad, E. Hossain, and V. K. Bhargava, "Energy efficiency in massive MIMO-based 5G networks: opportunities and challenges," *IEEE Wireless Communications*, vol. 24, no. 3, pp. 86–94, 2017.

[11] L. Liu and H. Liu, "Joint estimation of DOA and TDOA of multiple reflections in mobile communications," *IEEE Access*, vol. 4, pp. 3815–3823, 2016.

[12] R. Shafin, L. Liu, J. Zhang, and Y. C. Wu, "DoA estimation and capacity analysis for 3-D millimeter wave massive-MIMO/FD-MIMO OFDM systems," *IEEE Transactions on Wireless Communications*, vol. 15, no. 10, pp. 6963–6978, 2016.

[13] R. Schmidt, "Multiple emitter location and signal parameter estimation," *IEEE Transactions on Antennas and Propagation*, vol. 34, no. 3, pp. 276–280, 1986.

[14] T. Kailath, "ESPRIT–estimation of signal parameters via rotational invariance techniques," *Optical Engineering*, vol. 29, no. 4, p. 296, 1990.

[15] B.-s. Kim, Y. Jin, J. Lee, and S. Kim, "Low-complexity MUSIC-based direction-of-arrival detection algorithm for frequency-modulated continuous-wave vital radar," *Sensors*, vol. 20, no. 15, p. 4295, 2020.

[16] E. D. D. Claudio, R. Parisi, G. Jacovitti, and G. Jacovitti, "Space time MUSIC: consistent signal subspace estimation for wide-band sensor arrays," *IEEE Transactions on Signal Processing*, vol. 66, no. 10, pp. 2685–2699, 2018.

[17] M. Wagner, Y. Park, and P. Gerstoft, "Gridless DOA estimation and root-MUSIC for non-uniform linear arrays," *IEEE Transactions on Signal Processing*, vol. 69, pp. 2144–2157, 2021.

[18] T. T. Zhang, H. T. Hui, and Y. Lu, "Compensation for the mutual coupling effect in the ESPRIT direction finding algorithm by using a more effective method," *IEEE Transactions on Antennas and Propagation*, vol. 53, no. 4, pp. 1552–1555, 2005.

[19] J. Steinwandt, F. Roemer, and M. Haardt, "Generalized least squares for ESPRIT-type direction of arrival estimation," *IEEE Signal Processing Letters*, vol. 24, no. 11, pp. 1681–1685, 2017.

[20] J. Pan, M. Sun, Y. Wang, and X. Zhang, "An enhanced spatial smoothing technique with ESPRIT algorithm for direction of arrival estimation in coherent scenarios," *IEEE Transactions on Signal Processing*, vol. 68, pp. 3635–3643, 2020.

[21] T. J. Shan, M. Wax, and T. Kailath, "On spatial smoothing for direction-of-arrival estimation of coherent signals," *IEEE Transactions on Acoustics, Speech, and Signal Processing*, vol. 33, no. 4, pp. 806–811, 1985.

[22] S. Pillai and B. Kwon, "Forward/backward spatial smoothing techniques for coherent signal identification," *IEEE Transactions on Acoustics, Speech, and Signal Processing*, vol. 37, no. 1, pp. 8–15, 1989.

[23] M. Viberg and B. Ottersten, "Sensor array processing based on subspace fitting," *IEEE Transactions on Signal Processing*, vol. 39, no. 5, pp. 1110–1121, 1991.

[24] P. Stoica, B. Ottersten, M. Viberg, and R. Moses, "Maximum likelihood array processing for stochastic coherent sources," *IEEE Transactions on Signal Processing*, vol. 44, no. 1, pp. 96–105, 1996.

[25] J. Sheinvald, M. Wax, and A. J. Weiss, "On maximum-likelihood localization of coherent signals," *IEEE Transactions on Signal Processing*, vol. 44, no. 10, pp. 2475–2482, 1996.

[26] Y. H. Choi, "Maximum likelihood estimation for angles of arrival of coherent signals using a coherency profile," *IEEE Transactions on Signal Processing*, vol. 48, no. 9, pp. 2679–2682, 2000.

[27] A. B. Gershman and P. Stoica, "New MODE-based techniques for direction finding with an improved threshold performance," *Signal Processing*, vol. 76, no. 3, pp. 221–235, 1999.

[28] P. Stoica and K. Sharman, "Novel eigenanalysis method for direction estimation," *IEE Proceedings F Radar and Signal Processing*, vol. 137, no. 1, pp. 19–26, 1990.

[29] C. Qian, L. Huang, N. D. Sidiropoulos, and H. C. So, "Enhanced PUMA for direction-of-arrival estimation and its performance analysis," *IEEE Transactions on Signal Processing*, vol. 64, no. 16, pp. 4127–4137, 2016.

[30] P. Stoica and M. Jansson, "On forward–backward MODE for array signal processing," *Digital Signal Processing*, vol. 7, no. 4, pp. 239–252, 1997.

[31] A. Gershman and P. Stoica, "MODE with extra-roots (MODEX): a new DOA estimation algorithm with an improved threshold performance," in *1999 IEEE International Conference on Acoustics, Speech, and Signal Processing. Proceedings. ICASSP99 (Cat. No.99CH36258)*, vol. 5, pp. 2833–2836, Phoenix, AZ, USA, 1999.

[32] F. Wen and H. C. So, "Tensor-MODE for multi-dimensional harmonic retrieval with coherent sources," *Signal Processing*, vol. 108, pp. 530–534, 2015.

[33] C. Qian, L. Huang, M. Cao, J. Xie, and H. C. So, "PUMA: an improved realization of MODE for DOA estimation," *IEEE Transactions on Aerospace and Electronic Systems*, vol. 53, no. 5, pp. 2128–2139, 2017.

[34] S. Liu, Z. Mao, Y. D. Zhang, and Y. Huang, "Rank minimization-based Toeplitz reconstruction for DoA estimation using coprime array," *IEEE Communications Letters*, vol. 25, no. 7, pp. 2265–2269, 2021.

[35] W. Zhang, Y. Han, M. Jin, and X. S. Li, "An improved ESPRIT-like algorithm for coherent signals DOA estimation," *IEEE Communications Letters*, vol. 24, no. 2, pp. 339–343, 2020.

[36] C. Qian, L. Huang, W. J. Zeng, and H. C. So, "Direction-of-arrival estimation for coherent signals without knowledge of source number," *IEEE Sensors Journal*, vol. 14, no. 9, pp. 3267–3273, 2014.

[37] Y. Zhang, S. Liu, Z. Mao, and Y. Huang, "DoA estimation based on accelerated structured alternating projection using coprime array," in *Seventh Asia Pacific Conference on Optics Manufacture (APCOM 2021)*, pp. 1–9, Hong Kong, 2021.

[38] J. Dai and H. C. So, "Real-valued sparse Bayesian learning for DOA estimation with arbitrary linear arrays," *IEEE Transactions on Signal Processing*, vol. 69, pp. 4977–4990, 2021.

[39] B. Cai, Y.-M. Li, and H. Y. Wang, "Forward/backward spatial reconstruction method for directions of arrival estimation of uncorrelated and coherent signals," *IET Microwaves, Antennas and Propagation*, vol. 6, no. 13, pp. 1498–1505, 2012.

[40] W. Zhang, Y. Han, M. Jin, and X. Qiao, "Multiple-Toeplitz matrices reconstruction algorithm for DOA estimation of coherent signals," *IEEE Access*, vol. 7, pp. 49504–49512, 2019.

[41] Y. Chan, J. Lavoie, and J. Plant, "A parameter estimation approach to estimation of frequencies of sinusoids," *IEEE Transactions on Acoustics, Speech, and Signal Processing*, vol. 29, no. 2, pp. 214–219, 1981.

[42] E. GrosicKi, K. Abed-Meraim, and Y. Hua, "A weighted linear prediction method for near-field source localization," *IEEE Transactions on Signal Processing*, vol. 53, no. 10, pp. 3651–3660, 2005.

Hindawi
Wireless Communications and Mobile Computing
Volume 2022, Article ID 8367107, 7 pages
https://doi.org/10.1155/2022/8367107

WILEY | Hindawi

Research Article

Secrecy Performance by Power Splitting in Cooperative Dual-Hop Relay Wireless Energy Harvesting

Nabila Sehito,[1] Shouyi Yang,[1] Abdullh G. Al Harbi,[2] Muhammad Inam Abbasi,[3] Muhammad Abbas Khan,[4] Muhammad Amir Khan,[5] and Mian Muhammad Kamal[1]

[1]*School of Information Engineering, Zhengzhou University, 100, Science Avenue Zhengzhou 450001, China*
[2]*Department of Electrical Engineering, Faculty of Engineering, Jouf University, Sakaka 42421, Saudi Arabia*
[3]*Centre for Telecommunication Research & Innovation (CETRI), Faculty of Electrical and Electronic Engineering Technology (FTKEE), Universiti Teknikal Malaysia Melaka (UTeM), Melaka 76100, Malaysia*
[4]*Department of Electrical Engineering, Balochistan University of Information Technology, Engineering and Management Sciences, Quetta, Pakistan*
[5]*Department of Computer Science, COMSATS University Islamabad Abbottabad Campus, 22060, Pakistan*

Correspondence should be addressed to Shouyi Yang; nabila@gs.zzu.edu.cn
and Muhammad Inam Abbasi; muhammad_inamabbasi@yahoo.com

Received 17 February 2022; Accepted 22 April 2022; Published 14 May 2022

Academic Editor: Abdul Basit

In wireless communication systems, for secure communication between a transmitter and receiver over the communication channel, the physical layer security is widely utilized. The paper presents a dual-hop wireless full-duplex relay (FDR) network with a source relay and destination relay between two nodes and listening devices. The relay and source use energy harvesting to gain energy from power beacon. Two cooperative techniques are utilized to investigate the amplify-forward (AF) and decode-forward (DF) secrecy capacity in the energy harvesting power splitting system. It is shown that the secrecy performance of an AF relay is better than the secrecy performance of a DF relay in the given form. At 40-meter distance between the relay and the eavesdropper in an energy harvesting system, the AF relay outperforms the DF relay. The simulation is performed using the Monte-Carlo method in MATLAB.

1. Introduction

Cooperative techniques (AF and DF) are significant techniques in wireless communication which play a vital role in wireless networks utilized widely in different branches and applications, including green monitoring systems, social networks, Internet of Things (IoT), and banking systems [1–4]. Thus, the physical layer security of cooperative relaying systems has recently become a major research scope of direction. Significant amount of work has been done in physical layer security to improve secure communication and reduce limitations in cooperative relay networks at both indoor and outdoor propagating environments [5–9].

In [5], a radio signal transmission was secured using an optimum design model from source node to destination through the DF network. In [6], a new two-phase protocol was presented for efficient energy transfer and information relaying, in which the relay operates in full-duplex mode with simultaneous energy harvesting. Ref [7] presents cooperative schemes in dual-hop relaying systems with EH over indoor communication channels categorized by log-normal fading. Similarly, in [8], the cooperative systems are considered with joint time allocation and power splitting schemes.

In addition to enhancing spectrum efficiency, wireless nodes also have major issues in cooperative wireless networks, particularly in energy considerations. In [10], the authors investigated EH to improve the system performance and secrecy rate in a jamming system but did not show the full power of the EH system. In [11], the

Table 1: Paper layout.

Section I	Section II
1. Introduction 1.1. Paper organization	2. System model 2.1 Energy harvesting technique 2.1.1. Decode-forward relay scheme 2.1.2 Amplify-forward relay scheme
Section III	Section IV
3. Secrecy capacity performance 3.1. DF scheme 3.2. AF scheme	4. Simulation results and performance
Section V	
5. Conclusions	

performance and the secrecy rate for both TS and PS protocols were investigated, while [12] investigated the outage probability (OP) over the Rayleigh channel for DF and AF schemes in multiple antennas, respectively. Nevertheless, the EH from the interference node is not considered, and no interference is used, such that only EH from the source is analyzed [13, 14].

In [15], a secrecy performance is investigated comprising a single-hop relay system with improvement of EH of 8.89% for the AF relay and of 9.83% for the DF relay between the eavesdropper and the relay. Ref [16] investigated the secrecy performance of a single-hop relay network and observed a performance improvement of 30.47% for the DF cooperative scheme and of 23.63% for the AF cooperative scheme between the eavesdropper and the relay. A geometric programmed (GP) method in [17] was implemented on a full duplex relay network for physical secrecy in a dual-hop relay system. The GP program was applied to power allocation problem on the transmitter side. In [18], the secrecy rate performance of nonorthogonal multiple access and backscatter communication is considered. In [19], they investigated physical layer security ambient backscatter nonorthogonal multiple access in channel estimation errors and imperfect successive interference cancellation with emphasis on reliability and security. The authors in [20] investigated three hop relay cooperative communication networks to perform the two schemes AF and DF, improved by 50.55% (AF) and by 44.2% (DF).

In the current study, we have investigated a dual-hop relay cooperative network with a source, relay, eavesdropper, and EH scheme. The goal of this research is to increase the security performance of such a system, using cooperative scheme AF and DF techniques. We have examined the secrecy performance of our proposed model. The contribution of the present work is summarized as follows.

(i) First, we have investigated a dual-hop wireless relay system containing a single source and a single destination relay, along with two nodes and one eavesdropper

(ii) To propose AF and DF schemes and increase the system secrecy performance in the cooperative network

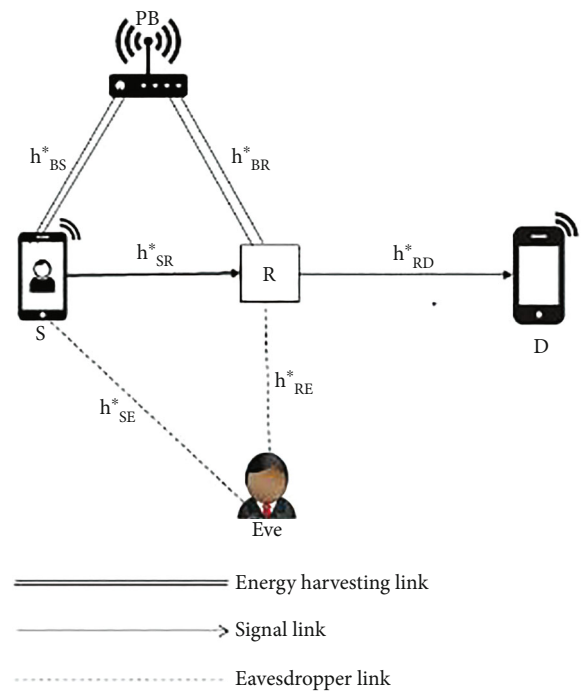

Figure 1: Dual-hop relay network.

(iii) Various parameters, like the time switching protocol, energy harvesting, power splitting ratio, interference relay, and eavesdropper distance, are investigated. The secrecy performance of designed schemes is discussed and compared to the secrecy performance in previous publications

1.1. Paper Organization. The layout of the paper is shown in Table 1.

2. System Model

In this section, we consider a network that relies on a single hop and consists of a relay node (R), source (S), eavesdropper (E), and destination node (D) as presented in Figure 1. It contains power from a beacon (P_B). In Figure 1, $h*_{SR}$, $h*_{RD}$, $h*_{RE}$, and $h*_{SE}$ define the complicated channel gain from P_B to S, while $h*_{BS}$ and $h*_{BR}$ define the

complex channel gain from P_B to R. Additionally, we note that noise is complex. Additive white Gaussian noise (AWGN) at each node has zero mean and variance σ^2 such that no interference is available. Additionally, the relay function is performed with mutual full-duplex relay and half-duplex relay mode techniques.

2.1. Energy Harvesting Technique. In the designed technique, the nodes relay (R) and source (S) harvest energy from the power beacon (P_B). That energy is used to transmit the signals from source S to R and R to D. For high quantities, the time switching- (TS-) based protocol is used for energy harvesting as shown in Figure 2.

The energy harvesting by S and R is given by [17]

$$\begin{aligned} \mathbf{E_S} &= \boldsymbol{\eta}\,\boldsymbol{\alpha}\,\mathbf{P_B}|\mathbf{h}_{\mathbf{BS}}^*|^2\frac{\mathbf{T}}{\mathbf{2}}, \\ \mathbf{E_R} &= \boldsymbol{\eta}\,\boldsymbol{\alpha}\,\mathbf{P_B}|\mathbf{h}_{\mathbf{BR}}^*|^2\frac{\mathbf{T}}{\mathbf{2}}. \end{aligned} \tag{1}$$

The competence coefficient of the proposed method is denoted by $\eta\,(0<\eta<1)$, and the power transmitted by B is denoted by P_B and $0<\alpha<1$. T represents the time taken to transmit the specific block by S and R [17]. Thus, the power transferred by R and S is given by

$$\begin{aligned} P_S &= \eta\,\alpha P_B|h_{BS}^*|^2(1-\alpha), \\ P_R &= \eta\,\alpha P_B|h_{BR}^*|^2(1-\alpha). \end{aligned} \tag{2}$$

2.1.1. Decode-Forward Relay Scheme. This scheme consists of two phases, the first of which is shown in Figure 3. During the initial transmission, the source sends a signal $X(n)$ to the relay and the relay sends the jamming signal $q(2n)$ to the eavesdropper at the same time. In time slot $2n$, the established signal at the R and E is given by [17]

$$Y_R(2n) = \sqrt{\rho P_S}h_{SR}^*x(n) + n_R(2n), \tag{3}$$

$$Y_E(2n) = \sqrt{\rho P_S}h_{SE}^*x(n) + \sqrt{\rho P_{RJ}}h_{RE}^*x(n) + n_E(2n), \tag{4}$$

where the strength of the interference signal from R is given by $n_R(2n)$. In the next time slot, as presented in Figure 4, the R simply sends the already decoded signal to a valid junction and no longer receives the signal. The source at this point sends the jamming signal to the eavesdropper E, and the signal established in time slots $(2n+1)$ at R and D is expressed as [17]

$$Y_R(2n+1) = \sqrt{\rho P_R}h_{RE}^*x(n) + \sqrt{\rho P_{SJ}}h_{SE}^*\,qx(n+1) + n_E(2n), \tag{5}$$

$$Y_D(2n+1) = \sqrt{\rho P_R}h_{RD}^*x(n) + n_D(2n+1). \tag{6}$$

2.1.2. Amplify-Forward Relay Scheme. This scenario part has two phases; further, in the first phase, it is the DF scheme. During the initial stages, the signal acquired at R and the eavesdropper E is applied; relay transmits enhanced performance of signals received at the destination in the second phase. The source sends jamming signals to D and E, in the time slot $(2n+1)$, which are received at the same time, given

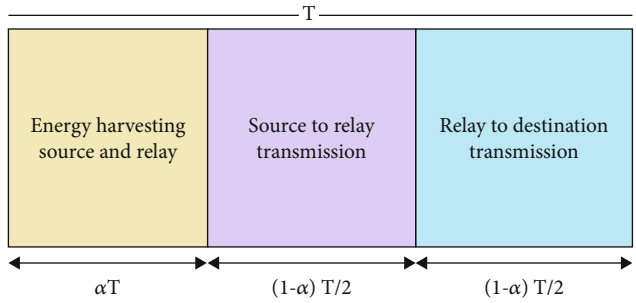

Figure 2: Time switching-based protocol.

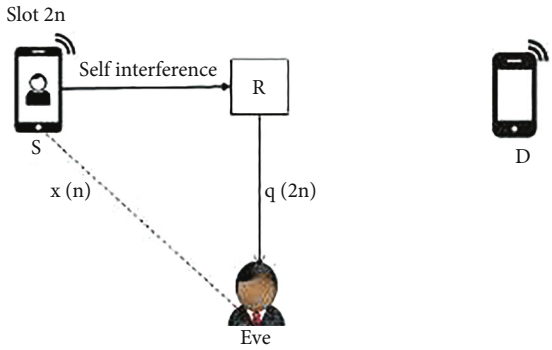

Figure 3: Illustration of the signal transmission for the $2n$ time slot.

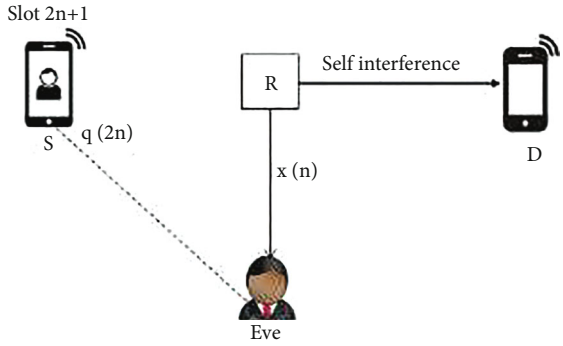

Figure 4: Illustration of the signal transmission in the $(2n+1)$ time slot.

$$Y_D(2n+1) = G\sqrt{\rho P_S}h_{RD}^*Y_R(2n) + n_D(2n+1), \tag{7}$$

$$Y_E(2n+1) = G\sqrt{\rho P_{SJ}}h_{SE}^*\,qx(2n+1) + n_E(2n+1). \tag{8}$$

Here, we defined the scaling factor G. The fluctuation of the channel coefficient is

$$G = \frac{1}{\sqrt{P_{R_1}|h_{SR1}|^2+N_0}}, \tag{9}$$

where N_0 is the AWGN noise variance.

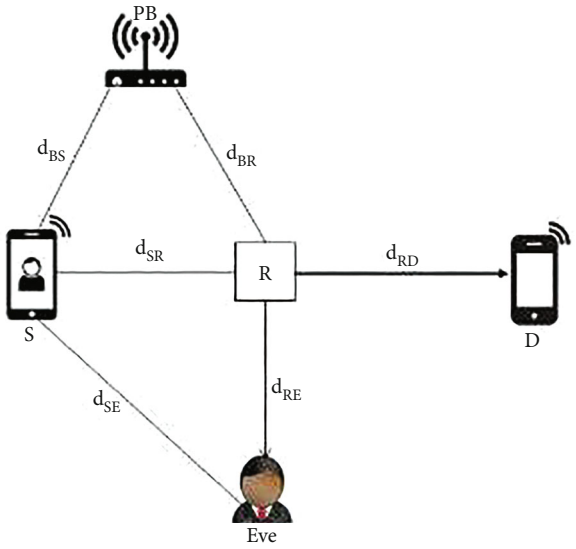

Figure 5: Numerical model.

Table 2: Parameter used for the simulation.

Parameter	Single-relay network
D_{SR}	25 m
D_{RE}	30 m
D_{RD}	15 m
D_{RB}	14 m
RNT	Line of sight (LOS)
PLE	3.5
Number of relay	1
Communicate energy	30 dBm
Make noise power	-40 dBm
α	0.999
ρ	3.5

3. Secrecy Capacity Performance

Further, we present a performance secrecy model in terms of secrecy rate. The signal information that may be transferred over a wireless channel to an eavesdropper is defined as the secrecy rate. The next two sections investigate the secrecy rate in AF and DF cooperative networks.

3.1. DF Scheme. The secrecy capacity at D and E is defined by equations (3)–(6) for a full-duplex relay in [17]. Thus, we obtain

$$R_d = \frac{1}{2}\log_2(1+\rho P_R \alpha_{RD}), \tag{10}$$

$$R_e = \frac{1}{2}\log_2\left(1+\frac{P_S\alpha_{SE}}{1+P_{RJ}\alpha_{RE}}+\frac{\rho P_R\alpha_{RE}}{1+\rho P_{RJ}\alpha_{SE}}\right). \tag{11}$$

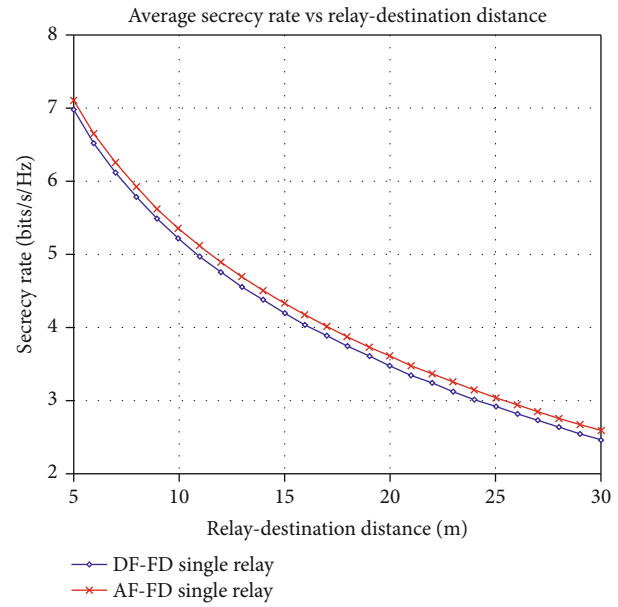

Figure 6: Secrecy rate vs. d_{RD} for the EH system.

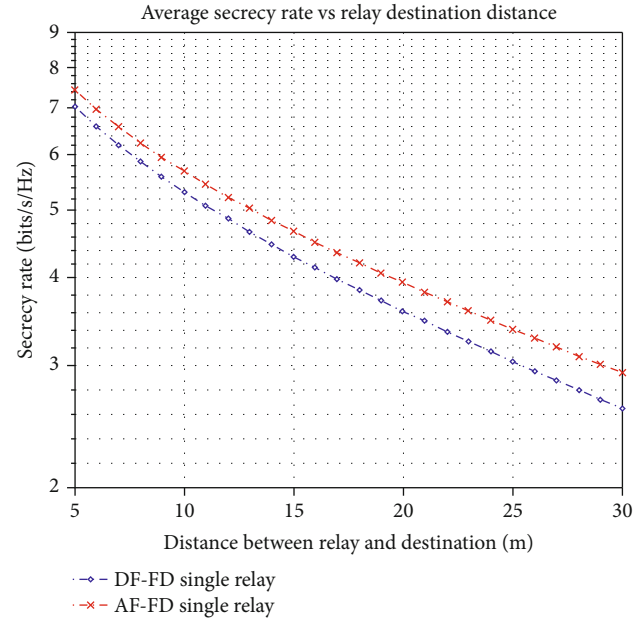

Figure 7: Secrecy rate vs. D_{RD} for the proposed EH and PS system.

Here, we define

$$\alpha_{RD} = \frac{|h_{RD}|^2}{\sigma^2}, \alpha_{SE} = \frac{|H_{SE}|^2}{\sigma^2}, \alpha_{RE} = \frac{|h_{RE}|^2}{\sigma^2}. \tag{12}$$

Using equations (6) and (7), the achievable secrecy rate is given by $R_S = \max\{R_d - R_e, 0\}$, where it is given in

$$R_d - R_e = \frac{1}{2}\log_2\left(\frac{1+\rho P_R\alpha_{RD}}{1+(\rho P_S\alpha_{SE}/(1+\rho P_R\alpha_{RE}))+(P_R\alpha_{RE}/(1+P_{SJ}\alpha_{SE}))}\right). \tag{13}$$

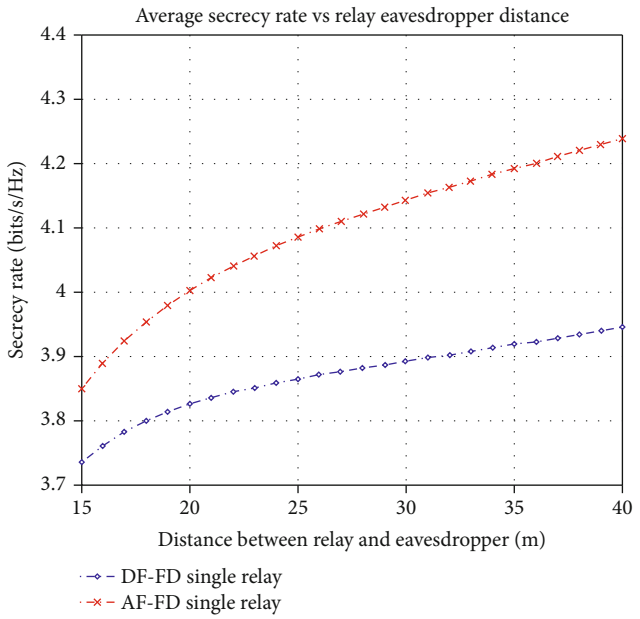

Figure 8: Secrecy rate vs. D_{RE} for the energy harvesting system.

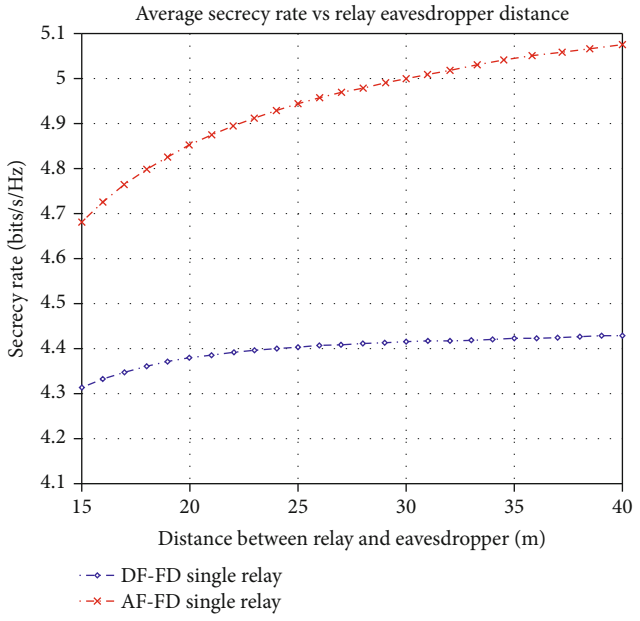

Figure 9: Secrecy rate vs. D_{RE} for the energy harvesting power splitting system.

3.2. AF Scheme. Using further equations (7) and (8) at D and E, the secrecy capacity rate can be obtained from

$$R_d = \frac{1}{2}\log_2\left(1 + G^2\rho P_S \alpha_{RD}\right), \tag{14}$$

$$R_e = \frac{1}{2}\log_2\left(\frac{1+\rho P_S\alpha_{SE}}{1+\rho P_{RJ}\alpha_{RE}} + \frac{G^2\rho P_S\alpha_{RE}}{1+P_{SJ}\alpha_{SE}}\right). \tag{15}$$

The secrecy rate is here obtained as given as $R_S = \max\{R_d - R_e, 0\}$, whereas

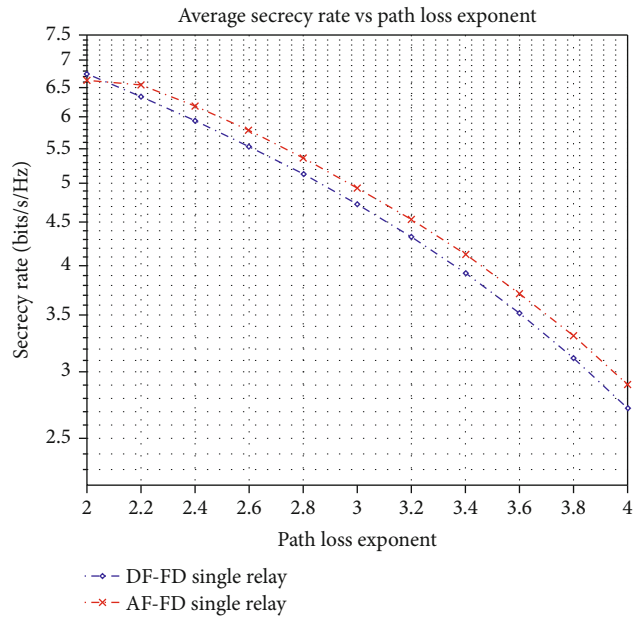

Figure 10: Secrecy capacity rate vs. PLE for the EH system.

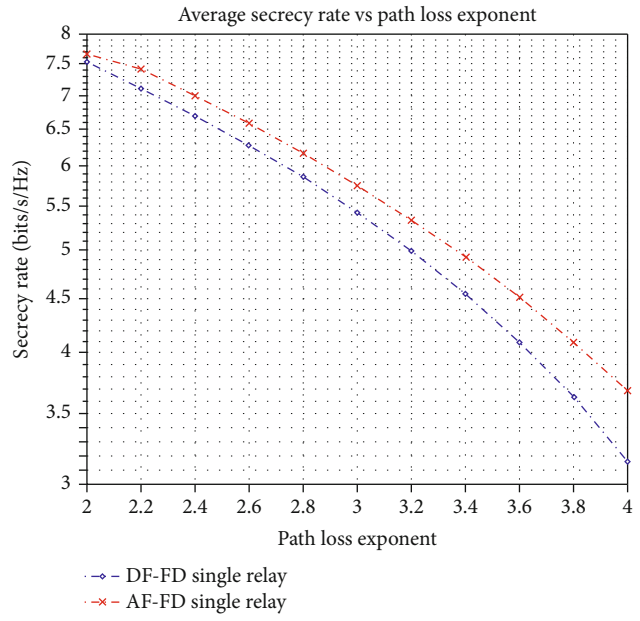

Figure 11: Secrecy capacity rate vs. PLE for the EH PS system.

$$R_d - R_e = \frac{1}{2}\log_2\left(\frac{1+\rho P_R\alpha_{RD}}{1+\left(P_S\alpha_{SE}/\left(1+P_J\alpha_{RE}\right)\right)+\left(G^2\rho P_S\alpha_{RE}/\left(1+P_{SJ}\alpha_{SE}\right)\right)}\right). \tag{16}$$

4. Numerical Results and Performance

This section presents the numerical results for the investigation of the secrecy performance of the proposed system model, in dual-hop EH and AF and DF cooperative scenarios in terms of relay distance. The numerical results based on the simulation model are shown in Figure 5; the S, R, and D are assumed to be the presence of a line of sight (LOS);

Table 3: Performance comparison of the cooperative scheme concerning their secrecy rate.

Reference	Techniques	Cooperative scheme	
		Amplify-forward	Decode-forward
[17]	HADF, FDR, EPA	29.26%	29.26%
[15]	Energy harvesting	8.89%	9.83%
[16]	Energy harvesting and jamming signal	23.63%	30.47%
[21]	AF and DF	11.9%	42.96%
[22]	HDR, AF, and DF	40%	41%
[20]	EH, TS, PS, FDR, SOP	50.5%	44.2%
Present article	EH, PS, AF, DF, single relay, HDR, FDR	65.5%	52.5%

moreover, d_{RD}, d_{RE}, d_{BS}, and d_{BR} indicate the distances between R and S nodes, between D and R, between E and R, between P_B and S, between R and P_B, and between S and R. The distance between S and E nodes can be, respectively, given as

$$d_{SE} = \sqrt{d_{SR}^2 + d_{RE}^2}. \quad (17)$$

Source, relay, and destination are located in the line of sight (LOS). The channel model configuration describes the channel between any two nodes, which is uniformly distributed within $[0, 2\pi]$, with path loss exponent $c = 3.50$ [17].

We assume that the transmission power of the beacon is $P_B = 30$ dBM and the noise power is $N_B = -40$ dBm.

Furthermore, it is assumed that $d_{BS} = id_{BR} = 14$ m. Moreover, $\alpha = 0.999$, $\eta = 1$, and $p = 3.5$.

The parameters used for the simulation of this research are shown in Table 2.

In Figures 6 and 7, we give the plot of the security performance AF and DF dual-hop scheme and distance between relay (R) and destination (D), when $d_{SR} = 25$ m, $d_{BR} = 14$ m , and $d_{RD} = 30$ m in the proposed EH system and PS EH system. The plot of secrecy capacity shows that the secrecy capacity decreases with increasing distance between destination and relay, but at the same time due to the power splitting receiver in the EH system, the secrecy rate is quite high which is good. Also, this figure clearly shows that the AF single-relay scheme gives a better secrecy rate than the DF single-relay scheme.

In Figures 8 and 9, we compare the secrecy rate distance between relay and eavesdropper between the AF and DF schemes, when $d_{SR} = 10$ m and $d_{RD} = 30$ m. The graph shows the secrecy rate in the energy harvesting (EH) system depending on the distance between R and E. In the proposed EH PS system, the secrecy rate is very high for the power splitting receiver. Also, in the AF scheme, the secrecy rate is better than that in the DF Scheme. Therefore, to increase the secrecy rate, it is important to use a share of useful power to relay jamming signals in both AF and DF.

In Figures 10 and 11, we plot the average secrecy rate as a function of the path loss exponent factor in the single-relay AF and DF schemes, when $d_{SR} = 10$ m, $d_{RD} = 15$ m, and $d_{RE} = 15$ m. Path loss plays a vital role in the calculation of the secrecy rate. The graph shows that as we increase the path loss exponent, the secrecy rate decreases gradually in both the existing EH systems and the proposed EH PS system. It is shown that the increment in the path loss exponent degraded the system secrecy capacity in both AF and DF schemes. This implies that self-interference should be minimized.

The comparison of the cooperative proposed techniques with the published literature is shown in Table 3.

5. Conclusions

In this study, we have proposed the energy harvesting single-relay cooperative system, to enhance the performance of secure wireless communications in the existence of one eavesdropper E and relay R. Under a total transmitted power constraint of 30 dBm and noise power of -40 dBm, the secrecy performance of a single-relay wireless cooperative system is investigated, and an innovative single-relay technique has been applied. In the proposed technique, each R transmits a signal to the E and gets a transmission signal at the same time. Two cooperative schemes have been examined: amplify-forward (AF) and decode-forward (DF) in energy harvesting. The results show that secrecy rate performance is improved by AF FDR for single relay to 65.5% and DF FDR for single relay to 52.5% in the energy harvesting power splitting system. Furthermore, we show that an increase in the path loss exponent degrades the performance of the system.

Notations

FDR: Full duplex relay
HADF: Hybrid decode forward
LOS: Line of sight
EPA: Equal power allocation
T: Transmission period of energy harvesting
n_E: Energy conversion efficiency of an eavesdropper
P_{RJ}: Power relay jamming
ρP_R: Signal of power relay
n_D: The energy efficiency of the destination
N_0: Noise variance
G: The fluctuation of the channel coefficient
h_{SR}^*: Channel gain source to relay
A: Time switching factor
P_E: Power signal eavesdropper

P_B: Power Beacon
d_{BR}: Distance beacon relay
R_e: Relay eavesdropper.

Data Availability

All the data have been included in the study.

Conflicts of Interest

The authors declare that they have no conflicts of interest.

References

[1] R. Francesco, N. Laurenti, and H. V. Poor, "Physical-layer secrecy for OFDM transmissions over fading channels," *IEEE Transactions on Information Forensics and Security*, vol. 7, no. 4, pp. 1354–1367, 2012.

[2] F. Jameel, W. U. Khan, M. A. Jamshed, H. Pervaiz, Q. Abbasi, and R. Jäntti, "Reinforcement learning for scalable and reliable power allocation in SDN-based backscatter heterogeneous network," in *IEEE INFOCOM 2020-IEEE Conference on Computer Communications Workshops (INFOCOM WKSHPS)*, Toronto, ON, Canada, 2020.

[3] W. U. Khan, N. Imtiaz, and I. Ullah, "Joint optimization of NOMA-enabled backscatter communications for beyond 5G IoT networks," *Internet Technology Letters*, vol. 4, no. 2, article e265, 2021.

[4] M. Bloch and J. Barros, *Physical-Layer Security: From Information Theory to Security Engineering*, Cambridge University Press, Cambridge, United Kingdom, 2011.

[5] F. Jameel, W. U. Khan, S. T. Shah, and T. Ristaniemi, "Towards intelligent IoT networks: reinforcement learning for reliable backscatter communications," in *2019 IEEE Globecom Workshops (GC Wkshps)*, pp. 1–6, Waikoloa, HI, USA, 2019.

[6] Y. Zeng and R. Zhang, "Full-duplex wireless-powered relay with self-energy recycling," *IEEE Wireless Communications Letters*, vol. 4, no. 2, pp. 201–204, 2015.

[7] K. M. Rabie, B. Adebisi, and M. -S. Alouini, "Half-duplex and full-duplex AF and DF relaying with energy-harvesting in log-normal fading," *IEEE Transactions on Green Communications and Networking*, vol. 1, no. 4, pp. 468–480, 2017.

[8] J. Shen, Y. Liu, H. Yang, and C. Yan, "Joint time allocation and power splitting schemes for amplify-and-forward relaying network over log-normal fading channel," in *2018 10th International Conference on Wireless Communications and Signal Processing (WCSP)*, pp. 1–5, Hangzhou, China, 2018.

[9] X. Li, M. Huang, C. Zhang et al., "Security and reliability performance analysis of cooperative multi-relay systems with nonlinear energy harvesters and hardware impairments," *Access IEEE*, vol. 7, pp. 102644–102661, 2019.

[10] T. M. Hoang, T. Q. Duong, N. S. Vo, and C. Kundu, "Physical layer security in cooperative energy harvesting networks with a friendly jammer," *IEEE Wireless Communications Letters*, vol. 6, no. 2, pp. 174–177, 2017.

[11] L. Elmorshedy, C. Leung, and S. A. Mousavifar, "RF energy harvesting in DF relay networks in the presence of an interfering signal," in *2016 IEEE International Conference on Communications (ICC)*, Kuala Lumpur, Malaysia, 2016.

[12] T. Mekkawy, R. Yao, F. Xu, and L. Wang, "Optimal power allocation for achievable secrecy rate in an untrusted relay network with bounded channel estimation error," in *2017 26th Wireless and Optical Communication Conference (WOCC)*, pp. 1–5, Newark, NJ, USA, 2017.

[13] G. Yanju and S. Aissa, "Interference aided energy harvesting in decode-and-forward relaying systems," in *IEEE International Conference on Communications, 2014 (ICC 2014)*, pp. 5378–5382, Sydney, NSW, Australia, 2014.

[14] Y. Alsaba, C. Y. Leow, and S. K. Abdul Rahim, "A game-theoretical modelling approach for enhancing the physical layer security of non-orthogonal multiple access system," *IEEE Access*, vol. 7, pp. 5896–5904, 2019.

[15] P. Jindal and R. Sinha, "Physical layer security with energy harvesting in single hop wireless relaying system," in *International Conference on Information Science and Applications*, pp. 249–256, Changsha, China, 2017.

[16] R. Sinha and P. Jindal, "A study of physical layer security with energy harvesting in single hop relaying environment," in *2017 4th International Conference on Signal Processing and Integrated Networks (SPIN)*, pp. 530–533, Noida, India, 2017.

[17] P. Jindal and R. Sinha, "Physical layer security with rf energy harvesting protocols for wireless networks," *Pertanika Journal of Science and Technology*, vol. 26, pp. 1677–1692, 2018.

[18] W. U. Khan, J. Liu, F. Jameel, M. T. R. Khan, S. H. Ahmed, and R. Jäntti, "Secure backscatter communications in multi-cell NOMA networks: enabling link security for massive IoT networks," in *IEEE INFOCOM 2020 - IEEE Conference on Computer Communications Workshops (INFOCOM WKSHPS)*, pp. 213–218, Toronto, ON, Canada, 2020.

[19] X. Li, M. Zhao, M. Zeng et al., "Hardware impaired ambient backscatter NOMA systems: reliability and security," *IEEE Transactions on Communications*, vol. 69, no. 4, pp. 2723–2736, 2021.

[20] N. Sehito, S. Yang, E. M. Ali et al., "Physical layer secrecy by power splitting and jamming in cooperative multiple relay based on energy harvesting in full-duplex network," *Electronics*, vol. 11, no. 1, 2021.

[21] S. Pal and P. Jindal, "Secrecy performance analysis for multi-hop and single-hop relaying model," in *Optical and Wireless Technologies Proceedings of OWT 2019*, Jaipur, India, 2020.

[22] K. D. Gawtham and P. Jindal, "Analysis of amplify and forward technique to improve secrecy rate in multi-hop relaying system," in *2016 IEEE International Conference on Recent Trends in Electronics, Information & Communication Technology (RTEICT)*, pp. 62–64, Bangalore, India, 2016.